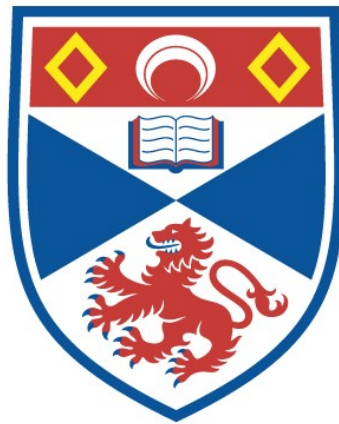


KINETIC MODELLING OF FUNDAMENTAL (00<sup>o</sup>1) AND  
SEQUENCE (00<sup>o</sup>2) BAND CO<sub>2</sub> LASERS

John Mellis

A Thesis Submitted for the Degree of PhD  
at the  
University of St Andrews



1984

Full metadata for this item is available in  
St Andrews Research Repository  
at:  
<http://research-repository.st-andrews.ac.uk/>

Please use this identifier to cite or link to this item:  
<http://hdl.handle.net/10023/14319>

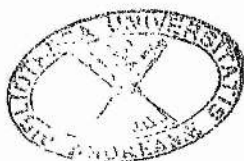
This item is protected by original copyright

(i)

KINETIC MODELLING OF FUNDAMENTAL ( $00^01$ )  
AND SEQUENCE ( $00^02$ ) BAND  $\text{CO}_2$  LASERS

John Mellis

A thesis submitted to the University  
of St. Andrews for the degree of  
Doctor of Philosophy.



ProQuest Number: 10166840

All rights reserved

INFORMATION TO ALL USERS

The quality of this reproduction is dependent upon the quality of the copy submitted.

In the unlikely event that the author did not send a complete manuscript and there are missing pages, these will be noted. Also, if material had to be removed, a note will indicate the deletion.



ProQuest 10166840

Published by ProQuest LLC (2017). Copyright of the Dissertation is held by the Author.

All rights reserved.

This work is protected against unauthorized copying under Title 17, United States Code  
Microform Edition © ProQuest LLC.

ProQuest LLC.  
789 East Eisenhower Parkway  
P.O. Box 1346  
Ann Arbor, MI 48106 – 1346

TR  
A117

Abstract

The vibrational kinetics of the CO<sub>2</sub> laser system are studied experimentally and theoretically. A sequence (00<sup>0</sup>2) band/fundamental (00<sup>0</sup>1) band gain ratioing technique is used to measure the CO<sub>2</sub> asymmetric stretch mode temperature (T<sub>3</sub>) in low-pressure cw laser discharges; the relationship of discharge current to electron density is determined by X-band microwave cavity resonance. The experimental measurements are compared to theory using a comprehensive computer model of CO<sub>2</sub> laser kinetics, based on the vibrational temperature approximation.

It is demonstrated that the observed saturation of vibrational temperature with increasing discharge current is caused by the de-activation of excited molecules by electron superelastic collisions, at a rate predicted by the principle of detailed balance. Superelastic collisions crucially determine the attainable vibrational temperatures, and limit T<sub>3</sub> to values below the optimum for 00<sup>0</sup>1 or 00<sup>0</sup>2 band laser action. The associated laser gain limitations are investigated, and it is shown that superelastic collisions inflict efficiency losses on pulsed TE CO<sub>2</sub> lasers even at moderate input energies.

The operating characteristics of CO<sub>2</sub> sequence band lasers are also examined. A comparison of oscillator performance with corresponding small-signal gain measurements indicates a sequence band saturation intensity which is higher than that of the fundamental band. This observation is supported by model computations, which predict that the extractable 00<sup>0</sup>2 band laser power ( $\alpha_o I_s$ ) is typically 60% of that available on the 00<sup>0</sup>1 band.

Dedicated with the greatest love  
and gratitude to my father  
William McCarroll Mellis 1921 - 1982

Acknowledgements

During this work, which spanned two Universities and more than four years, many people have made invaluable contributions. In particular I thank Professor A.L.S. Smith for his enthusiastic and very resourceful supervision, and it is a pleasure to acknowledge the fine technical assistance of Norrie Campbell and the skilful glass-blowing of Frits Akerboom and Donny Cringean. Great thanks are also due to Dr. Robin Thomson for his provision of output data from his BOLTZ program, and to Dr. Steve Moffatt, who originally designed the sequence band laser, for many fruitful and enjoyable discussions which ranged across (and well beyond!) the field of laser physics.

I thank my family and friends for their patience and tolerance during the preparation of this thesis, and I am indebted to Mrs. Anne Ogilvie and Mrs. Cathie Dickson for their careful typing of the manuscript. Finally, I gratefully acknowledge the financial support of the Science and Engineering Research Council and of the Laser Systems Department of British Aerospace Dynamics Group.

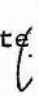
Career

John Mellis was born in Glasgow, Scotland in 1956 and educated there at Hillhead High School and the University of Strathclyde, where he graduated with First Class Honours from the Department of Applied Physics in 1978, after several short periods in the Laser Development Department of Barr & Stroud Limited and the Philips Research Laboratories, Surrey. The work described here was performed in the School of Physical Sciences of the University of St. Andrews and in the Department of Natural Philosophy at the University of Strathclyde, where since 1981 the author has been a Research Fellow, supported by the Laser Systems Department of British Aerospace.



Declaration

I was admitted as a research student under Ordinance No.12 in October 1978 and as a candidate for the degree of Ph.D. in October 1979; the higher study for which this is a record was carried out in the School of Physical Sciences of St. Salvators College in the University of St. Andrews and in the Department of Natural Philosophy of the University of Strathclyde between 1978 and 1982.

Date 13th July 1983 Signature of candidate 

In submitting this thesis to the University of St. Andrews I understand that I am giving permission for it to be made available for use in accordance with the regulations of the University Library for the time being in force, subject to any copyright vested in the work not being affected thereby. I also understand that the title and abstract will be published and that a copy of the work may be made and supplied to any bona fide library or research worker.

- (a) I hereby certify that this thesis, which is approximately 40,000 words in length, has been written by me, that it is the record of work carried out by me, and that it has not been submitted in any previous application for a higher degree.

Date 13th July 1983 Signature of candidate *f*

- (b) I hereby certify that the candidate has fulfilled the conditions of the Resolution and Regulations appropriate to the degree of Doctor of Philosophy of the University of St. Andrews and that he is qualified to submit this thesis in application for that degree.

Date \_\_\_\_\_ Signature of supervisor

CONTENTS

	<u>Page No.</u>
CHAPTER 1 : INTRODUCTION	
1.1 Fundamental ( $00^0_1$ ) and sequence ( $00^0_2$ ) band $\text{CO}_2$ lasers	1
1.2 Modelling $\text{CO}_2$ laser kinetics	
1.2.1 Review	4
1.2.2 Preview	9
CHAPTER 2 : BASIC PRINCIPLES OF $\text{CO}_2$ LASER KINETICS	
2.1 Discharge electron kinetics	
2.1.1 Electron energy distribution functions and the Boltzmann equation	14
2.1.2 Vibrational excitation rates and the principle of detailed balance	17
2.1.3 A Boltzmann equation solver: BOLTZ	19
2.2 The vibrational temperature approximation	20
2.3 Laser gain and line broadening mechanisms	27
CHAPTER 3 : $\text{CO}_2$ DISSOCIATION EFFECTS ON DISCHARGE KINETICS	
3.1 Introduction	31
3.2 Investigative methods and results	
3.2.1 $\text{CO}_2$ dissociation rates	32
3.2.2 Dissociation effects on vibrational excitation rates	36
3.2.3 Dissociation effects on the current-voltage characteristics of cw $\text{CO}_2$ laser discharges	41
3.3 Conclusions	46
CHAPTER 4 : X-BAND CAVITY RESONANCE MEASUREMENTS OF ELECTRON DENSITY	
4.1 Introduction	49
4.2 Method	
4.2.1 Theory	49
4.2.2 Previous work	52
4.2.3 Experimental arrangement	53
4.3 Results	
4.3.1 Pure Helium	56
4.3.2 Laser mixtures	61

	<u>Page No.</u>
4.3.3 Effect of CO <sub>2</sub> dissociation	67
4.3.4 Effect of Xe addition	69
4.4 Discussion and conclusions	71
 CHAPTER 5 : A MODEL OF VIBRATIONAL EXCHANGE IN THE CO <sub>2</sub> LASER SYSTEM: VIBEX	
5.1 Introduction	75
5.2 Model structure	
5.2.1 The population rate equations	75
5.2.2 Rate constant data	80
5.2.3 Solution method	83
5.3 5.3.1 Program flow-chart and definition of vibrational temperatures	90
5.3.2 Calculation of effective superelastic rate constants	92
5.3.3 Calculation of the symmetric stretch- bending mode temperature $T_1 = T_2$	93
5.3.4 Treatment of stimulated emission	94
5.4 Initial tests and results	95
 CHAPTER 6 : CO <sub>2</sub> LASER VIBRATIONAL KINETICS MODELLING - THEORY AND EXPERIMENT	
6.1 Background	102
6.2 Experimental equipment and procedure	104
6.3 Experimental results and comparison of model predictions	
6.3.1 Vibrational temperature saturation	107
6.3.2 Specification of effective superelastic rate constants	114
6.3.3 Effects on vibrational temperature of gas mixture, pressure and flow rates	117
6.4 Computer model experiments	
6.4.1 Effects of E/N and gas temperature	126
6.4.2 Effect of radial diffusion	134
6.4.3 Effect of stimulated emission	138
6.4.4 Consideration of third-order superelastic effects	144
6.5 Discussion and conclusions	146

	<u>Page No.</u>
CHAPTER 7 : MODELLING PULSED TE CO <sub>2</sub> LASERS	
7.1 Introduction	151
7.2 Background	151
7.3 Computer modelling	
7.3.1 Method	152
7.3.2 Results	154
7.4 Conclusions	162
CHAPTER 8 : OPERATING CHARACTERISTICS OF CO <sub>2</sub> SEQUENCE BAND LASERS	
8.1 Introduction	165
8.2 Recent background	167
8.3 Operating characteristics of a cw CO <sub>2</sub> laser on the OO <sup>0</sup> <sub>2</sub> sequence band	
8.3.1 Experimental arrangement and initial results	170
8.3.2 Effects of gas additives: Xe, CO and H <sub>2</sub>	178
8.3.3 Output power and gain measurements	186
8.3.4 Analysis and discussion	188
8.4 Modelling gain saturation on the OO <sup>0</sup> <sub>1</sub> and OO <sup>0</sup> <sub>2</sub> bands	192
8.5 Summary and conclusions	199
CHAPTER 9 : CONCLUSIONS AND RECOMMENDATIONS	
9.1 Summary	202
9.2 Discussion	204
9.3 Recommendations	206
Appendix A : Voltage-current characteristics of typical CO <sub>2</sub> laser discharges	210
Appendix B : The observation of an anomalous dependence of electron density on pressure	218
Appendix C : The calculation of T <sub>1</sub> = T <sub>2</sub> in VIBEX	225
Appendix D : Gain limitations in CO <sub>2</sub> lasers (reproduced from Optics Communications <u>41</u> , 2, 121 (1982))	227
Appendix E : Operating efficiencies in pulsed carbon dioxide lasers (reproduced from Applied Physics Letters <u>41</u> , 1037 (1982))	232
Appendix F : Listing of VIBEX	235

## CHAPTER 1 : INTRODUCTION

### 1.1 Fundamental (00<sup>0</sup>1) and Sequence (00<sup>0</sup>2) Band CO<sub>2</sub> Lasers

Since the discovery of laser action on the 00<sup>0</sup>1 - (10<sup>0</sup>0, 02<sup>0</sup>0)<sub>I,II</sub> bands by Patel<sup>1-3</sup>, the CO<sub>2</sub> laser has developed to become one of the most powerful, efficient and useful laser systems known. Its development has been accompanied by an increased understanding of the plasma and vibrational kinetics of the laser medium. For example, the addition of N<sub>2</sub> to the basic CO<sub>2</sub> increased the output power of the low pressure cw laser by three orders of magnitude<sup>4</sup> to around 10W; further improvements, to powers of around 100W and efficiencies of 10%, were obtained by the addition of He and water vapour and by the introduction of discharge tube cooling.<sup>5</sup> The beneficial effects of the additives were understood in terms of enhanced excitation of the CO<sub>2</sub>(00<sup>0</sup>1) upper laser level by vibration-vibration(V-V) resonant energy exchange with N<sub>2</sub>, and faster relaxation of the(10<sup>0</sup>0) and(02<sup>0</sup>0) lower laser level populations by vibration-translation (V-T) collisions with He, H<sub>2</sub> and H<sub>2</sub>O. The high thermal conductivity of He aided gas cooling, reducing the thermal population of the lower laser levels, and water vapour addition was found to have the beneficial effect of reducing the level of CO<sub>2</sub> dissociation caused by the impact of discharge electrons with energies 7eV or greater.<sup>6,7</sup> Dissociation control was shown to be crucial for the production of CO<sub>2</sub> lasers with long sealed-off lifetimes.

In 1969-70 the laser operating regime was extended to atmospheric pressure by the use of pulsed electrical excitation applied to electrodes positioned parallel to the axis of the optical

cavity.<sup>8,9</sup> Such transversely excited atmospheric pressure (TEA) lasers produced a further improvement in output energy densities and peak powers. However this improvement was at the expense of a truly stable electric discharge, and a variety of stabilising preionisation techniques have been developed using auxiliary discharge trigger wires,<sup>10</sup> UV photoionisation,<sup>11</sup> electron beam injection<sup>12</sup> and recently X-ray photo-preionisation.<sup>13</sup> Such techniques have allowed stable discharge operation to super-atmospheric pressures for a wide range of excitation pulse lengths.

New 10  $\mu\text{m}$  laser bands were observed in continuous emission from a cw  $\text{CO}_2$  laser by Reid and Siemsen<sup>14</sup> in 1976. These were identified as the  $00^0_2 - (10^0_1, 02^0_1)_{\text{I,II}}$  "sequence" bands, (shown in Figure 1.1) and share many of the characteristics of the fundamental  $00^0_1$  bands. However, the anharmonicity of the  $\text{CO}_2$  asymmetric stretch mode produces a small shift ( $\sim 0.5 \text{ cm}^{-1}$ ) in the relative emission frequencies of the  $00^0_2$  sequence band vibrational-rotational transitions. This gives rise to a number of applications well-suited to sequence band lasers, including long-path atmospheric propagation, molecular spectroscopy, and the optical pumping of far infra-red (FIR) laser transitions outside the tuning range of fundamental band  $\text{CO}_2$  lasers. Additionally, a most important use of sequence band lasers is the probing of the gain dynamics of  $\text{CO}_2$  laser discharges and the determination of  $\text{CO}_2$  asymmetric stretch mode vibrational temperatures.

The  $\text{CO}_2$  laser literature is voluminous, and it is outwith the scope of this work to consider the details of laser performance and technology. Instead, the aim is a comprehensive experimental and theoretical study of  $\text{CO}_2$  laser dynamics, taking full account of

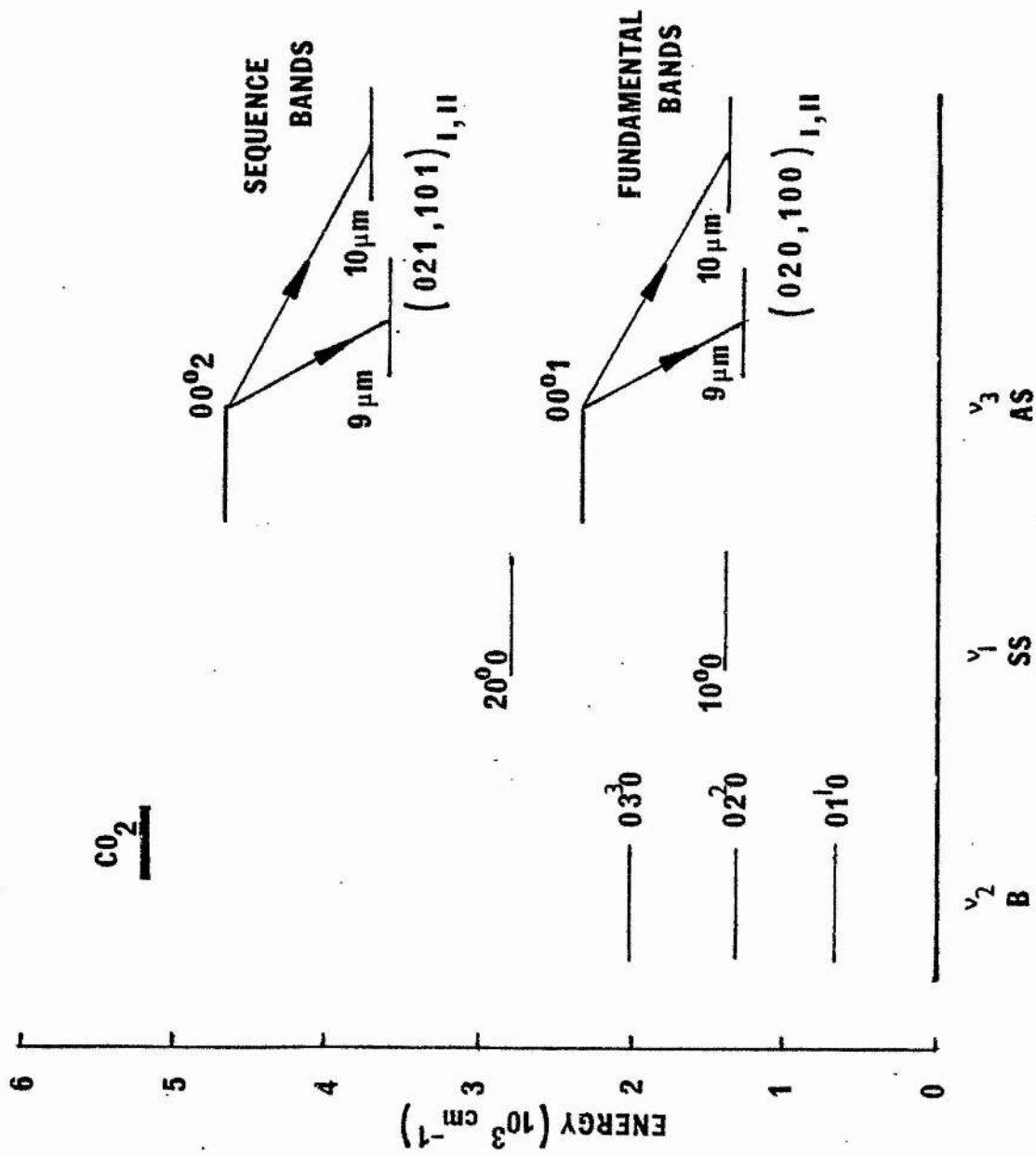


Fig. 1.1.1. Important vibrational energy levels in CO<sub>2</sub>.



the challenge and opportunity afforded by  $00^0_2$  sequence band lasers. Conventional models of  $\text{CO}_2$  kinetics are untested in the prediction of sequence band laser behaviour; the accurate prediction of  $00^0_2$  band gain and saturation intensity is therefore a demanding, but worthwhile requirement of any  $\text{CO}_2$  kinetics model. Conversely, the utility of sequence band lasers in the measurement of  $\text{CO}_2$  vibrational temperatures allows, for the first time, a comparison between theory and experiment at a basic level. In the following study such comparisons will be made in order to (i) improve our general understanding of  $\text{CO}_2$  laser kinetics (ii) establish valid kinetic modelling techniques and (iii) investigate the limitations of  $00^0_1$  and  $00^0_2$  band laser performance.

## 1.2 Modelling $\text{CO}_2$ laser kinetics

### 1.2.1 Review

The complexity of  $\text{CO}_2\text{-N}_2\text{-CO-He}$  vibrational kinetics precludes any attempt at mathematical simulation of the system without some simplifying assumptions. In 1967, Gordiets et al.<sup>15-17</sup> pointed out that the rate of V-V exchange within a given vibrational mode is much faster than the rate of energy transfer to translation, the rate of transfer between different modes, and the rate of pumping into the mode by electron impact excitation. Under these circumstances, the population within the vibrational mode should follow a Boltzmann distribution, described by a single vibrational temperature  $T_i$ . That is if  $n(v)$  is the population of the level with vibrational quantum number  $v$ , and  $h\nu_i$  is the vibrational level spacing of mode  $i$  (assumed harmonic), then

$$\frac{n(v)}{n(0)} = \exp\left(\frac{-v h \nu_i}{k T_i}\right) \quad (1.1)$$

This "vibrational temperature" approximation allowed the formulation of a relatively compact set of simultaneous rate equations describing the V-V and V-V-T inter-mode energy exchanges as well as the processes of electron excitation and de-excitation of the  $N_2$  and  $CO_2(v_3)$  modes. Since Gordiets et al. were interested in the simulation of low pressure D.C. excited lasers, they also included the loss of vibrational energy by radial diffusion of excited molecules and their quenching by collision with the discharge tube walls. The resulting rate equation system is non-linear and cumbersome to solve analytically; however further simplifying assumptions (viz. that the bending and symmetric stretch mode temperatures ( $T_1, T_2$ ) are low and  $N_2-CO_2(v_3)$  V-V exchange is much faster than the other V-V-T processes) allowed an analytic solution in terms of the vibrational mode temperatures, which were then interpreted to yield laser level populations and population inversions. No explicit predictions of vibrational temperatures were made, but the predicted variations of population inversion with gas mixture, pressure and temperature showed good qualitative agreement with experiment. Quantitative agreement was poor, with predicted inversions around 5-7 times the typical measured values. This is possibly due to the large uncertainty surrounding the electron impact excitation rates, which were only roughly estimated on the basis of poorly known excitation cross-sections, assuming a Maxwellian plasma electron energy distribution. Nevertheless the work of Gordiets et al. represented an important development in the modelling of  $CO_2$  laser kinetics, and the overwhelming majority of kinetics models have adopted a very similar approach. For example, Tyte and Wills (1969) used an analytic solution of a rate equation model based on the vibrational mode scheme to predict the parametric

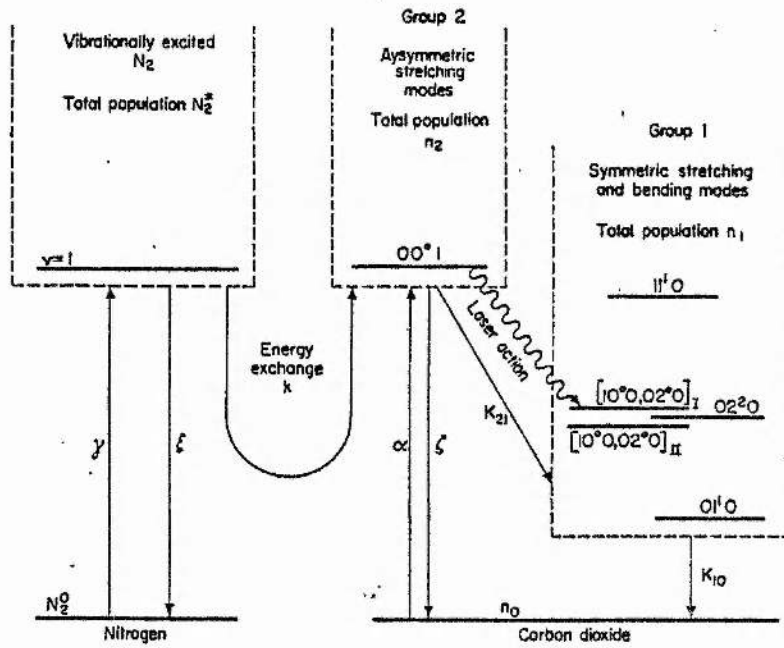


Fig. 1.2. Structure of the kinetics model of Tyte and Wills, showing the partition of the energy level system into convenient vibrational mode groups (from reference 18).

dependence of the saturation intensity in cw CO<sub>2</sub> lasers.<sup>18</sup> Figure 1.2 illustrates their model. Electron excitation and de-excitation rates are represented by Greek letters; combined electron and collisional de-excitation rates in CO<sub>2</sub> are represented by  $K_{21}$  and  $K_{10}$ . Again the electron excitation rates were estimates based on inadequately known cross-sections and discharge electron densities. Tyte and Wills' solution of their rate equation model revealed the principle disadvantage of analytic methods: their expression for the saturation intensity in CO<sub>2</sub> lasers was a complex function of all the system rate constants, obscuring the parametric dependence of the saturation intensity and making tedious any calculation of the effect of systematic changes. This limitation was overcome by Tulip (1970) who calculated saturation intensities using a computerised solution of his vibrational rate equation system.<sup>19</sup> Electron excitation rates were arbitrary, and the process of electron de-excitation was neglected. The solutions predicted a CO<sub>2</sub> asymmetric mode vibrational temperature which rises monotonically with increasing electron excitation, and saturation intensities of the order of 50W cm<sup>-2</sup>.

The first numerical analysis of the CO<sub>2</sub> TEA laser was that of Manes and Seguin<sup>20</sup> in 1972. A five temperature model of the CO<sub>2</sub>-N<sub>2</sub>-He system was used to predict the output power pulse-shape dependence on gas mixture, optical cavity parameters and electric pumping levels. Here the electron excitation rates were again estimated from earlier cross-sections and a knowledge of the effective electric fields and electron densities which prevail in atmospheric pressure pulsed CO<sub>2</sub> lasers. (It should be noted that the spatial homogeneity of high-pressure discharges makes the estimates

of electron density and  $E/N$  rather more reliable than in the low-pressure positive column laser, where radial profiles of gas temperature and discharge current are a complicating factor). Manes and Seguin neglected the role of electron de-excitation, and made the approximation of constant gas temperature during the excitation and laser pulse. Nevertheless their calculated pulse shapes showed good agreement with corresponding laboratory measurements.

More recent years have seen the appearance of numerous  $\text{CO}_2$  laser discharge and kinetics models. An important development has been the construction of increasingly sophisticated computer-based solutions of the Boltzmann electron transport equation, allowing the detailed calculation of discharge electron energy distribution functions (E.D.F.'s), transport properties (drift velocity, diffusion coefficients) and effective electron impact excitation and ionisation rate constants. Such calculations take account of the inherently non-Maxwellian E.D.F.'s which typify molecular gas discharges, and usually include the effects of electron impact vibrational excitation, de-excitation, ionisation and elastic scattering. In particular, the Boltzmann codes of Nighan,<sup>21</sup> Nighan and Bennett<sup>22</sup> and Lowke et al.<sup>23</sup> enabled the calculation of the power lost by electrons to all the important inelastic excitation channels in the  $\text{CO}_2$  system, predicting that for an optimum  $E/N$  ( $\sim 3 \times 10^{-16} \text{Vcm}^2$ ) then 60-90% of the discharge power is used usefully in  $\text{CO}_2$  ( $\nu_3$ ) or  $\text{N}_2$  vibrational excitation. A Boltzmann analysis by Judd<sup>24</sup> showed that vibrational excitation rates scale well with the average electron energy for a wide range of  $\text{CO}_2$ - $\text{N}_2$ -He gas mixtures, and recently Thomson et al.<sup>25</sup> have used a Boltzmann code to predict vibrational excitation rates in

CO<sub>2</sub> laser mixtures including the effects of dissociation products CO and O<sub>2</sub>.

### 1.2.2 Preview

The increasingly sophisticated and detailed electron kinetics codes mentioned above have not been complemented by any great improvement in the formulation and use of vibrational kinetics models. For example, Cohen (1976)<sup>26</sup> drew heavily on the earlier models of Gordiets et al. and Moore et al.<sup>27</sup> to obtain analytic solutions of a rate equation system describing the small-signal gain dynamics of CO<sub>2</sub> waveguide lasers. Davies et al. (1976)<sup>28</sup> and Comly et al. (1981)<sup>29</sup> have respectively modelled the vibrational kinetics of CO<sub>2</sub> TEA and electron-beam controlled lasers. Despite the fact that these models used Boltzmann codes to calculate the required electron excitation rate constants, neither took account of the possible importance of electron collisional deactivation of excited molecules, and must be considered incomplete for this reason. A more general criticism of such models can also be made: usually predictions are made of laser gains, saturation intensities, output pulse shapes, etc. These parameters are complex functions of the laser medium's kinetic processes; reasonable accuracy in their prediction is not a rigorous test of the correctness of the underlying kinetics model. A more stringent examination of kinetic modelling techniques is required, such as would be provided by a comparison of calculated and measured vibrational temperatures or vibrational mode populations. The advent of the CO<sub>2</sub> sequence band laser has provided a convenient method for the laboratory measurement of vibrational temperatures, and the prediction of sequence band laser parameters provides a new and

additional test for CO<sub>2</sub> kinetics models.

Therefore we can anticipate the requirements of an improved approach to CO<sub>2</sub> laser kinetic modelling:

(i) All kinetics processes of likely importance should be analysed, including the effects of the dissociation products CO and O<sub>2</sub>, electron collisional deactivation of excited molecules, thermal populations of vibrational energy levels and radial diffusion in low-pressure discharges.

(ii) Model input data, particularly electron excitation rate coefficients and molecular V-V-T relaxation rates, should be as well-founded as possible: the use of a Boltzmann code to generate the electron transport coefficients is desirable.

(iii) Predictive model calculations should be testable by comparison to experiment at a fundamental level: laboratory measurements of CO<sub>2</sub> vibrational temperatures are required.

(iv) Laser parameters for the important 00<sup>0</sup>2 sequence band must be characterised.

This report describes the formulation of a kinetics model designed to meet these requirements, and its use in a theoretical and experimental study of CO<sub>2</sub> laser operation on the fundamental (00<sup>0</sup>1) and sequence (00<sup>0</sup>2) bands. The following section details the basic principles of CO<sub>2</sub> vibrational, electron and gain dynamics. Chapters 3 and 4 describe preliminary experiments used to derive information on discharge electric fields (E/N) and electron densities. The structure of the vibrational kinetics model is explained in Chapter 5 and subsequently its predictions are compared to laboratory measurements of vibrational temperatures and laser efficiencies.

Finally, an experimental investigation of the operating characteristics of the cw  $00^{\circ}2$  band laser is described in Chapter 8, and the kinetics model is used to study  $00^{\circ}2$  band gain and gain saturation. Conclusions and recommendations are presented in Chapter 9.



References for Chapter 1

1. C.K.N. Patel, W.L. Faust and R.A. McFarlane, Bull. Amer. Phys. Soc. 9, 500 (1964).
2. C.K.N. Patel, Phys. Rev. Lett. 12, 588, (1964).
3. C.K.N. Patel, Phys. Rev. 136A, 1187, (1964). The subscript notation is now in common use and allows for the Fermi resonant mixing of the  $10^{\circ}0$  and  $02^{\circ}0$  levels. The zero-order notation is not strictly appropriate for the resulting pair of mixed levels, which are labelled I, II in descending order of vibrational energy. Thus the regular  $9.4 \mu\text{m}$  lower level, written  $02^{\circ}0$  in zero-order notation, becomes the  $(10^{\circ}0, 02^{\circ}0)_I$  level.
4. C.K.N. Patel, Phys. Rev. Lett. 13, 617 (1964).
5. T.J. Bridges and C.K.N. Patel, Appl. Phys. Lett. 7, 244, (1965).
6. W.J. Witteman, IEEE J. Quant. Electron. QE-2, 375 (1966).
7. A.L.S. Smith, Brit. J. Phys. D. (Appl. Phys), Ser. 2, 2, 1129 (1969).
8. R. Dumanchin and J. Rocca-Sierra, C.R. Acad. Sci. 269, 916 (1969).
9. A.J. Beaulien, Appl. Phys. Lett. 16, 504, (1970).
10. H.M. Lamberton and P.R. Pearson, Electronics Lett. 7, 141, (1971).
11. H. Seguin and J. Tulip, Appl. Phys. Lett. 21, 414, (1972).
12. C.A. Fenstermacher, M.J. Nutter, W.T. Leland and K. Boyer, Appl. Phys. Lett. 20, 56 (1972).
13. S.C. Lin and J.I. Levatter, Appl. Phys. Lett. 34, 305, (1979).
14. J. Reid and K.J. Siemsen, Appl. Phys. Lett. 29, 250 (1976).
15. B.F. Gordiets, N.N. Sobolev, V.V. Sokovikov and L.A. Shelepin, Phys. Lett. 25A, 2, 173 (1967).
16. B.F. Gordiets, N.N. Sobolev and L.A. Shelepin, Sov. Phys. JETP, 26, 5, 1039, (1968).

17. B.F. Gordiets, N.N. Sobolev, V.V. Sokovikov and L.A. Shelepin, IEEE J. Quant. Electron. Quant. Electron. QE-4, 11, 796 (1968).
18. D.C. Tyte and M.S. Wills, Proc. IERE Conf. On Lasers and Opto-electronics, Southampton (1969); reviewed by D.C. Tyte in "Progress in Quantum Electronics" Vol. 1 (Academic Press, 1970).
19. J. Tulip, IEEE J. Quant. Electron. QE-6, 4, 206 (1970).
20. K.R. Manes and H.J. Seguin, J. Appl. Phys. 43, 12, 5073 (1972).
21. W.L. Nighan, Appl. Phys. Lett. 15, 355 (1969).
22. W.L. Nighan and J.H. Bennett, Appl. Phys. Lett. 14, 240 (1969); Phys. Rev. A2, 1989 (1970).
23. J.J. Lowke, A.V. Phelps and B.W. Irwin, J. Appl. Phys. 44, 4664 (1973).
24. O.P. Judd, J. Appl. Phys. 45, 4572 (1974).
25. R.M. Thomson, K. Smith and A.R. Davies, Comp. Phys. Commun. 11, 369 (1976).
26. S.C. Cohen, IEEE J. Quant. Electron, QE-12, 4, 237, (1976).
27. C.B. Moore, R.E. Wood, B.L. Hu and Y.T. Yardley, J. Chem. Phys. 46, 4222 (1967).
28. A.R. Davies, K. Smith and R.M. Thomson, J. Appl. Phys. 47, 2037 (1976). (1976).
29. J.R. Comly, W.T. Leland, C.J. Elliott, A.M. Hunter and M.J. Kircher, IEEE J. Quant. Electron, QE-17, 9, 1786 (1981).

CHAPTER 2 : BASIC PRINCIPLES OF CO<sub>2</sub> LASER KINETICS

2.1 Discharge electron kinetics

2.1.1 Electron energy distribution functions and the Boltzmann transport equation

In a gaseous plasma, the energy distribution of the free electrons is governed by the Boltzmann equation, analysis of which is well developed.<sup>1,2</sup> For a spatially uniform gas in the presence of a steady electric field  $\underline{E}$  the Boltzmann equation has the form

$$\frac{-e\underline{E}}{m} \cdot \nabla_{\underline{v}} f(\underline{v}) = \frac{\delta f}{\delta t}(\underline{v}) \quad (2.1)$$

where  $e$ ,  $m$  and  $\underline{v}$  are the electron charge, mass and velocity and  $f(\underline{v})$  is the electron velocity distribution function. The right hand side of (2.1) represents the rate of change of  $f(\underline{v})$  due to electron collisions of all types and is called the collision integral. The effects of both elastic and inelastic collisions must be included. For elastic electron-molecule collisions the large mass difference results in small energy transfers and large electron deflections. It follows that  $f(\underline{v})$  can be separated into two parts:

$$f(\underline{v}) = f_0(\underline{v}) + \frac{\underline{v}}{v} \cdot \underline{f}_1(\underline{v}) \quad (2.2)$$

where  $f_0(\underline{v})$  is isotropic (i.e. spherically symmetric in velocity space) and  $\underline{f}_1(\underline{v})$  is the small anisotropy induced by the applied electric field. Using the expansion, (2.1) is resolved into two coupled equations:

$$\frac{-e\underline{E}}{3mv^2} \cdot \frac{d}{dv} (v^2 \underline{f}_1(\underline{v})) = \frac{\delta f_0}{\delta t}(\underline{v}) \quad (2.3)$$

$$\frac{-e\underline{E}}{m} \frac{df_0(\underline{v})}{dv} = \frac{\delta \underline{f}_1}{\delta t}(\underline{v}) \quad (2.4).$$

These equations are derived using the fact that since the distribution of  $\underline{v}$  is nearly isotropic, terms depending on the directions of  $\underline{v}$ , yet quadratic in  $\underline{v}$ , can be replaced by their average over all directions<sup>3</sup>. Terms of the form  $\underline{v} \cdot (\underline{v} \cdot \underline{A})$  where  $\underline{A}$  is independent of

the direction of  $\underline{v}$  have been replaced by  $\frac{1}{3} v^2 \underline{A}$ .

The right hand side of (2.4) represents the effect of collisions on the asymmetry of the distribution function. Here electron-heavy particle momentum transfer collisions play the major role, so assuming the rate of decrease of the asymmetric part  $\underline{f}_1$  is proportional to the number of collisions times the degree of asymmetry,

$$\frac{\delta \underline{f}_1(\underline{v})}{\delta t} = -\nu_m(\underline{v}) \underline{f}_1(\underline{v}) \quad (2.5).$$

The momentum transfer collision frequency  $\nu_m$  is related to the corresponding heavy species number density and momentum transfer cross-section by  $\nu_m = N Q_m(\underline{v}) v$ . Combining (2.3), (2.4) and (2.5) we obtain an equation for the isotropic part of  $f(\underline{v})$ . After transformation to the new variable  $u = mv^2/2e$  where  $u$  is the electron kinetic energy (eV), this takes the form

$$-\frac{E^2}{3} \frac{d}{du} \left\{ u \frac{df_0}{du} (\sum_s N_s Q_{ms}(u))^{-1} \right\} = \frac{\delta f_0}{\delta t} \quad (2.6)$$

where the sum is over all  $s$  species of heavy particle. This is the generalised form of the Boltzmann equation, normalised so that

$$\int_0^\infty u^{1/2} f_0(u) du = 1 \quad (2.7)$$

which implies that the fraction of electrons with energy between  $u$  and  $(u + du)$  is  $u^{1/2} f_0(u) du$ . The right-hand side of (2.6) represents the combined effect on the distribution function of elastic and inelastic electron-neutral collisions, as well as electron-electron and electron-ion collisions. A general solution for  $f_0(u)$  when all types of collision are important is practically impossible because of the lack of collision cross-section data. However for weakly ionised ( $<10^{-5}$ )  $\text{CO}_2$  laser discharges, electron-electron and electron-ion collisions are not important. Furthermore elastic electron-neutral collisions have a negligible effect on  $f(u)$  since the energy exchanged is

negligible compared to that transferred by inelastic collisions (resulting in molecular vibrational and electronic excitation) and superelastic collisions (resulting in molecular de-excitation). Thus only the effects of inelastic and superelastic collisions need be included in the collision integral and

$$\frac{\delta f}{\delta t} = \sum_{s,l} N_j \left\{ (u + u_{sl}) f(u + u_{sl}) Q_{sl}(u + u_{sl}) - u f(u) Q_{sl}(u) \right\} \quad (2.8)$$

where  $Q_{sl}(u)$  is the electron cross-section for excitation (or de-excitation) of the vibrational or electronic level of neutral species  $s$ , with a corresponding energy loss (or gain)  $u_{sl}$ . A working equation for  $f(u)$  is obtained by substituting (2.8) in (2.6), dividing by the total neutral molecule density  $N$ , and integrating

$$-\frac{1}{3} \left(\frac{E}{N}\right)^2 u \frac{df}{du} \left( \sum_s \delta_s Q_{sl}(u) \right)^{-1} = \sum_{s,l} \delta_s \int_u^{u+u_{sl}} u f(u) Q_{sl}(u) du \quad (2.9)$$

where  $\delta_s = N_s/N$  is the fractional concentration of species  $s$ . This is the form of the Boltzmann equation derived by Nighan.<sup>2</sup> For a specific value of  $E/N$  and a given gas mixture, knowledge of the relevant cross-sections allows a solution for  $f(u)$ . Reliable cross-section data are available for  $\text{CO}_2$ ,  $\text{N}_2$ ,  $\text{CO}$  and  $\text{He}$ , and distribution functions in  $\text{CO}_2$  laser mixtures have been calculated by Nighan and other workers.<sup>4,5</sup> The results show that at very low  $E/N$  ( $< 3 \times 10^{-17} \text{ Vcm}^2$ ) a Maxwell-Boltzmann distribution applies, defined by a single electron

temperature  $T_e$ :

$$f(u, T_e) = (2\pi)^{-3/2} T_e^{-3/2} \exp\left(\frac{-u}{kT_e}\right) \quad (2.10).$$

However, at  $E/N$  typical of laser discharge conditions ( $3 \times 10^{-16} \text{ Vcm}^2$ ) the distribution functions are markedly non-Maxwellian, showing a depletion of electrons with energy greater than about 2eV. This

reflects the large  $N_2$ , CO and  $CO_2$  vibrational cross-sections in the 2 - 5eV range; these present a barrier which prevents electrons from reaching higher energies.

### 2.1.2 Vibrational excitation rates and the principle of detailed balance

The solution of the time-independent Boltzmann equation (2.9) is  $f(u, E/N, T)$  where  $T$  is the ambient gas temperature. In terms of this solution, the electron-molecule vibrational excitation rate is<sup>3</sup>

$$X_n \left( \frac{E}{N}, T \right) = \frac{\sum_{\ell} \alpha_{\ell n} (2e/m)^{1/2} \int_0^{\infty} Q_{s\ell}(u) f(u, E/N, T) u \, du}{\int_0^{\infty} f(u, E/N, T) u^{1/2} \, du} \quad (2.11)$$

where the summation is over the vibrational levels  $\ell$  of mode  $n$ . That is,

$$X_n(E/N, T) = \sum_{\ell} \alpha_{\ell n} X_{\ell n} \quad (2.12)$$

where

$$X_{\ell n} = (2e/m)^{1/2} \frac{\int_0^{\infty} Q_{s\ell}(u) f(u, E/N, T) u \, du}{\int_0^{\infty} f(u, E/N, T) u^{1/2} \, du} \quad (2.13).$$

$X_n$  is the effective excitation rate to the vibrational mode  $n$  comprising  $\ell$  levels. The  $\alpha_{\ell n}$  weighting factors are conventionally determined by weighting the excitation in accordance with its energy loss<sup>2, 6</sup>

$$\alpha_{\ell n} = u_{s\ell} / u_{s1} \quad (2.14).$$

The effective vibrational excitation rate is then assigned the energy loss appropriate to excitation of the first vibrational level. The excitation rate defined in this manner is useful for laser modelling estimates of the net fractional energy transfer to the various inelastic excitation channels within the molecular system.

The cross-section for superelastic collisions  $Q_{-s1}$  can be related to the corresponding excitation cross-section  $Q_{s1}$  by the principle of detailed balance. This states<sup>7</sup> that at thermodynamic equilibrium each interaction, taken by itself and in the microscopic limit, must yield the appropriate thermodynamic population. Consider the two level system

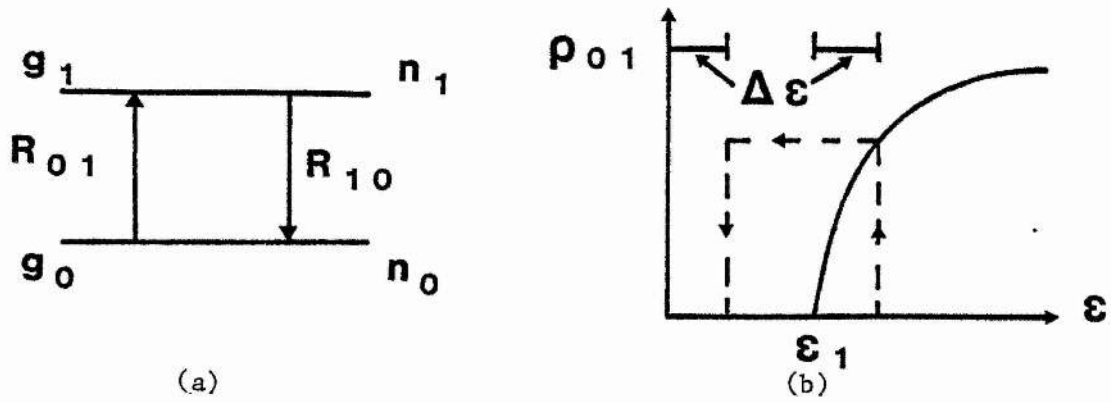


Fig. 2.1. A two-level system and typical excitation cross-section.

TABLE 2.1. Physical constants of the CO<sub>2</sub> system

<u>Constant</u>	<u>Description</u>	<u>Value(cm<sup>-1</sup>)</u>
$\nu_1/C$	Symmetric stretch frequency	1337
$\nu_2/C$	Bending frequency	667
$\nu_3/C$	Asymmetric stretch frequency	2349
$\nu_4/C$	N <sub>2</sub> vibrational frequency	2330
$\nu_6/C$	CO vibrational frequency	2150
B <sub>1</sub>	Rotational constant for CO <sub>2</sub> lower laser level	0.3897
B <sub>2</sub>	Rotational constant for CO <sub>2</sub> upper laser level	0.3866

of figure 2.1, and the corresponding excitation cross-section with threshold  $\epsilon_1$ , equal to the spacing of the levels (figure 2.1.b). In thermodynamic equilibrium the population of the system is a Boltzmann distribution<sup>8</sup> at the electron temperature  $T_e$ :

$$n_1 = n_0 \frac{g_1}{g_0} \exp\left(-\frac{\epsilon_1}{kT_e}\right) \quad (2.15)$$

and the rate  $R_{01}$  exactly balances the de-excitation rate  $R_{10}$ . That is

$$R_{01} = n_e n_0 \langle \sigma_{01} v_e \rangle = n_e n_1 \langle \sigma_{10} v_e \rangle = R_{10} \quad (2.16)$$

where the brackets represent integrals over the electron distribution function. Substituting (2.15) in (2.16) we obtain

$$\langle \sigma_{10} v_e \rangle = \frac{g_0}{g_1} \exp\left(\frac{\epsilon_1}{kT_e}\right) \cdot \langle \sigma_{01} v_e \rangle \quad (2.17)$$

which relates the superelastic rate to the inelastic excitation rate.

Reverting to the notation of 2.13, and dropping the degeneracies,

$$X_{-ln} = \exp\left(\frac{u_{sl}}{kT_e}\right) X_{ln} \quad (2.18).$$

This statement is completely general so long as the electron distribution function can be described by a single temperature  $T_e$ , and, since cross-sections are properties of the atom or molecule, can be applied to non-equilibrium situations. A still more generalised approach can be used to relate the excitation and de-excitation cross-sections for arbitrary distribution functions, yielding<sup>7,8</sup>

$$\sigma_{10}(\epsilon) = \left(\frac{\epsilon_1 + \epsilon}{\epsilon}\right) \frac{g_0}{g_1} \sigma_{01}(\epsilon_1 + \epsilon) \quad (2.19)$$

or, in the notation of (2.13):

$$Q_{-sl}(u) = \left(\frac{u_{sl} + u}{u}\right) Q_{sl}(u_{sl} + u) \quad (2.20).$$

The calculation of the corresponding rate constants requires numerical integration of the cross-sections over the distribution function.

### 2.1.3 A Boltzmann equation solver: BOLTZ

The solution of the Boltzmann equation (2.9) and the subsequent calculation of electron impact excitation rates and transport coefficients requires the use of computer-based numerical integration



codes. Recent years have seen the development of many such Boltzmann codes. One of these is BOLTZ, developed by Thomson et al.<sup>9</sup> to provide the electron vibrational excitation rates required as input data for a CO<sub>2</sub> laser kinetics model. Given the appropriate momentum transfer and inelastic cross-sections the code will compute the electron distribution function, vibrational excitation and ionisation rates, and electron drift velocities etc., for any gas mixture of up to nine gases. The program is a set of two sub-programs, BOLTZOLD and BOLTZNEW. A flow diagram for a job using the two programs is shown in figure 2.2. The Boltzmann equation is solved by writing it in terms of the number density  $N(u)$  of electrons with energy in the range  $u$  to  $(u + du)$ . By partitioning the electron energy axis into  $K$  cells the time independent Boltzmann equation is converted to a set of  $K$  simultaneous linear equations. ( $K = 100$  in BOLTZOLD,  $1000$  in BOLTZNEW). The equations are first solved ignoring the effects of superelastic collisions. An approximate electron distribution function is produced, and the vibrational excitation rates and transport coefficients are then obtained as the appropriate weighted integrals over the distribution function. Superelastic collision rates are now calculated and their effect on the distribution function is taken into account. New excitation rates and transport coefficients are re-calculated using the revised distribution function. On an ICL 1906A computer the code takes about 50 sec. if the effects of superelastic collisions are ignored and 2 mins. if they are included.

## 2.2 The vibrational temperature approximation

The CO<sub>2</sub> molecule has four normal modes of vibration<sup>10</sup>: the symmetric stretch (frequency  $\nu_1$ ), the doubly degenerate bending mode

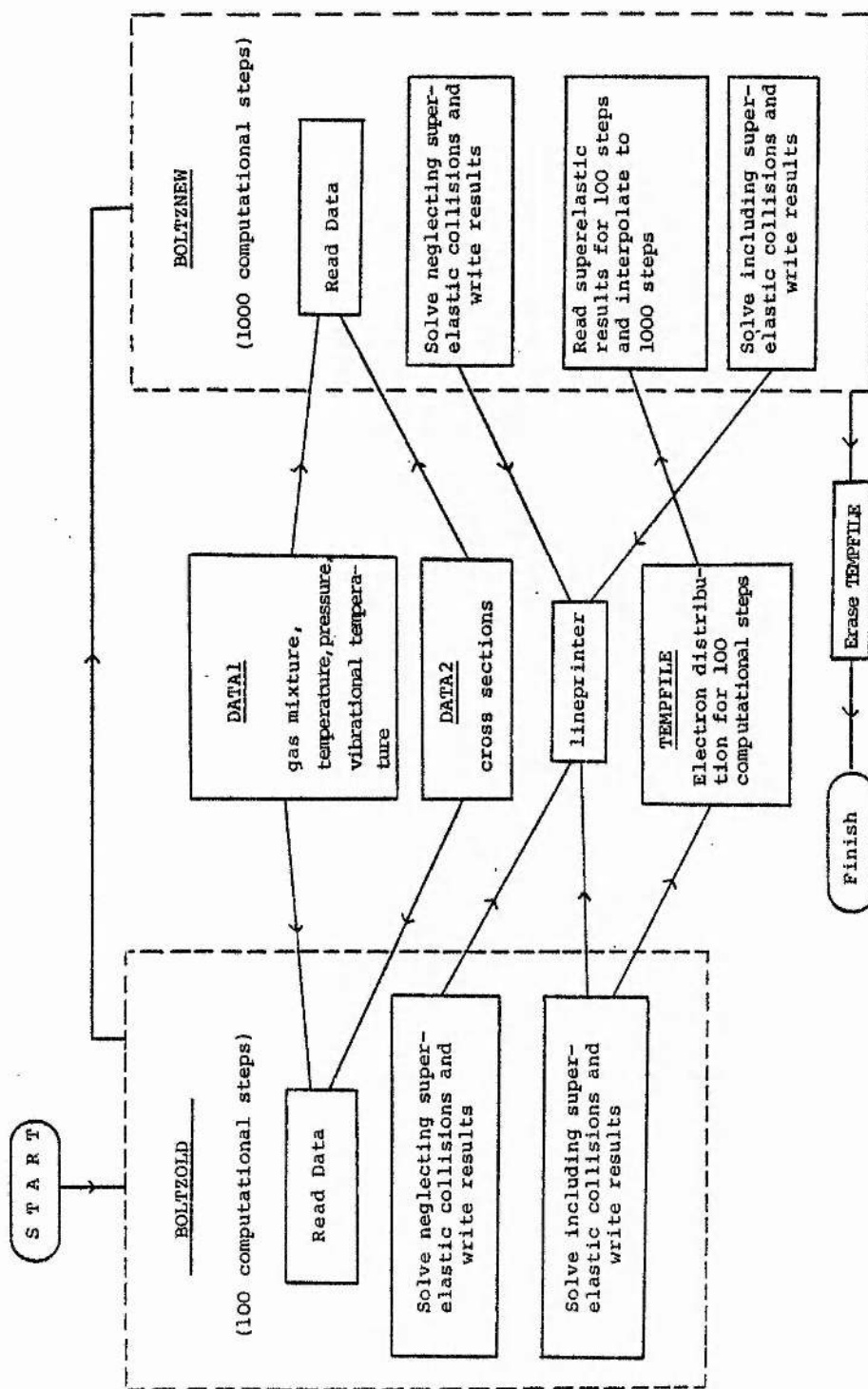


Fig. 2.2. Flow chart for Boltzmann code BOLTZ (from reference 9).

( $\nu_2$ ) and the anti-symmetric stretch ( $\nu_3$ ). Any vibrational state can therefore be described  $(l, m^s, n)$  where  $l, m$  and  $n$  are the  $\nu_1, \nu_2$  and  $\nu_3$  mode quantum numbers and the superscript  $s$  specifies the vibrational angular momentum about the symmetry axis. This can take the values

$$s = m, m-2, m-4, \dots, 1 \text{ or } 0$$

and the values  $0, 1, 2, 3, \dots$  correspond to the wave function designations  $\Sigma, \pi, \Delta, \Phi, \dots$ . These values are important because of the degeneracy of the bending mode. When two quanta of the  $\nu_2$  mode are excited, they can be divided between the orthogonal bending vibrations as  $1;1, 0;2$  or  $2;0$ . That is, the  $(0, 2, 0)$  level is triply degenerate. In general, when  $m$  bending quanta are excited the degree of degeneracy is  $m + 1$ . As a consequence of the vibrational anharmonicity, the different energy levels belonging to the same  $m$  are split according to the allowed  $s$  values. Thus the  $(0, 2, 0)$  level is split into the  $(0, 2^0, 0)$  level (corresponding to the 1:1 division of quanta) and the doubly degenerate  $(0, 2^2, 0)$  level corresponding to the 0:2 and 2:0 divisions). Such superscripted sub-levels are always doubly degenerate unless the superscript is 0, in which case the degeneracy is unity.

In the vibrational temperature approximation, the total population of  $\text{CO}_2$  vibrational level  $(l, m, n)$  is

$$N(l, m, n) = N_T x_1^l (m + 1) x_2^m x_3^n / Q_v \quad (2.21)$$

where

$$x_i = \exp(-h\nu_i/kT_i) \quad i = 1, 2, 3$$

the vibrational partition function  $Q_v$  is

$$Q_v = \{(1 - x_1)(1 - x_2)^2(1 - x_3)\}^{-1} \quad (2.22)$$

and  $N_T$  is the total number density of  $\text{CO}_2$ . The accidental energy coincidence of the  $(1, 0, 0)$  and  $(0, 2, 0)$  levels results in degenerate mixing of these levels (the Fermi resonance) and results in very efficient energy transfer between the  $\nu_1$  and  $\nu_2$  modes. Thus the modes usually share a common vibrational temperature, and the fractional population of any  $\text{CO}_2$  level is defined by specifying the values of the mode temperatures  $T_1 = T_2$ , and  $T_3$ . Given the fundamental mode frequencies of  $\text{CO}_2$ , (listed in Table 2.1), equation 2.21 can be used to examine the populations of the  $\text{CO}_2$  laser levels at normal temperatures. Figure 2.3 shows the dependence of the  $00^{\circ}1$  and  $00^{\circ}2$  upper laser level populations on  $T_3$  for an assumed constant  $T_2$ . An interesting corollary of the vibrational temperature approximation is the existence of optimum  $T_3$  values for  $00^{\circ}1$  and  $00^{\circ}2$  population (around 4500 K and 9000 K respectively). Also, the ratio  $N(00^{\circ}2)/N(00^{\circ}1)$  is always less than unity but is a single-valued, monotonically increasing function of  $T_3$ . A similar calculation including the  $(10^{\circ}0)$  and  $(10^{\circ}1)$  lower laser level populations is shown in figure 2.4. For the assumption  $T_2 = 400$  K it can be seen that the  $10^{\circ}0$  level contains less than 1% of the total population, while for the  $10^{\circ}1$  lower sequence band level the fractional population is less than 0.15%. These populations are of course strong functions of  $T_1 = T_2$ , as illustrated in figure 2.5. However, even for  $T_2 = 800$  K, the  $10^{\circ}0$  fractional population is less than 4%, compared to the typical  $00^{\circ}1$  upper laser level population of 15%. These conclusions conflict with some traditional interpretations of  $\text{CO}_2$  laser gain dynamics which invoke thermal population of the lower laser levels as the main reason for the observed deterioration in gain with increasing input discharge power.

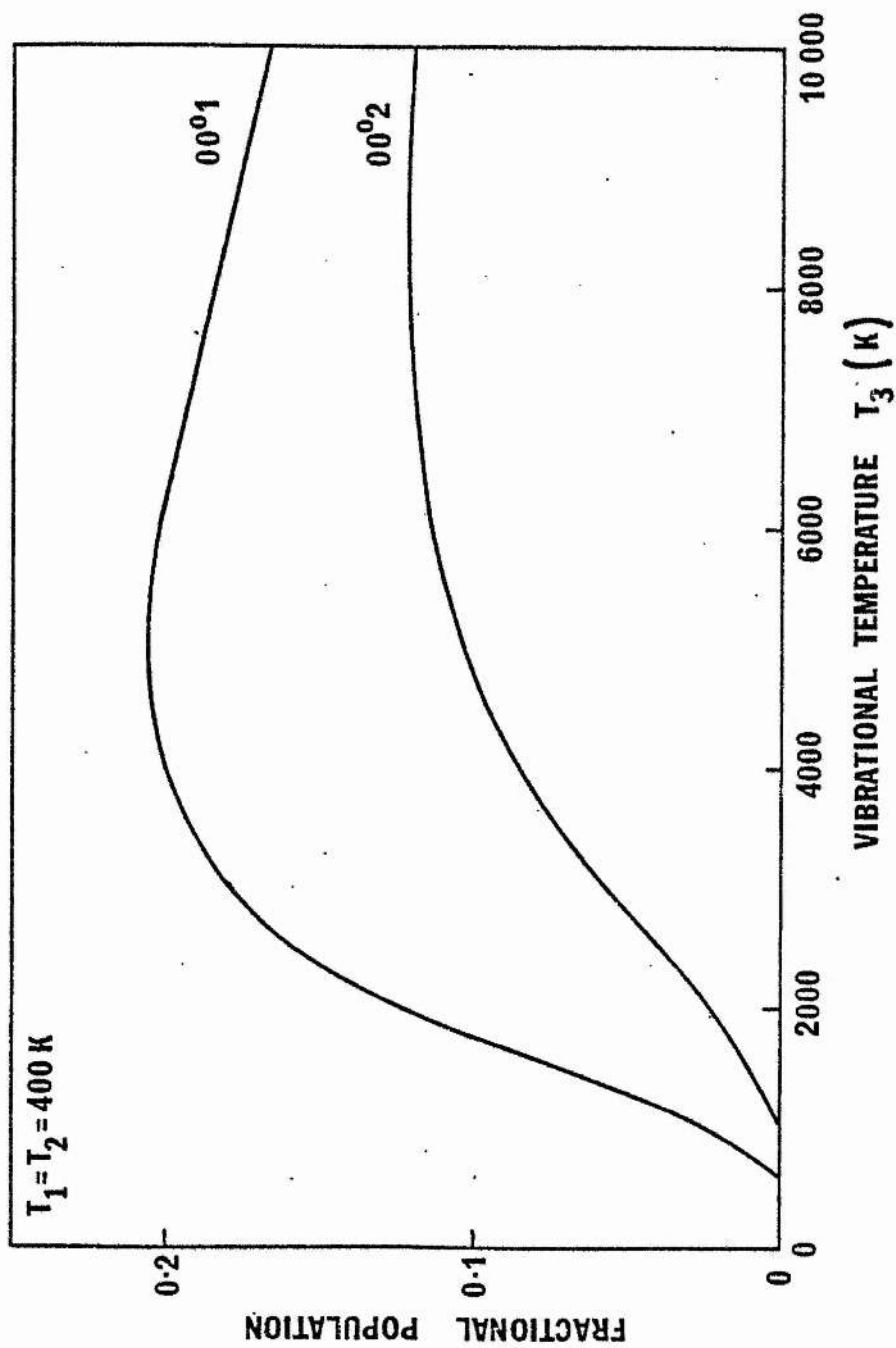


Fig. 2.3. Calculated  $(00^0 1)$  and  $(00^0 2)$  populations in the vibrational temperature approximation.

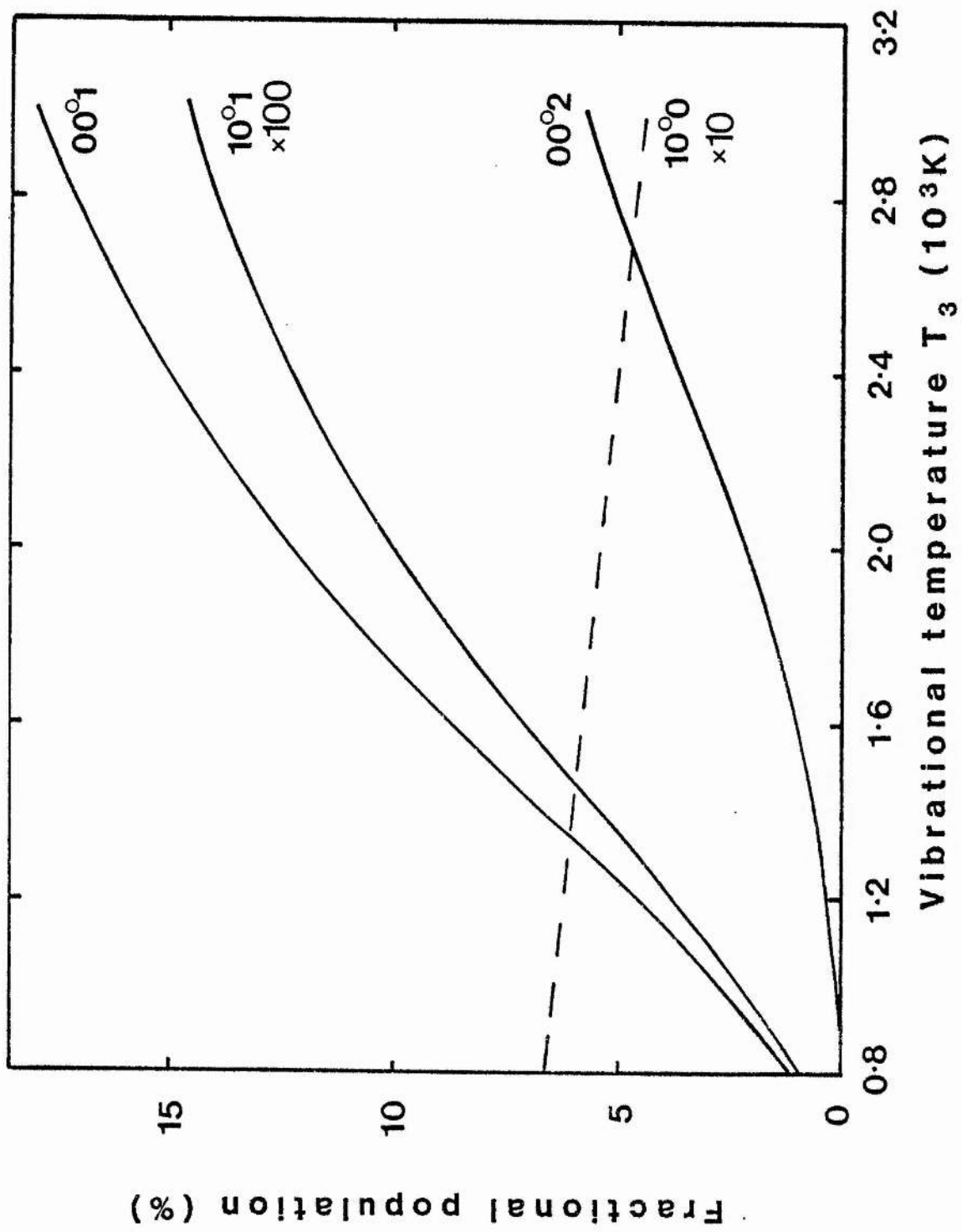


Fig. 2.4. Calculated vibrational level populations assuming T<sub>1</sub> = T<sub>2</sub> = 400 K, expressed as a fraction of total CO<sub>2</sub> population.

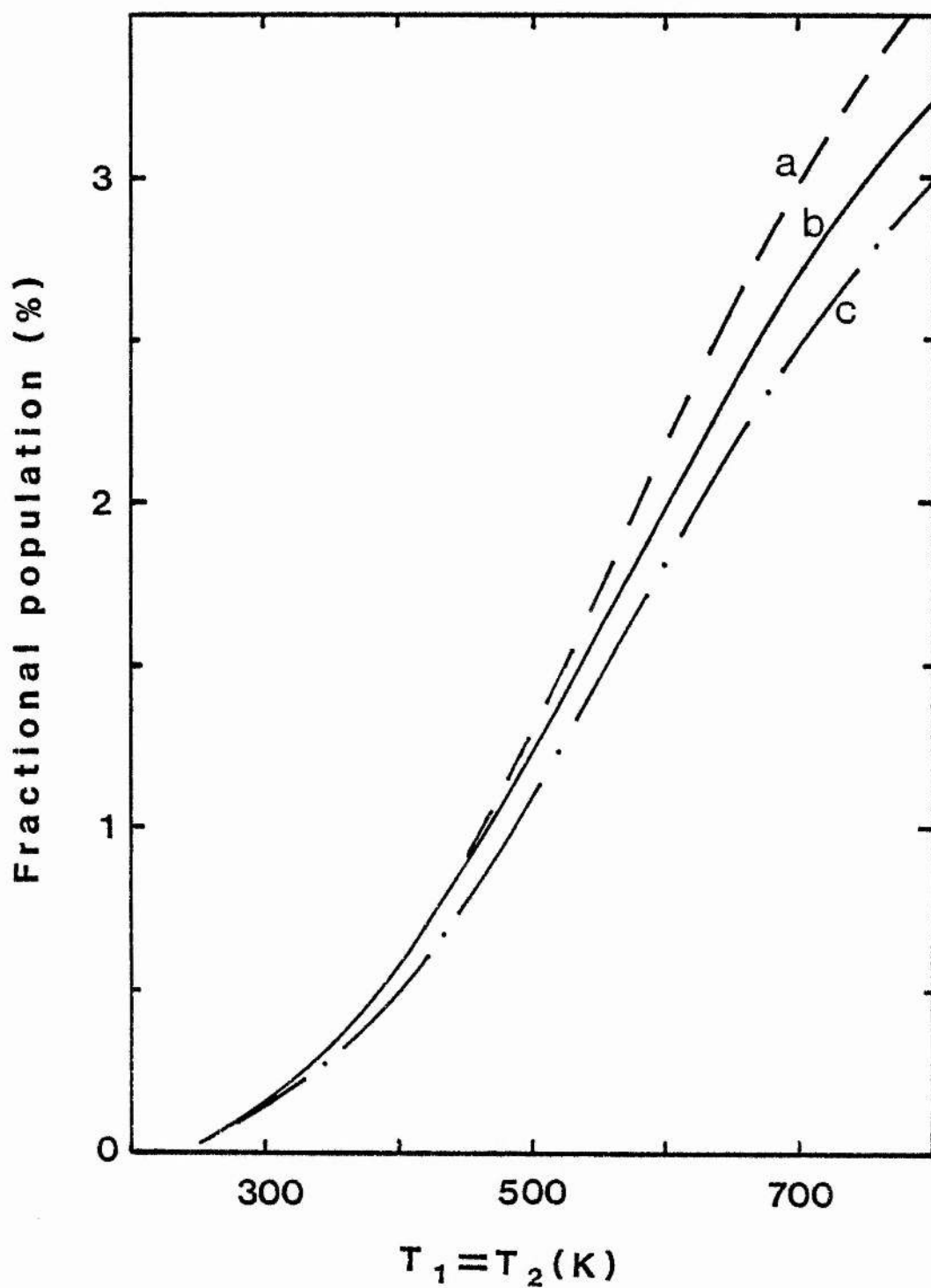


Fig. 2.5. Dependence of  $10^0$  level fractional population on  $T_1$ ,  $T_2$  for constant  $T_3$ : (a)  $T_3 = 1500$  K, (b)  $2000$  K and (c)  $2500$  K.

This conflict will be discussed later in an analysis of gain limitations in CO<sub>2</sub> lasers.

### 2.3 Laser gain and line broadening mechanisms

The small-signal gain coefficient,  $\alpha$  (m<sup>-1</sup>), of a laser transition at line centre ( $\nu = \nu_0$ ) is

$$\alpha(\nu_0) = \frac{\lambda^2}{8\pi} A_{21} (n_2 - g_2 n_1 / g_1) g(\nu_0) \quad (2.23)$$

where  $\lambda$  is the transition wavelength,  $A_{21}$  is the spontaneous transition probability,  $n_1$  and  $n_2$  are the population densities of the lower and upper levels having statistical weights  $g_1$  and  $g_2$ , and  $g(\nu_0)$

is the normalised line-shape function. The number densities  $n_1$  and  $n_2$  are given for the CO<sub>2</sub> laser by Robinson<sup>11</sup> as

$$n_i = N_i \left( \frac{2hcB_i}{kT} \right) g_i \exp(-B_i J_i (J_i + 1) hc/kT) \quad (2.24)$$

$i = 1, 2$  where  $N_i$  and  $B_i$  are the total number density and rotational constant for vibrational level  $i$ . The translational temperature  $T$  is assumed to equal the rotational temperature, and the  $B_i$  are given in Table 2.1.

In the limit of high pressure, but with no overlap of the individual rotational-vibrational lines,  $g(\nu_0)$  can be written

$$g(\nu_0) = \frac{2}{\pi(\Delta\nu)} \quad (2.25)$$

where the  $\Delta\nu$ , the full line width at half maximum (FWHM) is given for CO<sub>2</sub>-N<sub>2</sub>-He mixtures by Abrams<sup>12</sup>

$$\Delta\nu = 7.58 (\psi_c + 0.73\psi_n + 0.64\psi_h) P_{TOT} \left( \frac{300}{T} \right)^{1/2} \quad (2.26)$$

Here  $\Delta\nu$  is in MHz,  $P_{tot}$  is the total pressure (torr),  $T$  is the ambient gas temperature (K) and the  $\psi$  are the fractional concentrations of CO<sub>2</sub>, N<sub>2</sub> and He.

At low pressure, Doppler broadening dominates the line shape function, which becomes a Gaussian with line centre value



$$g(\nu_0) = \frac{2(\ln 2)^{1/2}}{\pi(\Delta\nu)} \quad (2.27)$$

where

$$\Delta\nu = \frac{2\nu_0}{c} \left( \frac{2kT\ln 2}{m} \right)^{1/2} \quad (2.28)$$

for  $\Delta\nu$  in Hz and  $m$  the mass of the radiating molecule (kg). For  $\text{CO}_2$  at  $10.6 \mu\text{m}$ ,

$$\Delta\nu \text{ (MHz)} = 2.962 T^{1/2} \quad (2.29).$$

It is interesting to compare the ranges of applicability of 2.26 and 2.29. Figure 2.6 shows calculated homogeneous (pressure) and inhomogeneous (Doppler) broadened linewidths for a 13  $\text{CO}_2$  - 9  $\text{N}_2$  - 78 He gas mixture at various total pressures and temperatures. Clearly for pressures above 50 torr, homogeneous broadening is dominant (i.e.  $\Delta\nu_H \gg 4\Delta\nu_I$ ) and pure pressure broadening is a good approximation. However for pressures typical of cw  $\text{CO}_2$  laser operation ( $\sim 20$  torr), the homogeneous and inhomogeneous linewidths are of roughly the same magnitude. In this regime neither pure pressure nor pure Doppler broadening is an accurate description of reality, and the transition lineshape is a relatively complicated convolution of Gaussian and Lorentzian shapes, called the Voigt profile. This cannot be calculated analytically however, and in laser modelling calculations pure pressure or pure Doppler broadening is often conveniently assumed.

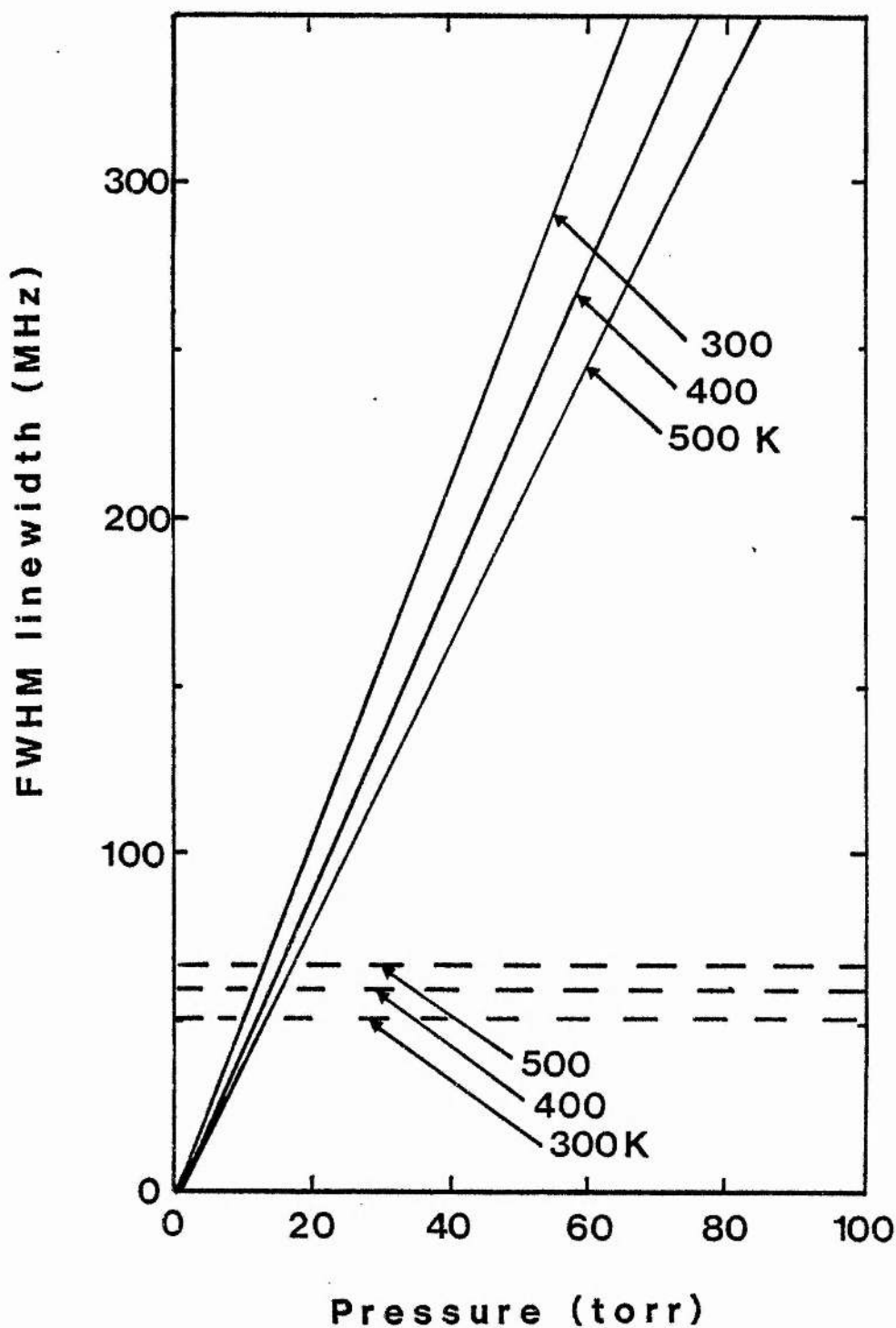


Fig. 2.6. Calculated  $10\ \mu\text{m}\ 00^0_1$  band linewidths assuming pure pressure broadening (solid curves) and pure Doppler broadening (dashed curves) for a 13%  $\text{CO}_2$  : 9%  $\text{N}_2$  : 78% He mixture at various ambient temperatures.

References for Chapter 2

1. I.P. Shkarofsky, T.W. Johnston and M.O. Bachynski, "The Particle Kinetics of Plasmas", (Addison-Wesley, Reading Mass, 1966).
2. W.L. Nighan, Phys. Rev. A 2, 5, 1989 (1970).
3. K. Smith and R.M. Thomson "Computer Modelling of Gas Lasers". (Plenum, New York, 1978).
4. W.L. Nighan and J. H. Bennett, Appl. Phys. Lett. 14, 8, 240 (1969).
5. J.J. Lowke, A.V. Phelps and B.W. Irwin, J. Appl. Phys. 44, 10, 4664 (1973).
6. M.C. Fowler, J. Appl. Phys. 43, 8, 3482 (1972).
7. J.T. Verdeyen "Laser Electronics". pp 424-428 (Prentice Hall, Englewood Cliffs N.J., 1981).
8. B.E. Cherrington "Gaseous electronics and gas lasers" pp 55, 57 Pergamon Press, Oxford 1980).
9. R.M. Thomson, K. Smith and A.R. Davies, Comput. Phys. Commun. 11, 369 (1976).
10. G. Herzberg "Molecular spectra and molecular structure", Vol. 2 Van Nostrand, New York (1945).
11. A.M. Robinson, Can. J. Phys. 50, 2471, (1972).
12. R.L. Abrams, Appl. Phys. Lett. 25, 609 (1974).

## CHAPTER 3: CO<sub>2</sub> DISSOCIATION EFFECTS ON DISCHARGE KINETICS

### 3.1 Introduction

In the CO<sub>2</sub> laser, the accurate application of the theoretical principles outlined in the last chapter requires practical knowledge of the gas mixture composition in the active medium. Modern vacuum technology allows full control of gross gas mixture composition and pressure; however, subtler changes in gas composition occur due to electron impact dissociation of the CO<sub>2</sub>, and these are more difficult to control. CO<sub>2</sub> dissociation can have significant effects on the optical gain and electric discharge characteristics of laser devices, and these must be quantified in any comparison of observed and predicted laser behaviour.

Electron impact dissociation of CO<sub>2</sub> proceeds by the reaction



with 6-7 eV electrons most important<sup>1</sup>. Some oxygen atoms form molecular oxygen by the reaction



where M is a collision partner.

CO<sub>2</sub> re-formation also takes place by



or



in the presence of small amounts of water vapour or hydrogen. Various materials, e.g. hot platinum and Hopcalite (MnO CuO), are known to catalyse the CO<sub>2</sub> reformation reactions. Net CO<sub>2</sub> dissociation will have four main effects:

- (i) CO<sub>2</sub> concentration will decrease, possibly causing loss of

laser gain.

- (ii) CO and O<sub>2</sub> concentrations will increase, leading to a considerable population of vibrationally excited CO. These gas composition changes may cause
- (iii) changes in the vibrational excitation, de-excitation, and exchange kinetics of the system, and
- (iv) changes in the discharge electron density and electron mobility, which will be evidenced by a change in the voltage-current characteristic of the electric discharge.

The interaction of these effects is potentially complex, and hence some caution must be exercised before adopting the generally accepted naive view which is "the less loss of CO<sub>2</sub>, the better". For example, it is known that CO has a cross-section for vibrational excitation which is larger than that of N<sub>2</sub>, and that this excitation can be effectively transferred (by V-V collisions) to the CO<sub>2</sub> upper laser level. It is possible that in some circumstances CO<sub>2</sub> dissociation could produce sufficient CO, and hence a sufficient increase in vibrational excitation rate, to out-weigh the effect of the CO<sub>2</sub> loss. Clearly a more detailed analysis of CO<sub>2</sub> dissociation effects is required.

### 3.2 Investigative methods and results

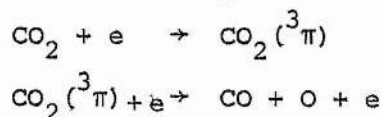
#### 3.2.1 CO<sub>2</sub> dissociation rates

For small dissociation levels, where CO<sub>2</sub> re-formation and other effects of the dissociation products can be neglected, the rate of change of the CO<sub>2</sub> partial pressure  $p$  is<sup>1</sup>:

$$\frac{dp}{dt} = -(k_1 n_e + k_2 n_e^2) p \quad (3.6)$$

where  $k_1$  (cm<sup>3</sup>s<sup>-1</sup>) is the rate constant for direct electron impact

dissociation and  $k_2$  the constant for the two-step process



which is also thought important in some conditions. However in low pressure DC discharges

$$n_e k_2 \ll k_1$$

so

$$-\ln\left(\frac{p_T}{p_0}\right) = k_1 n_e T$$

where  $T$  is the molecular dwell-time in the discharge.<sup>8</sup> For current  $I$ , flow-rate  $Q$  and active discharge length  $l$  we obtain

$$-\ln\left(\frac{p_T}{p_0}\right) = \frac{k_1 I l}{v_d e Q} \quad (3.7)$$

where  $v_d$  is the electron drift velocity. Defining  $\alpha$  as the number of dissociations per electron per cm drift, and with the  $\text{CO}_2$  partial pressure  $p$  in torr,

$$\frac{\alpha}{p} = \frac{k_1}{v_d} \cdot \frac{N_0}{760} \quad (3.8)$$

where  $N_0$  is Loschmidts number ( $= 3.6 \times 10^{16}$  particles  $\text{cm}^{-3}$  at S.T.P.). Thus

$$\frac{\alpha}{p} = \frac{-n_e e Q}{760 I l} \ln\left(\frac{p_T}{p_0}\right) \quad (3.9)$$

is the dissociation rate ( $\text{electron}^{-1} \text{cm}^{-1} \text{torr}^{-1}$ ) in a flowing gas discharge at low dissociation levels. The analysis implies that

$$\ln(p_0/p_T) \propto I/Q$$

provided  $k_1/v_d$  is a constant. Smith and Austin<sup>1</sup> have shown this to be true for current densities less than  $15 \text{ mAcm}^{-2}$ , demonstrating that the single-step impact dissociation model is a good description for  $\text{CO}_2$  mixtures at low pressures and currents. For a variety of gas mixtures  $\alpha/p$  was observed to rise almost linearly with the ratio of

discharge electric field to total pressure ( $E/P$ ). This requires a rise in  $k_1/v_d$ , by equation (3.8). Since  $k_1$  is simply defined by the dissociation cross section integrated across the electron energy distribution function, changes in  $\alpha/p$  correspond to a changing population of discharge electrons with energy greater than 6 eV, the threshold for single-step dissociation.

Equation (3.9) was used in an experimental investigation of  $\text{CO}_2$  dissociation rates in various laser mixtures. The pre-mixed gas was flowed through a fused silica discharge tube (1 cm i.d., 50 cm active length) at a rate measured by a Rotameter on the backing pump exhaust. Additive gases could be leaked through the system via a precision needle valve, and total pressure was controlled by a feedback loop control system similar to that described by Ferran and Sullivan.<sup>2</sup> This comprised an MKS Baratron 221 capacitance manometer commanding a Veeco PV10 piezo-electric leak valve via the appropriate control electronics.  $\text{CO}_2$  dissociation and partial pressures of gas additives were measured using a Kratos-AEI MS 10 S magnetic sector mass spectrometer, sampling downstream from the dissociation tube. The dissociation level was calculated directly from the relative mass 44 peaks at constant pressure, with and without a discharge current in the tube. Fractional dissociation was restricted to less than 20% to satisfy the "low-level" dissociation requirement of the previous analysis. The pressure-reduced electric field,  $E/P$ , was derived from anode-cathode discharge voltage measurements without allowance for possible cathode fall or gas heating effects. Results were obtained for two typical  $\text{CO}_2:\text{N}_2:\text{He}$  mixtures, in the ratios 6:12:82 and 13:9:78, and are plotted in figure 3.1. It is clear that for both gas mixtures

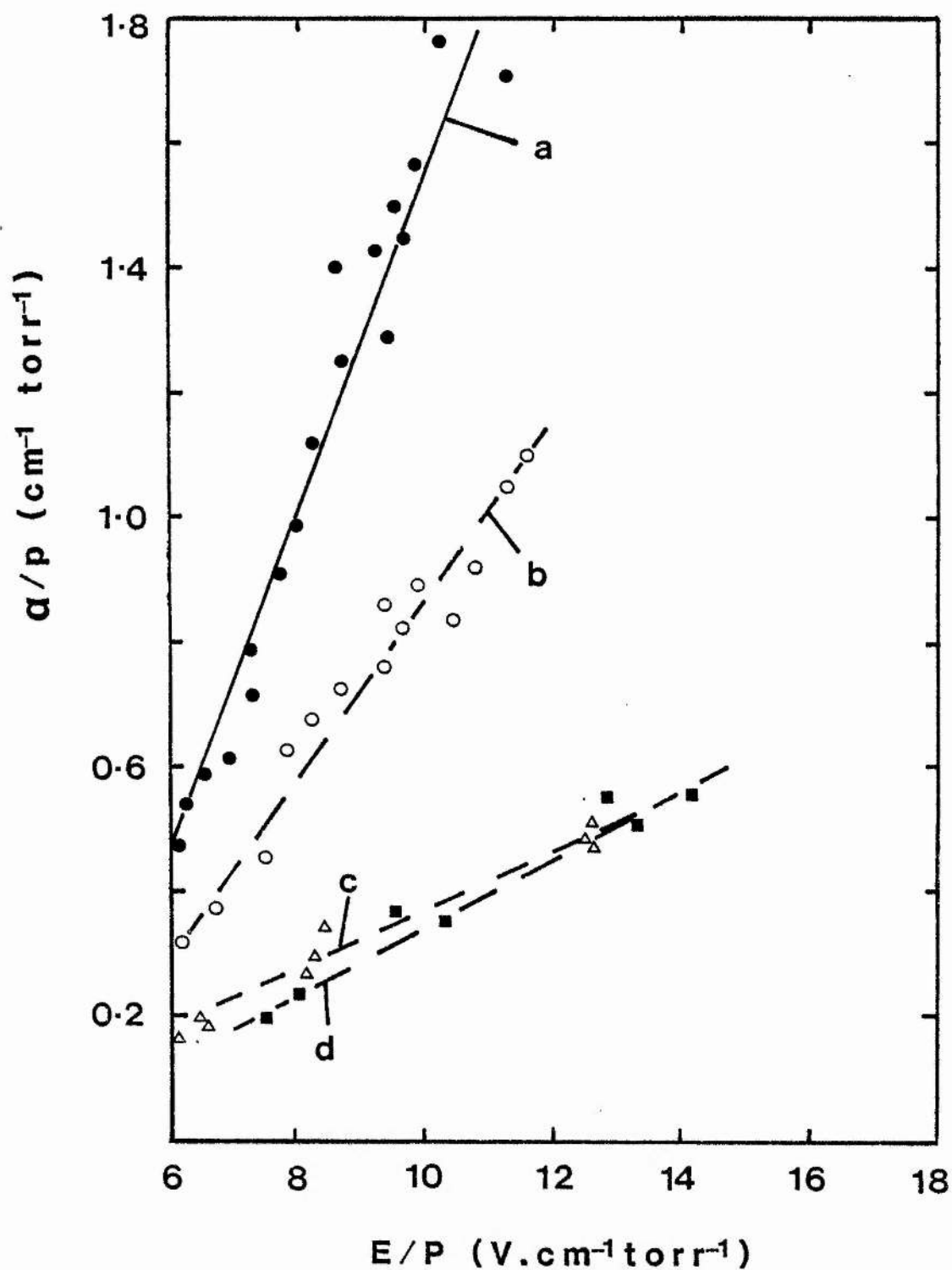


Fig. 3.1. Dissociation rate constant measurements

(a) 6  $\text{CO}_2$  : 12  $\text{N}_2$  : 82 He, (b) 13  $\text{CO}_2$  : 9  $\text{N}_2$  : 78 He,

(c) 13 : 9 : 78 mix + 5%  $\text{O}_2$  (d) 13 : 9 : 78 mix + 5% CO



the dissociation rate rises roughly linearly with E/P. However, at a constant E/P, the dissociation rate is significantly lower in the 13:9:78 mixture. This observation agrees with the results of D'Amico and Smith<sup>3</sup> who also observed that dissociation rates were lower in gas mixtures with a high fractional CO<sub>2</sub> or N<sub>2</sub> content. This can be attributed to the large cross-sections for vibrational excitation of CO<sub>2</sub> and N<sub>2</sub> by low energy ( $\sim 0.3$  eV) electrons; these present a "barrier" which inhibits electrons from attaining very high energies at normal E/P. Thus mixtures with a high molecular content are characterised by lower average electron energies, resulting in a smaller population of electrons capable of single-step dissociation. To test this explanation, small amounts of CO and O<sub>2</sub> were added to the 13:9:78 mixture; since these additives also possess large inelastic cross-sections, a further decrease in dissociation rate could be expected. As shown in figure 3.1, this was in fact the case, and the addition of 5% CO or O<sub>2</sub> approximately halved the dissociation rate at constant E/P. This result has interesting implications for CO<sub>2</sub> dissociation levels in sealed-off lasers, suggesting that as dissociation proceeds, an equilibrium CO<sub>2</sub> level will quickly be reached since the dissociation products will have the effect of (a) re-forming CO<sub>2</sub> by reactions like (3.4) and (3.5), and (b) inhibiting the dissociation rate by reducing the average discharge electron energy. The suggestion is supported by routine observations in sealed-off lasers that a dissociation equilibrium is reached within a few seconds of switching on the discharge current.

### 3.2.2. Dissociation effects on vibrational excitation rates

A Boltzmann equation analysis of the electrical behaviour of a

positive column discharge depends on an adequate knowledge of all relevant elastic and inelastic collisional processes. Usually any  $\text{CO}_2$  dissociation products have been regarded as minor trace additive species which may contribute to ionisation and electron attachment rates, but which do not affect the overall discharge parameters. However, Thomson<sup>4</sup> has considered inelastic processes involving  $\text{CO}$  and  $\text{O}_2$ , including  $\text{O}_2$  dissociative attachment and  $\text{CO}$  vibrational excitation. Typical results are reproduced in figure 3.2, which illustrates the effect of  $\text{CO}_2$  dissociation on the electron temperature  $T_e$  and drift velocity  $v_d$  for the  $13\text{CO}_2:9\text{N}_2:78\text{He}$  gas mixture. The drift velocity is very little affected, but the electron temperature is decreased over the whole  $E/N$  range of interest ( $1$  to  $5 \times 10^{-16} \text{Vcm}^2$ ), in agreement with the arguments of the previous section. Figure 3.3 shows the variation of  $\text{CO}_2(\nu_3)$ ,  $\text{N}_2$  and  $\text{CO}$  vibrational excitation rate constants with  $E/N$  for dissociation between 0 and 75%. The rate constant for  $\text{CO}_2(\nu_3)$  mode excitation is small and almost constant with varying  $E/N$  or dissociation level. The  $\text{N}_2$  and  $\text{CO}$  rate constants are much larger and vary considerably with  $E/N$  and dissociation, with the peak rates occurring at higher  $E/N$  as the dissociation increases. It should be noted that the excitation rate constant for  $\text{CO}$ ,  $X_6$ , is greater than that for  $\text{N}_2$ ,  $X_4$ ; hence if the excitation is effectively transferred from the  $\text{CO}$  to the  $\text{CO}_2(\nu_3)$  mode by V-V-T collisions (as it is from  $\text{N}_2$ ), then this could make a significant contribution to the laser efficiency, especially in the presence of high  $\text{CO}$  concentrations.

Thomson has produced similar excitation rate constants for  $13\text{CO}_2:9\text{N}_2:78\text{He}$  and  $10\text{CO}_2:20\text{CO}:70\text{He}$  gas mixtures, and these are

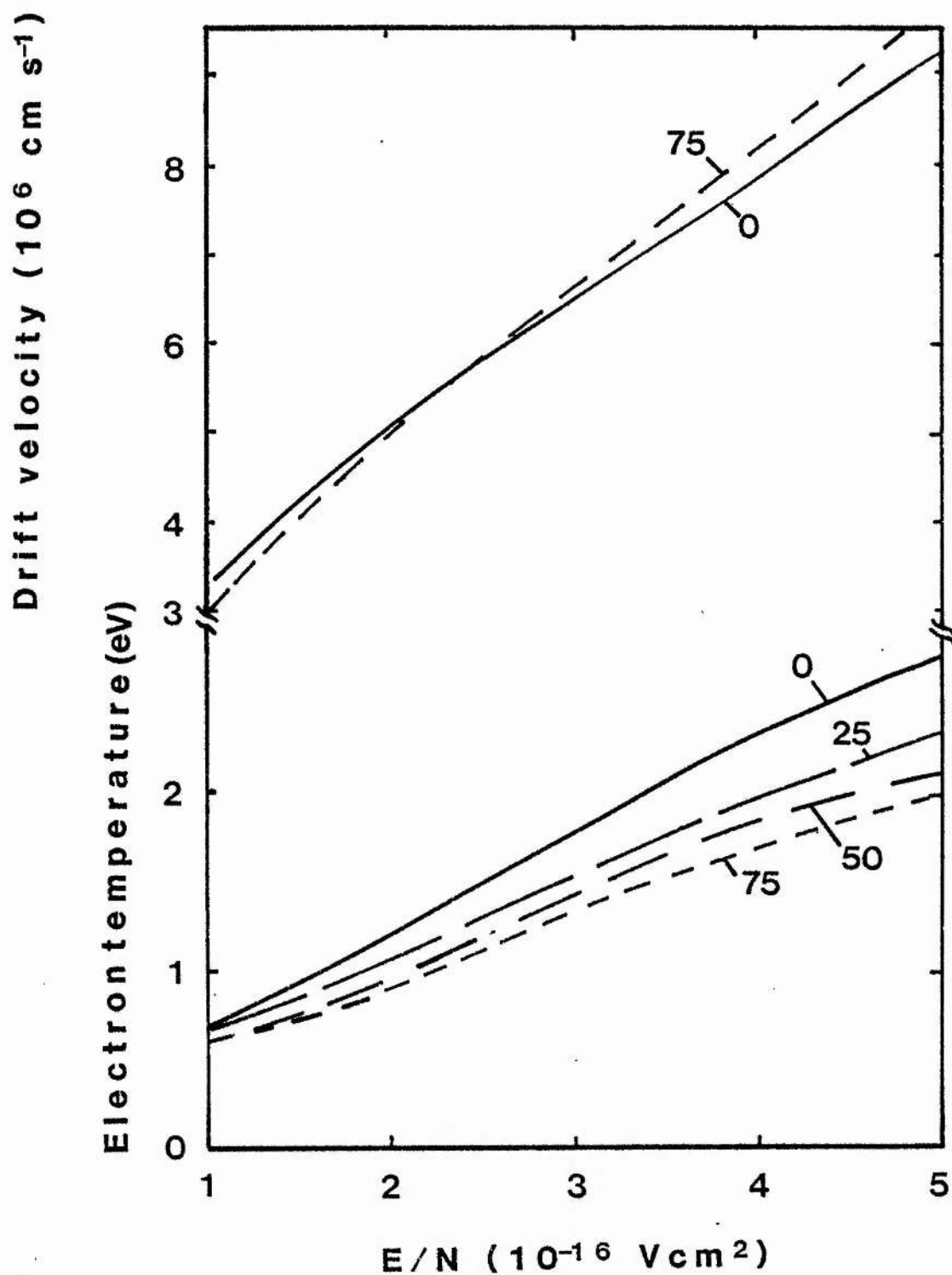


Fig. 3.2. BOLTZ - calculated variation of electron drift velocity and temperature with  $E/N$  in 13 CO<sub>2</sub> : 9 N<sub>2</sub> : 78 He gas mixture at various levels of CO<sub>2</sub> dissociation (%).

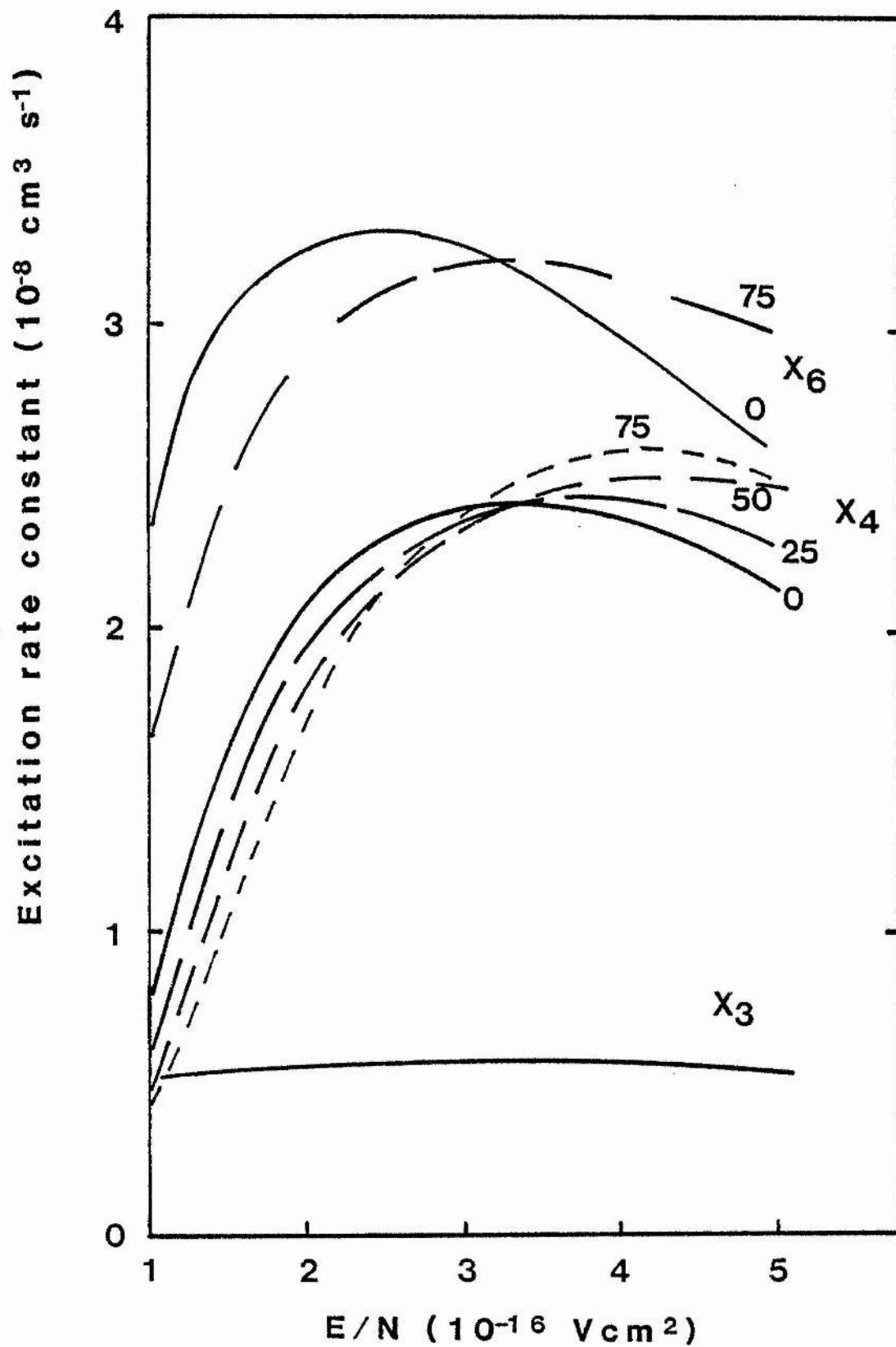


Fig. 3.3. BOLTZ - calculated excitation rate constants for  $\text{N}_2$  ( $X_4$ ),  $\text{CO}$  ( $X_6$ ) and  $\text{CO}_2$  ( $v_3$ ) modes ( $X_3$ ) as a function of  $\text{CO}_2$  dissociation (%) in  $6 \text{ CO}_2 : 12 \text{ N}_2 : 82 \text{ He}$  mixture.

TABLE 3.1 Summary of BOLTZ calculations of vibrational excitation rate constants and

average electron energies.

Gas mix	E/N (Td)	$X_3$ ( $\text{cm}^3 \text{s}^{-1}$ )	$X_4$ ( $\text{cm}^3 \text{s}^{-1}$ )	$X_T$ ( $\text{cm}^3 \text{s}^{-1}$ )	$X_6$ ( $\text{cm}^3 \text{s}^{-1}$ )	$\bar{u}$ (eV)
13 CO <sub>2</sub> : 9 N <sub>2</sub> : 78 He	30	5.57(-9)	2.60(-8)	4.57(-8)	-	1.80
6 CO <sub>2</sub> : 12 N <sub>2</sub> : 82 He	30	5.56(-9)	2.42(-8)	4.31(-8)	-	1.82
10 CO <sub>2</sub> : 20 CO : 70 He	32	5.41(-9)	-	3.75(-8)	2.88(-8)	1.22

Data (by courtesy of Dr. R.M. Thomson) from CVD project RU - 11 - 8 Technical Memoranda

TM 53, TM 59 and TM 74, for zero CO<sub>2</sub> dissociation.

5.57(-9) is equivalent to  $5.57 \times 10^{-9}$ , etc.

summarised in Table 3.1. However, such results alone are not sufficient to determine vibrational excitation rates in the appropriate gas mixtures : laboratory measurements of the operating E/N and dissociation levels are also required.

### 3.2.3 Dissociation effects on the current-voltage characteristics of cw CO<sub>2</sub> laser discharges

Figure 3.4 shows the apparatus used to obtain the v-i characteristics under conditions of controlled gas mixture, pressure and flow-rate. As before, pre-mixed gas was flowed through the system at a rate determined by throttle valves in the vacuum pump backing line and measured by a Rotameter. CO<sub>2</sub> dissociation could be induced in the 50 cm long discharge tube at variable current density (typically 50mAcm<sup>-2</sup>). The gas was cooled to room temperature in a water bath heat exchanger before the dissociation level was measured by the mass spectrometer. During v-i measurements the gas flow was directed through the triple anode measurement tube (internal diameter 0.8 cm, total active length 9 cm).

The measurement tube discharge was powered by an Irvin C1096 current stabilised DC supply, in series with a 30 k $\Omega$  ballast resistance. Discharge current was measured on a standard AVO meter, while the voltage drop across two electrodes inserted in the positive column was measured to within 3% by a Dymar kilovoltmeter. Electrode separation, measured by a travelling microscope, was 3.35  $\pm$  0.05 cm. The triple anode side-arm cathode geometry of the tube ensured that the positive column electric field was measured without interference from cathode fall effects, and allowed the axial uniformity of the positive column to be tested; the measurements showed that the axial

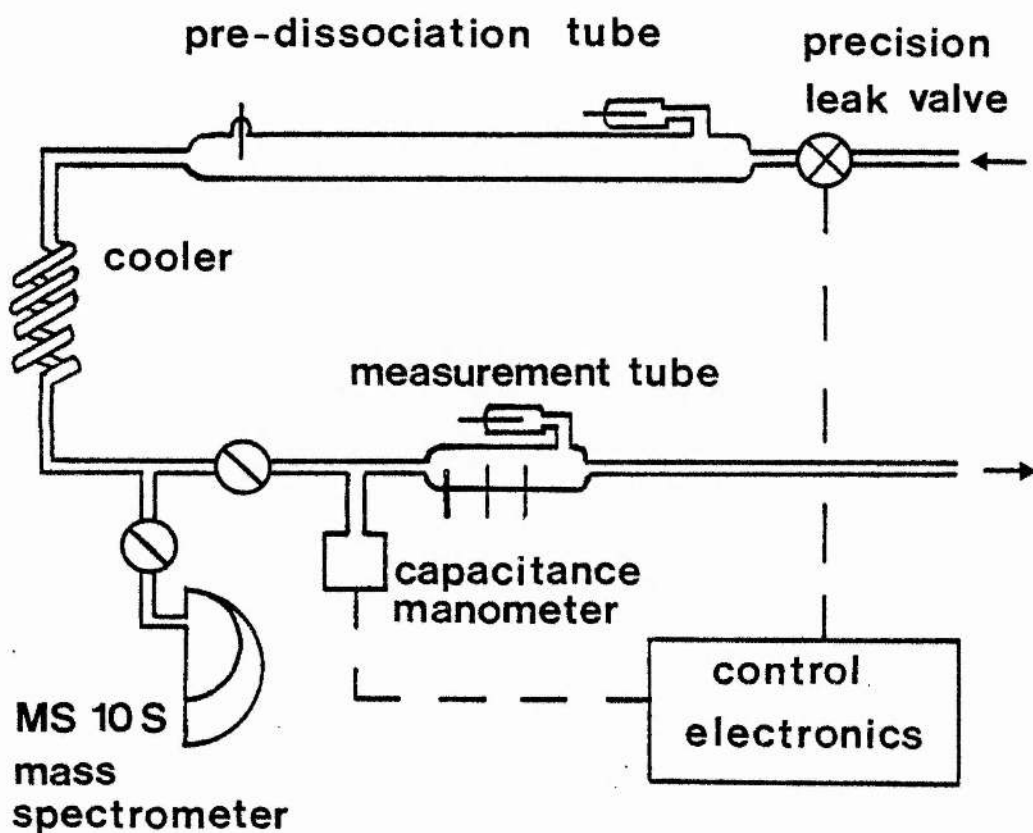


Fig. 3.4. Experimental arrangement for measurement of  $V-i$  characteristics under conditions of controlled pressure and  $\text{CO}_2$  dissociation.

field, including the anode fall, was constant to within 5% along its whole length. Gas temperature in the positive column was not measured, since results have shown<sup>5</sup> that for the useful range of gas mixtures and pressure-diameter (pd) values, the relationship between gas temperature and discharge input power is well described by the empirical formula:

$$T_G = 60.8 \left(\frac{P}{L}\right)^{0.77} + T_{WALL} \quad (3.10)$$

for P in watts, and where L is the active discharge length in cm.  $T_G$  is a radially averaged value.

The choice of gas flow rates was constrained by two considerations:-

(a) the rate should be low enough to ensure that diffusive cooling dominates convective cooling in the 9 cm discharge.

(b) the rate should be high enough to render negligible the extra dissociation of  $CO_2$  in the v-i measurement region.

Calculations showed that the axis to wall molecular diffusion time in typical discharge conditions ( $p = 20$  torr,  $R = 4$  mm,  $T = 360K$ ) is around 1 ms. It is known that  $CO_2$  dissociation proceeds on time scales of 0.1 s to a few seconds; a suitable range for gas discharge dwell time is therefore 5-50 ms. In practice this restricted the flow rate to  $60-600 \text{ cm}^3 \text{ min}^{-1}$  as measured at N.T.P. It was experimentally confirmed<sup>6</sup> that the constant-current voltage drop in the positive column of the measurement discharge was independent of gas flow rate over this range.

Typical discharge voltage-current characteristics are shown in figure 3.5 for various levels of  $CO_2$  dissociation (0, 25, 50 and  $75 \pm 5\%$ ). Each 25% increase in dissociation level causes a  $\sim 5\%$  increase in the constant-current positive column voltage. Knowledge



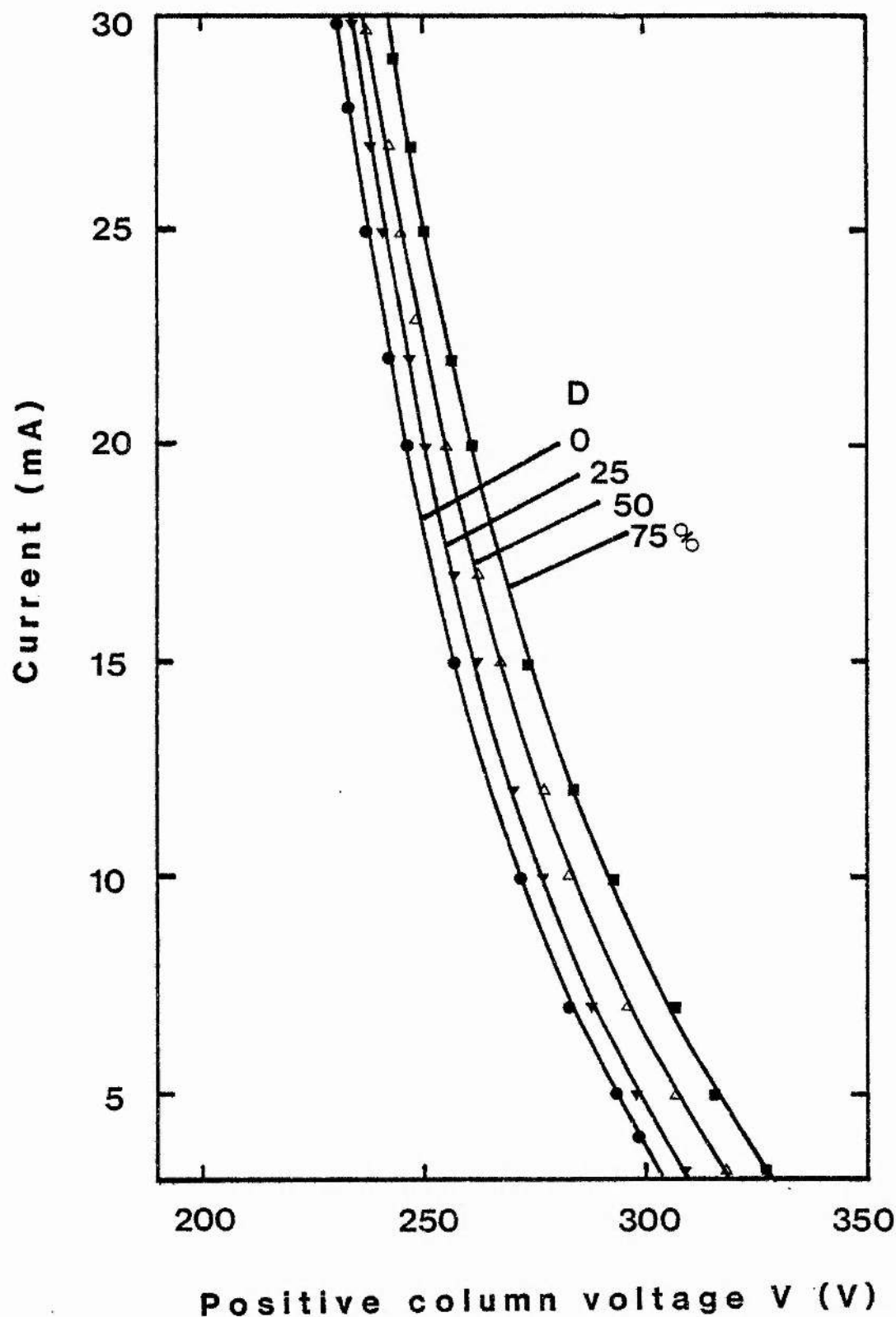


Fig. 3.5. Voltage - current characteristics for 6% CO<sub>2</sub> : 12% N<sub>2</sub> : 82% He mixture at 10 torr with various levels of CO<sub>2</sub> dissociation (D). Electrode separation = 3.35 cm.

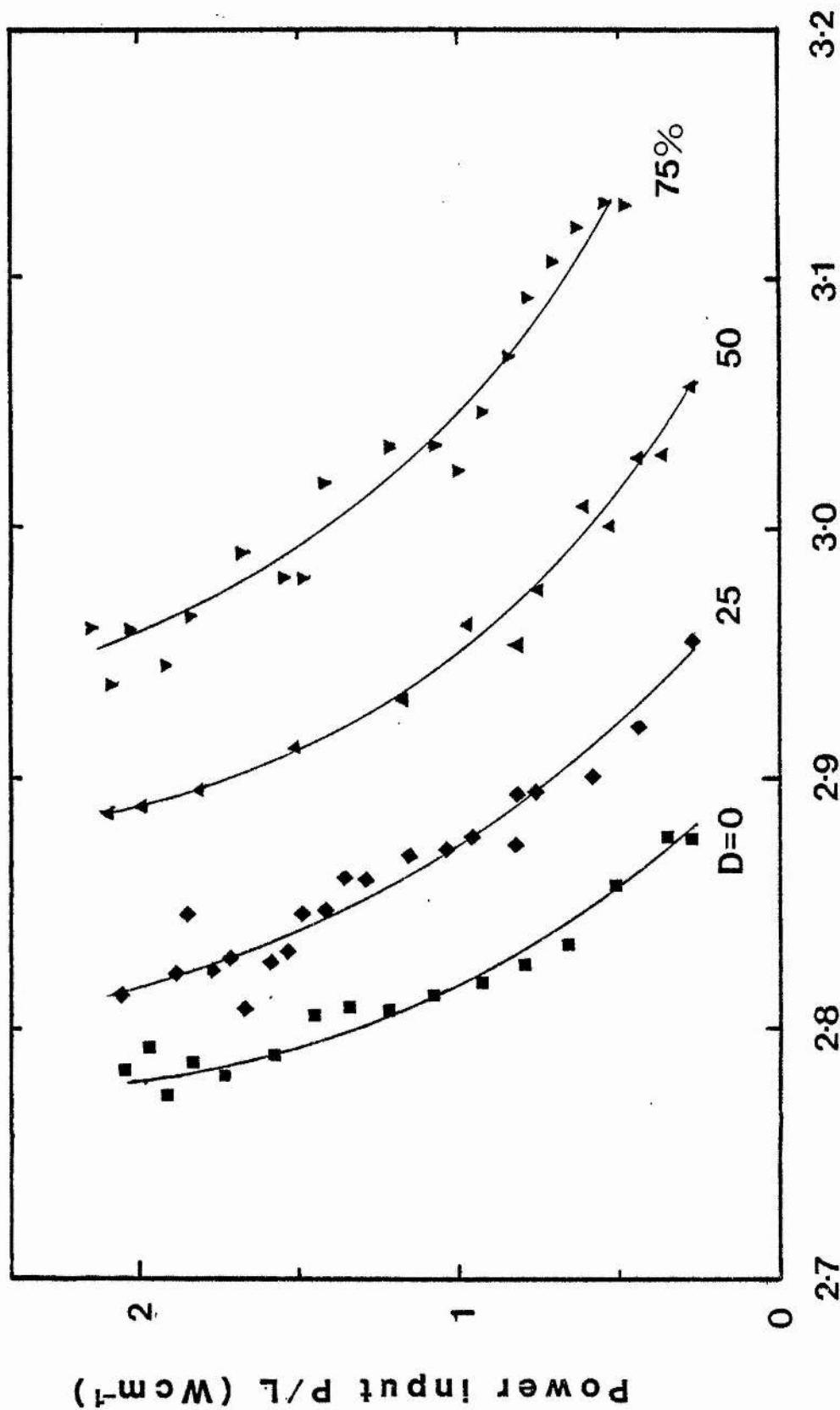


Fig. 3.6. Electrical power input per unit length against  $E/N$  for 6 : 12 : 82 mix at 10 torr with various dissociation levels.

of the gas pressure (10 torr), probe electrode spacing (3.35 cm) and the gas temperature (from equation 3.10) allows the  $v-i$  curves to be re-plotted in the form  $E/N$  vs.  $P/L$  as in figure 3.6.  $P/L$  ( $W\text{ cm}^{-1}$ ) is the electrical power input per unit discharge length, and can be a useful parameter<sup>6</sup> in the estimation of cw laser operating efficiencies. For constant  $P/L$ , it can be seen that each 25% increment in  $CO_2$  dissociation level causes a small increase (3-4%) in the discharge  $E/N$ . However, as shown by figure 3.3, such small  $E/N$  changes can produce disproportionately large changes in the  $N_2$  and CO vibrational excitation rates, especially at low  $E/N$ .

Voltage-current characteristics were measured over a range of pressures and gas mixtures to provide a database for subsequent kinetic modelling calculations. Some additional results are presented in Appendix A.

### 3.3 Conclusions

Several potentially important effects of  $CO_2$  dissociation have been identified and quantified. The dissociation products CO and  $O_2$  reduce the  $CO_2$  dissociation rate,  $\alpha/p$ , in low pressure flowing discharges. Boltzmann-code calculations by Thomson support the hypothesis that this is due to a reduction in the population of electrons in the high-energy 'tail' of the distribution function which results in reduced electron impact dissociation and a lowering of the discharge electron temperature.<sup>7</sup> Thomson's calculations also show that the rate constants for  $N_2$  and CO vibrational excitation have a significant dependence on  $CO_2$  dissociation at constant  $E/N$ . Laboratory measurements of positive column voltage-current characteristics reveal a tendency for  $CO_2$  dissociation to alter the operating

points of CO<sub>2</sub> laser discharges: to maintain a constant current in the presence of dissociation, a shift to slightly higher discharge voltage is required. For typical laser mixtures and pressures operating E/N values are in the region of  $3 \times 10^{-16} \text{ Vcm}^2$ , which is near-optimum for N<sub>2</sub> and CO vibrational excitation.

The combination of experimental v-i characteristics and Boltzmann-code calculations is sufficient to determine the appropriate vibrational excitation rate constants for a given gas mixture, pressure and discharge current. However the calculation of the resultant excitation rates demands knowledge of the density of free electrons in the discharge plasma. The determination of discharge electron density is considered in the next chapter.

References for Chapter 3

1. A.L.S. Smith and J.M. Austin, J. Phys. D. 7, 314, (1974).
2. R.J. Ferran and J.J. Sullivan, J. Vac. Sci. Technol. 12, 1 (1975).
3. K.M. D'Amico and A.L.S. Smith, unpublished.
4. R.M. Thomson, M.O.D. C.V.D. Research Project RU-11-8, Technical Memoranda 53, 59, 61 and 67 (1979, 1980).
5. H. Shields and A.L.S. Smith, J. App. Phys. 48, 11, 4807 (1977).
6. A.L.S. Smith, A.E. Webb and J. Mellis, CVD Research Project RU-16/6, Annual Report 1979.

7. Even when the distribution function is non-Maxwellian it is conventional to define an effective electron temperature

$$T_e = \frac{2}{3} \int_0^{\infty} u^{3/2} f(u, \frac{E}{N}, T) du.$$

Although this effective electron temperature does not completely specify the distribution function it can be considered characteristic of the "average" discharge electron energy.

8. Here  $p_0$  is the initial  $CO_2$  partial pressure and  $p_T$  is the pressure after time  $T$  where  $T$  is the time of flow along the positive column of the DC discharge.

CHAPTER 4 : X-BAND CAVITY RESONANCE MEASUREMENTS OF  
ELECTRON DENSITY

4.1 Introduction

In the modelling of gas discharge laser operation, knowledge of the local discharge electron density is a prerequisite in the calculation of electron impact excitation rates. Boltzmann codes can be used to predict electron drift velocities ( $v_d$ ) as a function of  $E/N$  for a given gas mixture; these can be combined with experimental voltage-current characteristics to obtain an estimate of electron density via the current transport equation:

$$j = e\bar{n}_e v_d(E/N) \quad (4.1)$$

where  $j$  is the current density and  $\bar{n}_e$  the spatially averaged electron density. However, most Boltzmann codes solve the spatially independent Boltzmann equation in which the effects of discharge boundaries are ignored. Such free-space calculations are unlikely to be reliable for low-pressure gas discharges; here the ambipolar diffusion of electrons and ions to the discharge tube walls, and subsequent three-body recombination, causes a steep radial gradient of electron density, which ranges from near-zero on the walls to a maximum on the centre axis. Under these circumstances a direct measurement of the discharge electron density is required.

4.2 Method

4.2.1 Theory

A convenient technique for electron density measurement in gaseous plasmas is the microwave cavity resonance method.<sup>1,2</sup> In concept this is very simple; the plasma to be studied is introduced into a microwave cavity and the resulting shift in the cavity resonant frequency, and

change in the cavity Q-factor, are measured. These can be related to the plasma electron density and its spatial distribution, and the electron collision frequency for momentum transfer and its spatial distribution. A first-order perturbation theory is normally used to obtain the relationship between these parameters and the experimental measurements. The limitations of the perturbation theory have been examined in detail by Persson<sup>3</sup> who showed that in the general case the theory is valid only for low plasma densities where the characteristic plasma frequency

$$\omega_p = \left[ \frac{e^2 n_e}{\epsilon_0 m_e} \right]^{1/2} \quad (4.2)$$

is much less than the microwave probing frequency  $\omega$ . However, when special configurations of the probing field are used, so that no a.c. polarisation is induced in the plasma, the perturbation theory remains valid for values of  $\omega_p/\omega$  of the order of unity or larger. The theory relates the shift in cavity resonant frequency ( $\Delta\omega$ ) and change in Q factor to the complex plasma conductivity by the expression<sup>4</sup>

$$\Delta\left(\frac{1}{Q}\right) - 2i \frac{\Delta\omega}{\omega_0} = \frac{1}{\epsilon_0 \omega_0} \frac{\int_V \sigma(r) E^2 dV}{\int_V E^2 dV} \quad (4.3)$$

where the 0 subscript represents unperturbed values, the integrations are over the cavity volume  $V$ , and  $\sigma$  is the complex conductivity of the plasma. This can be written

$$\sigma = \frac{e^2 n_e}{m_e (\langle v_m \rangle + i\omega)} \quad (4.4)$$

Inserting this in (4.3), equating real and imaginary parts, and using  $f = \omega/2\pi$  gives

$$\frac{\Delta f}{f_0} = \frac{\int_V \frac{\eta E^2}{1+\gamma^2} dV}{2 \int_V E^2 dV} \quad (4.5)$$

and

$$\frac{1}{Q} - \frac{1}{Q_0} = \frac{\int_V \frac{\gamma \eta}{1 + \gamma^2} E^2 dv}{\int_V E^2 dv} \quad (4.6)$$

where  $\eta = n_e e^2 / \epsilon_0 m_e \omega^2$  is the critical electron density and  $\gamma = \langle v_m \rangle / \omega$  is a measure of the damping in the plasma. Slater<sup>5</sup> presents a detailed derivation of the resonance criterion (4.3), involving the solution of Maxwell's equations for boundary conditions appropriate to a metallic cavity. Assuming a cylindrical cavity of radius R surrounding a plasma column of radius  $R_p$  we can define an effective plasma volume

$$\alpha = \frac{\int_0^{R_p} r |E(r)|^2 dr}{\int_0^R r |E(r)|^2 dr} \quad (4.7)$$

such that (4.5) and (4.6) become

$$\frac{\Delta f}{f_0} = \frac{\alpha \bar{\eta}}{2(1 + \gamma^2)} \quad (4.8)$$

$$\Delta\left(\frac{1}{Q}\right) = \frac{\alpha \bar{\eta} \gamma}{(1 + \gamma^2)} \quad (4.9)$$

where the bar denotes a radial average. These expressions can be easily rearranged to yield

$$\bar{n}_e = 8\pi^2 f_0 \frac{m_e \epsilon_0}{\alpha e^2} (1 + \gamma^2) \Delta f \quad (4.10)$$

$$\gamma = \frac{\Delta\left(\frac{1}{Q}\right)}{\frac{2\Delta f}{f_0}} \quad (4.11)$$

$$v_m = \gamma \cdot 2\pi f_0 \quad (4.12)$$

which explicitly relate the average electron density and collision frequency to the measured perturbations.

The choice of cavity oscillation mode is dictated by two considerations:

(i) The elimination of a.c. polarisation space charge effects can be



achieved if the applied microwave field  $\underline{E}$  is everywhere normal to the electron density gradient, allowing the measurement of high electron densities.

(ii) Maximum sensitivity (i.e. maximum frequency shift per unit electron density) will be obtained for a mode with the electric field maximum on the discharge tube axis.

The simplest cylindrical cavity mode satisfying these requirements is the  $TM_{020}$  whose electric field components are

$$\begin{aligned} E_r &= 0 \quad E_\phi = 0 \\ E_z(r) &= E_0 J_0(x_{02} \frac{r}{R}) \end{aligned} \quad (4.13)$$

for the radial, azimuthal and axial directions respectively.  $J_0$  is the zero-order Bessel function and  $x_{02} = 5.52$  is its second root.

#### 4.2.2 Previous Work

The microwave resonant cavity technique has been applied to the study of gas laser discharges by several authors. Electron densities and drift velocities in the positive column of He-Cd laser discharges were measured by Dunn<sup>6</sup> using X-band microwave cavities oscillating in the  $TE_{011}$  or  $TM_{020}$  modes, the latter being used to measure low electron densities ( $< 5 \times 10^{11} \text{ cm}^{-3}$ ) where the sensitivity of the  $TE_{011}$  cavity was inadequate. Pure helium measurements were also made, returning a value for the electron collision frequency of  $\nu_m = 2 \times 10^9 \text{ s}^{-1} \text{ torr}^{-1}$  and showing electron density linear with discharge current. Murray<sup>7,11</sup> also used  $TE_{011}$  and  $TM_{020}$  X-band cavities, to measure electron densities in CO laser positive columns, with resulting electron densities  $\sim 4 \times 10^9 \text{ cm}^{-3} \text{ mA}^{-1}$ . Neither of these investigations involved measurements of the current dependence of  $\gamma$ , the reduced electron collision frequency. Dunn made the assumption  $\gamma \ll 1$ , a good

approximation for atomic gas discharges where elastic collisions predominate. Murray estimated  $\chi$  at high currents for a given gas mixture by determining the maximum measurable frequency shift and  $\Delta(\frac{1}{Q})$  before resonance broadening rendered the cavity resonance undetectable. The resulting high current value for  $\chi$  ( $I \sim 12 \text{ mA}, \chi \sim 1.25$ ) was then taken as constant for the gas mixture. Novgorodov et al.<sup>8</sup> used a more sophisticated approach using simultaneous measurements of the frequency shift and  $Q$  broadening. Results for  $\text{CO}_2 - \text{N}_2 - \text{He}$  mixtures at pressures below 6 torr and for various discharge tube diameters showed that electron density scaled with current density,  $j$  ( $\text{mA cm}^{-2}$ ); the gradient was typically  $5 \times 10^8 \text{ cm}^{-1} \text{ mA}^{-1}$ . Constant pressure momentum transfer collision frequencies were found to decrease with increasing current, but had approximate values of  $3 \times 10^9 \text{ s}^{-1} \text{ torr}^{-1}$ . The uncertainty in the measurements precluded any firm deductions on the effect of changing gas mixture ratios. No attempt was made to examine the effect of  $\text{CO}_2$  dissociation.

#### 4.2.3 Experimental arrangement

Figure 4.1 shows the experimental arrangement for the electron density measurements. The resonant cavity was constructed from phosphor-bronze and copper, with an internal diameter of 54 mm and an overall width of 40 mm. Microwaves were generated in a Flann Microwave Instruments model 449X Gunn diode signal source and coupled via a uni-directional isolator to the X-band (8.2 - 12.5 GHz) waveguide. A -10dB directional coupler was used to direct some microwave energy into the reference sidearm which contained an FMI model 16/7 precision calibrated frequency meter and was terminated by a broadband crystal diode detector. The main microwave energy was injected into a hybrid junction ("magic tee") and thereby directed to the measurement cavity. The reflected cavity signal was re-directed by the hybrid

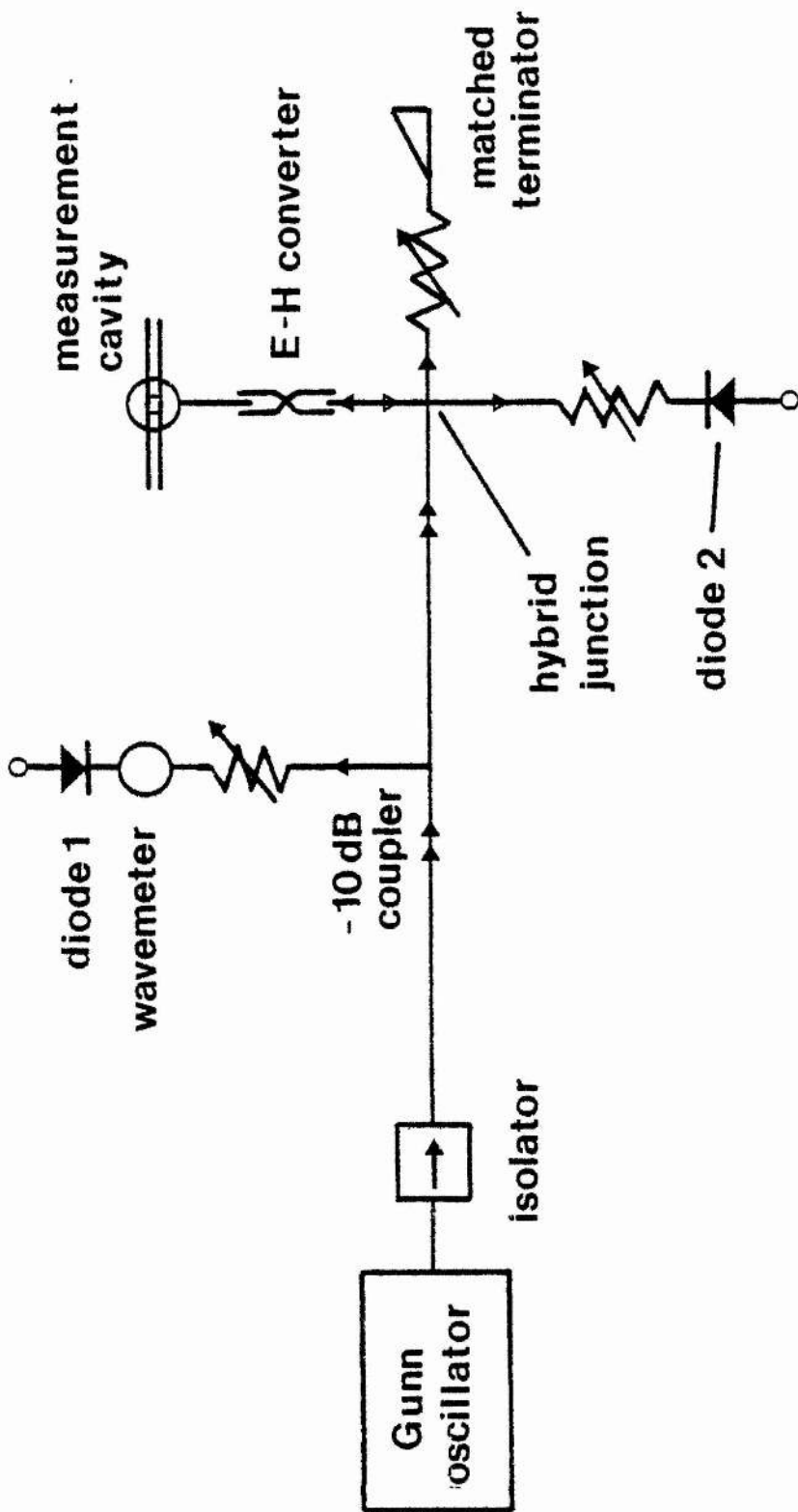
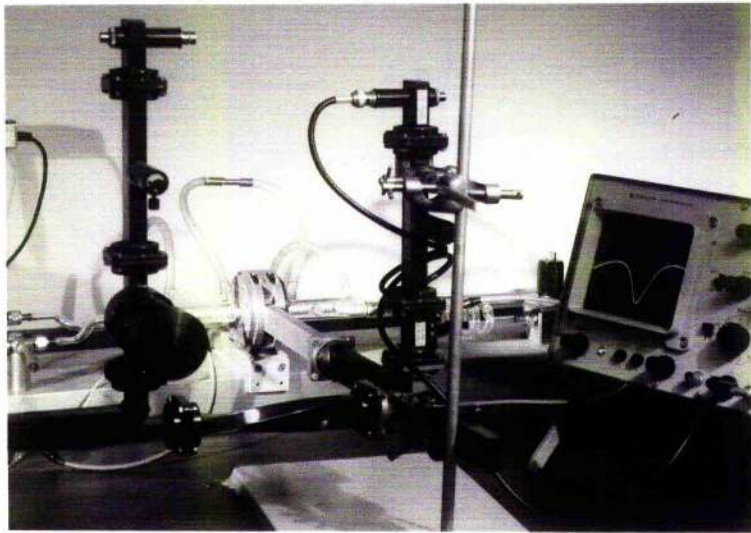
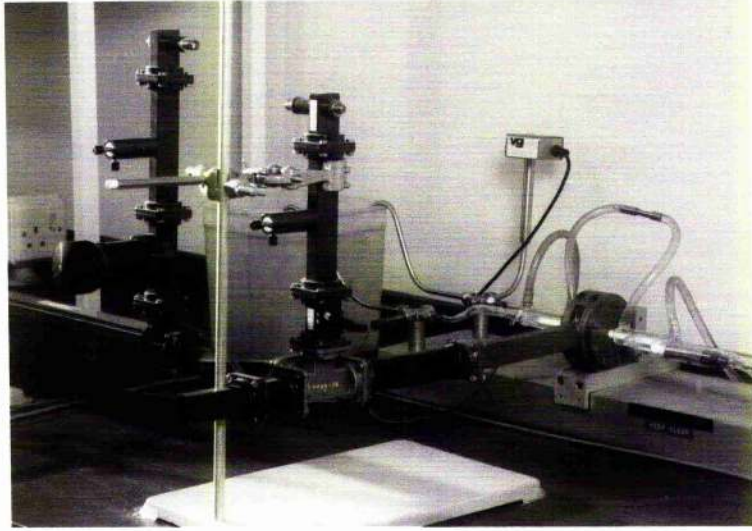


Fig. 4.1. Schematic of electron density measurement system.



Plates I and II: Experimental set-up for electron density measurement by X-band microwave cavity resonance.

junction into the measurement arm, which comprised a variable stub tuning element, padding attenuator and diode detector. The response of the detectors was governed by a square-law characteristic, i.e. voltage output  $\propto$  microwave power. In practice the microwave source signal was frequency modulated by a 3kHz saw-tooth to produce a frequency deviation greater than the resonance bandwidths of the frequency meter and measurement cavities. The detected signals could then be fed to a synchronously triggered dual channel oscilloscope to directly display the resonance curves of the two cavities. By adjusting the frequency meter to visually superimpose the resonance nodes, the resonant frequency of the measurement cavity could be determined to a precision of  $\sim 0.2$  MHz. The full-width half maximum frequency difference was also measured on the oscilloscope screen and used to obtain direct measurements of the cavity Q as a function of discharge current. Plates 1 and 2 show general views of the microwave equipment and the measurement discharge tube. This had an internal diameter of 8 mm and an active length of 15cm. Most measurements were made in flowing gas, with total pressure set by a closed-loop control system as described in section 3.2. Pre-dissociation of the  $\text{CO}_2$  could be achieved by activating a discharge in a long ( $\sim 40$  cm) tube which formed the first part of the gas flow circuit. Both the pre-dissociation discharge and the measurement discharge were powered by smoothed, stabilised high-voltage D.C. supplies.

The effective plasma volume in the  $\text{TM}_{020}$  cavity can be calculated by inserting equation (4.13) in (4.7) to obtain:

$$\alpha = \frac{\int_0^{R_p} |J_0(5.52 \frac{r}{R})|^2 r dr}{\int_0^R |J_0(5.52 \frac{r}{R})|^2 r dr} \quad (4.14).$$

Using the relationships

$$\int_0^X x |J_n(kx)|^2 dx = \frac{X^2}{2} \{ |J_n(kx)|^2 - J_{n-1}(kx)J_{n+1}(kx) \} \quad (4.15)$$

and

$$J_{-n}(x) = (-1)^n J_n(x) \quad (4.16)$$

then

$$\alpha = \frac{R_P^2 \{ [J_0(5.52 \frac{R_P}{R})]^2 + [J_1(5.52 \frac{R_P}{R})]^2 \}}{R^2 \{ [J_0(5.52)]^2 + [J_1(5.52)]^2 \}} \quad (4.17)$$

For the experimental conditions  $R = 27$  mm,  $R_P = 4$  mm then

$$\alpha = 0.1604$$

Using this value in (4.10) and evaluating leads to

$$\bar{n}_e = 1.4296 \times 10^9 (1 + \gamma^2) \Delta f \quad (4.18)$$

for  $\Delta f$  in MHz and  $\bar{n}_e$  in  $\text{cm}^{-3}$ . This equation was used to derive  $\bar{n}_e$  and  $v_m$  from the experimental measurements. Two other details of experimental technique are important. Since the section of discharge tube through the microwave cavity was uncooled, prolonged running of the discharge caused a measurable drift in the resonant frequency due to cavity heating ( $\approx 0.18 \text{ MHz}/^\circ\text{C}$ ). Hence, when the discharge current was switched on or altered, several minutes were allowed for thermal equilibration. On current switch-off, the frequency meter was quickly re-tuned to the zero-current resonance before appreciable cavity cooling could occur. In addition to the measurements of cavity resonance, discharge axial electric fields were measured using electrodes (spacing 13 cm) inserted directly into the positive column to avoid cathode fall effects.

### 4.3 Results

#### 4.3.1 Pure Helium

Initial measurements of the resonance characteristics of the

cavity, enclosing the discharge tube but with zero current, are displayed in Table 4.1. Measurement uncertainties were  $\pm 0.2$  MHz for the resonant frequency,  $f_0$ , and larger ( $\pm 0.5$  MHz) for the FWHM frequencies  $f_1$  and  $f_2$ , due to the need to estimate the position of half power points. Electron density measurements were first made in pure helium at pressures below 3 torr. Results are plotted against discharge current in figure 4.2, and show good linearity. The current transport equation was used to convert these data, combined with the corresponding voltage-current characteristics, to drift velocities

$$v_d \left( \frac{E}{P} \right) = b_e E = \frac{j}{en_e} \quad (4.19)$$

where  $b_e$  is the electron mobility. The results are tabulated (Table 4.2) and compared to those of Dunn and of Phelps et al<sup>9</sup> in figure 4.3. Agreement is good, despite the fact that the E/P values are uncorrected for gas heating effects, and confirms the validity of equation 4.18 for low pressures. For higher pressures the relatively high helium electron densities, and concomitant high electron-molecule collision frequencies, caused severe Q degradation which rendered the resonance curve undetectable. This "low Q" limitation applied to all the measurements and also imposed a maximum tolerable discharge current (12-15 mA depending on gas mixture). Although the total number of electron-He collisions was large, the collision frequency per electron, as represented by the parameter  $\gamma = v_m/\omega$ , was relatively small (for 2 torr of He typically  $\gamma \sim 5 \times 10^{-2}$ ) and could not be measured accurately by the Q broadening method. Consequently the effective collision frequency in He was calculated using elementary theory:

$$j = \sigma E$$

TABLE 4.1 Characteristics of electron density measurement cavity at zero discharge current.

Centre resonant frequency	$f_0$	$9245.5 \pm 0.2$	MHz
Full - width half - maximum resonance curve frequencies	$f_1$	$9244.7 \pm 0.5$	MHz
	$f_2$	$9246.5 \pm 0.5$	MHz
Cavity Q factor	$Q_0$	$5100 \pm 1500$	

TABLE 4.2 Measured and derived quantities in pure He.

Pressure (torr)	Current I (mA)	Specific electric field E/P (V cm <sup>-1</sup> torr <sup>-1</sup> )	Electron density $n_e$ (10 <sup>9</sup> cm <sup>-3</sup> )	Drift velocity $v_d$ (10 <sup>6</sup> cms <sup>-1</sup> )	Effective collision frequency $\nu_{eff}$ (10 <sup>9</sup> s <sup>-1</sup> )
1.0	1.5	15.9	1.7	10.6	2.6
1.0	3.0	15.5	3.5	10.6	2.6
1.0	5.0	15.1	5.8	10.7	2.5
1.0	10.0	14.5	11.3	10.9	2.3
1.0	15.0	14.2	16.9	11.0	2.3
1.3	3.0	11.7	4.2	8.9	3.0
1.3	5.0	11.5	7.3	8.4	3.1
1.3	10.0	11.2	14.5	8.5	3.0
1.3	15.0	11.0	20.9	8.8	2.9
2.0	2.0	8.2	4.4	5.6	5.1
2.0	5.0	7.8	11.0	5.6	4.9
2.0	7.0	7.7	15.6	5.6	4.9
2.0	10.0	7.6	21.5	5.6	4.6



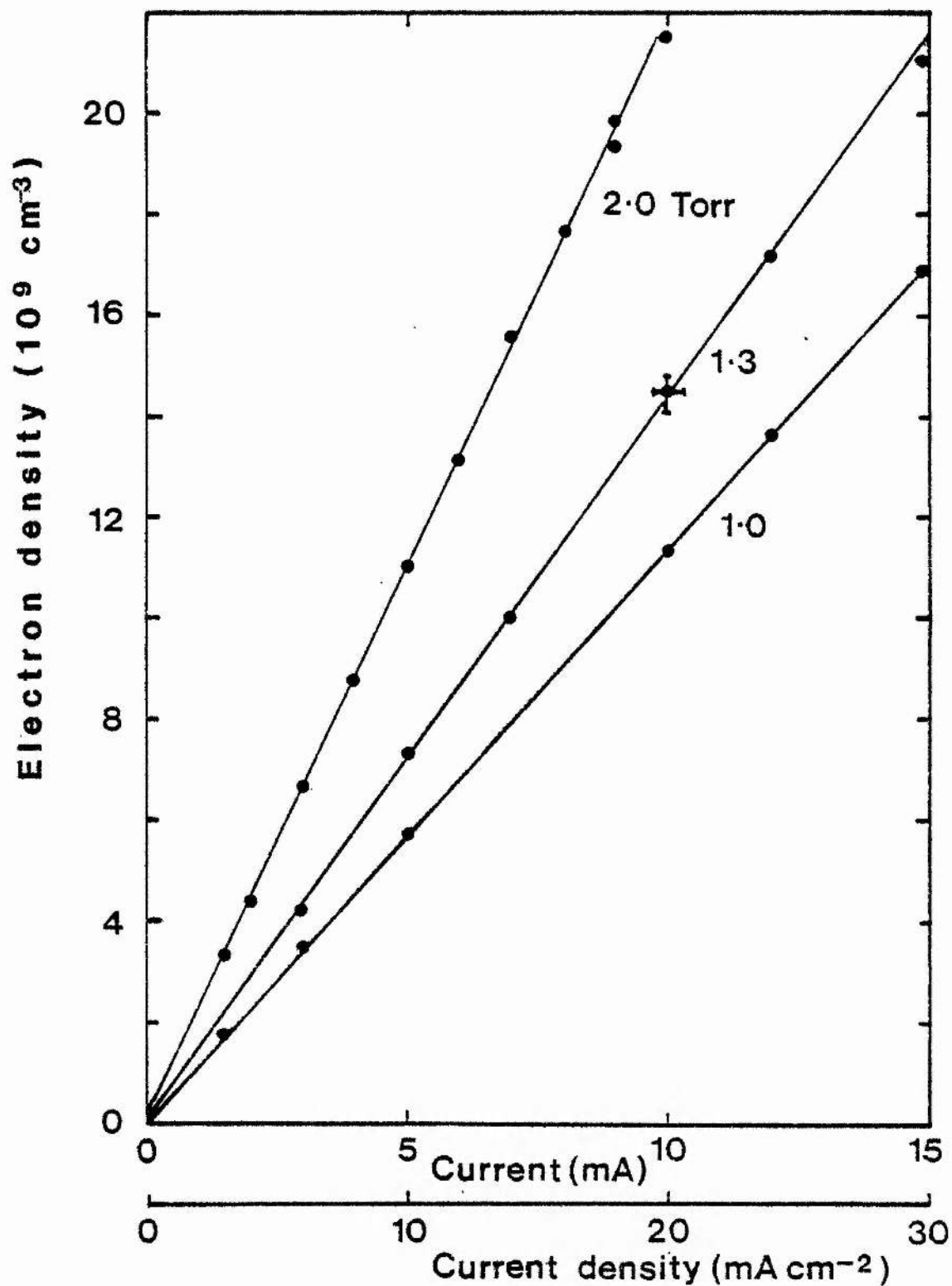


Fig. 4.2. Measured electron density in pure He at various pressures (flowing gas, 50 sccm, in 0.8 cm dia. tube).

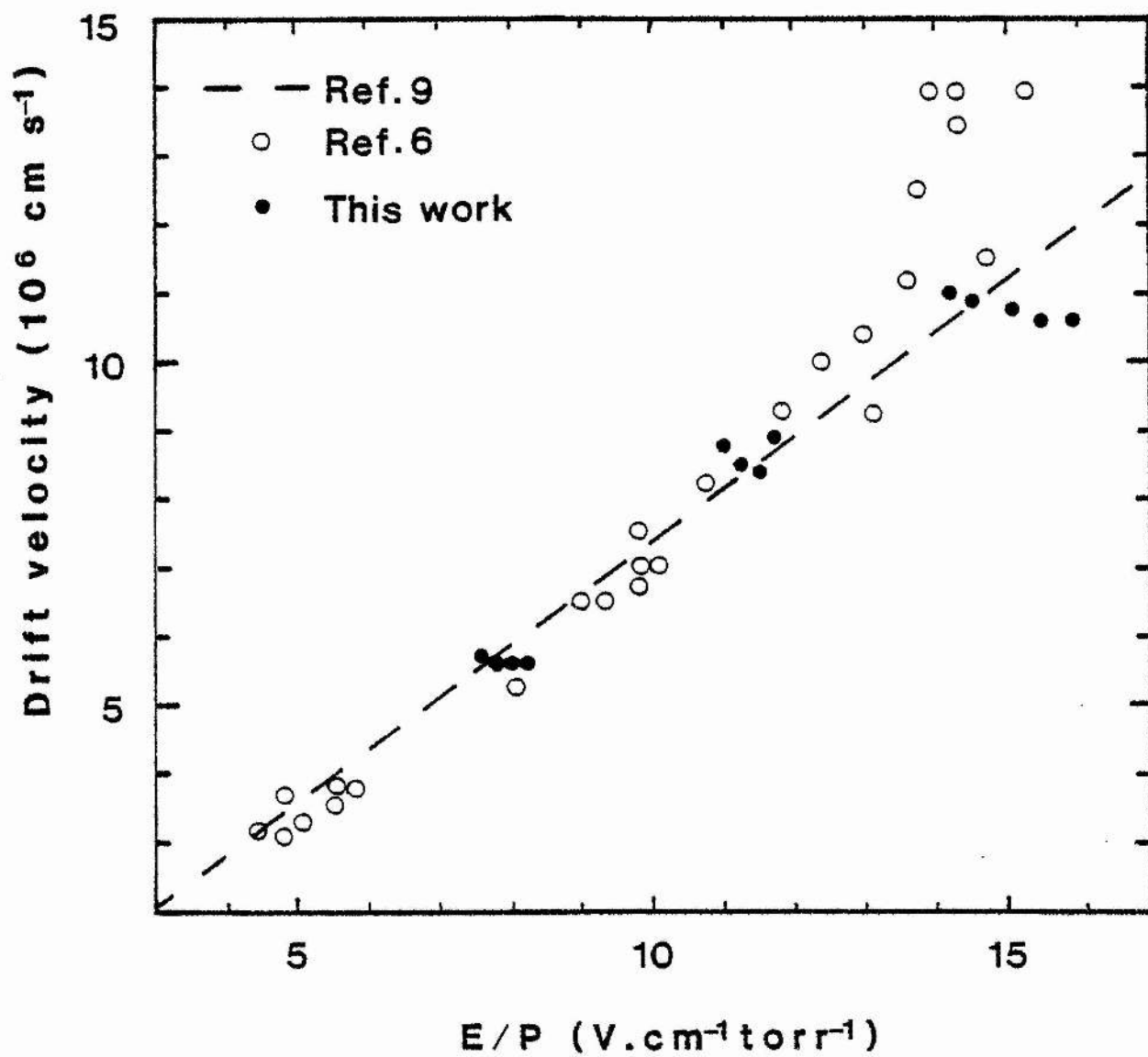


Fig. 4.3. Derived electron drift velocities in pure He and comparison to measurements of Dunn and Phelps et al. (after Dunn).

where

$$\sigma = \frac{\bar{n}_e e^2}{m v_{\text{eff}}}$$

so

$$v_{\text{eff}} = \left(\frac{e}{m}\right) \frac{\bar{n}_e}{j} E = \left(\frac{e}{m}\right) \frac{1}{b_e} \quad (4.20)$$

Calculated  $v_{\text{eff}}$  values are listed in Table 4.2, and show good agreement with Dunn's measurement of  $2 \times 10^9 \text{ s}^{-1} \text{ torr}^{-1}$ .

#### 4.3.2 Laser Mixtures

Several typical laser mixtures were studied : three standard  $\text{CO}_2 - \text{N}_2 - \text{He}$  mixtures in the ratios 6:12:82, 13:9:78 and 33:33:33, and an unconventional  $\text{N}_2$  - free mixture of composition 10% $\text{CO}_2$ : 20% $\text{CO}$ : 70% He. In all these mixtures the 'low-Q' limit restricted measurements to currents less than 13mA (see figure 4.4) corresponding to a maximum measurable electron density of  $\sim 1.6 \times 10^{10} \text{ cm}^{-3}$ . However, significant differences were observed between mixtures. As shown in figure 4.5, the largest specific electron densities (i.e. electron densities per unit discharge current) were observed in the mixtures with the highest He content. The mixtures with high concentrations of  $\text{CO}_2$ ,  $\text{N}_2$  or  $\text{CO}$  returned specific electron density values  $\sim 30\%$  lower. This observation is explained qualitatively by considering (i) the ionisation potentials of the constituent gas species, (ii) the likely population of discharge electrons with sufficient energy to cause electron impact ionisation. In a plasma of pure He (ionisation potential 24.6 eV) the electron energy distribution will be Maxwellian with a long high-energy "tail".  $\text{CO}_2$ ,  $\text{N}_2$  and  $\text{CO}$  have lower ionisation potentials (13.8, 15.6 and 14.0 eV respectively) but their large cross sections for vibrational excitation by low energy

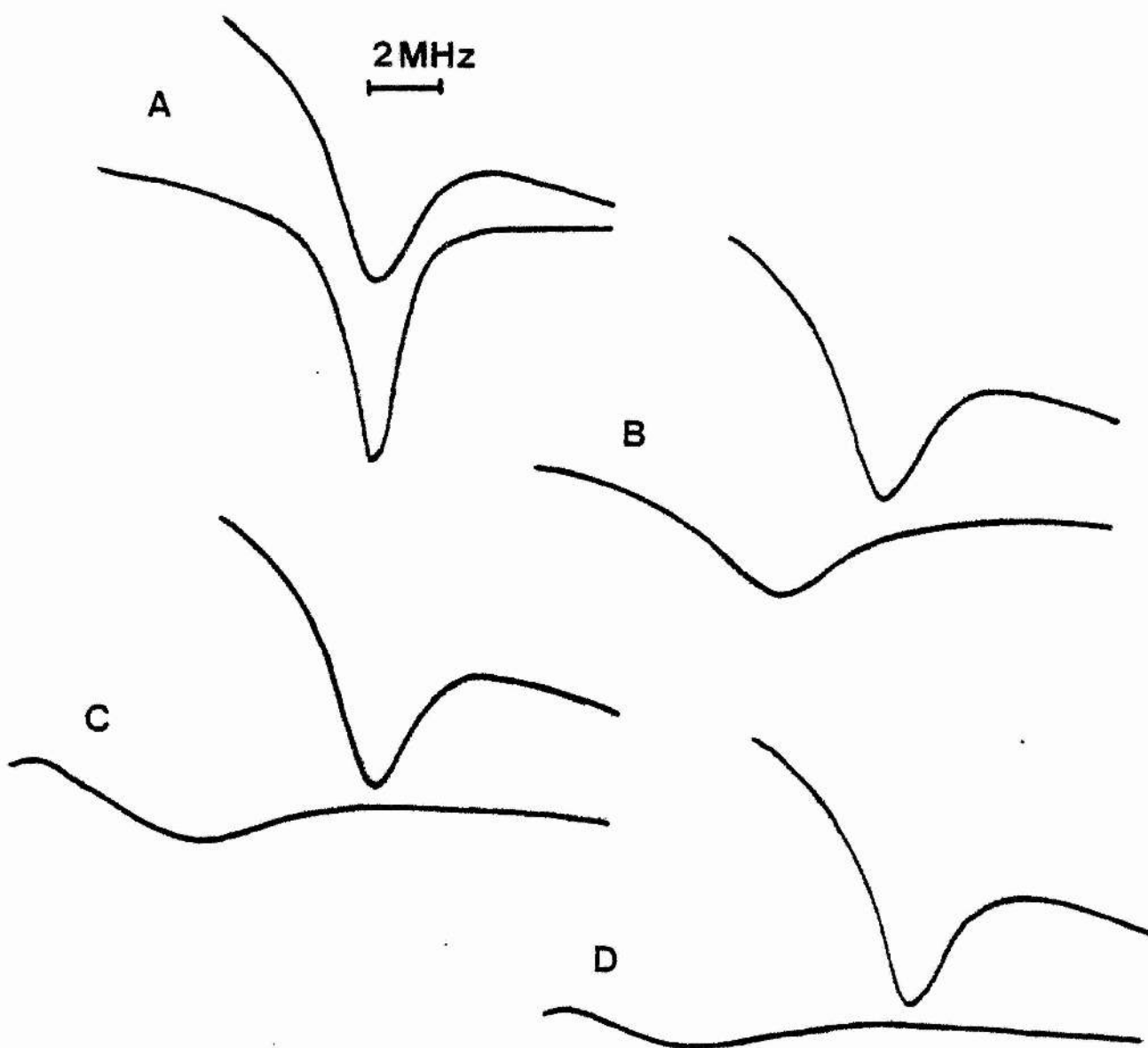


Fig. 4.4. Oscilloscope traces of microwave cavity resonances.

In each case the upper curve is the frequency meter resonance and the lower curve is that of the measurement cavity for various discharge currents in 10 torr of 10%  $\text{CO}_2$  : 20%  $\text{CO}$  : 70%  $\text{He}$  : (A) 0mA, (B) 5mA (C) 9mA, (D) 11mA.

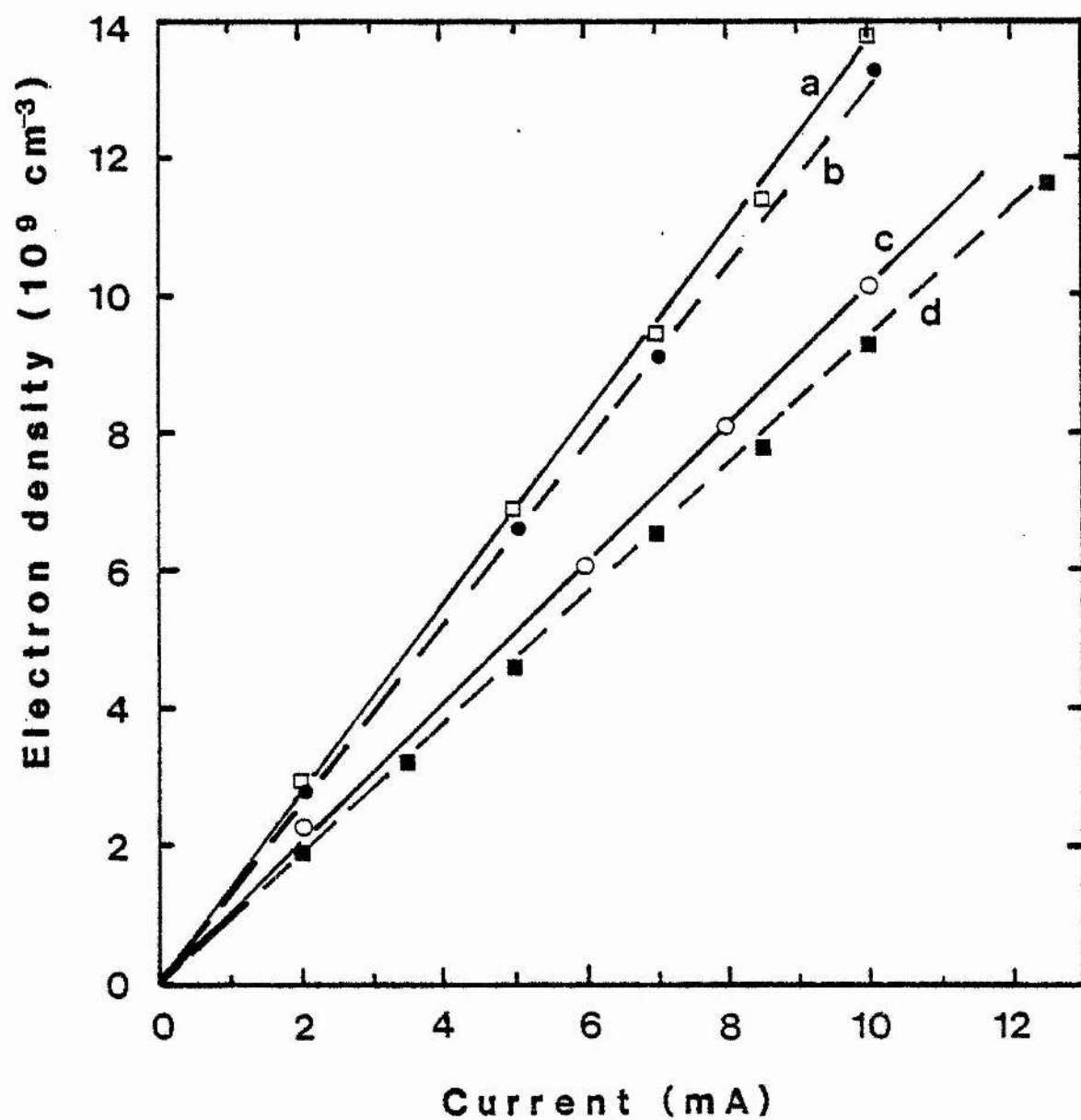


Fig. 4.5. Measured electron densities in various flowing gas mixtures (50 sccm) at 20 torr : (a) 6%  $\text{CO}_2$  : 12%  $\text{N}_2$  : 82% He, (b) 13%  $\text{CO}_2$  : 9%  $\text{N}_2$  : 78% He, (c) 10%  $\text{CO}_2$  : 20% CO : 70% He, (d) 33%  $\text{CO}_2$  : 33%  $\text{N}_2$  : 33% He.

electrons have the effect of lowering the average discharge electron energy and truncating the high energy tail of the distribution function. Thus the addition of these molecular species to a He plasma has the effect of reducing the net ionisation rate, which by plasma charge neutrality leads to a decreased electron density. This explanation is therefore similar to that proposed in Chapter 3 to explain the observed reduction of  $\text{CO}_2$  dissociation rate in molecule-rich gas mixtures.

The pressure dependence of both electron density and momentum transfer collision frequency was investigated over the range 5-40 torr. Results for the 13:9:78 mix are presented in figures 4.6 and 4.7. Electron density was found to decrease with increasing pressure at a rate of  $\sim 0.7\% \text{ torr}^{-1}$ , and some loss of linearity with current was observed at high pressures. The collision frequency per electron increased with pressure at constant current (as expected), and for a given pressure decreased monotonically with increasing current (decreasing  $E/N$ ). These observations agree with those of Novgorodov et al., who also found a similar inverse dependence of electron density on pressure. This dependence contrasts with that observed in He (fig. 4.2) and is clearly anomalous, since an increase in pressure at constant current causes a decrease in the measured  $E/N$ . This should result in a drift velocity decrease and therefore, by the transport equation (4.1), a rise in electron density. A further investigation of the anomaly was made, involving the consideration of possible systematic errors due to the large  $\gamma$ -values at high pressure, and the measurement of the electron density - pressure characteristic in various pure gases. This investigation is described in Appendix B, where it is shown that systematic errors are unlikely and that the

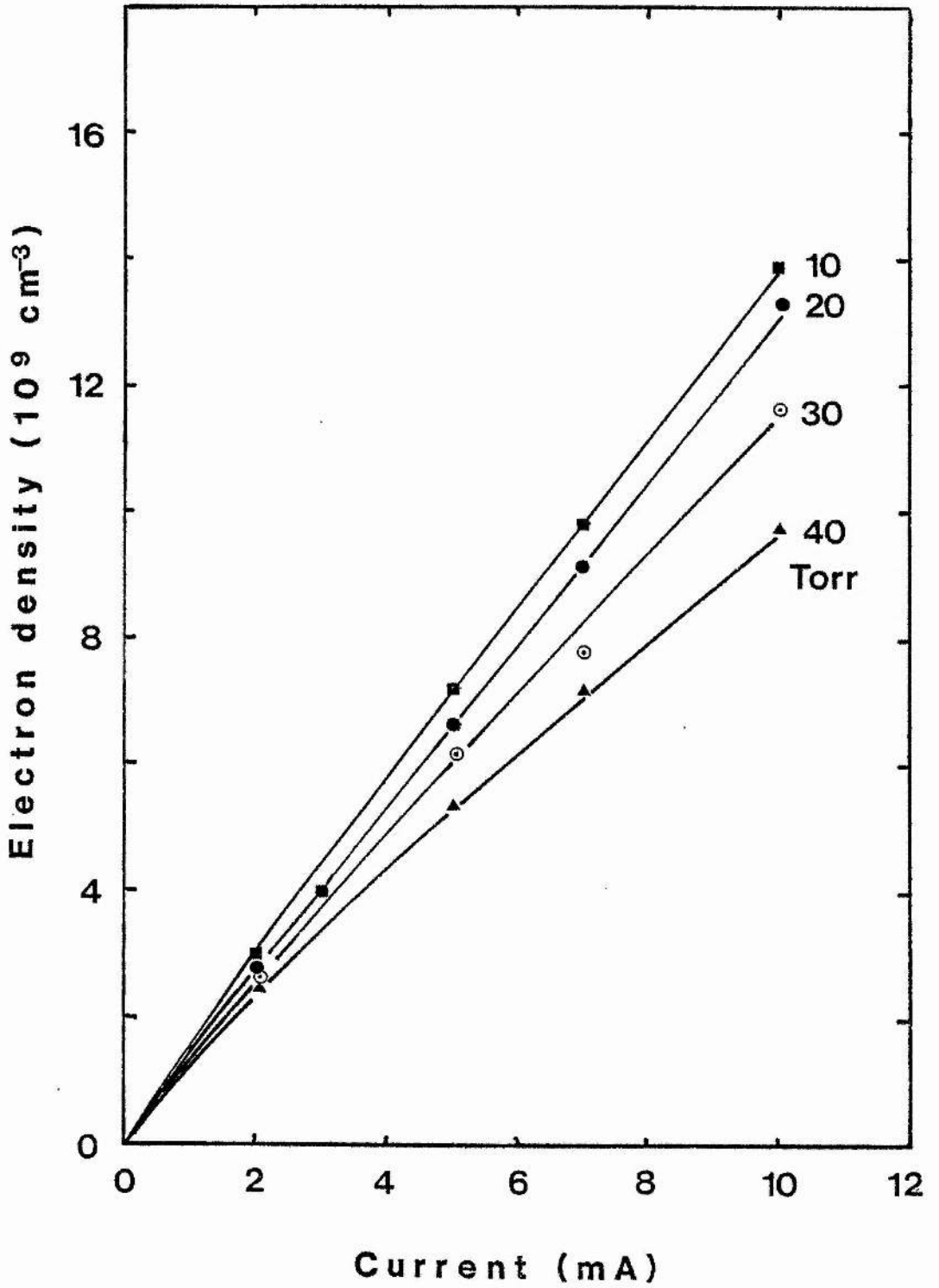


Fig. 4.6 Measured electron densities in  $13\text{CO}_2 : 9\text{N}_2 : 78\text{He}$  gas mixture at various pressures (flowing, 50 sccm).

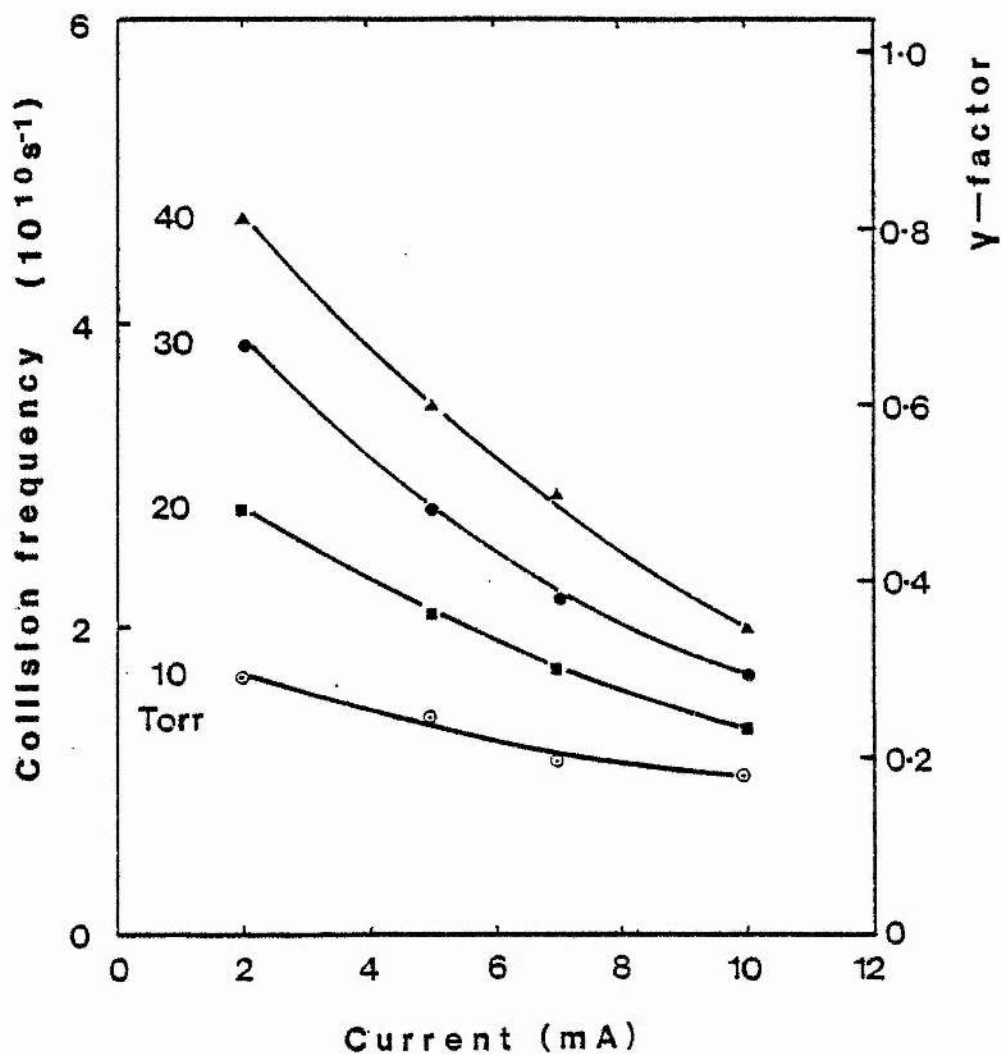


Fig. 4.7 Measured electron momentum transfer collision frequency and associated  $\gamma$ -factors in  $^{13}\text{CO}_2$  :  $9\text{N}_2$  :  $78\text{He}$  mixture at various pressures (flowing 50 sccm).



anomalous pressure dependence is probably due to changes in the radial profile of electron density.

#### 4.3.3 Effect of CO<sub>2</sub> dissociation

The effect of CO<sub>2</sub> dissociation on electron density and collision frequency was studied using the pre-dissociation discharge tube. To maximise any changes, the gas mixture richest in CO<sub>2</sub> was used (i.e. the 33%CO<sub>2</sub>: 33%N<sub>2</sub>: 33%He mixture). CO<sub>2</sub> dissociation levels at the input of the measurement discharge tube were monitored using the MSIOS mass spectrometer. For a total pressure of 5 torr and a flow rate of 50 sccm it was found that a predissociation tube discharge current of 15 mA was sufficient to induce ~ 50% dissociation. As seen in figure 4.8, the resultant change in specific electron density was not measurable. However, the collision frequency per electron was increased by about 20% (at low current), and about 8% (high current). These increases correspond well to the measured increase in the constant current electric field (~10%), as can be seen by considering equation (4.20). Since changes in dissociation level have no effect on the specific electron density ( $\bar{n}_e/j$ ), any increase in the discharge electric field must be due to a corresponding increase in the effective electron collision frequency (i.e. a decrease in the electron mobility). Within experimental uncertainty this is in fact the case. Thus the dissociation-induced current-voltage characteristic changes described in Chapter 3 can be solely attributed to an electron mobility which decreases with rising CO<sub>2</sub> dissociation, due to the replacement of CO<sub>2</sub> by O<sub>2</sub> and CO molecules with larger net inelastic collision cross-sections. The independence of electron density on dissociation also explains the experimental observation

Collision frequency

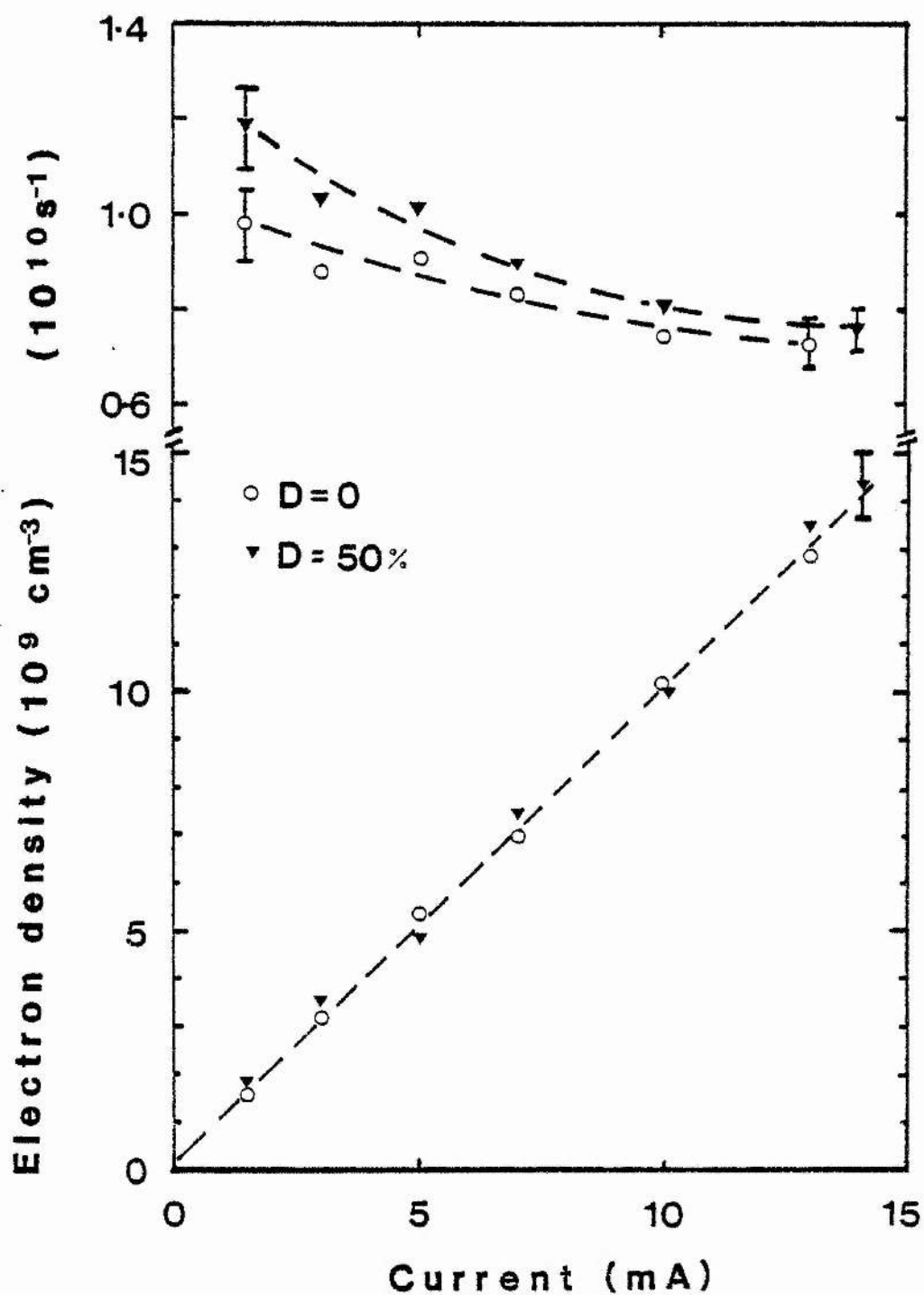


Fig. 4.8 Effect of  $\text{CO}_2$  dissociation on electron density and collision frequency in 33  $\text{CO}_2$  : 33  $\text{N}_2$  : 33 He at 5 torr pressure, 50 sccm flow rate.

that the electron density at constant pressure was not influenced by gas flow rate over the range 0-200 sccm.

#### 4.3.4 Effect of Xe addition

Xenon is often used as a CO<sub>2</sub> laser additive, since its effects of increasing the gain and output power and decreasing the constant current discharge voltage are well documented.<sup>10</sup> These beneficial effects have been shown to arise from an increase in discharge electron density and a fall in average electron energy, resulting in reduced CO<sub>2</sub> dissociation. To quantify these trends in conditions of practical interest, small amounts of Xe were added to the 6%CO<sub>2</sub>: 12%N<sub>2</sub>: 82%He and 10%CO<sub>2</sub>: 20%CO: 70%He mixtures at 20 torr total pressure in a sealed-off discharge. The results are plotted in figure 4.9 and show that in each case the addition of 2 torr of Xe resulted in an increase in specific electron density. The improvement was greater for the 6:12:82 mixture (30% compared to 20% for the N<sub>2</sub>- free mixture), and the good linearity of electron density with current was maintained. Addition of more Xe produced only slight further improvements, as shown in the diagram inset. No effect of Xe on the momentum transfer collision frequency was discernible. This supports the work of Murray and Smith<sup>11</sup> who observed the effect of Xe addition on CO laser discharges and concluded that the enhanced electron densities were the result of Xenon's relatively low ionisation potential (12.1 eV), but that Xe addition had no effect on the electron mobility which was completely dominated by inelastic collisions with CO and N<sub>2</sub>. Thus small Xe additions lower the discharge operating voltage for a given current; this results in higher electron densities and less VI gas heating, producing improved laser

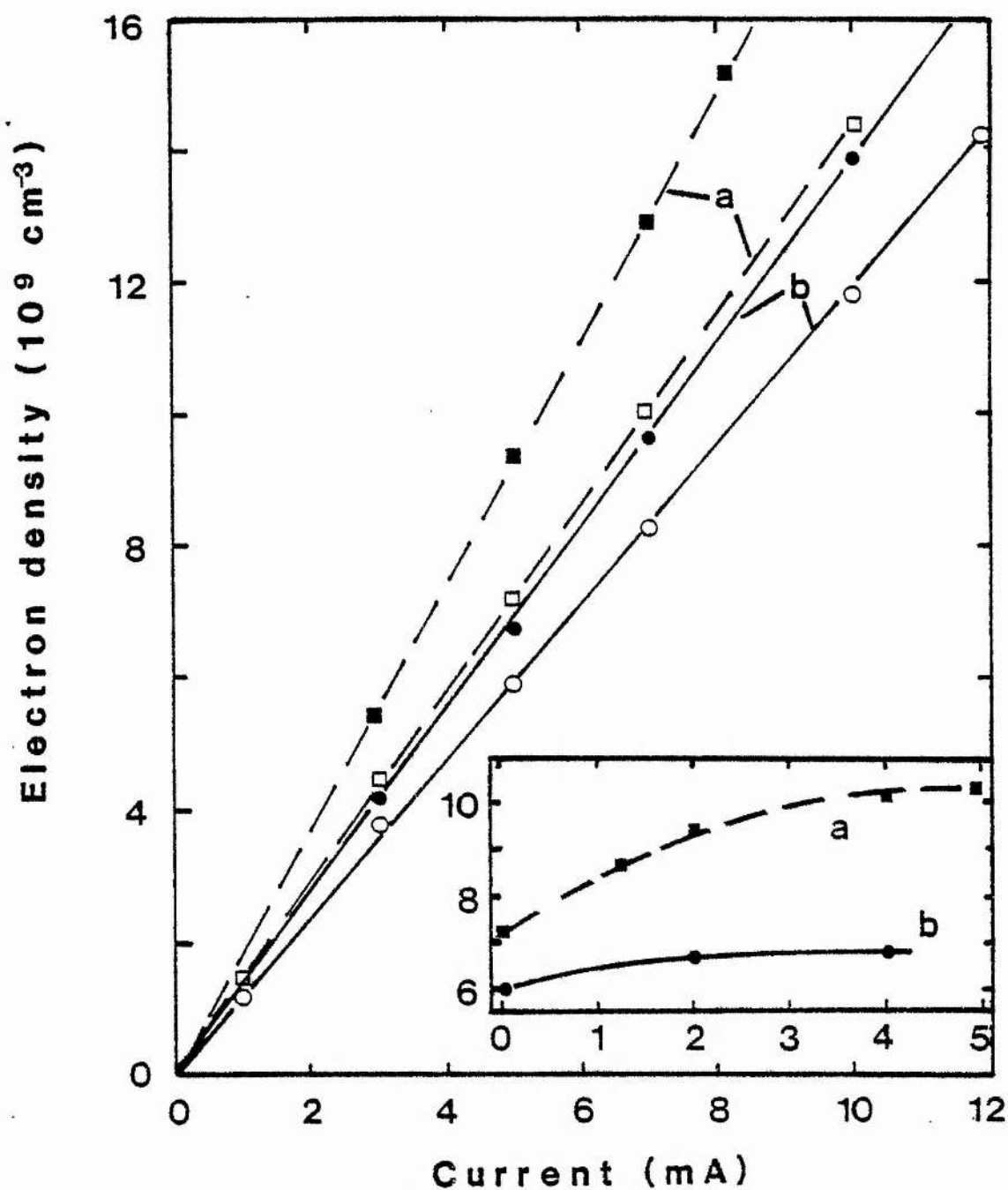


Fig. 4.9. Effect of Xe addition on measured electron density  
 (a) 6 CO<sub>2</sub> : 12 N<sub>2</sub> : 82 He mixture (b) 10 CO<sub>2</sub> : 20 CO :  
 70 He mixture. Open symbols are measurements in 20 torr  
 of basic mixture, closed symbols with 2 torr added Xe.  
 The inset shows electron density ( $10^9 \text{ cm}^{-3}$ ) against  
 added Xe (torr) for each case at constant current (5 mA).

efficiency and output power. Adding larger amounts produces no further improvement, since the Xe concentration quickly becomes far larger than that of the electrons so that the ionisation rate is wholly controlled by the electron density and temperature. Similarly, the beneficial effect of Xe addition will be larger in mixtures with initially high electron temperatures, explaining the experimental observation.

#### 4.4 Discussion and conclusions

The microwave cavity resonance technique has been used to examine electron densities and collision frequencies in a range of pure gases and CO<sub>2</sub> laser mixtures. The results for pure He are in excellent agreement with previous work and confirm the underlying validity of the technique. In the laser mixtures the current and pressure dependences of  $\bar{n}_e$  and  $V_m$  have been quantified and agree with those observed under similar conditions by Novgorodov et al. However, the pressure dependence of the averaged electron density seems inexplicable in terms of elementary discharge theory, and (as shown in Appendix B) is probably due to the effect of pressure on the radial profiles of electron density and gas number density. Nevertheless, the microwave electron density data are valuable in the accurate calculation of vibrational excitation rates in CO<sub>2</sub> laser discharges, and can be compared to electron densities predicted by the free-space Boltzmann code BOLTZ. Table 4.3 shows the comparison for three of the measured gas mixtures at typical operating E/N (no BOLTZ data was available for the 33:33:33 mixture). In each case the calculated electron density is roughly twice the measured value, which could be expected if the Boltzmann code was

TABLE 4.3 Comparison of measured electron densities with free-space

Boltzmann - code predictions.

<u>Mixture</u>	$\frac{E/N}{(\text{Td})}$	$\frac{v_d}{(\text{cm s}^{-1})}$	$\frac{n_e/j}{(\text{cm}^{-1} \text{ mA}^{-1})}$ (a)	$\frac{n_e/j^{(b)}}{(\text{cm}^{-1} \text{ mA}^{-1})}$
6 CO <sub>2</sub> : 12 N <sub>2</sub> : 82 He	30	6.5(6)	6.9(8)	1.1(9)
13 CO <sub>2</sub> : 9 N <sub>2</sub> : 78 He	30	6.5(6)	6.5(8)	1.1(9)
10 CO <sub>2</sub> : 20 CO : 70 He	32	6.9(6)	4.9(8)	9.0(8)

(a) Measured by microwave resonance at 20 torr pressure.

(b) Calculated by combination of BOLTZ drift velocity with the current transport equation.

Note: 1.1 (9) is equivalent to  $1.1 \times 10^9$ , etc.

accurate in its prediction of the drift velocity on the central axis of the discharge tube; this would correspond to a correct prediction of the axial electron density, which will be approximately twice the measured radial average if the electron density profile is close to a quadratic or Bessel function. Since the real profile is unknown, it is better to regard the computed and measured electron densities of Table 4.3 as respective upper and lower bounds on the values appropriate to the central region of the discharge tube diameter. It will be shown later that the uncertainty which this imposes on the vibrational kinetics modelling is acceptable.

The measurement discharge tube had an internal diameter of 0.8 cm. However, by using the similarity laws for CO<sub>2</sub> laser discharges,<sup>12,13</sup> which show that the current density  $j$  is a good scaling parameter, the tabulated electron density measurements can be applied to discharges in larger or smaller bore tubes.

In conclusion, the relationship between electron density and discharge current has been established for typical cw laser operating conditions. The effects of CO<sub>2</sub> dissociation and Xe addition have been measured, demonstrating that Xe increases constant-current electron densities by 20-30%, and that CO<sub>2</sub> dissociation has a negligible effect on electron density but reduces the electron mobility. A comparison of the measured electron densities to values computed by the Boltzmann code shows agreement to within a factor of 2. For a discharge current of  $1 \text{ mA cm}^{-2}$ , predicted electron densities are in the region  $0.5 - 1.0 \times 10^9 \text{ cm}^{-3}$ .

References for Chapter 4

1. S.J. Buchsbaum and S.C. Brown, Phys. Rev. 106, 2, 196 (1957).
2. S.J. Buchsbaum, I. Mower and S.C. Brown, Phys. Fluids 3, 5, 806 (1960).
3. K.B. Persson, Phys. Rev. 106, 2, 191, (1957).
4. M.A. Heald and C.B. Wharton "Plasma diagnostics with microwaves" (Wiley, New York, 1965).
5. J.C. Slater, Rev. Mod. Phys. 18, 441, (1946).
6. M.H. Dunn, J. Phys. B. Atom. Molec. Phys., 5, 665, (1972).
7. G.A. Murray, Ph.D. thesis, University of St. Andrews (1979).
8. M.Z. Novgorodov, A.G. Sviridov and N.N. Sobolev, Sov. Phys. Tech. Phys. 16, 4, 589, (1971).
9. A.V. Phelps, J.L. Pack and L.S. Frost, Phys. Rev. 117, 470, (1960).
10. P.O. Clark and J.Y. Wada, IEEE J. Quant. Electron QE-4, 5, 263 (1968).
11. G.A. Murray and A.L.S. Smith, J. Phys. D.: Appl. Phys., 11, 2477 (1978).
12. E.T. Antropov and I.A. Silin-Bekchurin, Sov. Phys. Tech. Phys., 16, 2, 269, (1971).
13. V.K. Konyukhov, Sov. Phys. Tech. Phys., 15, 8, 1283, (1971).



CHAPTER 5: A MODEL OF VIBRATIONAL EXCHANGE IN THE CO<sub>2</sub> LASER  
SYSTEM: VIBEX

5.1 Introduction

It has previously been argued that numerical models of the CO<sub>2</sub> laser system should be testable by comparison to experiment at a fundamental level. The vibrational temperature approximation offers a convenient and accurate simplification for such models, and CO<sub>2</sub> vibrational temperatures in laser discharges are measurable by the sequence band technique or by laser diode spectroscopy. The excitation rate constant data required by a vibrational kinetics model can be reliably generated by Boltzmann codes. In this Chapter, the formulation and solution of a vibrational population rate equation model is detailed.

5.2 Model Structure

5.2.1 The population rate equations

The basis of the kinetics model is the conventional vibrational mode scheme, whose use is justified by the very fast resonant exchange rates which occur within molecular vibrational modes. Only the comparatively slow energy exchange processes between modes are explicitly considered, using rate constants extracted from the literature. The structure of the vibrational kinetics model, and its relationship to the required input data, are shown in Figure 5.1. The formalism is essentially that of Tyte<sup>1</sup>; however, in distinction to Tyte's model, allowance is made for a vibrationally excited CO population and its interaction by V-V-T exchange with the N<sub>2</sub> and CO<sub>2</sub>(v<sub>3</sub>) modes. For the case of zero stimulated emission, and neglecting diffusional and wall quenching effects, the system rate equations for population transfer

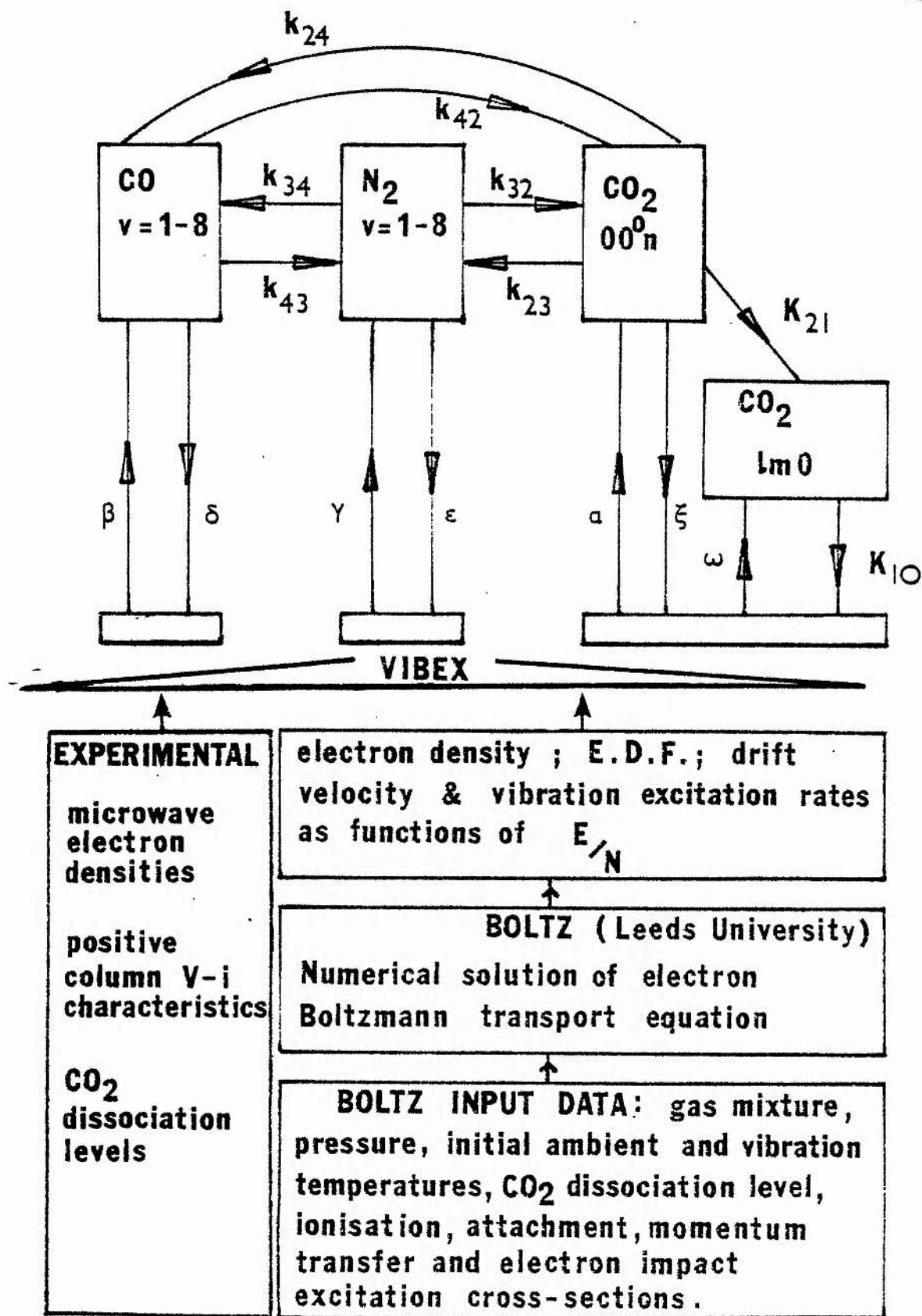


Fig. 5.1. Logical structure of the kinetics model.

are:

$$\frac{dn_1}{dt} = K_{21}n_2 - K_{10}n_1 + (K_{01} + \omega)(n - n_1 - n_2) \quad (5.1)$$

$$\begin{aligned} \frac{dn_2}{dt} = & \alpha(n - n_1 - n_2) - \xi n_2 + k_{32}(n - n_1 - n_2)N^* \\ & + k_{42}(n - n_1 - n_2)C^* - k_{23}n_2(N - N^*) \\ & - k_{24}n_2(C - C^*) - K_{21}n_2 \end{aligned} \quad (5.2)$$

$$\begin{aligned} \frac{dN^*}{dt} = & \gamma(N - N^*) - \epsilon N^* - k_{32}N^*(n - n_1 - n_2) \\ & + k_{43}C^*(N - N^*) - k_{34}(C - C^*)N^* \\ & + k_{23}n_2(N - N^*) \end{aligned} \quad (5.3)$$

$$\begin{aligned} \frac{dC^*}{dt} = & \beta(C - C^*) - \delta C^* - k_{43}(N_2 - N^*)C^* \\ & + k_{34}N^*(C - C^*) - k_{42}(n - n_1 - n_2)C^* \\ & + k_{24}n_2(C - C^*) \end{aligned} \quad (5.4)$$

where  $n_1$  and  $n_2$  are the population densities ( $\text{cm}^{-3}$ ) of the  $\text{CO}_2(\nu_1, \nu_2)$  and  $\text{CO}_2(\nu_3)$  modes respectively, and  $C^*$  and  $N^*$  are the CO and  $\text{N}_2$  vibrationally excited population densities.

Implicit in the equations as written is the conservation of species populations:

$$n = n_0 + n_1 + n_2 \quad (5.5)$$

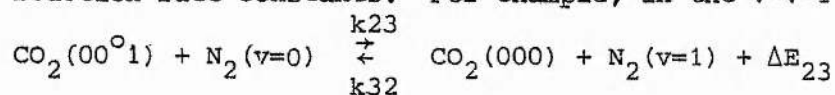
$$N = N_0 + N^* \quad (5.6)$$

$$C = C_0 + C^* \quad (5.7)$$

where  $n, N$  and  $C$  represent the total  $\text{CO}_2$ ,  $\text{N}_2$  and  $\text{CO}$  populations respectively, the subscript 0 indicates ground state populations and the asterisks denote total vibrationally excited populations. The rate constants  $\alpha, \beta, \gamma$  and  $\omega (\text{s}^{-1})$  are effective electron impact excitation rates summed over the first eight vibrational levels in each mode; they are related to the Boltzmann code calculated excitation rate constants of Chapter 2 by:

$$\begin{aligned}\alpha &= n_e X_3 \\ \beta &= n_e X_6 \\ \gamma &= n_e X_4 \\ \omega &= n_e X_T\end{aligned}\quad (5.8)$$

where  $n_e$  is the volume averaged discharge electron density ( $\text{cm}^{-3}$ ). The de-activation rate constants  $\delta, \epsilon, \xi$ , and  $K_{10}$  include two distinct contributions: (i) V-T relaxation by molecular collisions, and (ii) de-activation by superelastic electron collisions, at a rate determined by the principle of detailed balance from the corresponding electron excitation rate constants. The  $k$ 's ( $\text{cm}^3 \text{s}^{-1}$ ) are rate constants for V-V-T exchange; the back-reaction rates are derived from the forward reaction rate constants. For example, in the V-V-T exchange



the rate constants are related by a simple Boltzmann factor:

$$k_{23} = k_{32} \exp\left(\frac{\Delta E_{23}}{kT}\right)$$

where  $E_{23} = +18 \text{ cm}^{-1}$  is the energy difference between the  $(00^0_1)$  and  $\text{N}_2(v=1)$  levels, and  $T$  is the ambient gas temperature. For such a small energy difference at typical temperatures ( $T = 400\text{K}$ ) the Boltzmann factor is close to unity, and in the case above

$$k_{23} = 1.07 k_{32} .$$

However, for the  $\text{CO}_2 \rightarrow \text{CO}$  and  $\text{N}_2 \rightarrow \text{CO}$  exchanges, with energy surpluses of  $206 \text{ cm}^{-1}$  and  $188 \text{ cm}^{-1}$  respectively, then

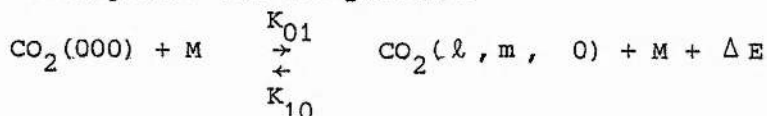
$$k_{24} = 2.10 k_{42}$$

and

$$k_{34} = 1.97 k_{43}$$

at the same temperature.

The rate constant  $K_{01}$  defines the rate of thermal excitation of  $\text{CO}_2$  molecules from the ground state to the combined symmetric stretch-bending mode via the process.



where for the moment  $K_{10}$  includes only a V-T component. As usual  $K_{10}$  is calculated by summing the rate constants of each possible collision partner M:

$$K_{10} = \sum_s K_s N_s$$

where  $N_s$  is the number density ( $\text{cm}^{-3}$ ) of molecular species  $s$ . The  $K_{01}$  rate constant for the reverse process is calculated by again applying the principle of detailed balance, that is by imposing the condition that, in the absence of any other transfer processes, the balance of excitation and de-excitation must yield a  $(\ell, m, 0)$  population appropriate to thermal equilibrium at the gas temperature  $T$ . In the vibrational temperature approximation, the ratio of the  $(\ell m 0)$  to ground state population is

$$\frac{n_1}{n_0} = \sum_{\ell=1}^{\infty} x_1^{\ell} + \sum_{m=1}^{\infty} (m+1)x_2^m \quad (5.9)$$

where as before

$$x_i = \exp\left(\frac{-h\nu_i}{kT_i}\right) \quad i = 1, 2.$$

Equation (5.9) can be evaluated using the relations<sup>2</sup>

$$\sum_{n=1}^{\infty} x^n = \frac{x}{1-x} \quad (5.10)$$

$$\sum_{n=1}^{\infty} nx^n = \frac{x}{(1-x)^2} \quad (5.11)$$

so that

$$\frac{n_1}{n_0} = \frac{x_1}{1-x_1} + \frac{x_2}{1-x_2} + \frac{x_2}{(1-x_2)^2} \quad (5.12)$$

= R, say.

Assuming thermal equilibrium at  $T_1 = T_2 = 400\text{K}$  and putting  $h\nu_1 = 1337 \text{ cm}^{-1}$ ,

$h\nu_2 = 667 \text{ cm}^{-1}$  yields

$$R = 0.218$$

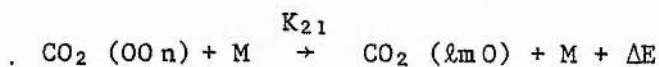
and

$$K_{01} = R \cdot K_{10}$$

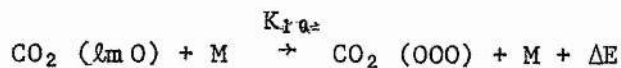
### 5.2.2 Rate constant data

The inter-mode exchange processes described by the population rate equations have been extensively studied by various techniques including laser-excited vibrational fluorescence, high temperature infrared emission in shock tubes, and room temperature ultrasonic absorption. As a result the rate constants for most of the processes are reasonably well known. Taylor and Bitterman<sup>3</sup> and Stephenson and Moore<sup>4</sup> have published useful surveys of the most important rate data. The experimental techniques cannot reveal the exact origin or destination of energy exchanged between vibrational modes other than to identify the modes themselves; that is, they cannot discriminate between vibrational levels within a mode. Thus caution is required in the physical interpretation of the rate constants. However the rate constants are directly

TABLE 5.1.    Standard rate constants used in VIBEX  
assuming 400K ambient gas temperature

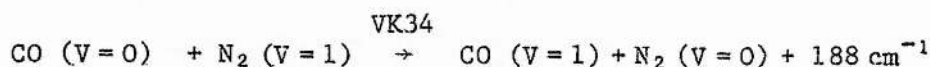
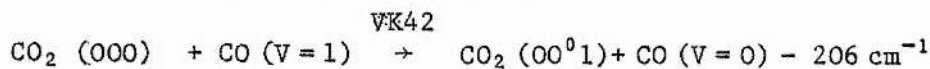
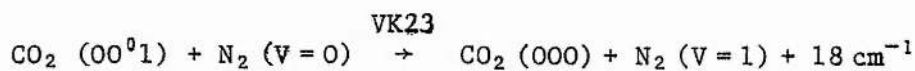
(1) CO<sub>2</sub> V-V-T deactivation (K<sub>21</sub>)

<u>M</u>	<u>Label</u>	<u>Rate constant (cm<sup>3</sup>s<sup>-1</sup>)</u>	<u>Ref.</u>
CO <sub>2</sub>	A(1)	1.1 (-14)	4, 12
N <sub>2</sub>	A(2)	4.2 (-15)	8, 12
CO	A(3)	8.5 (-15)	4
O <sub>2</sub>	A(4)	4.8 (-15)	8
He	A(5)	2.8 (-15)	9, 12

(2) CO<sub>2</sub> V-T deactivation (K<sub>10</sub>)

<u>M</u>	<u>Label</u>	<u>Rate constant (cm<sup>3</sup>s<sup>-1</sup>)</u>	<u>Ref.</u>
CO <sub>2</sub>	B(1)	6.0 (-15)	3, 10
N <sub>2</sub>	B(2)	2.0 (-15)	3, 10
CO	B(3)	6.9 (-13)	11
O <sub>2</sub>	B(4)	2.0 (-15)	3, 10
He	B(5)	1.5 (-13)	3, 10

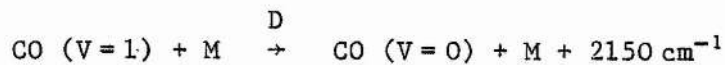
## (3) V-V exchanges



<u>Label</u>	<u>Rate constant (cm<sup>3</sup>s<sup>-1</sup>)</u>	<u>Ref.</u>
VK 23	2.5 (-13)	3, 12, 20
VK 42	9.7 (-14)	4, 13
VK 34	1.7 (-14)	14

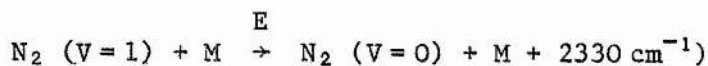
TABLE 5.1      CONTINUED

(4) CO V-T deactivation



<u>M</u>	<u>Label</u>	<u>Rate constant(cm<sup>3</sup>s<sup>-1</sup>)</u>	<u>Ref.</u>
CO <sub>2</sub>	D(1)	Not available	7
N <sub>2</sub>	D(2)	Not available	7
CO	D(3)	3.7 (-19)	8, 15
O <sub>2</sub>	D(4)	1.0 (-16)	18
He	D(5)	3.7 (-17)	17, 19

(5) N<sub>2</sub> V-T deactivation



<u>M</u>	<u>Label</u>	<u>Rate constant(cm<sup>3</sup>s<sup>-1</sup>)</u>	<u>Ref.</u>
CO <sub>2</sub>	E(1)	Not available	7
N <sub>2</sub>	E(2)	1.0 (-18)	3
CO	E(3)	Not available	7
O <sub>2</sub>	E(4)	1.0 (-18)	3
He	E(5)	5.3 (-18)	3



applicable to the formulation of (5.1) - (5.7). For an assumed ambient gas temperature of 400K, the model rate constants are tabulated in Table 5.1.

### 5.2.3 Solution method

The system of rate equations (5.1) - (5.4) forms a set of simultaneous ordinary differential equations (O.D.E.'s) in the unknowns  $n_1$ ,  $n_2$ ,  $N^*$  and  $C^*$ . In recent years numerical solutions of such systems have been intensively studied, resulting in many reliable computer-based algorithms. These include the Euler method and Runge-Kutta and predictor-corrector techniques. The relative merits and de-merits of these techniques are thoroughly discussed in reference 5; it can be shown that a particularly convenient combination is obtained by starting the solution using a one-step technique (e.g. the improved Euler method), followed by convergence using predictor-corrector iterations. This process is best understood by considering in detail its treatment of the population rate equations. These can be represented by

$$\frac{dn_1}{dt} = R_1(n_1, n_2)$$

$$\frac{dn_2}{dt} = R_2(n_1, n_2, N^*, C^*)$$

$$\frac{dN^*}{dt} = R_3(n_1, n_2, N^*, C^*)$$

$$\frac{dC^*}{dt} = R_4(n_1, n_2, N^*, C^*)$$

or, more generally,

$$\frac{dX_i}{dt} = R_i(X_1, X_2, X_3, X_4) \quad i = 1 \text{ to } 4$$

where  $X_1 = n_1$ ,  $X_2 = n_2$ ,  $X_3 = N^*$  and  $X_4 = C^*$

are the system unknowns, and the  $R_i$  are the time dependent rates of change of population. We first define the initial population levels at time  $t = 0$ :

(Step 1)

$$X_i(0) = X_{i0}$$

and denote

$$R_{i0} = R_i(0) = R_i(X_{10}, X_{20}, X_{30}, X_{40})$$

as the initial rates of change.

(Step 2)

The improved Euler method is used to estimate the populations at time  $t_1 = t_0 + h$ :

$$X_{11} = X_{10} + \frac{h}{2} \{ R_{10} + R_1(X_{10} + hR_{10}, X_{20} + hR_{20}, X_{30} + hR_{30}, X_{40} + hR_{40}) \}$$

$$X_{21} = X_{20} + \frac{h}{2} \{ R_{20} + R_2(X_{10} + hR_{10}, X_{20} + hR_{20}, X_{30} + hR_{30}, X_{40} + hR_{40}) \}$$

and so on.

(Step 3)

The populations at  $t_2 = t_0 + 2h$  are now predicted from the  $t_0$  and  $t_1$  values

$$X_{12}^{(0)} = X_{10} + 2hR_1(X_{11}, X_{21}, X_{31}, X_{41})$$

$$= X_{10} + 2hR_{11}$$

$$X_{22}^{(0)} = X_{20} + 2hR_{21}$$

$$X_{32}^{(0)} = X_{30} + 2hR_{31}$$

$$X_{42}^{(0)} = X_{40} + 2hR_{41}$$

(Step 4)

The predictions are corrected using the iterations

$$x_{12}^{(j)} = x_{11} + \frac{h}{2} \left( R_{11} + R_1(x_{12}^{(j-1)}, x_{22}^{(j-1)}, x_{32}^{(j-1)}, x_{42}^{(j-1)}) \right)$$

$$x_{22}^{(j)} = x_{21} + \frac{h}{2} \left( R_{21} + R_2(x_{12}^{(j-1)}, x_{22}^{(j-1)}, x_{32}^{(j-1)}, x_{42}^{(j-1)}) \right)$$

etc., which are repeated until the  $x_i^{(j)}$  converge to steady values. In this step there is an interaction between the four equations; if we were to try to obtain a final solution for  $x_{12}$ , by iterating on it alone, we would have to work exclusively with the predicted values  $x_{22}^{(0)}$ ,  $x_{32}^{(0)}$ ,  $x_{42}^{(0)}$ , which are only approximations. If we then iterated to get a more accurate  $x_{22}$ , we would develop a value different from that used in computing  $x_{12}$ . In short, the simultaneity of the equations demands that the formulae of Step 4 be applied in strict rotation. (Step 5).

The truncation errors in the predictor-corrector stage are estimated from

$$E_T(x_{12}) = \frac{1}{5}(x_{12}^{(0)} - x_{12}^{(j)})$$

$$E_T(x_{22}) = \frac{1}{5}(x_{22}^{(0)} - x_{22}^{(j)})$$

etc., and used to correct the final solutions of the  $x_{i2}$ , e.g.:

$$x_{12} = x_{12}^{(j)} + \frac{1}{5}(x_{12}^{(0)} - x_{12}^{(j)})$$

(Step 6)

The  $x_{i0}$  and  $x_{i1}$  are replaced in the predictor formulae (Step 3) by the  $x_{i1}$  and  $x_{i2}$  values respectively. Thus the predictor calculates the  $x_i$  values after the next time-step (i.e. at  $t_3 = t_0 + 3h$ ) and so the cycle repeats.

When only steady-state population densities are of interest, the calculation is allowed to run on until all the population changes in a single time-step are less than some pre-determined limit, in which

case population equilibrium is deemed to be established. However it is obvious that the time evolutions of the excited populations are also produced, and accurate time-evolved calculations are possible for a suitable choice of time-steps and initial conditions.

A FORTRAN computer program was constructed, based on the algorithms; the flow-chart of Figure 5.2 illustrates the main features. Necessary input data includes the values of the molecular V-V-T rate constants, and electron excitation rates as computed by BOLTZ for the appropriate gas mixture, temperature, pressure and E/N. Additionally the numerical solution requires values for H (the time-step size), TOLER (the predictor-corrector iteration convergence tolerance), MAX (the maximum allowed number of corrector iterations before convergence) and CHANGE (the minimum percentage population change per time-step before the establishment of equilibrium is accepted). The population rate equations are set up as arithmetical function statements and the initial conditions are specified and printed. Values for vibrational populations after the first time step are denoted X11, X21, etc. Subsequent time-dependent populations are calculated according to Steps 3 and 4 above. The notational convention is that X12NEW, X22NEW etc. in the figure and program correspond to the  $X_{i2}^{(j)}$  of Step 4, and are initially derived from the  $X_{i2}^{(0)}$  values which are simply denoted X12, X22, etc. in the program. The truncation error  $E_T(X_{i2})$  of Step 5 is designated ERRX1 and is used to correct the current X12NEW value after its convergence within the fractional tolerance limit TOLER. After printing the current or corrected values T2, X12, X22, X32, X42 and the truncation errors, the predictor-corrector method can be applied again for the next time-step. Before this is done, X10 is given the value previously assigned to X11, and X11 that previously

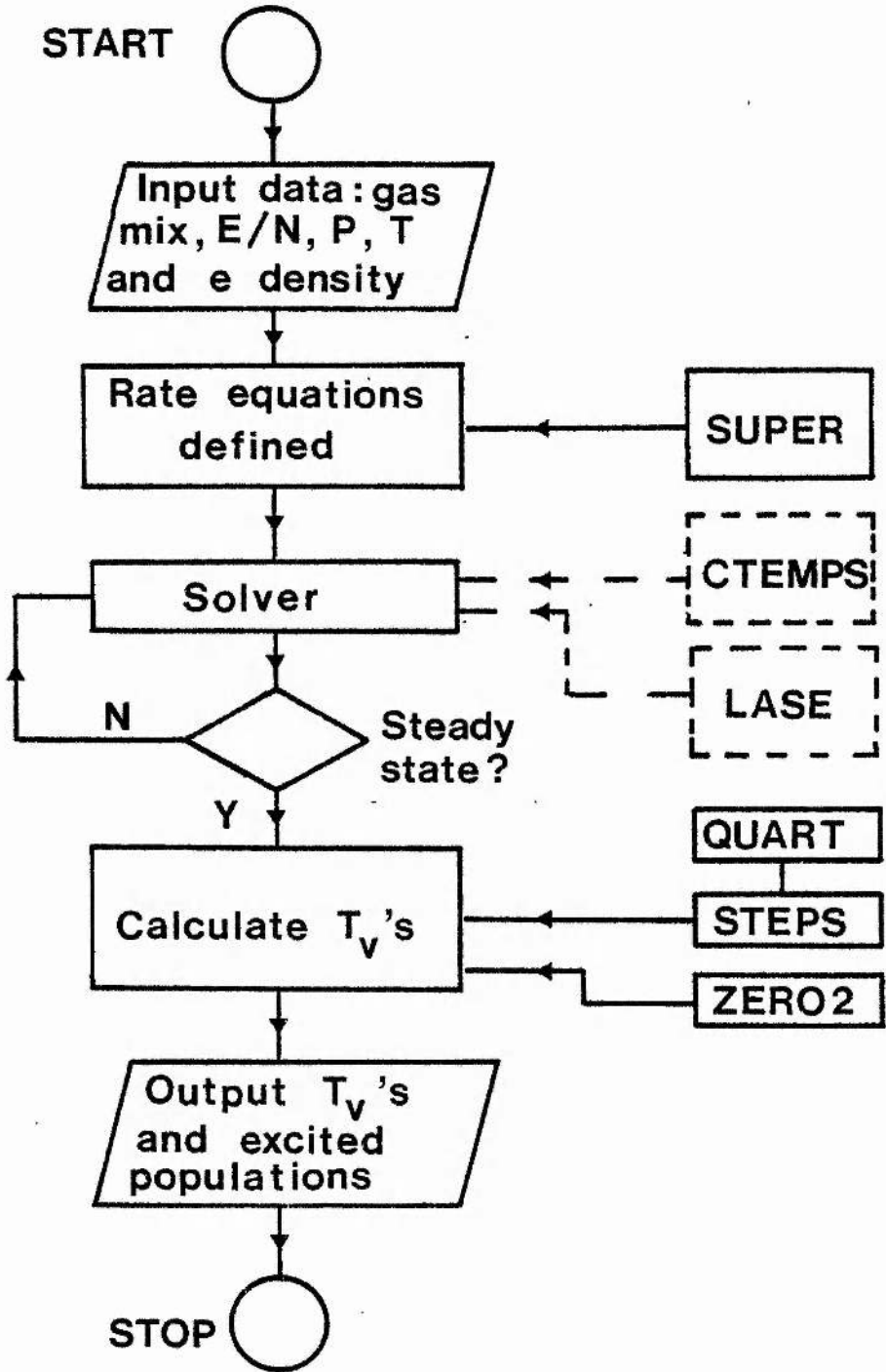


Fig. 5.2. Flow-chart for steady-state VIBEX calculations (see text).

TABLE 5.2      Glossary of terms used in system rate  
equations and in VIBEX code.

<u>Description</u>	<u>Text and system equations</u>	<u>VIBEX</u>
Total CO <sub>2</sub> population (cm <sup>-3</sup> ).	n	TCO2
CO <sub>2</sub> asymmetric mode population.	n <sub>2</sub>	X2
Combined CO <sub>2</sub> symmetric stretch and bending mode population.	n <sub>1</sub>	X1
Total N <sub>2</sub> population	N	TN2
Vibrationally excited N <sub>2</sub> population	N*	X3
Total CO population	C	TCO
Vibrationally excited CO population	C*	X4
Total He population	-	THE
Total O <sub>2</sub> population	-	TO2
V-V rate constants (cm <sup>3</sup> s <sup>-1</sup> )	k <sub>NM</sub>	VKNM
V-V-T rate constants (s <sup>-1</sup> )	K <sub>NM</sub>	TKNM
Electron excitation and de-excitation rate constant (s <sup>-1</sup> )	α	ALPH
"	β	BETA
"	γ	GAMM
"	δ	DELT
"	ε	EPSI
"	ζ	ZETA
Computation time step(s)	-	H
Initial time origin	-	TO
Population rate of change (cm <sup>-3</sup> s <sup>-1</sup> )	$\frac{dn_1}{dt}$	R1
"	$\frac{dn_2}{dt}$	R2
"	$\frac{dN^*}{dt}$	R3
"	$\frac{dC^*}{dt}$	R4

TABLE 5.2 continued

<u>Description</u>	<u>Text and system equations</u>	<u>VIBEX</u>
Estimated population at time $T1 = T0 + H$	$X_{11}$ etc.	X11 etc.
Predictor population at time $T2 = T1 + H$	$X_{12}^{(o)}$ etc.	X12OLD etc.
Corrector population at time $T2 = T1 + H$	$X_{12}^{(j)}$ etc.	X12NEW etc.
Truncation error in predictor- corrector stage	$E_T(X_{12})$ etc.	ERRX1 etc.
Corrected population at time $T2 = T1 + H$	$X_{12}$	X12
Convergence tolerance	-	TOLER
Steady-state population tolerance	-	CHANGE

assigned to X12; the same re-initialisations are required for the variables TO, X20, X30, X40 etc. After each time-step, the percentage population changes are compared to the set value of the parameter CHANGE; if all the population changes are less than CHANGE, steady-state is declared and the current values X12, X22, X32, and X42 are printed as equilibrium vibrational mode populations. A glossary of the notation used in the computer model is presented in Table 5.2.

The algorithms described by Figure 5.2 form a simultaneous differential equation "solver", which can be applied to the population rate equation system (5.1) - (5.4), or to variants of it. This solver was incorporated into a larger computer model designed to predict vibrational temperatures in low pressure cw and high pressure pulsed CO<sub>2</sub> lasers. A listing of the resultant code, "VIBEX", is presented in an Appendix, and the details of some important calculational routines are explained below.

### 5.3 Calculational details and subroutines

#### 5.3.1 Program flow-chart and definition of vibrational temperatures

The basic version of the VIBEX computer model is flow-charted in Figure 5.2. The required input data are gas mixture, pressure, temperature, electron density, electron excitation rate constants and electron temperature. The population rate equations are defined and where necessary back-reaction rate constants are evaluated as discussed in Section 5.2.1. Effective superelastic rate constants for the CO<sub>2</sub> (V<sub>3</sub>), N<sub>2</sub> and CO vibrational modes are calculated by detailed balancing in subroutine SUPER (see below), and the solution of the rate equations proceeds according to Section 5.2.3. In the case of zero stimulated emission, the solution is straightforward and when steady-state is



attained the equilibrium mode populations are printed. The corresponding vibrational temperatures are then calculated. For the  $\text{CO}_2$  anti-symmetric stretch mode, the total excited population density,  $n_2$ , is related to the ground state population by

$$\frac{n_2}{n_0} = \sum_{i=1}^{\infty} x_3^i \quad (5.13)$$

where as before

$$x_3 = \exp\left(\frac{-h\nu_3}{kT_3}\right).$$

Again using the infinite summation (5.10), we have

$$\frac{n_2}{n_0} = \frac{x_3}{1-x_3} \quad (5.14)$$

and so

$$x_3 = 1 - \frac{1}{n_2/n_0 + 1} \quad (5.15)$$

and

$$T_3 = \frac{h\nu_3}{k} \left\{ \ln\left(1 - \frac{1}{n_2/n_0 + 1}\right) \right\}^{-1} \quad (5.16).$$

The  $\text{N}_2$  and  $\text{CO}$  vibrational temperatures are calculated similarly. A more complicated procedure is required to extract the vibrational temperature of the combined  $\text{CO}_2$  ( $\nu_1, \nu_2$ ) mode. Since this mode combines the degenerate bending mode and the symmetric stretch mode, knowledge of the total mode population does not uniquely define the combined mode temperature  $T_1 = T_2$ . In fact, as shown in Appendix C, the mode temperature is obtained by solving a quartic equation,

$$\left(\frac{An}{n_0}\right) X^4 - \left(\frac{n_1}{n_0} + 2\right) X^2 + 1 = 0 \quad (5.17)$$

where  $A = 1 - x_3$  is known from equation (5.15) and  $X = 1 - x_2$  is the unknown. In practice (5.17) is solved by using two root-determining

sub-routines, ZERO2 and STEPS. The operation of these, and other, important sub-routines is described below.

### 5.3.2 Calculation of effective superelastic rate constants

In sub-routine SUPER the principle of detailed balance is applied to calculate the superelastic components of the relaxation rate constants DELT, EPSI, ZETA, AND TK10. From equation (2.17), the rate constant for superelastic collisions from, say, the  $N_2$  vibrational mode will have the form

$$X_{-4} = X_4 \exp\left(\frac{E_v}{kT_e}\right) \quad (5.18)$$

where  $X_4$  is the electron excitation rate constant, as in equation (5.8).  $T_e$  is the discharge electron "temperature" and  $E_v$  is the energy of the excited vibrational level under consideration. In BOLTZ, the  $N_2$  electron excitation rate (like those for the CO and  $CO_2$  ( $v_3$ ) modes) is a weighted sum over the first eight vibrational levels, as in equations (2.12) - (2.14); such effective vibrational excitation rates are traditionally assigned an energy loss equal to the energy of the first vibrational level in the mode. Therefore the simplest approximation is  $E_v = h\nu_4$ , the  $N_2$  vibrational mode spacing, so that

$$X_{-4} = X_4 \exp\left(\frac{h\nu_4}{kT_e}\right) \quad (5.19)$$

This approximation was used to calculate superelastic rates in early versions of the computer model. However, (5.19) is equivalent to assuming that all superelastic de-excitation is from the first excited level of the mode. Clearly what is required is a superelastic rate constant which is averaged over the first 8 levels, analagous to the excitation rate average

$$X_4 = \sum_{i=1}^8 \alpha_i k_i \quad (5.20)$$

where  $k_i$  is the excitation rate constant for the  $i$ th level and  $\alpha_i$  are weighting factors  $\alpha_i = h\nu_i/h\nu_1$ . We therefore define the superelastic rate constant for the vibrational mode by a similar sum

where the superelastic rate constant for level  $i$  is

$$k_{-i} = k_i \exp\left(-\frac{ih\nu_4}{kT_e}\right) \quad (5.22)$$

Therefore,

$$X_{-4} = \sum_{i=1}^8 ik_i \exp\left(-\frac{ih\nu_4}{kT_e}\right) \quad (5.23)$$

since  $\alpha_i = i$  in the harmonic oscillator approximation, (5.23) will be uniquely defined if the inter-relationship of the  $k_i$  is known. Examination of the  $N_2$  and CO vibrational excitation cross-section data of Schulz<sup>6</sup> shows that a reasonable approximation is

$$k_i = \frac{k_1}{i}, \quad i = 1 \text{ to } 8 \quad (5.24)$$

Inserting this in (5.21) yields  $X_4 = 8k_1$  and from (5.23),

$$X_{-4} = k_1 \sum_{i=1}^8 \exp\left(-\frac{ih\nu_4}{kT_e}\right)$$

i.e.,

$$X_{-4} = \frac{X_4}{8} \sum_{i=1}^8 \exp\left(-\frac{ih\nu_4}{kT_e}\right) \quad (5.25)$$

This is the more sophisticated relationship used to calculate  $N_2$  superelastic rate constants in sub-routine SUPER; similar expressions are used to calculate the effective rate constants for the CO and CO<sub>2</sub> ( $\nu_3$ ) modes.

### 5.3.3 Calculation of the symmetric stretch-bending mode temperature $T_1 = T_2$

Sub-routines ZERO2 and STEPS are used to solve equation (5.17) for the lower laser level mode temperature  $T_1 = T_2$ . The coefficients of the quartic are first evaluated and the equation is defined in the function sub-program QUART, which is available for calls from the other two sub-routines. An initial estimate of the position of the physically significant root is produced by STEPS; this evaluates the quartic

function for various X values in the range of interest, stepping X by a fixed increment and testing for a change of sign in the value of the function. When such a change occurs, the bounding X values, between which the zero of the function must lie, are returned to the main program. ZERO2 is then called to refine the solution by progressively tightening the bounding X values, until the root of the quartic is determined to a preset accuracy (normally 0.1%). The  $(\lambda_m 0)$  mode temperature  $T_2$  is then calculated and printed.

#### 5.3.4 Treatment of stimulated emission

When the effects of stimulated emission are to be considered, the running of the program is slightly altered. The stimulated emission rate can be written

$$\rho_s = \Delta N W I \quad (5.26)$$

where I is the applied laser radiation field intensity ( $\text{W cm}^{-2}$ ),  $\Delta N$  is the appropriate rotational-vibrational population inversion on the  $(00^0_1-10^0_0)$  or  $(00^0_1-02^0_0)$  transitions, derived from equation (2.24), and

$$W = \frac{\lambda^2}{8\pi} A_{21} g(\nu_0) \quad (5.27)$$

from equation (2.23). The calculation of the population inversion,  $\Delta N$ , requires knowledge of the  $00^0_1$  and  $10^0_0$  level populations, which in turn requires the vibrational temperatures  $T_3$  and  $T_2$ ; since the population inversion and stimulated emission rate must be calculated after each time-step, the temperatures  $T_3$  and  $T_2$  must also be calculated after each time-step. In practice this is done in sub-routine CTEMPS, using equations (5.16) and (5.17) as before. The population inversion and stimulated emission rate are calculated in sub-routine LASE by (5.26) and (5.27) assuming pure pressure broadening, and the new  $\rho_s$  value is

returned to the main program to modify the rate equations (5.1) and (5.2) which become:

$$\frac{dn_1}{dt} = K_{21}n_2 - K_{10}n_1 + (K_{01} + \omega)(n - n_1 - n_2) - \rho_s \quad (5.28)$$

$$\frac{dn_2}{dt} = \alpha(n - n_1 - n_2) + \dots + K_{21}n_2 - \rho_s \quad (5.29)$$

#### 5.4 Initial tests and results

Initial program tests were conducted using the rate constant data of Table 5.1, and assuming the simplest form of superelastic balancing as exemplified by equation (5.19). It was found that careful program "tuning" was required to produce results with optimum speed and accuracy. In particular, since there is no facility for automatic time-step doubling or halving, a suitable progression of time-step values was needed to ensure both accuracy in the early stages of the calculation ( $t < 10^{-4}$  s) and a reasonably fast attainment of population equilibrium ( $t \sim 3 \times 10^{-3}$  s). At any point in the calculation, the time-step must be small enough to allow convergence within the permitted number of corrector iterations, but large enough to avoid unnecessarily small population changes per time-step which waste computational effort and can prompt a premature end to the calculation with a false declaration of equilibrium. A judicious choice of time-step progression and TOLER and CHANGE values is therefore required. Suitable values for steady-state calculations, arrived at by trial-and-error, are reproduced in Table 5.3.

Typical calculated excited population time evolutions are plotted in Figure 5.4, assuming a  $6\text{CO}_2 : 12\text{N}_2 : 82\text{He}$  gas mixture at 10 torr, with 25%  $\text{CO}_2$  dissociation. The calculation also assumes a constant electron density of  $5 \times 10^{10} \text{ cm}^{-3}$  at  $E/N = 3.0 \times 10^{-16} \text{ Vcm}^2$ . The relative levels of excited  $\text{CO}$ ,  $\text{N}_2$  and  $\text{CO}_2(\text{V}_3)$  molecules reflect the

TABLE 5.3      Parameters used in VIBEX rate-equation solver  
for steady-state calculations.

<u>Description</u>	<u>Label</u>	<u>Value</u>
Iteration time-step	H	$1 \times 10^{-5} \text{ s}$ , for $T < 10^{-4} \text{ s}$
	H	$2 \times 10^{-5} \text{ s}$ , $10^{-4} \text{ s} < T < 10^{-2} \text{ s}$
	H	$4 \times 10^{-5} \text{ s}$ , $10^{-2} \text{ s} < T < 10^{-1} \text{ s}$
Fractional population convergence required at each time-step	TOLER	$10^{-4}$
Maximum number of predictor-corrector iterations per time-step	MAX	50
Maximum percentage change per time-step in excited populations at declaration of steady-state.	CHANGE	0.001

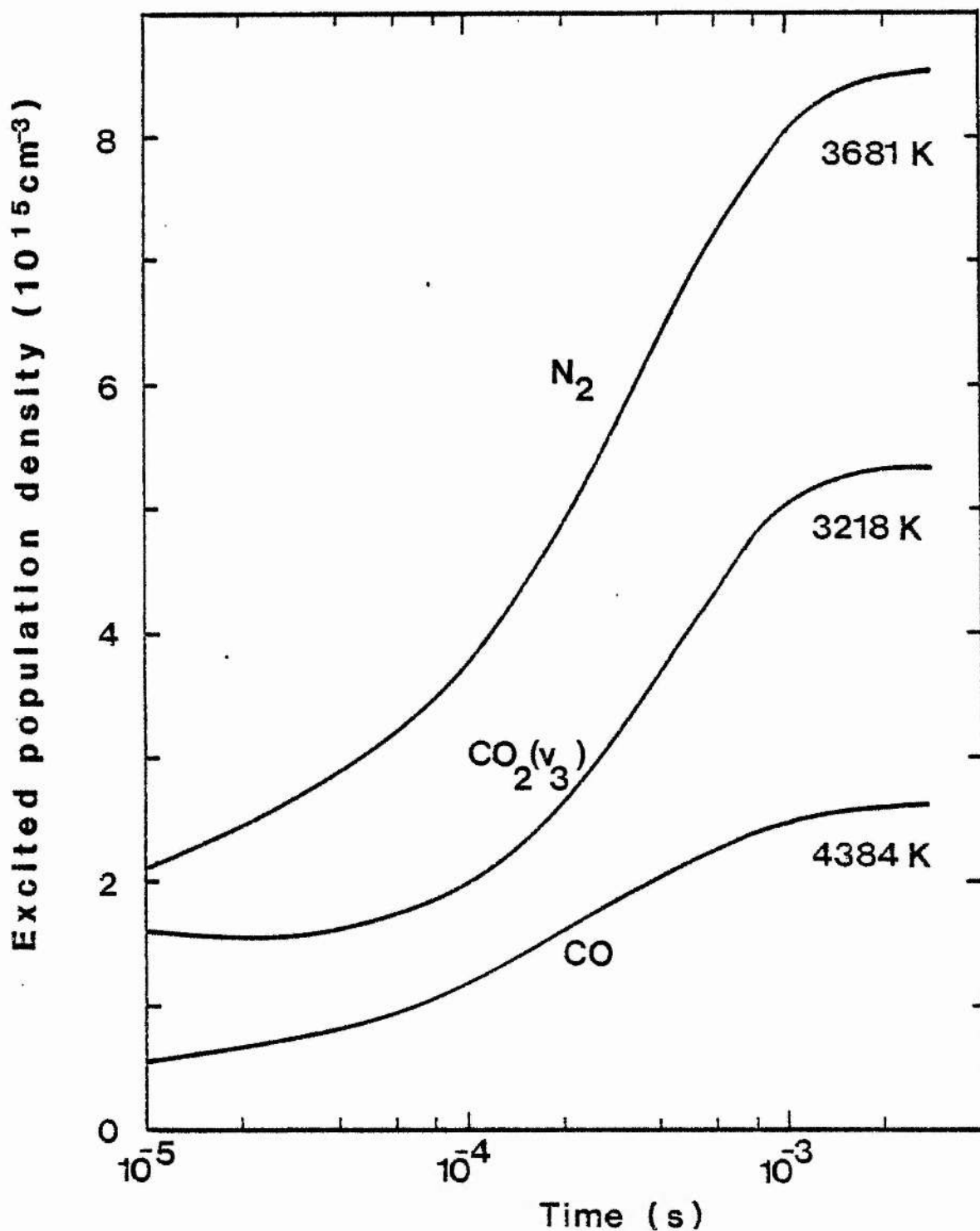


Fig. 5.3. Calculated vibrationally excited populations versus time for 6  $\text{CO}_2$  : 12  $\text{N}_2$  : 82 He at 10 torr assuming 25% dissociation, electron density =  $5 \times 10^{10} \text{ cm}^{-3}$ ,  $E/N = 3.0 \times 10^{-16} \text{ V cm}^2$ , and 10% initially excited populations. Also shown are vibrational temperatures at steady-state.

dominance of  $N_2$  and  $CO_2$  in the gas mixture; however at population equilibrium, the vibrational temperature of the CO is by far the highest; the  $N_2$  temperature is also higher than that of the  $CO_2(v_3)$  mode. This was a ubiquitous trend which will be discussed in detail later. The validity of the calculated equilibrium can be demonstrated by varying the initial conditions, as in Figure 5.4, which shows that changing the initially excited population densities by a factor of 10 has no effect on the final solution.

To conclude, a computer model of the  $CO_2$  laser vibrational kinetics system has been constructed and tested. Its use in the prediction of steady-state and temporally evolving vibrational temperatures, and their comparison to experiment, is described in the next chapters.



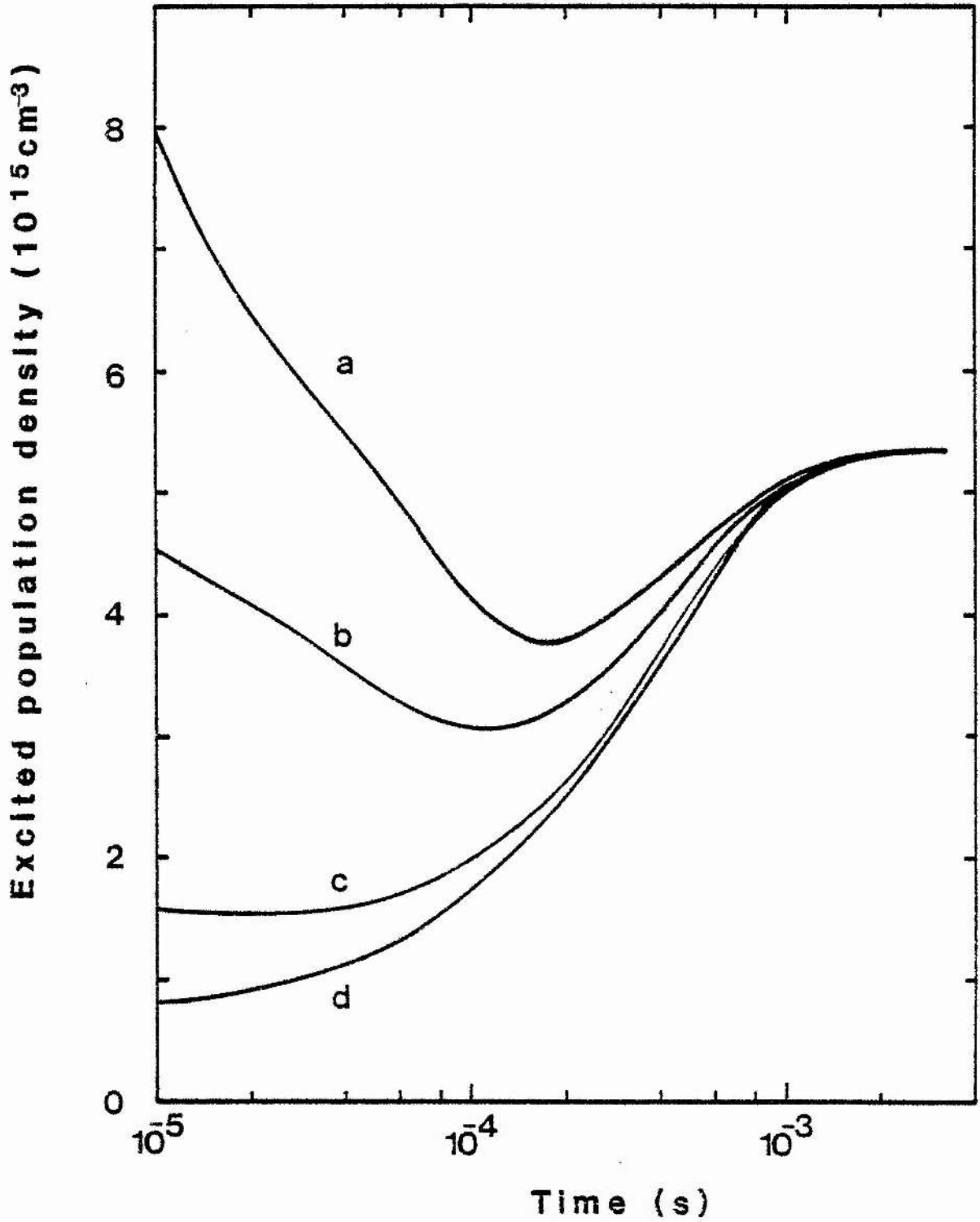


Fig. 5.4. Calculated time dependence of  $\text{CO}_2(v_3)$  mode population for conditions of fig.5.3, but with varying initially excited populations: (a) 50% of total  $\text{CO}_2$  number density (b) 30% (c) 10% (d) 5%.

References for Chapter 5

1. D.C. Tyte, "Progress in Quantum Electronics", (Academic Press, 1970).
2. E.R. Hanson, "A Table of Series and Products", p64. (Prentice-Hall, 1975).
3. R.L. Taylor and S. Bitterman, Rev. Mod. Phys., 41, 1, 26 (1969).
4. J.C. Stephenson and C.B. Moore, J. Chem. Phys. 56, 3, 1295 (1972).
5. D.D. McCracken and W.S. Dorn, "Numerical Methods and FORTRAN programming", Wiley, London (1968).
6. G.G. Schulz, Phys. Rev., 135, 4A, 988, (1964).
7. In general the V-T deactivation rate constants for N<sub>2</sub> and CO are negligibly small, since in a collision with another polyatomic molecule the probability of the V-T process is negligible compared to the probability for V-V exchange.
8. W.A. Rosser, A.D. Wood and E.T. Gerry, J. Chem. Phys. 50, 11, 4996, (1969).
9. W.A. Rosser, A.D. Wood and E.T. Gerry, J. Chem. Phys. 51, 2286 (1969).
10. R.L. Taylor and S. Bitterman, J. Chem. Phys. 41, 1, 30 (1969).
11. Such high rates are supported by calculation (P.K. Cheo, IEEE J. Quant. Electron. QE-4, 587 (1968)) and some experimental measurements (M.C. Gower and A.I. Carswell, J. Appl. Phys. 45, 9, (1974)). However recently more detailed photoacoustic studies (J. Taine, F. Lepoutre and G. Louis, Chem. Phys. Lett. 58, 611 (1978), J. Taine and F. Lepoutre, Chem. Phys. Lett. 65, 554 (1979)) have indicated that the rate of 01<sup>1</sup>0 level deactivation by CO is similar to that by N<sub>2</sub> i.e. around 200 torr<sup>-1</sup>s<sup>-1</sup> ( $5 \times 10^{-15}$  cm<sup>3</sup>s<sup>-1</sup>) at 400K. The high rates probably resulted from a confusion of V-T and internal bending mode V-V relaxation of the 01<sup>1</sup>0 level.

12. C.B. Moore, R.E. Wood, B.L. Hu and J.T. Yardley, *J. Chem. Phys.* 46, 11, 4222 (1967).
13. D.F. Starr and J.K. Hancock, *J. Chem. Phys.* 63, 11, 4730 (1975).
14. H.K. Shin, *J. Chem. Phys.* 61, 6, 2474 (1974).
15. M.A. Kovacs and M.E. Mack, *Appl. Phys. Lett.* 20, 487 (1972).
16. W.J. Hooper and R.C. Millikan, *J. Chem. Phys.* 38, 214 (1963).
17. D.J. Miller and R.C. Millikan, *J. Chem. Phys.* 53, 3384, (1970).
18. T. Price, D.C. Allen and C.J.S.M. Simpson, *Chem. Phys. Lett.* 53, 182 (1978).
19. W.H. Green and J.K. Hancock, *J. Chem. Phys.* 59, 4326, (1973).
20. H. Guegin, F. Yzambert, A. Chakroun, M. Margottin-Maclou, L. Doyenette and L. Henry, *Chem. Phys. Lett.* 35, 198 (1975).

CHAPTER 6: CO<sub>2</sub> LASER VIBRATIONAL KINETICS MODELLING - THEORY  
AND EXPERIMENT

6.1 Background

The vibrational temperature approximation has been the basis of most mathematical models of CO<sub>2</sub> laser vibrational kinetics.<sup>1-4</sup> The credibility of the approximation derives from the fact that the rate of energy exchange within a given vibrational mode is faster than the rate of transfer to other modes and the rate of electron impact vibrational excitation. For example,<sup>5</sup> in a low pressure (15 torr) 1CO<sub>2</sub>: 1N<sub>2</sub>: 8He gas mixture the characteristic time for CO<sub>2</sub>( $\nu_3$ ) intra-mode resonant energy sharing is roughly 200 ns; the corresponding time for N<sub>2</sub>-CO<sub>2</sub>( $\nu_3$ ) mode V-V exchange is 65  $\mu$ s, while for typical electron densities 1 ms is a characteristic time for N<sub>2</sub> vibrational excitation. It is therefore reasonable to assume that the population of levels within a vibrational mode is described by a Boltzmann distribution characterised by a single temperature. However, the vibrational temperature model has not been accessible to direct experimental confirmation. Measurements of CO<sub>2</sub> and N<sub>2</sub> vibrational temperatures in laser discharges have generally used indirect methods such as observation of visible and UV emission from the N<sub>2</sub> 2+ system<sup>6</sup> or of the 4.3  $\mu$ m fluorescence from the CO<sub>2</sub> (00<sup>0</sup>1) level.<sup>7</sup> Moreover, such measurements have not subjected the vibrational temperature model to test, but rather have assumed the validity of the model in order to interpret the experimental results. The situation has been further complicated by various theoretical predictions of the peak value of the CO<sub>2</sub> asymmetric mode temperature ( $T_3$ ) in TEA lasers<sup>8,9</sup>: predicted values span the range 1000K-7000K.

In recent years two important experimental techniques have emerged to clarify the problem. First, the advent of the CO<sub>2</sub> sequence band laser<sup>10</sup> made possible direct measurements of T<sub>3</sub> in laser discharges. This method<sup>11</sup> compares the amplification of fundamental 00<sup>0</sup>1 - (10<sup>0</sup>0, 02<sup>0</sup>0)<sub>I,II</sub> radiation to that of sequence band 00<sup>0</sup>2 - (10<sup>0</sup>1, 02<sup>0</sup>1)<sub>I,II</sub> radiation in a probed discharge gain cell. Since the population of a vibrational level (ℓ, m, n) in CO<sub>2</sub> can be written

$$N(\ell, m, n) = N_{\text{TOT}} x_1^\ell (m+1) x_2^m x_3^n / Q_v$$

where the symbols have their usual meanings (Section 2.2), then it is straightforward to show that the ratio of 00<sup>0</sup>2 gain to 00<sup>0</sup>1 gain on the 10 μm branches is<sup>12</sup>

$$\frac{\alpha_2}{\alpha_1} = \frac{2(x_3^2 - x_3 x_1)}{x_3 - x_1} = 2x_3$$

Thus the ratio of the small signal gains depends only on T<sub>3</sub> which is given by

$$T_3 = \frac{h\nu_3}{k \ln(2\alpha_1/\alpha_2)} \quad (6.1)$$

and can be easily measured.

The sequence band technique probes only the first and second excited levels of the CO<sub>2</sub> asymmetric vibrational mode. Development of a second technique, tunable diode laser spectroscopy in the 4 μm spectral region, has enabled the investigation of discharge excited CO<sub>2</sub>(ν<sub>3</sub>) populations in levels as high as 00<sup>0</sup>9. The results<sup>13</sup> confirmed that the population distributions are describable by a single vibrational temperature, even in the presence of a saturating laser radiation field inducing strong stimulated emission. Vibrational anharmonicity means that a Treanor distribution<sup>14</sup> was required to fit the measured populations in the highest levels, but Boltzmann statistics proved accurate for levels up to 00<sup>0</sup>4.

In summary, tunable diode laser spectroscopy has confirmed the validity of the vibrational temperature approximation in  $\text{CO}_2$  laser kinetics, while the sequence band probe technique provides a convenient vibrational temperature measurement method. The following sections present a comprehensive study of vibrational temperatures in  $\text{CO}_2$  laser discharges, in which experimental measurements (obtained by the sequence band technique) are compared to theoretical predictions (produced by the computer model described in Chapter 5). Macroscopic phenomena are explained in terms of microscopic processes, and wider implications for the performance of  $\text{CO}_2$  laser devices are discussed.

## 6.2 Experimental equipment and procedure

Fundamental ( $00^0_1 - 10^0_0$ ) and sequence ( $00^0_2 - 10^0_1$ ) band small-signal gain coefficients were measured using the oscillator-amplifier configuration of figure 6.1. The probe laser could be made to oscillate on the sequence band by filling the intra-cavity hot cell with pure  $\text{CO}_2$  to a pressure of around 30 torr. A PZT-mounted output coupler allowed cavity length tuning over a number of rotational lines in the  $10\ \mu\text{m}$   $00^0_1$  and  $00^0_2$  bands. (Detailed performance characteristics of the probe laser are presented and analysed in Chapter 8). The gain cell was a simulated laser discharge tube of 52 cm active length and 1 cm internal diameter, sealed by KCl Brewster windows. The gain cell and its associated vacuum system were of clean quartz and stainless steel construction and allowed either flowing-gas or sealed-off operation. Gas pressures and flow rates were measured and regulated by an MKS Baratron type 254 control unit which monitored thermal conductance flow meters and capacitance manometers on the

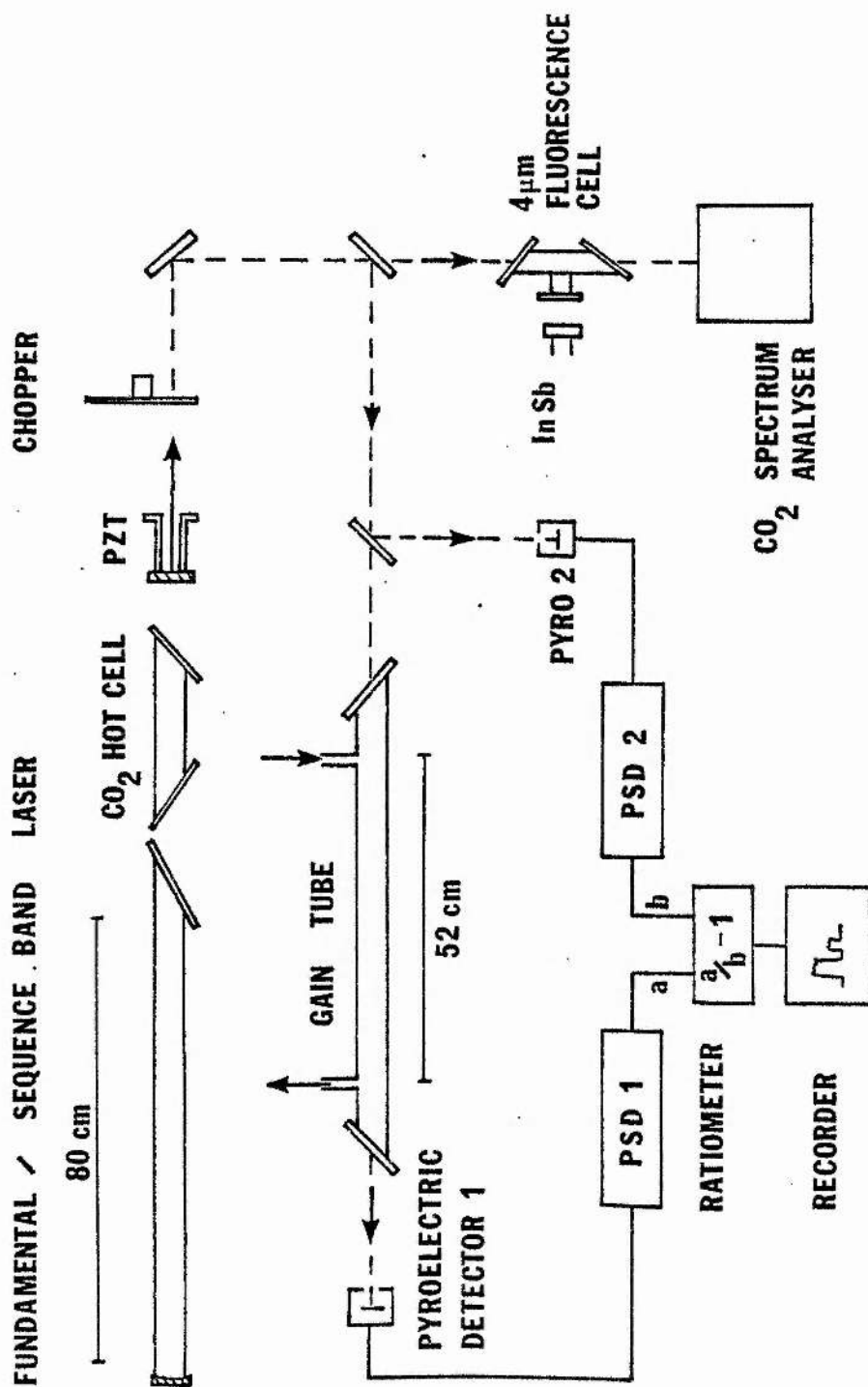


Fig. 6.1. Schematic of gain and vibrational temperature measurement system.

tube outlet and inlet. If necessary, the composition of the research grade gas mixture was measured at the gain cell outlet using the MS10S mass spectrometer.

Small-signal gain coefficients on the axis of the gain cell were measured by mechanically chopping the probe beam ( $\sim 4$  mm diameter) at a convenient frequency ( $\sim 120$  Hz). The beam was split by an uncoated Ge flat into amplified and reference beams which were collected by large-area pyroelectric detectors. The resulting signals were amplified by phase-sensitive detectors (PSD's), ratioed to remove the effect of source intensity fluctuations, and displayed on a chart recorder. A potentiometer on one of the PSD outputs was used to null the ratiometer output for zero discharge current in the gain cell. Gain coefficients were calculated from the recorded change in output signal when the D.C. current was switched on. The ratiometer performed the operation  $a/b - 1$  on the input signals from amplified channel a and reference channel b. Thus if switching on the gain cell current produces an output signal of height H volts in a full-scale range of 10 volts, the gain coefficient is given by

$$\alpha_o = \frac{1}{L} \ln\left(1 + \frac{H}{10}\right) \quad (6.2)$$

where  $L = 0.52$  m and  $\alpha$  is in units ( $m^{-1}$ ) or ( $\% cm^{-1}$ ). Care was taken to limit the probe beam power to  $\lesssim 700mW$  to avoid gain saturation effects. Discharge currents and cathode-anode voltages were measured simultaneously with the gain coefficients, allowing an estimation of the operating  $E/N$ .

The oscillating probe transition was assigned in vibrational band and rotational quantum number by using a conventional Optical Engineering  $CO_2$  spectrum analyser and a  $4 \mu m$  fluorescence detection

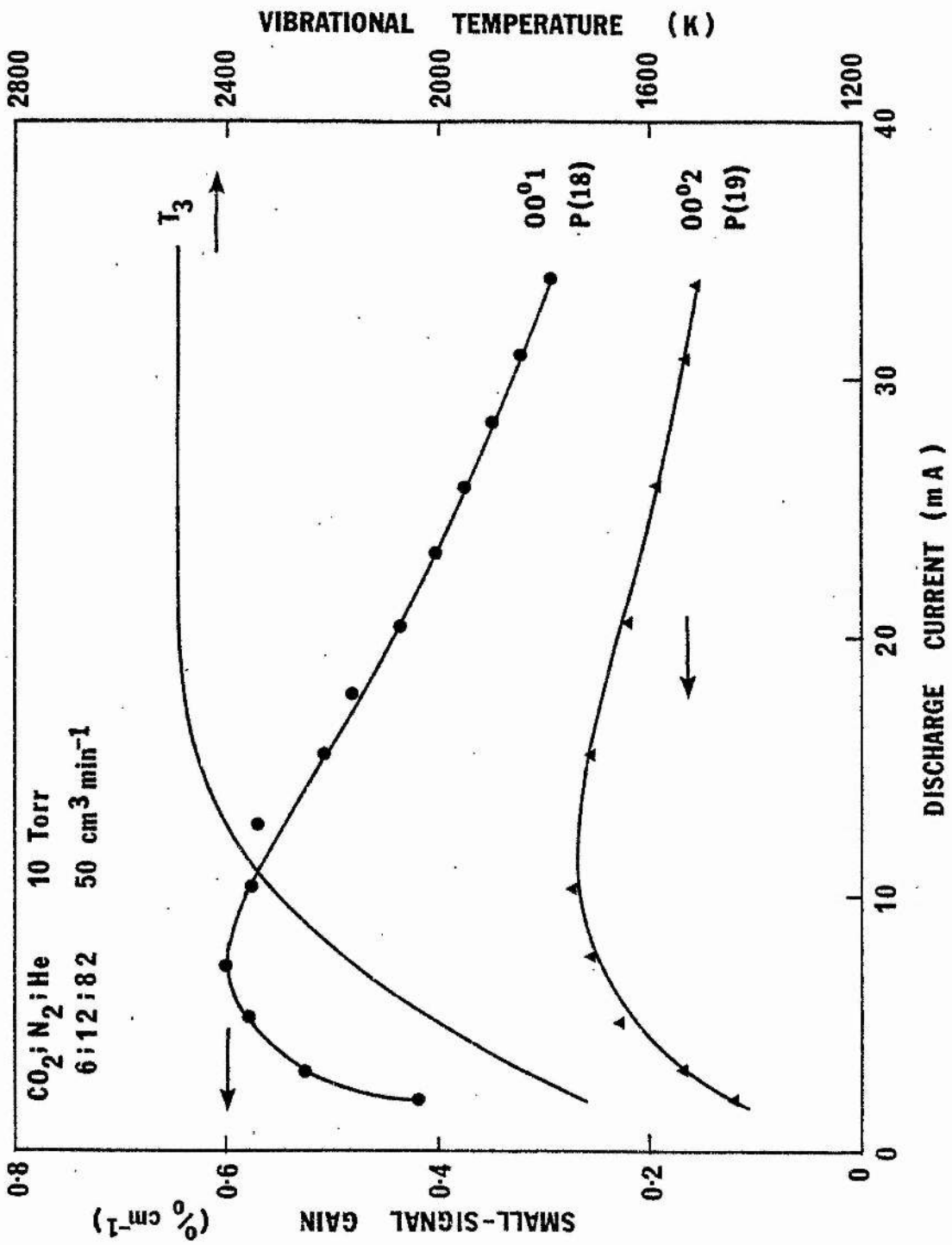


system. This comprised a low pressure ( $\sim 1$  torr)  $\text{CO}_2$  absorption cell of 0.5 cm internal diameter, and a liquid  $\text{N}_2$  - cooled InSb photo-cell with a  $4 \mu\text{m D}^*$  of  $\sim 7 \times 10^9 \text{ cm Hz}^{\frac{1}{2}} \text{ W}^{-1}$ . The passage of  $00^0_1$  band radiation through the cell induces strong  $00^0_1$  - ground state  $4.3 \mu\text{m}$  fluorescence. Sequence band lines are not absorbed, produce no fluorescence, and can therefore be distinguished from neighbouring fundamental band transitions.

### 6.3 Experimental results and comparison to model predictions

#### 6.3.1 Vibrational temperature saturation

Typical results obtained from the gain measurement system are shown in figure 6.2 for a  $6\text{CO}_2 : 12\text{N}_2 : 82\text{He}$  gas mixture at 10 torr pressure and a flow rate of  $50 \text{ cm}^3/\text{min}$  at S.T.P. (i.e. 50 sccm). Peak gain coefficients for the  $00^0_1$  10P(18) and  $00^0_2$  10P(19) lines were 0.60 and  $0.26\% \text{ cm}^{-1}$  respectively. Experimental uncertainty in the gain coefficient values was around  $\pm 4\%$  and was mainly due to the imperfect passive frequency stability of the probe laser which, despite the use of the ratiometer, produced some random amplitude variations in the measurement system. The smooth curves through the experimental points were used to calculate the corresponding  $T_3$  values from equation (6.1). Above 15 mA the 'levelling-off' or saturation of  $T_3$  is striking and was observed for all the gas mixtures and pressures studied. This observation supports the measurements of Siemsen et al, who also reported  $T_3$  saturation at relatively low values in cw laser discharges. They interpreted this as being caused by a rapid increase in the collisional de-excitation of the upper laser level due to increased gas temperature, coupled with faster diffusion to the tube walls and a decrease in the electron excitation efficiency. However, it seems likely that such a decrease in excitation efficiency could occur as a


 Fig. 6.2. Typical gain measurements and derived T<sub>3</sub>.

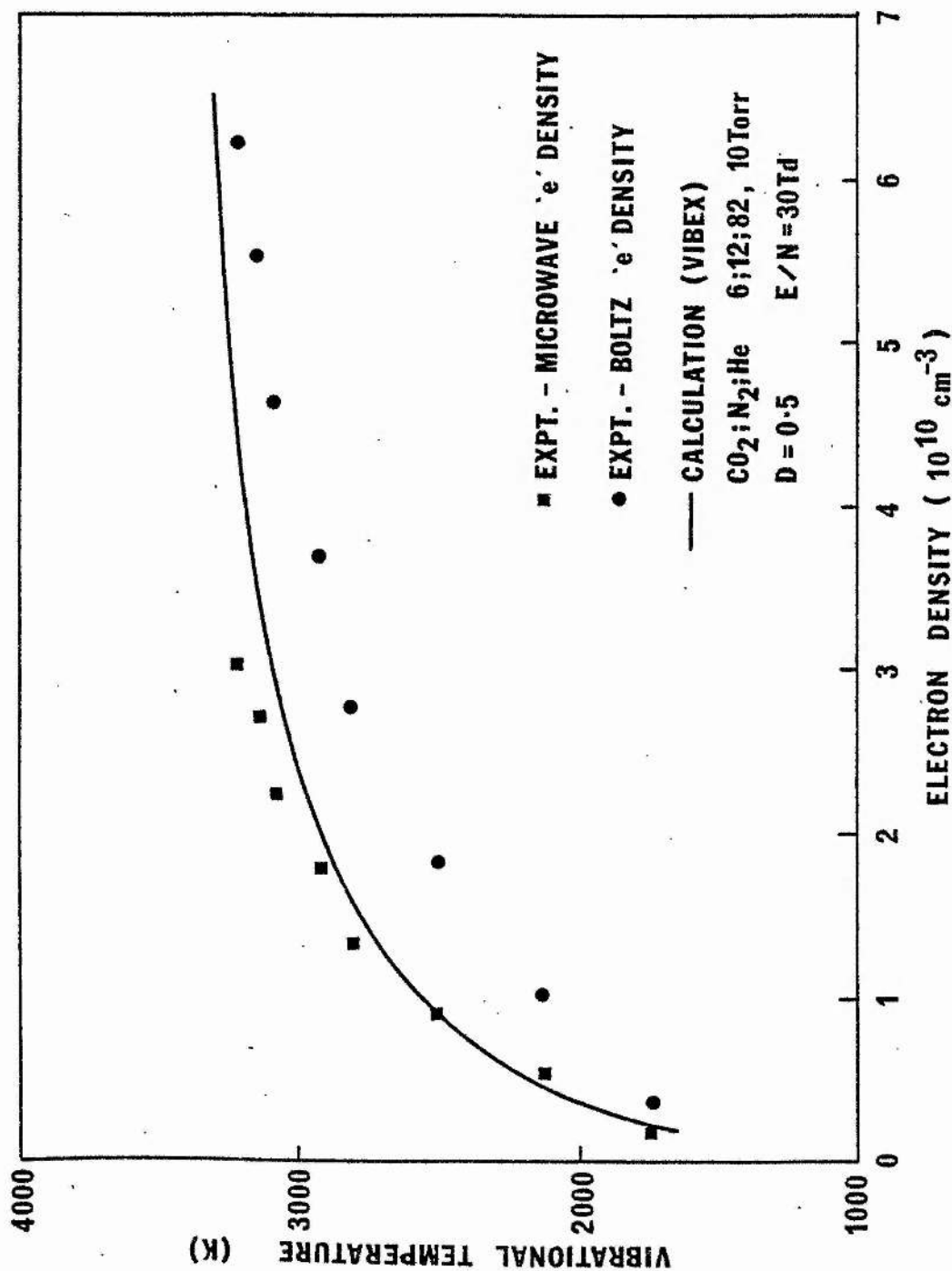


Fig. 6.3. Comparison of model calculation to experimental measurements in sealed-off 6 : 12 : 82 gas mixture.

result of large electron superelastic collision rates at high electron densities. This hypothesis is easily tested using the vibrational exchange rate equation model (VIBEX), which includes all the relevant electron excitation and de-excitation processes. A series of steady state vibrational temperature calculations were performed using the simplest superelastic balancing approximation of section 5.3.2 (as in equation 5.19) for a range of electron densities. The resultant curve (figure 6.3) displays strong saturation for electron densities greater than  $\sim 2 \times 10^{10} \text{ cm}^{-3}$ . This limits the maximum attainable  $T_3$  to around 3000K. Also shown are experimental  $T_3$  measurements which have been converted from discharge current dependence to electron density dependence by using both the microwave cavity measurements and the BOLTZ-calculated drift velocities as described in Chapter 4. These methods yield specific electron densities which differ by a factor of  $\sim 2$ , but agreement between experiment and theory is reasonable. More importantly, the origin of the calculated vibrational temperature saturation was investigated by making artificial changes in the various de-activation rate constants of the computer model. The results are illustrated by figure 6.4, which shows the effect on calculated vibrational temperature of halving and doubling the rates of (i) molecular V-T and V-V-T collisional relaxation and (ii) electron superelastic collisional relaxation. Clearly the dominant control over the temperature saturation is imposed by superelastic collisions. This was confirmed by deleting all the superelastic terms from the system rate equations: this resulted in the complete removal of the saturation, giving an almost linear increase of vibrational temperature with electron density. It is significant that the calculated temperature saturation is not restricted to the  $\text{CO}_2$  asymmetric mode.

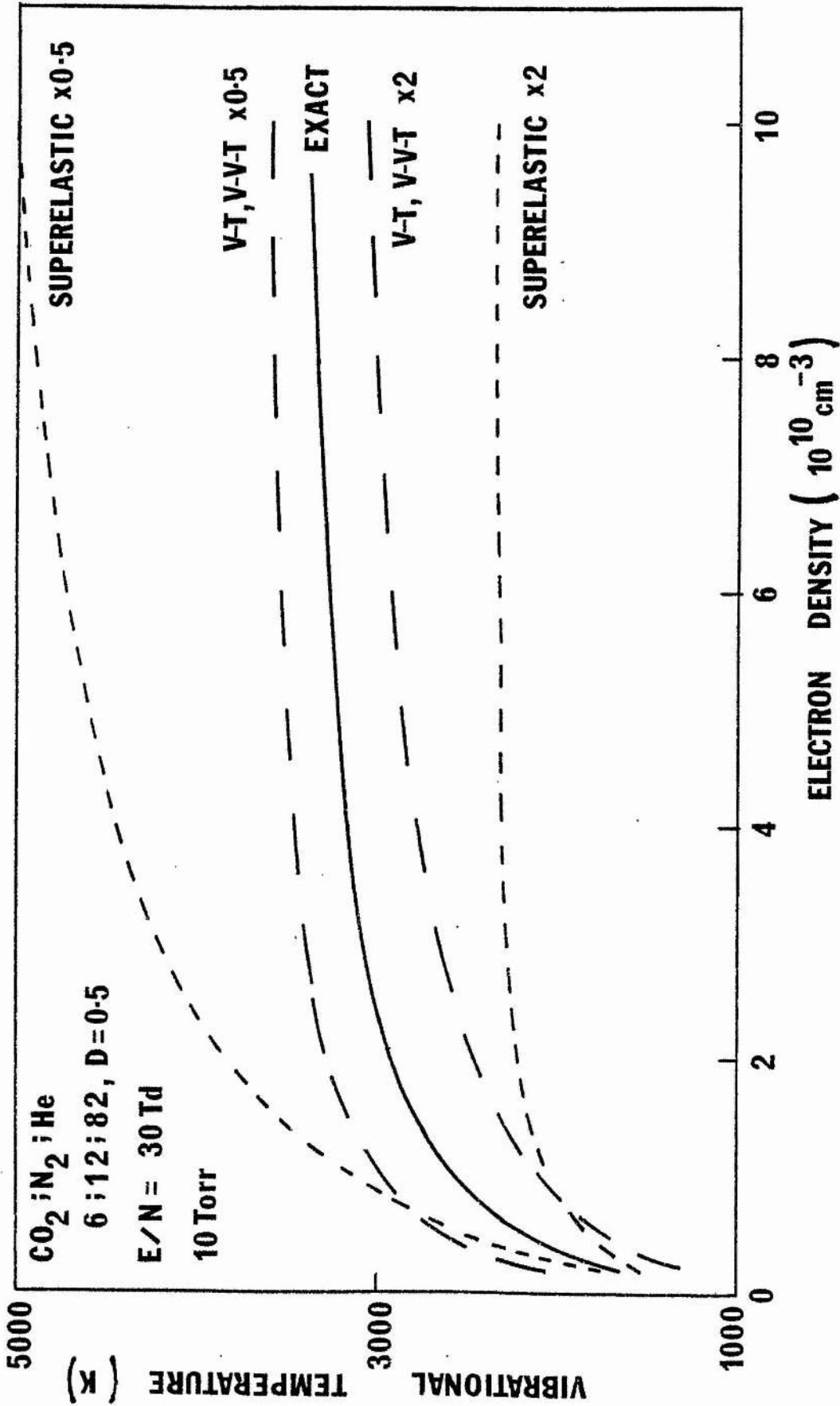


Fig. 6.4. Effect of artificial changes in model rate constants.

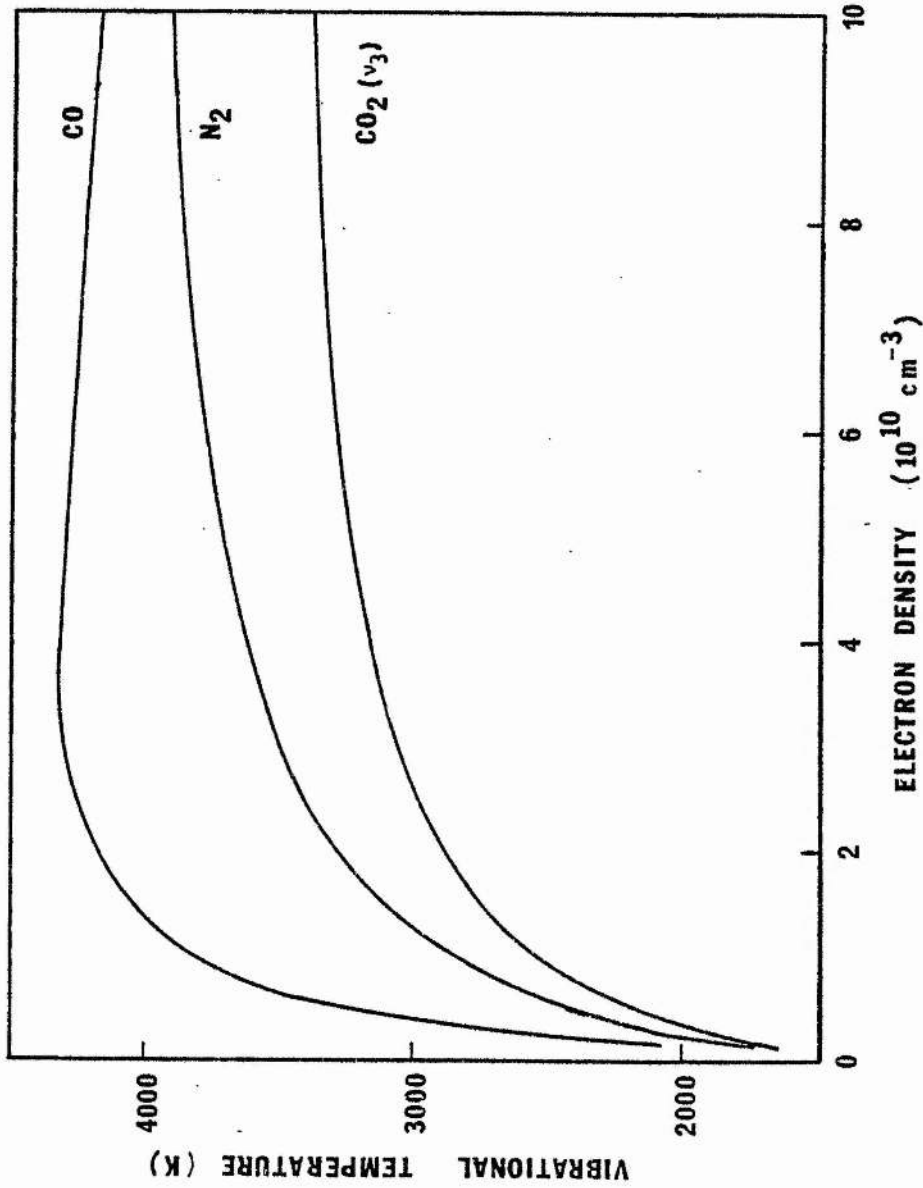
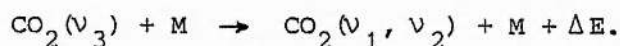


Fig. 6.5. Calculated vibrational temperatures (10 torr, 6 CO<sub>2</sub> : 12 N<sub>2</sub> : 82 He, assuming 50% CO<sub>2</sub> dissociation).

Figure 6.5 shows computed steady-state temperatures for the  $N_2$ , CO and  $CO_2(v_3)$  modes in 10 torr of  $6CO_2:12N_2:82He$  assuming 50%  $CO_2$  dissociation. The  $N_2$  and CO temperatures also saturate, but at higher ultimate values ( $\sim 3800K$  and  $4200K$  respectively). The CO saturation is especially severe due to the large CO electron excitation cross-section and the relative weakness of CO V-T relaxation by molecular collisions. Hence the CO vibrational temperature is most dominated by the balance of electron excitation and de-excitation.

The weakness of CO and  $N_2$  V-T relaxation (and absence of V-V-T relaxation) is also partially responsible for the prediction of relatively high CO and  $N_2$  vibrational temperatures. Apart from super-elastic processes the major deactivation of the CO,  $N_2$  and  $CO_2(v_3)$  mode group is by  $CO_2$  V-V-T collisions:-



This relaxation channel, combined with the small rate of direct electron excitation of the  $CO_2(v_3)$  mode, results in  $T_3$  values which are lower than the corresponding CO or  $N_2$  temperatures. Moreover the "drain" of energy from the  $CO_2(v_3)$  mode is transmitted to the CO and  $N_2$  modes by V-V coupling. This coupling is stronger for  $N_2$  than for CO at normal gas temperatures. Thus it is the comparative inefficiency of the CO- $CO_2(v_3)$  coupling which allows the CO to maintain a higher vibrational temperature despite the energy loss channel through the  $CO_2$ . This is an interesting prediction since it has sometimes been assumed<sup>6,20</sup> than in a non-lasing steady-state discharge the CO,  $N_2$  and  $CO_2(v_3)$  mode temperatures are roughly equal. However very recent tunable diode laser measurements of CO vibrational temperatures in low-pressure dc discharges (Reid and Dang<sup>15</sup>) have confirmed that high

CO temperatures ( $\sim 3000\text{K}$ ) are reached for corresponding  $T_3$  values of around  $1500\text{K}$ . The main qualitative features of the VIBEX calculations (the temperature saturation with current and the inequality of the CO,  $\text{N}_2$  and  $\text{CO}_2$  temperatures) are therefore in agreement with recent laboratory experiments.

It is appropriate to consider here the practical implications of  $T_3$  saturation at values well below the theoretical optimum for population of the  $00^0_1$  upper laser level (see figure 2.3). One such implication will be a limitation of attainable small-signal gain in  $\text{CO}_2$  laser amplifiers. Therefore the vibrational temperature analysis was extended to the calculation of small-signal gains, and the relative importance of superelastic relaxation, gas heating and  $\text{CO}_2$  dissociation was assessed. A full treatment of laser gain in low pressure discharges requires the calculation of Voigt-profiled lineshapes which include the effects of both Doppler and pressure broadening. For a simplified analysis the approximation of pure pressure broadening was adopted and provided adequate agreement between theory and experiment. However this agreement was obtained only when due account was taken of current-dependent  $\text{CO}_2$  dissociation which has the main influence on the gain-current characteristic of sealed and slow-flow discharges. A full description of the gain analysis is presented in reference 16, included here as Appendix D.

### 6.3.2 Specification of effective superelastic rate constants

The modelling calculations of the previous section showed good qualitative agreement with the available experimental measurements, and allowed some important deductions concerning the behaviour of vibrational temperatures in the  $\text{CO}_2$  laser system. Good quantitative



agreement was also occasionally obtained. In general, however, the model predicted vibrational temperatures which were higher than those measured in the laboratory. This is not surprising, because the simplest approximation was used to calculate effective superelastic rate constants (see for example equation 5.19): this neglects the higher energy levels in the vibrational modes, and assumes that superelastic collisions act only on the first excited level of each mode. Since the superelastic rate constant depends exponentially on the energy of the interacting molecule, such a neglect of higher energy levels causes a substantial under-estimation of the net rate of superelastic relaxation from any particular vibrational mode. A more sophisticated approximation was therefore adopted, in which the effective superelastic rate constant for each mode is obtained by a weighted averaging over the first 8 excited levels, as in equation 5.25 for the case of  $N_2$ . It is instructive to compare the implications of the different approximations (5.19) and (5.25). Assuming an electron temperature of 1eV, and putting  $h\nu_4 = 0.289\text{eV}$  ( $2330\text{ cm}^{-1}$ ) then from equation 5.19 we obtain

$$X_{-4} = 1.33 X_4$$

For the same electron temperature, the weighted average (5.25) yields

$$X_{-4} = 4.53 X_4$$

Very similar factors relate the  $CO$  and  $CO_2(\nu_3)$  superelastic rate constants ( $X_{-6}$  and  $X_{-3}$ ) to the corresponding excitation rate constants.

Figure 6.6 shows  $CO_2$  asymmetric mode temperatures calculated for various conditions using both the simplified approximation (dotted curves) and weighted average approximation (solid curves). The latter method, involving higher superelastic collision rates, produces pre-

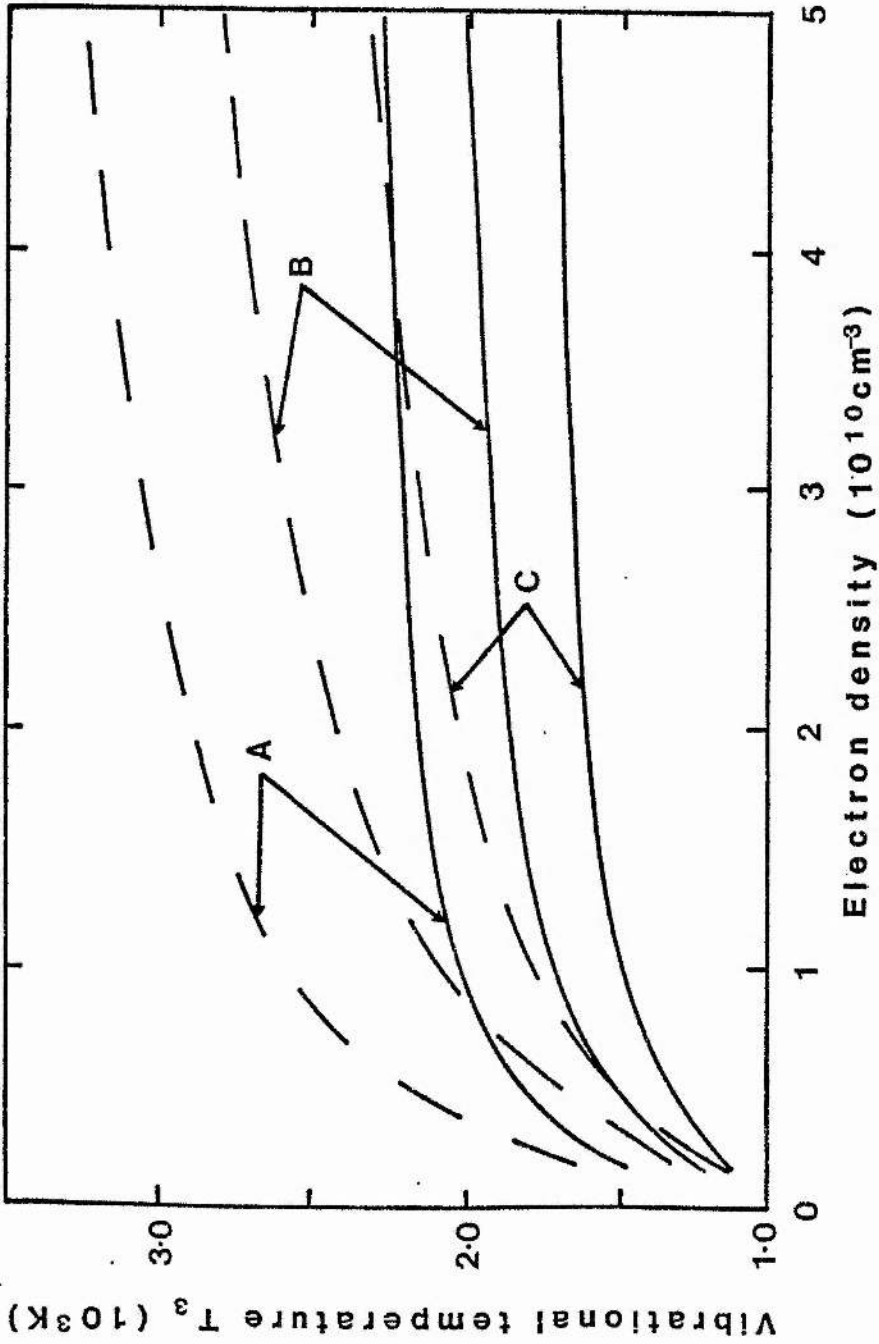


Fig. 6.6. Comparison of calculations using simple superelastic approximation (dashed curves) and weighted average (solid curves). (A) 6 CO<sub>2</sub> : 12 N<sub>2</sub> : 82 He, 30 Td. (B) 13 CO<sub>2</sub> : 9 N<sub>2</sub> : 78 He, 30 Td. (C) 10 CO<sub>2</sub> : 20 CO : 70 He, 36 Td.

dicted vibrational temperatures which are lower and saturate more strongly than in previous calculations. However it will be shown in the following section that these strongly saturating curves are in good agreement with laboratory measurements.

### 6.3.3 Effects on vibrational temperatures of gas mixture, pressure and flow rates

The effects of varying gas mixture, pressure and flow-rate on the  $\text{CO}_2(\nu_3)$  mode temperature were investigated experimentally. Results are shown in figure 6.7 for the 6:12:82 mixture under sealed and flowing conditions. Gas pressure in the discharge tube was 10 torr, obtained by averaging the upstream and downstream measurements to avoid pressure gradient errors. Sequence  $(00^0_2)$  band gain is lower than the fundamental  $(00^0_1)$  band gain for both sealed and flowing operation, and it is noticeable that the  $00^0_1$  gain peaks at lower currents. Sealed gains are smaller, and peak at lower current than the corresponding flowing gains. When equation (6.1) is used to derive the vibrational temperature  $T_3$  from the smooth curves through the experimental gain points, it is seen that the sealed vibrational temperatures are significantly higher than those in the flowing gas discharge. This is attributed to an increased average level of  $\text{CO}_2$  dissociation in the sealed discharge: in a considerably dissociated mixture the excitation of the  $\text{CO}_2(\nu_3)$  mode is favoured both by the increased  $\text{N}_2:\text{CO}_2$  and  $\text{CO}:\text{CO}_2$  ratios and by the reduced rate of  $\text{CO}_2(\nu_3) \rightarrow \text{CO}_2(\nu_1, \nu_2)$  deactivations which is mainly caused by collisions with other  $\text{CO}_2$  molecules. In general this leads to high  $\nu_3$  temperatures in mixtures with low  $\text{CO}_2$  partial pressures.

Figures 6.8 and 6.9 illustrate the effect of flow-rate changes on the  $13\text{CO}_2: 9\text{N}_2: 78\text{He}$  and  $10\text{CO}_2: 20\text{CO}: 70\text{He}$  gas mixtures. These

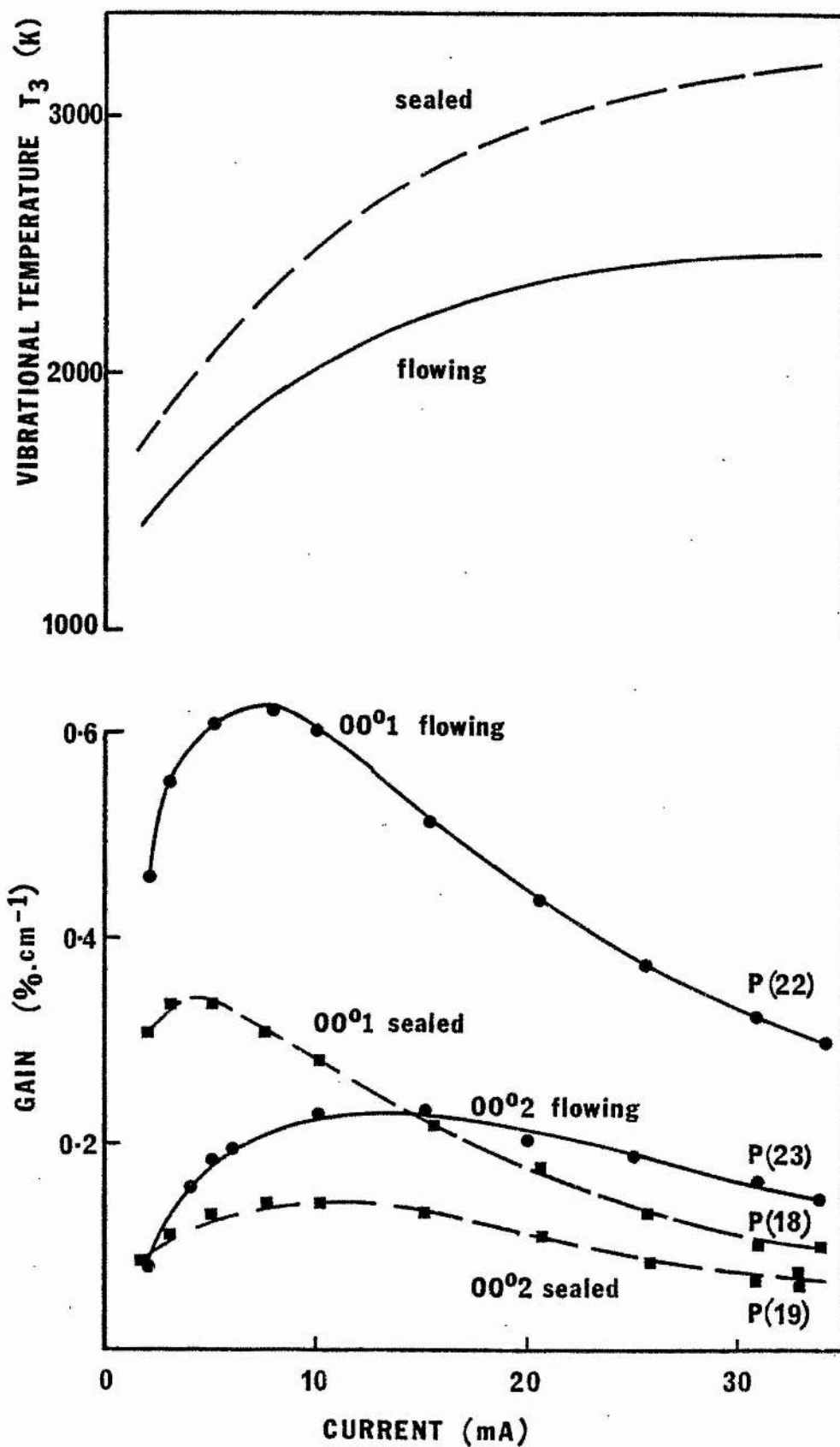


Fig. 6.7. Measured gain and derived  $T_3$  for 6:12:82 mix at 10 torr, sealed (dashed curves) and flowing (solid curves, flow rate 50 sccm).

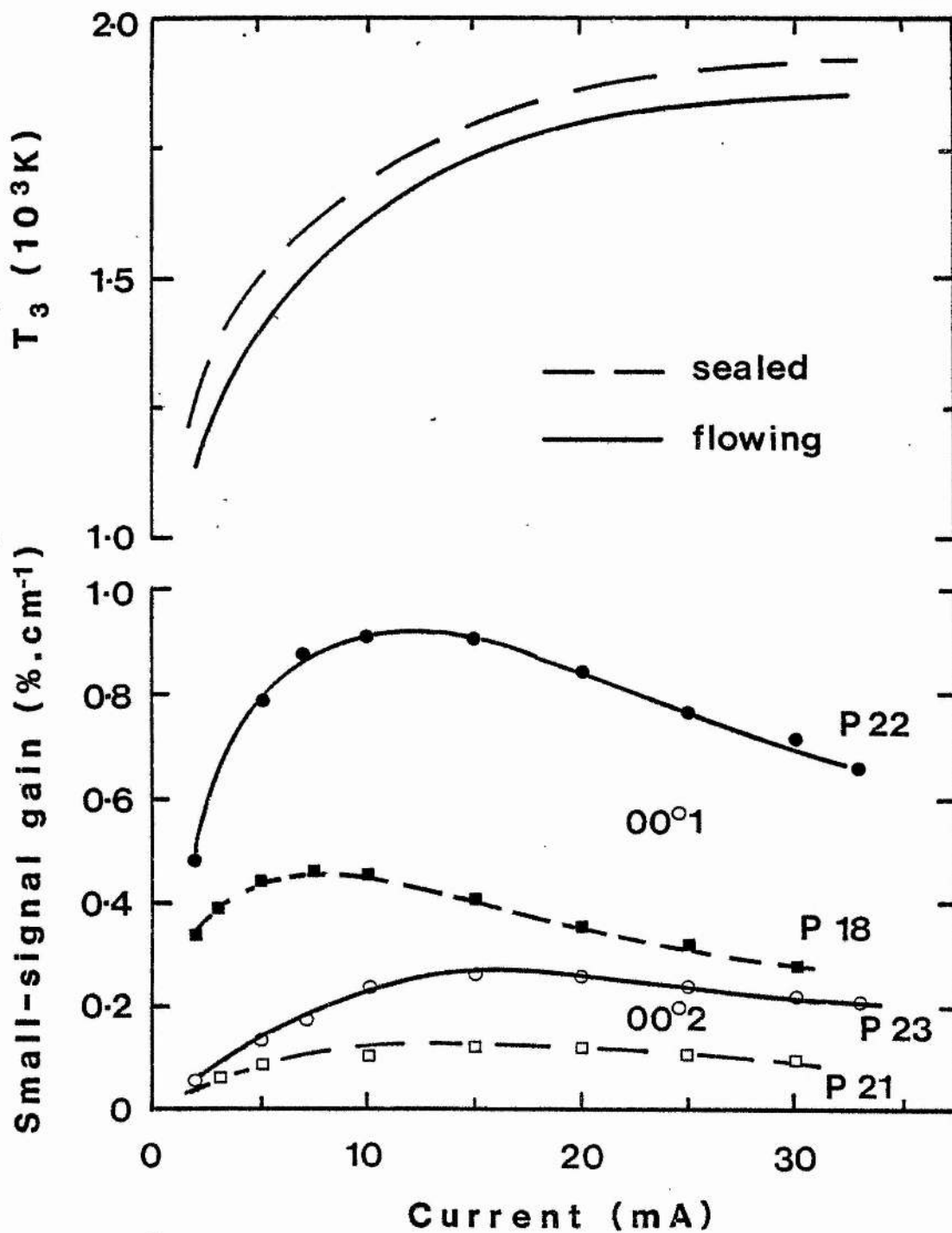


Fig. 6.8. Measured gain and derived  $T_3$  for  $^{13}\text{CO}_2 : 9 \text{N}_2 : 78 \text{He}$ , 10 torr; sealed and flowing (50 sccm).

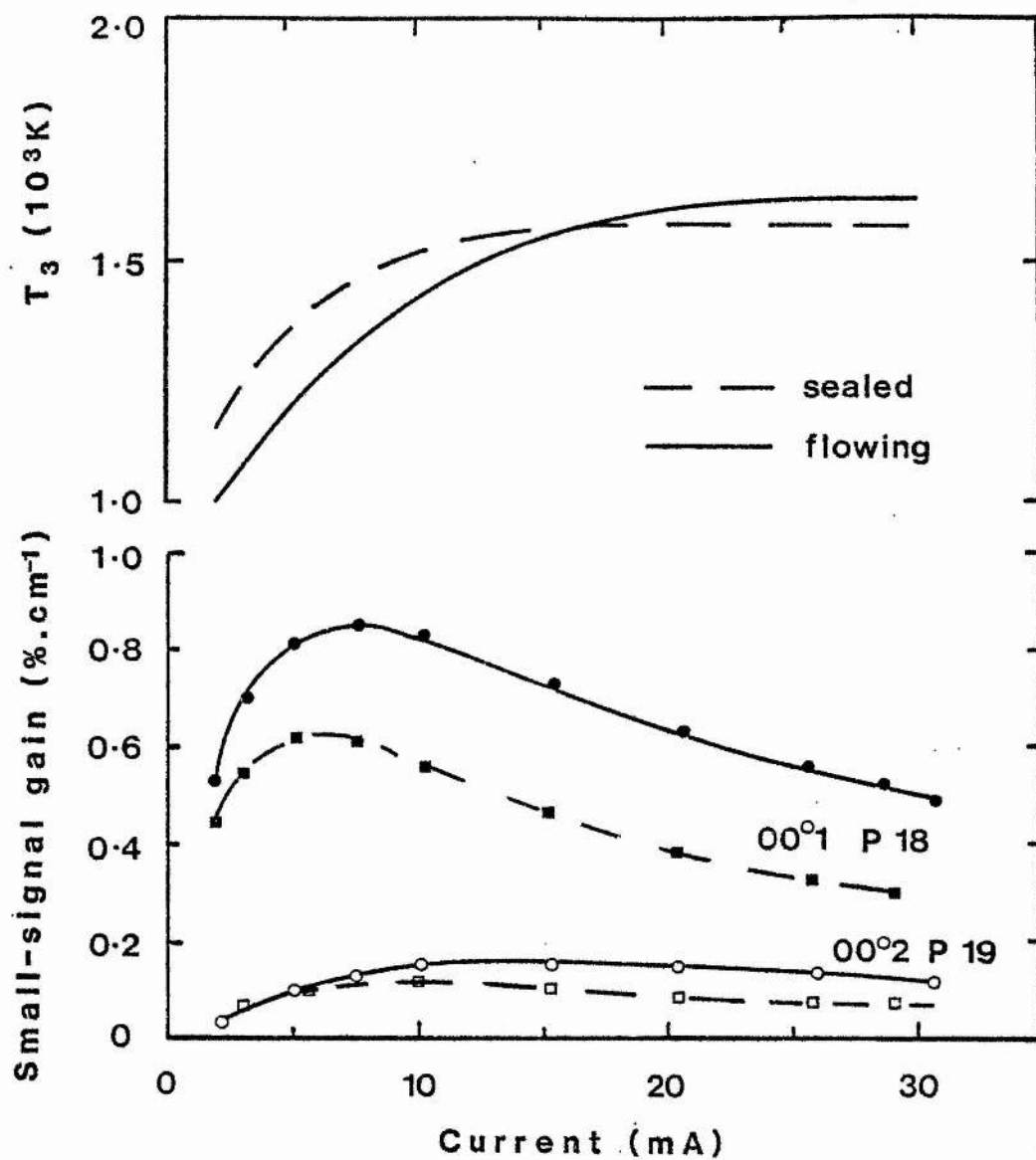


Fig. 6.9. Measured gain and derived  $T_3$  for 10  $\text{CO}_2$  : 20  $\text{CO}$  : 70  $\text{He}$ , 10 torr, sealed and flowing (50 sccm).

also exhibit an inverse dependence of  $T_3$  on flow-rate; however for the 13:9:78 mixture the dependence is very weak, and in the  $\text{CO}_2$ -CO-He case the sealed and flowing vibrational temperatures are equal within experimental uncertainty. This trend can be understood in terms of the gas mixture dependence of  $\text{CO}_2$  dissociation levels. These were measured as a function of discharge current using the MS10S mass spectrometer to sample from the gain cell gas outlet. The results (figure 6.10) show that the mixtures rich in molecular species ( $\text{CO}_2$ ,  $\text{N}_2$ , CO) are resistant to  $\text{CO}_2$  dissociation; conversely the 6:12:82 mixture, leanest in  $\text{CO}_2$ , showed the highest dissociation levels. This is fully consistent with the dissociation rate measurements of Chapter 3 and explains the insensitivity of  $T_3$  to flow-rate changes in the  $13\text{CO}_2: 9\text{N}_2: 78\text{He}$  and  $10\text{CO}_2: 20\text{CO}: 70\text{He}$  mixtures.

The effect of pressure changes was determined under sealed tube conditions to avoid the complication of flow dependent pressure gradients. Power supply limitations restricted operating pressures to less than 30 torr. Figure 6.11 shows gain and  $T_3$  results for the 13:9:78 mixture. An optimum pressure for  $00^0_1$  and  $00^0_2$  gain exists around 18 torr; the derived vibrational temperature falls monotonically with increasing pressure in the range 10-26 torr; the rate of  $T_3$  decrease is  $\sim 15 \text{ K torr}^{-1}$ . The decrease presumably results from the increased collisional relaxation rates at higher pressure. The optimum pressure for  $00^0_1$  band gain results from the conflicting gain requirements of (i) a high  $\nu_3$  mode temperature and (ii) a high  $\text{CO}_2$  partial pressure.

The experimental results can be compared to the computer model predictions. Voltage-current characteristics at each pressure were

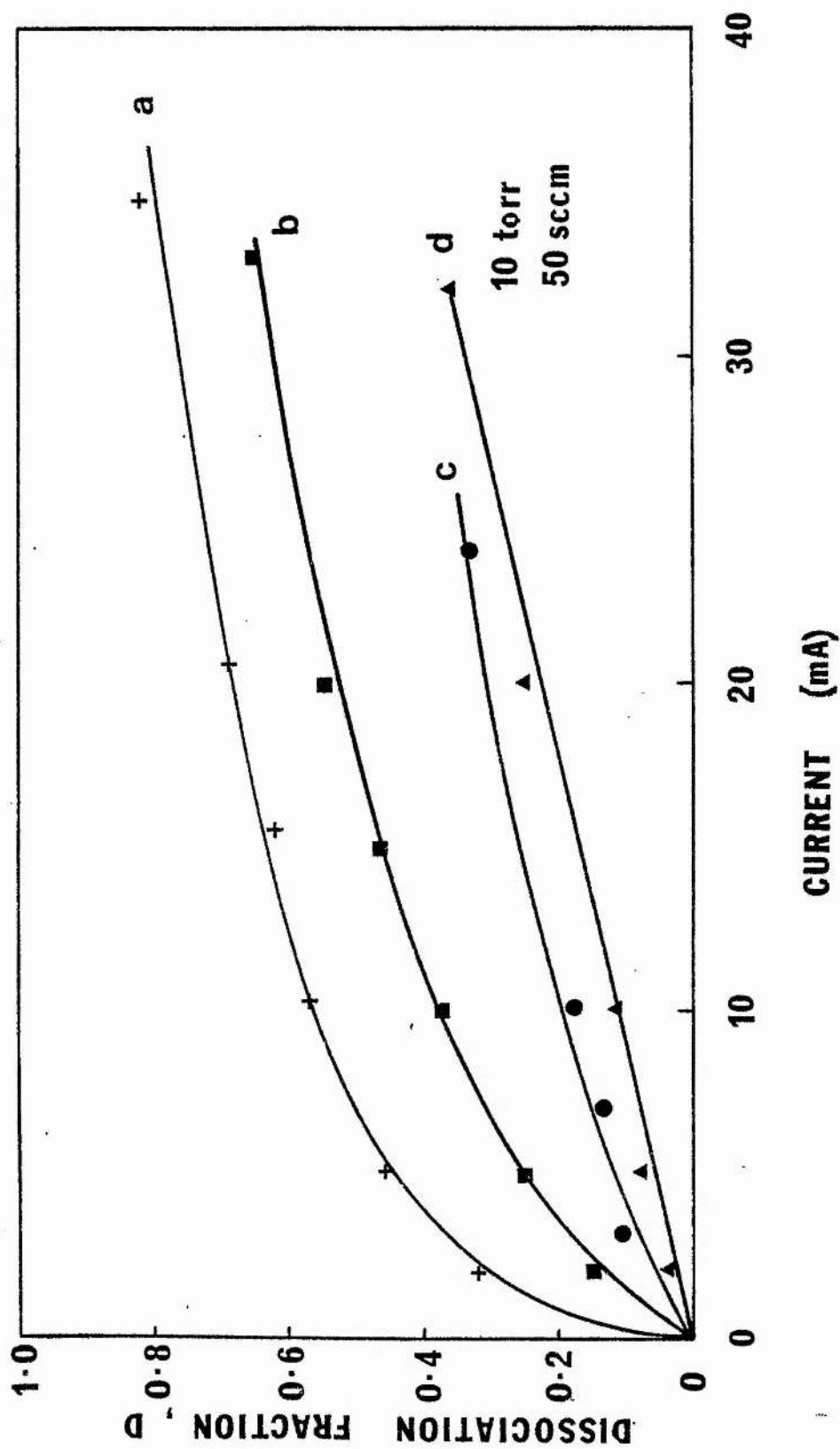


Fig. 6.10. Measured dissociation levels in (a) 6 CO<sub>2</sub> : 12 N<sub>2</sub> : 78 He, (b) 13 CO<sub>2</sub> : 9 N<sub>2</sub> : 78 He, (c) 33 CO<sub>2</sub> : 33 N<sub>2</sub> : 33 He, (d) 10 CO<sub>2</sub> : 20 CO : 70 He at 50 sccm flow rate.



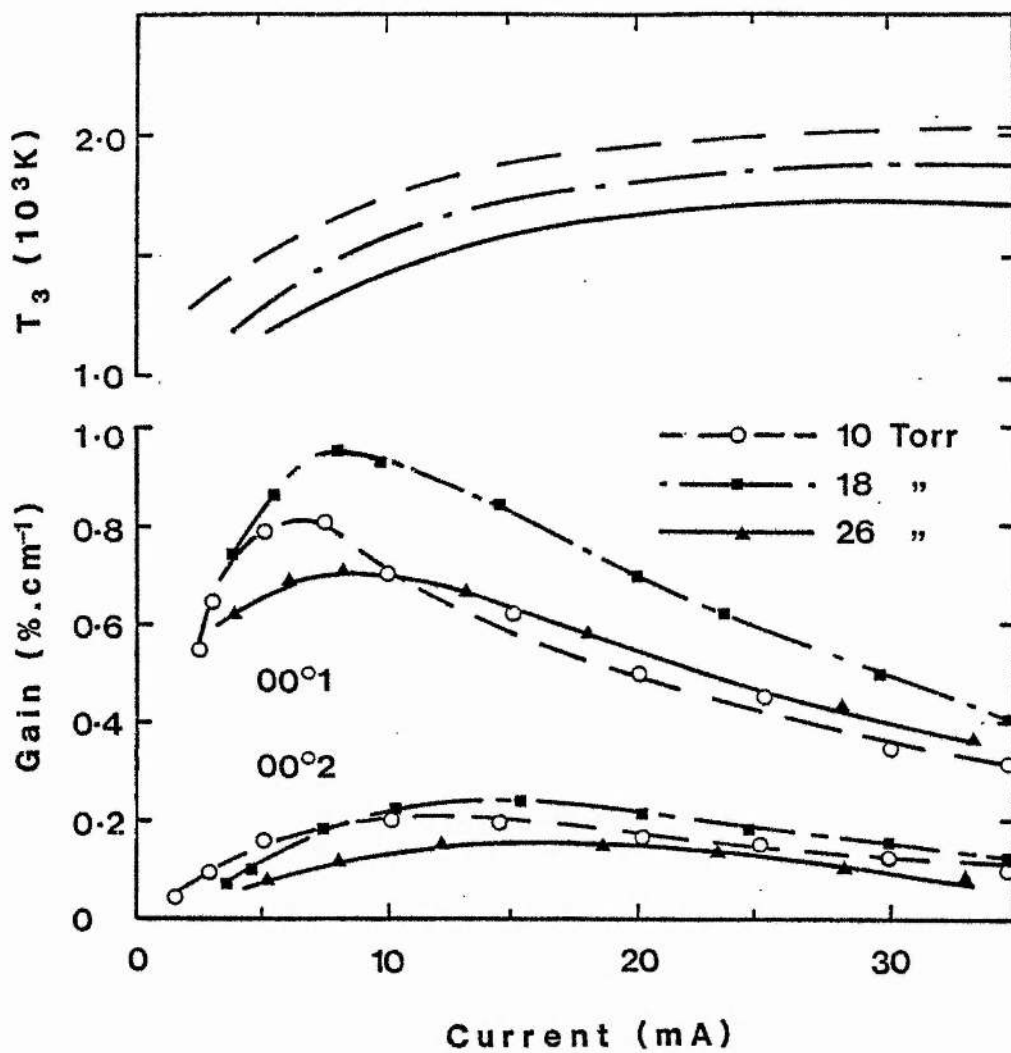


Fig. 6.11. Dependence of small-signal gain and  $T_3$  on pressure for  $^{13}\text{CO}_2 : ^9\text{N}_2 : ^4\text{He}$  (sealed).

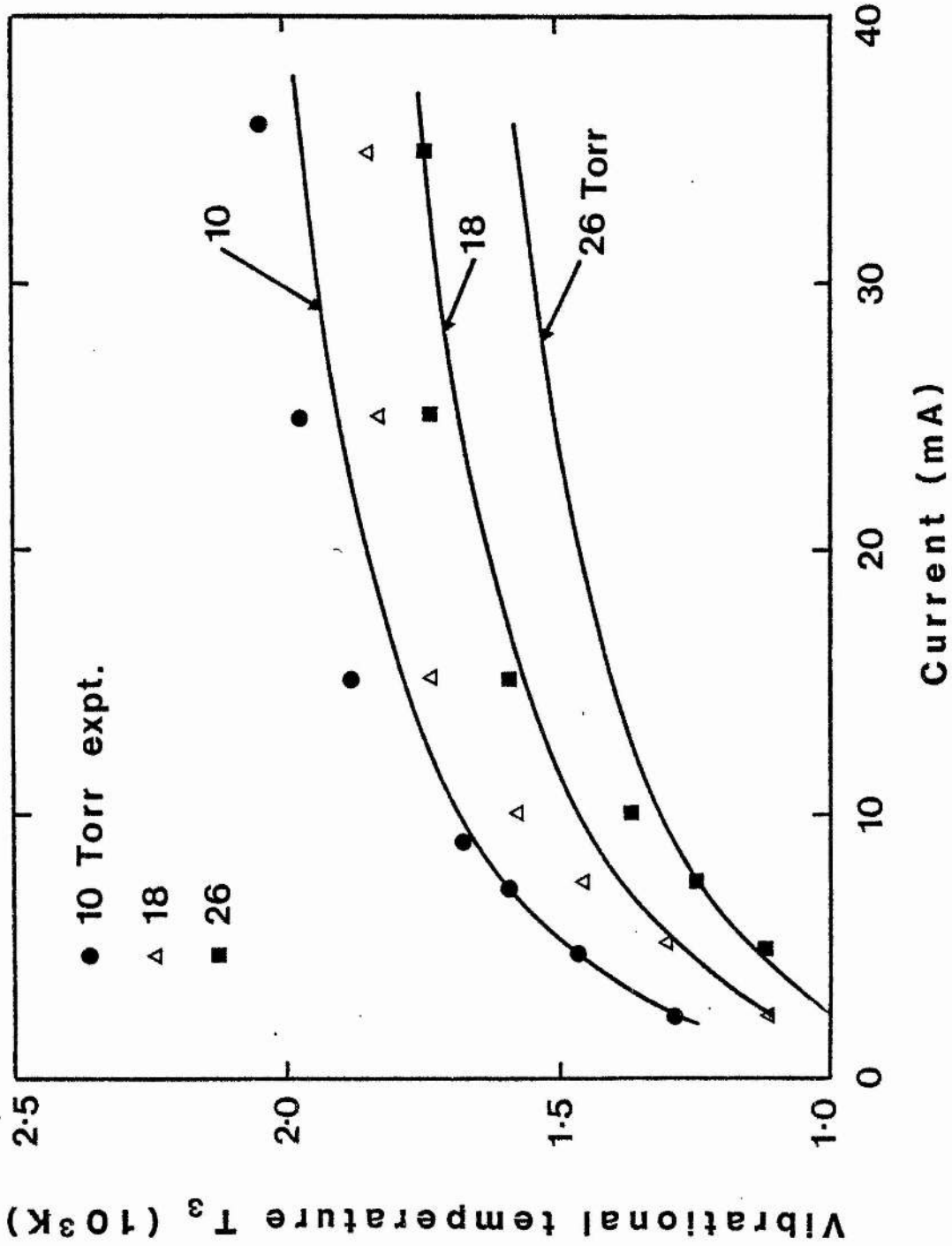


Fig. 6.12. Comparison of calculation and experiment for 13%  $CO_2$  : 9%  $N_2$  : 78% He (sealed).

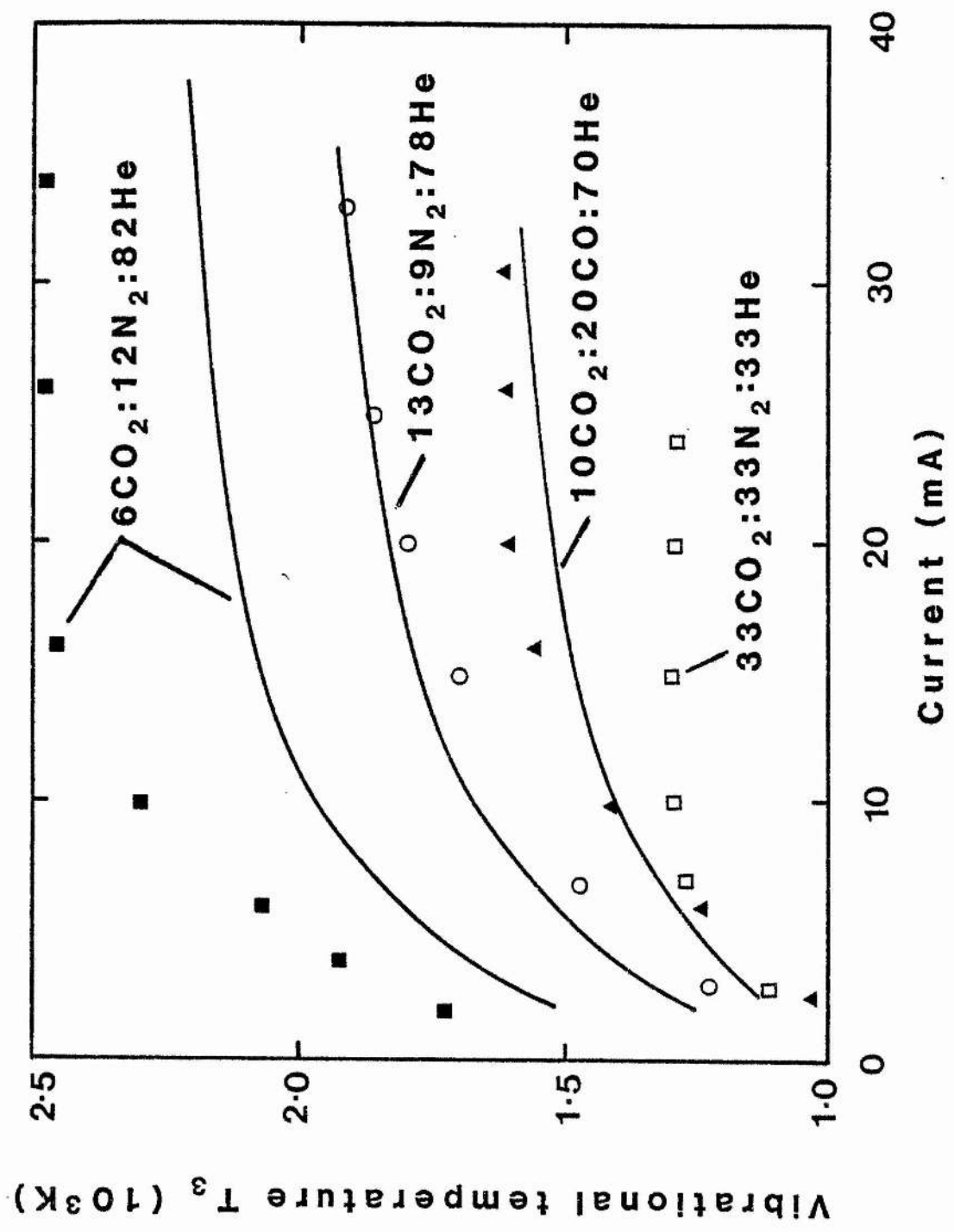


Fig. 6.13. Comparison of calculation and experiment at 10 torr (flowing, 50 sccm).

used to calculate the corresponding values of E/N assuming the gas heating power law of equation 3.10. The calculations showed that E/N is nearly independent of current with the values 32 Td (for 10 torr) 27 Td (18 torr) and 23.5 Td (26 torr) where 1 Td =  $10^{-17}$  V cm<sup>2</sup>. These values were used in the computer model to produce the results of figure 6.12, where the conversions from electron density to discharge current are based on the microwave resonance measurements of Chapter 4. In the computer calculations the "strong" superelastic approximation was used, as described in section 6.3.2. This more sophisticated approximation produces much improved agreement with experiment. The agreement is not perfect, however: the model predicts a vibrational temperature decrease with pressure of 25 K torr<sup>-1</sup>, a slight over-estimate compared to the measured rate.

The ability of the model to predict the effect of gross gas mixture changes was also tested. Vibrational temperatures in four different gas mixtures were measured at 10 torr total pressure and the operating E/N values were derived. The results are plotted in figure 6.13 and are compared with the corresponding model calculations, again assuming the specific electron densities measured by the microwave method. The model successfully predicts the vibrational temperature 'ranking' of the mixtures, and yields good numerical agreement for the 13:9:78 and 10:20:70 mixtures. For the 6:12:82 mixture the calculated T<sub>3</sub> values are 15-20% low. Lack of the appropriate BOLTZ data precluded calculations for the 33:33:33 mix.

#### 6.4 Computer model experiments

##### 6.4.1 Effects of E/N and gas temperature

The dependence of the model predictions on a wider range of para-

meters was investigated, although no experimental data were available for comparison. The effect of varying the reduced electric field ( $E/N$ ) on the BOLTZ-calculated electron impact excitation rate constants and on the average discharge electron energy is plotted in figure 6.14 for the  $13\text{CO}_2: 9\text{N}_2: 78\text{He}$  gas mixture. These data were used in VIBEX to calculate steady state  $\text{N}_2$  and  $\text{CO}_2(v_3)$  vibrational temperatures ( $T_4$  and  $T_3$ ) at constant electron density for the  $E/N$  range 10 to 100 Td. As usual, the results (see figure 6.15) predict that  $T_4$  is greater than  $T_3$ , and that both rise monotonically with electron density. At low electron densities the highest vibrational temperatures are attained for  $E/N \sim 35$  Td, as expected since this is the  $E/N$  value which maximises the electron excitation.

The effect of ambient gas temperature on the model calculations is mainly to influence the magnitudes of the V-V and V-V-T rate constants, many of which are highly temperature dependent. A convenient listing of various temperature dependences has been compiled by Smith and Thomson.<sup>17</sup> These dependences and the resultant rate constant values for 300, 400 and 600 K are listed in Table 6.1 and compared to the 400 K rate constants normally used in the model. Agreement is reasonable, and so the Smith and Thomson expressions were used in the model to calculate the sensitivity of  $T_2$ ,  $T_3$  and  $T_4$  to changes in ambient gas temperature ( $T$ ) in the range 300-500K. It was found that the Smith and Thomson rate constants for 400K resulted in calculated  $T_3$  values (figure 6.16) which were about 200K higher than the values calculated using the standard VIBEX rate constants of Table 5.1. It can be seen that the effect of increasing the assumed gas temperature is to increase the calculated  $T_2$  by about the same amount, but to decrease

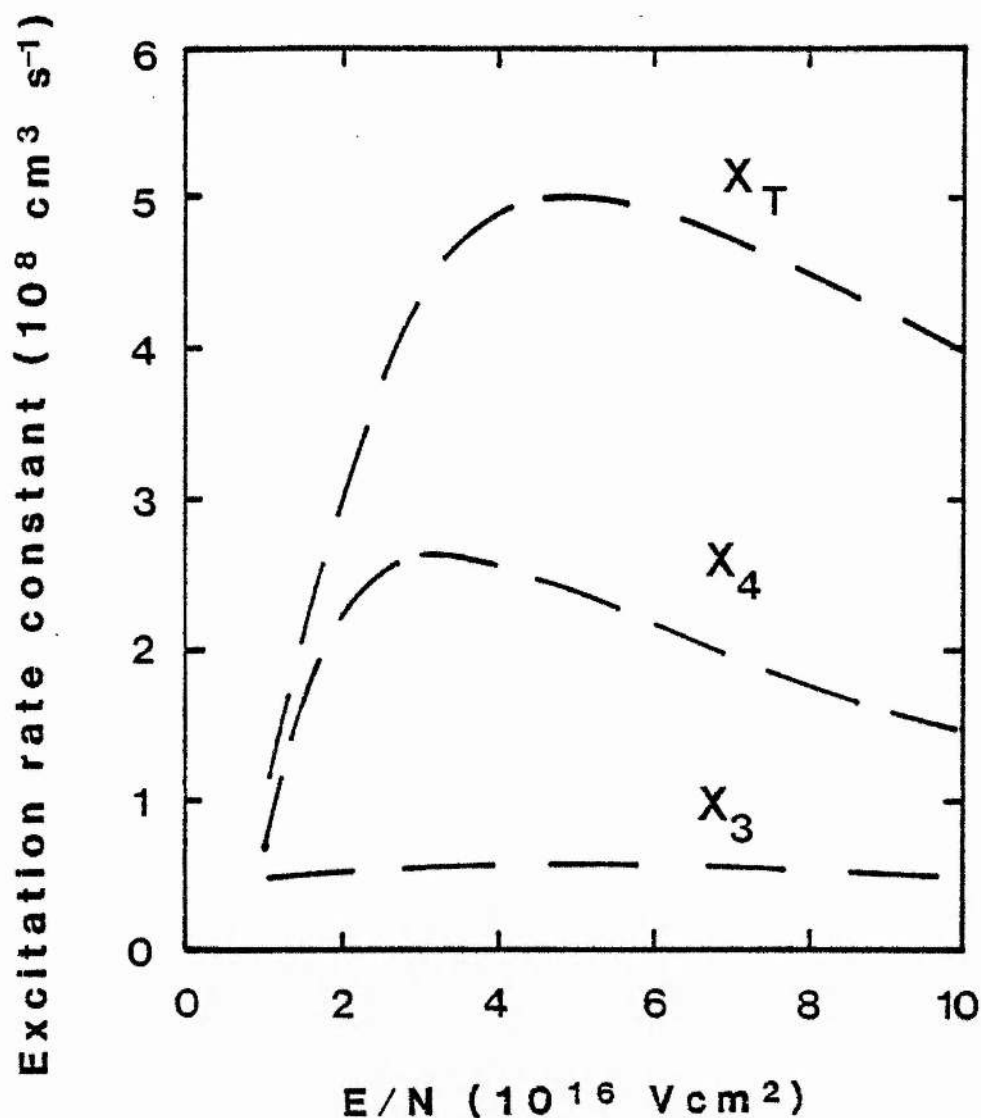


Fig. 6.14. BOLTZ - calculated rate constants for vibrational excitation of  $\text{N}_2$  ( $X_4$ ),  $\text{CO}_2$  asymmetric ( $X_3$ ) and  $\text{CO}_2$  symmetric and bending modes ( $X_T$ ) assuming 13%  $\text{CO}_2$  : 9%  $\text{N}_2$  : 78% He mixture (no dissociation). These data were used to calculate the dependence of vibrational temperature on  $E/N$ .

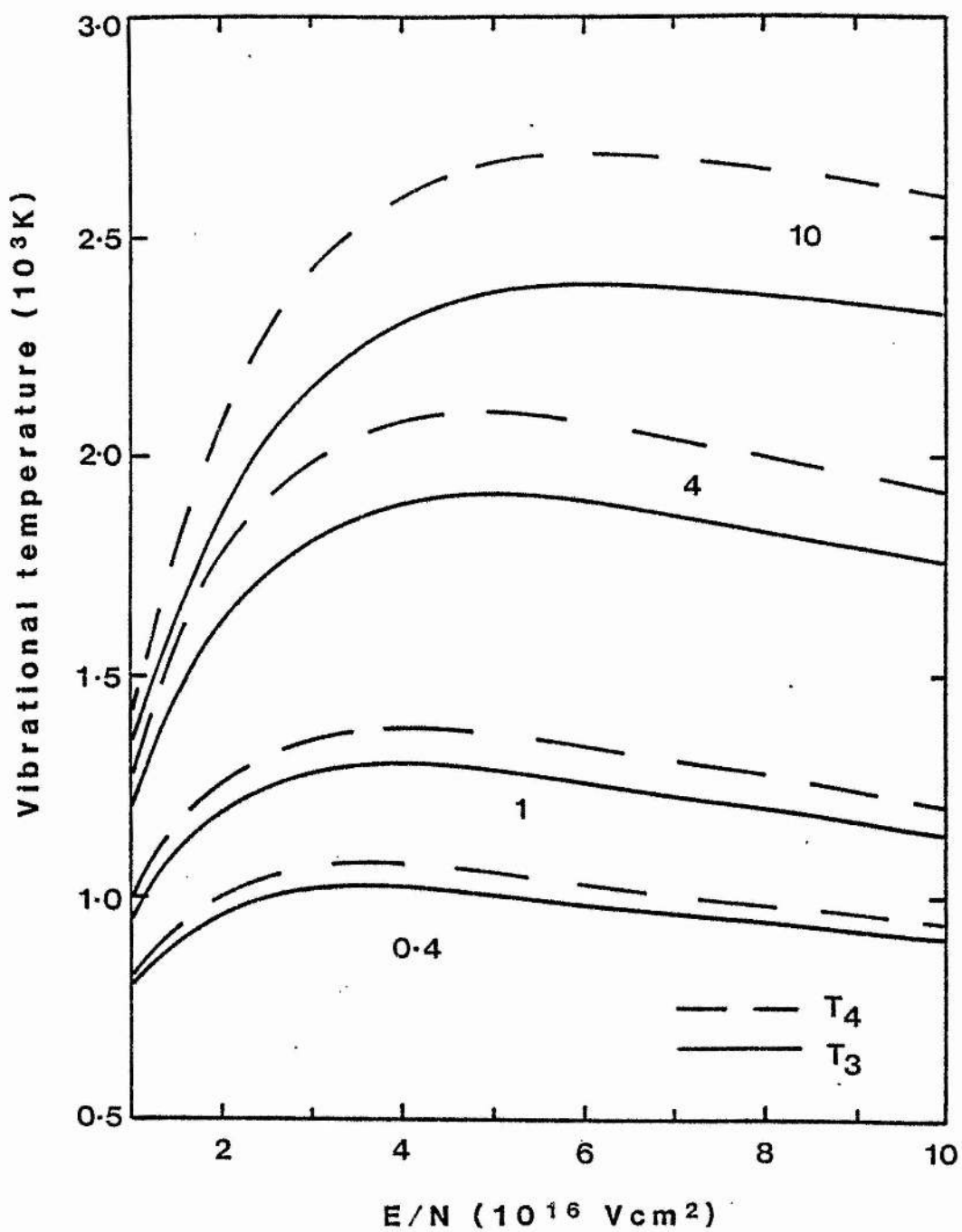


Fig. 6.15. Effect of  $E/N$  on calculated  $\text{N}_2$  and  $\text{CO}_2$  vibrational temperatures with electron density ( $10^{10}\text{ cm}^{-3}$ ) as parameter.

TABLE 6.1

Temperature dependence of principle system rate constants (from Smith and Thomson<sup>17</sup>)

Process	M	Standard VIBEX constant (400K)	Temperature dependence	300K	Rates 400K	600K
CO <sub>2</sub> (ν <sub>3</sub> ) + M	CO <sub>2</sub>	1.1 (-14)	9.6 x 10 <sup>23</sup> F(T)	3.6 (-15)	6.3 (-15)	1.7 (-14)
→ CO <sub>2</sub> (ν <sub>1</sub> , ν <sub>2</sub> )	N <sub>2</sub>	4.2 (-15)	6.87 x 10 <sup>23</sup> F(T)	2.5 (-15)	4.5 (-15)	1.2 (-14)
+ M + ΔE	CO	8.5 (-15)	As for N <sub>2</sub>		As for N <sub>2</sub>	
	He	2.8 (-15)	2.43 x 10 <sup>23</sup> F(T)	9.0 (-16)	1.6 (-15)	4.3 (-15)
CO <sub>2</sub> (ν <sub>1</sub> , ν <sub>2</sub> ) + M	CO <sub>2</sub>	6.0 (-15)	4.6 x 10 <sup>10</sup> G(T)	4.5 (-15)	1.3 (-14)	4.9 (-14)
→ CO <sub>2</sub> (000) + M	N <sub>2</sub>	2.0 (-15)	9.6 x 10 <sup>-11</sup> G(T)	9.5 (-16)	2.7 (-15)	1.0 (-14)
+ ΔE	CO	6.9 (-13)	6.82 x 10 <sup>-8</sup> G(T)	6.7 (-13)	1.9 (-12)	7.2 (-12)
	He	1.5 (-13)	8.1 x 10 <sup>-11</sup> H(T)	9.6 (-14)	1.8 (-13)	3.9 (-13)



TABLE 6.1 continued

<u>Process</u>	<u>Standard VIBEX constant (400K)</u>	<u>Temperature dependence</u>	<u>300K</u>	<u>Rates 400K</u>	<u>600K</u>
$\text{CO}_2(000) + \text{CO}(v = 1)$	9.7 (-14)	$1.56 \times 10^{-11} \exp(-30.1/T^{1/3})$	1.7 (-13)	2.6 (-13)	4.4 (-13)
$\rightarrow \text{CO}_2(001) + \text{CO}(v = 0)$					
$\text{CO}_2(000) + \text{N}_2 (v = 1)$	2.3 (-13)	$6.07 \times 10^{-4} \exp(15.3/T^{1/3})$	6.0 (-13)	4.8 (-13)	3.7 (-13)
$\rightarrow \text{CO}_2(001) + \text{N}_2(v = 0)$					
$\text{N}_2(v = 0) + \text{CO} (v = 1)$	8.8 (-15)	$6.98 \times 10^{-13} \exp(25.6/T^{1/3})$	3.2 (-11)	2.2 (-11)	1.4 (-11)
$\rightarrow \text{N}_2(v = 1) + \text{CO}(v = 0)$					

Notes: 1. All rate constants in  $\text{cm}^3 \text{s}^{-1}$

2.  $F(T) = T^{-5.89} \exp(-4223/T - 672.7/T^{1/3} + 2683/T^{2/3})$

$G(T) = \exp(-77/T^{1/3})$

$H(T) = \exp(-45/T^{1/3})$

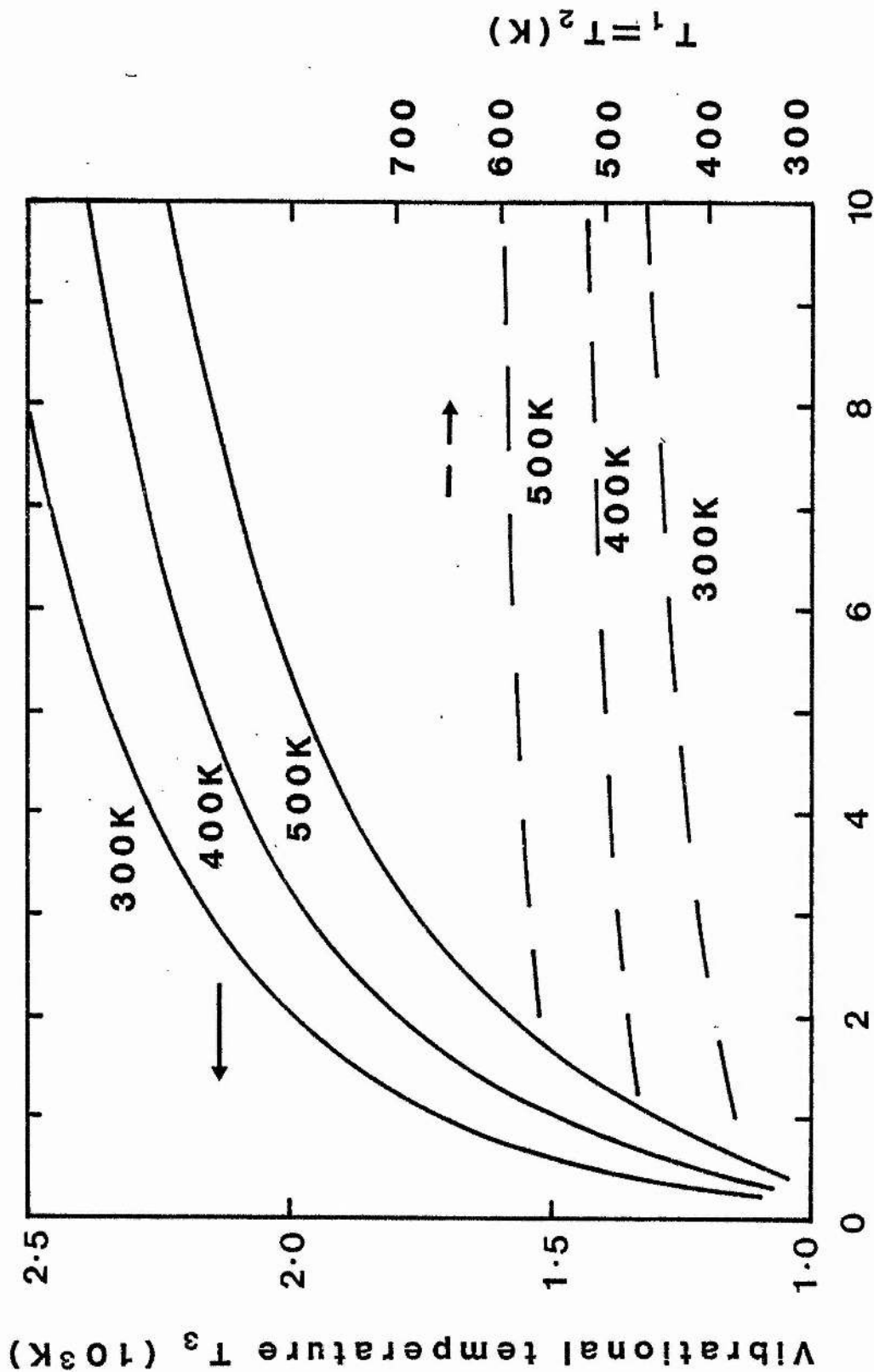


Fig. 6.16. Effect of temperature on calculated  $\text{CO}_2$  vibrational temperatures assuming rate constants of Smith and Thomson.

TABLE 6.2

Calculated effect of ambient temperature on CO<sub>2</sub> vibrational temperatures and

laser level populations at constant electron density ( $3 \times 10^{10} \text{ cm}^{-3}$ ).

Ambient temperature $T$ (K)	Vibrational $T_1 = T_2$ (K)	Temperatures $T_3$ (K)	$(00^0 1)$	Fractional population $(10^0 0)$	$(00^0 2)$	$(10^0 1)$	Population inversions $(00^0 1 - 10^0 0)$	$(00^0 2 - 10^0 1)$
300	410	2170	1.35(-1)	5.85(-3)	2.83(-2)	1.23(-3)	1.29(-1)	2.71(-2)
400	490	1970	1.07(-1)	1.17(-2)	1.92(-2)	2.10(-3)	9.53(-2)	1.71(-2)
500	575	1760	7.95(-2)	1.91(-2)	1.16(-2)	2.80(-3)	6.04(-2)	8.80(-3)

Note. The level populations and population inversions are expressed as a fraction of the total CO<sub>2</sub> population.

The vibrational temperatures are taken from Fig. 6.16.

$T_3$  and  $T_4$  at a rate of approximately  $2\text{K}\cdot\text{K}^{-1}$ . The implications of these changes in the vibrational temperatures can be evaluated. Table 6.2 shows the vibrational temperature predictions of figure 6.16 (assuming an electron density of  $3 \times 10^{10} \text{ cm}^{-3}$ ), and the corresponding  $00^{\circ}1$  and  $00^{\circ}2$   $10 \mu\text{m}$  band laser level populations (expressed as a fraction of the total  $\text{CO}_2$  population). For an ambient gas temperature of 300K the lower laser level populations are only 4% of those in the upper laser levels. At  $T = 500\text{K}$  this figure has increased to 24%, and the population inversions have fallen by a factor of 2-3. Notice however that this is largely due to the decrease in the  $00^{\circ}1$  and  $00^{\circ}2$  populations rather than any serious increase in the lower level populations. Therefore the frequently expressed view that the deleterious effect of high gas temperature on gain is due to the thermal population of the lower laser level is shown to be unjustified. The more important effect is the increased collisional relaxation of the  $\text{CO}_2(\nu_3)$  mode which causes a serious reduction in the  $00^{\circ}1$  and  $00^{\circ}2$  populations.

#### 6.4.2 Effect of radial diffusion

Radial diffusion of vibrationally excited molecules to the discharge tube walls, and their subsequent de-activation by wall collisions, can be an important energy loss channel in low-pressure cw lasers. However, little experimental work has been devoted to radial diffusion in  $\text{CO}_2$  lasers, and considerable uncertainty surrounds the values of the diffusion coefficients for vibrationally excited  $\text{CO}_2$ ,  $\text{CO}$  and  $\text{N}_2$  and the probability of molecular deactivation in a wall collision. Nevertheless it is interesting and important to quantify the likely effect of radial diffusion and wall quenching on the vibrational

temperature productions of the computer model. Two approximations were required: (i) the diffusion coefficients of a vibrationally excited molecule were assumed equal to those of the unexcited molecule, and (ii) the probability of vibrational deactivation to the ground state in a wall collision was taken as unity. The population rate equation system (5.1-5.4) was then modified by the addition of diffusion terms according to the transformations:-

$$\frac{dn_1}{dt} \rightarrow \frac{dn_1}{dt} - \frac{D_{CO_2} n_1}{\Lambda^2} \quad (6.3)$$

$$\frac{dn_2}{dt} \rightarrow \frac{dn_2}{dt} - \frac{D_{CO_2} n_2}{\Lambda^2} \quad (6.4)$$

$$\frac{dn_3}{dt} \rightarrow \frac{dn_3}{dt} - \frac{D_{N_2} n_3}{\Lambda^2} \quad (6.5)$$

$$\frac{dn_4}{dt} \rightarrow \frac{dn_4}{dt} - \frac{D_{CO} n_4}{\Lambda^2} \quad (6.6)$$

where  $\Lambda = R/2.4$  relates the diffusion length to the tube radius, assuming the radial profile of excited molecules is a Bessel function. The  $D$ 's ( $\text{cm}^2 \text{s}^{-1}$ ) are the coefficients of diffusion of gas molecules in the laser gas mixture, e.g.

$$\frac{1}{D_{CO_2}} = \frac{p_{CO_2}}{D_{CO_2-CO_2}} + \frac{p_{N_2}}{D_{CO_2-N_2}} + \frac{p_{He}}{D_{CO_2-He}} + \dots$$

where the  $p_K$  are gas species partial pressures in torr and  $D_{J-K}$  is the coefficient of diffusion of gas J in 1 torr of gas K at 400K. These coefficients are governed by the relation

$$D_{K-J} = D_{J-K} \quad (6.7)$$

and the temperature and pressure variation can be written <sup>18</sup>

TABLE 6.3    Diffusion coefficients in CO<sub>2</sub> laser media, D<sub>ij</sub>.

	j	CO <sub>2</sub>	N <sub>2</sub>	CO	O <sub>2</sub>	He
i						
CO <sub>2</sub>		146	221	211	215	851
N <sub>2</sub>		221	272	296	280	954
CO		211	296	254	286	954

Notes.

- (1) Diffusion coefficients are in (cm<sup>2</sup>s<sup>-1</sup>) and assume 400K ambient temperature with 1 torr total pressure.
- (2) Data derived from
  - (a) Amer. I. of Phys. Handbook page 2 - 252.
  - (b) Gordiets et al. Sov. Phys. JETP 26, 5, 1043 (1968).
  - (c) Bretszjander "Transport and Physical Properties of Fluids" p.333 (Pergamon 1971) with appropriate pressure and temperature scaling where necessary (see text, section 6.4.2).

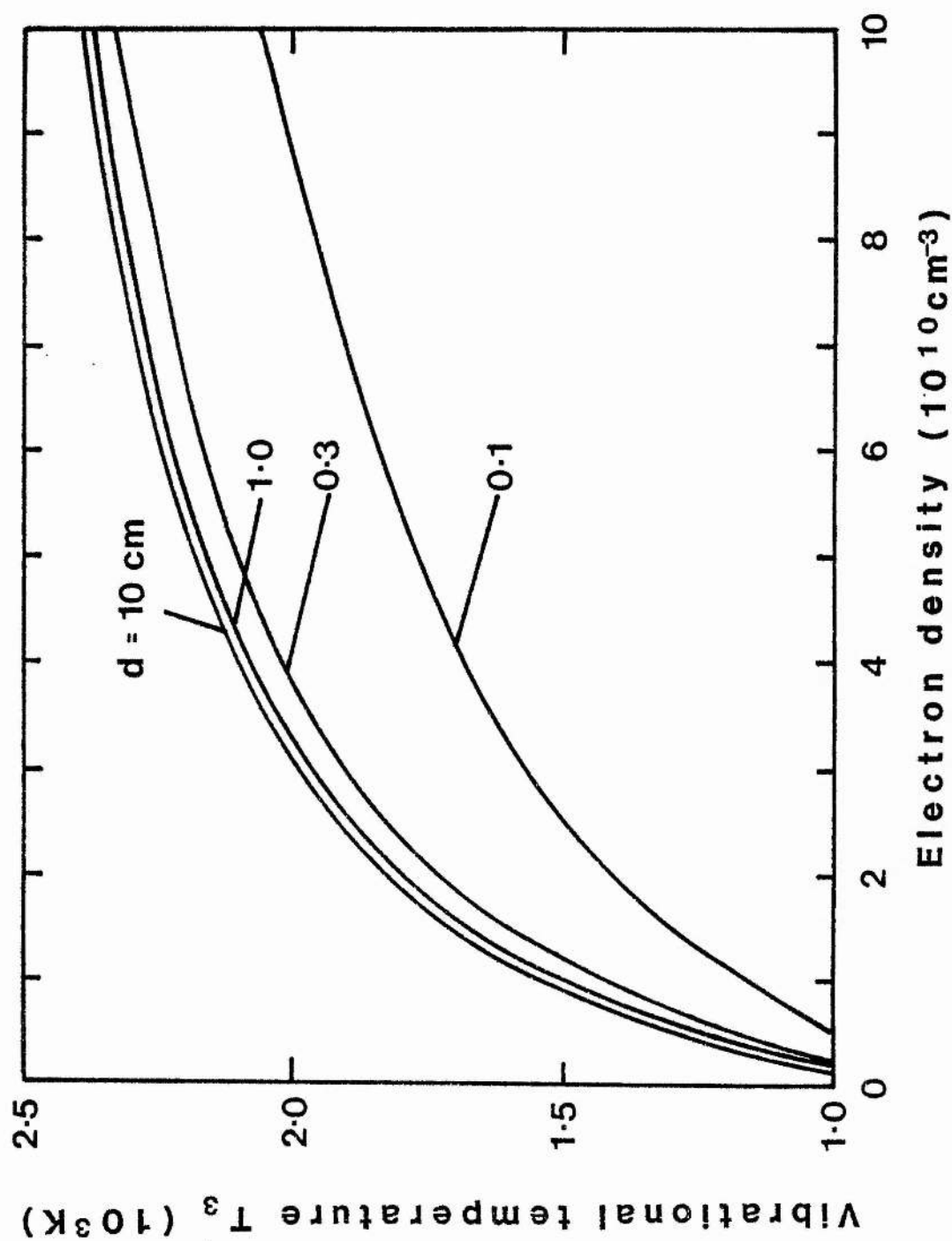


Fig. 6.17. Effect of radial diffusion on calculated axial  $T_3$  for various tube diameters (13 CO<sub>2</sub> : 9 N<sub>2</sub> : 78 He, 10 torr).

$$D(p, T) = D_o \left( \frac{T}{T_o} \right)^{\beta} \frac{p_o}{p} \quad (6.8)$$

where

$$1.75 < \beta < 2.0$$

and the subscript o indicates S.T.P. This equation was used (assuming  $\beta = 1.85$ ) to compile Table 6.3 which lists the self-diffusion and diffusion coefficients of importance in the  $\text{CO}_2$  laser system for 1 torr, 400K conditions. These data were in turn used to calculate the mixture-weighted coefficients which appear in the modified rate equations.

Calculated vibrational temperatures ( $T_3$ ) assuming various tube diameters are graphed in figure 6.17 for a  $13\text{CO}_2: 9\text{N}_2: 78\text{He}$  mixture at 10 torr total pressure. These vibrational temperature should now be regarded as the values appropriate to the centre-axis of the discharge tube. Even for the low pressure of 10 torr, the effect of radial diffusion is insignificant in 10 cm and 1 cm diameter tubes. For diameters of 0.3 cm or less, the effect of wall quenching reduces the centre-axis vibrational temperature considerably. However, since the pressure-diameter regime of practical interest is 10-30 torr cm, the neglect of radial diffusion seems justified when only axial vibrational temperatures are important. Where the radial distribution of current density is known, the radial profile of vibrational temperature can be calculated. Comparison of calculated profiles to experimental observations might provide a check on the diffusion rates and wall quenching probabilities of vibrationally excited molecules.

6.4.3 Effect of stimulated emission

Stimulated emission on the  $9 \mu\text{m}$  or  $10 \mu\text{m}$   $00^0_1$  bands will be a major perturbation to the molecular energy dynamics of  $\text{CO}_2$  laser



oscillators and high-power amplifiers. Consider an active (i.e. amplifying)  $\text{CO}_2$  laser medium subject to irradiation by a steady-state laser field of intensity  $I$  ( $\text{Wcm}^{-2}$ ). The stimulated emission rate will be

$$\rho_s = \alpha_{\text{eff}} I = \Delta N W I \quad (6.9)$$

where the effective gain coefficients  $\alpha_{\text{eff}} (\text{cm}^{-1})$  and the steady-state population inversion  $\Delta N (\text{cm}^{-3})$  are determined mainly by the composition of the active medium, the strength of pumping, and the laser intensity  $I$ .  $W$  is a constant given by

$$W = \frac{\lambda^2}{8\pi} A_{21} \frac{2}{\pi(\Delta\nu)}$$

in the pressure broadening approximation (see section 2.3). The calculation of vibrational temperatures, population inversion and effective gain in the presence of the laser field involves the computation of a new dynamic equilibrium via the solution of the modified population rate equations:

$$\frac{dn_1}{dt} \rightarrow \frac{dn_1}{dt} + \Delta N W I \quad (6.10)$$

$$\frac{dn_2}{dt} \rightarrow \frac{dn_2}{dt} - \Delta N W I \quad (6.11)$$

together with the system (5.3-5.4). For "lasing" on the  $10 \mu\text{m } 00^0_1$  band the population inversion  $\Delta N$  is that which occurs on a designated rotational-vibrational transition between the  $00^0_1$  and  $10^0_0$  levels:

$$\Delta N = \frac{2hc}{kT} \left\{ N_{001} B_2 \exp\left(-B_2 J_2 (J_2 + 1) \frac{hc}{kT}\right) - N_{100} B_1 \exp\left(-B_1 J_1 (J_1 + 1) \frac{hc}{kT}\right) \right\}$$

where the  $B_1$  are rotational constants and  $J_2 = 17$ ,  $J_1 = 18$  for the P(18) transition. In the process of solving the population rate equations for the steady-state, the population inversion  $\Delta N$  must be calculated from the current values of the vibrational temperatures  $T_2$  and  $T_3$  after each time-step. The computational procedure is described more fully in section 5.3.4.

Results showing the effect of applied laser field intensity on calculated  $T_3$  are plotted in figure 6.18. Strong "lasing" is seen to greatly reduce the vibrational temperature for a given electron density; also, the saturation of  $T_3$  with electron density is reduced. This results from the decreased importance of electron de-excitation in the presence of strong stimulated emission, which "competes" successfully for excited  $\text{CO}_2(v_3)$  molecules. The molecular energy dynamics are now dominated by electron excitation and stimulated emission. It is interesting to compute the effect of "lasing" on the  $\text{N}_2$  vibrational temperature. As seen in figure 6.19,  $T_4$  is also reduced by strong  $\text{CO}_2$  stimulated emission, but by a lesser amount, due to the large  $\text{N}_2$  vibrational excitation rate and the imperfect  $\text{N}_2\text{-CO}_2(v_3)$  coupling.

These calculations are compared to experiment in figure 6.20. The measurements are those made recently by Dang et al.<sup>19</sup>, who used a tunable diode laser to determine the  $\text{CO}_2$  asymmetric mode temperature in the presence and absence of a saturating  $10\ \mu\text{m}$  P(22) laser field with intensity approximately  $560\text{Wcm}^{-2}$ . Discharge conditions were as listed in the diagram. The shaded areas indicate the uncertainty in the calculated values due to the conversion from electron density to discharge current: the microwave measurements and Boltzmann code predictions differ by a factor of  $\sim 2$ . In the "non-lasing" case agreement between theory and experiment is good. However when a

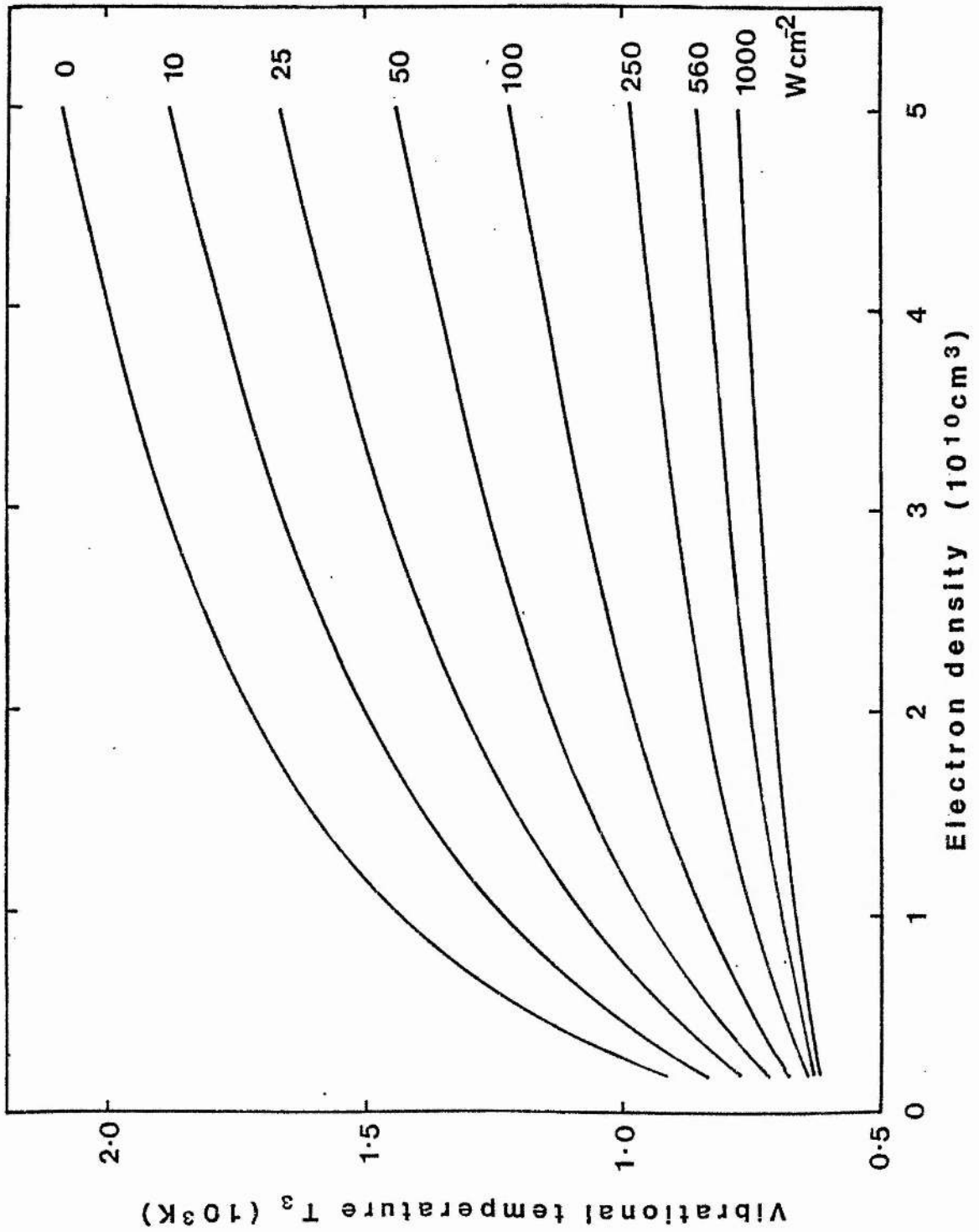


Fig.6.18. Effect of laser field intensity on calculated  $T_3$  (9 CO $_2$  : 11 N $_2$  : 80 He, 20 torr)

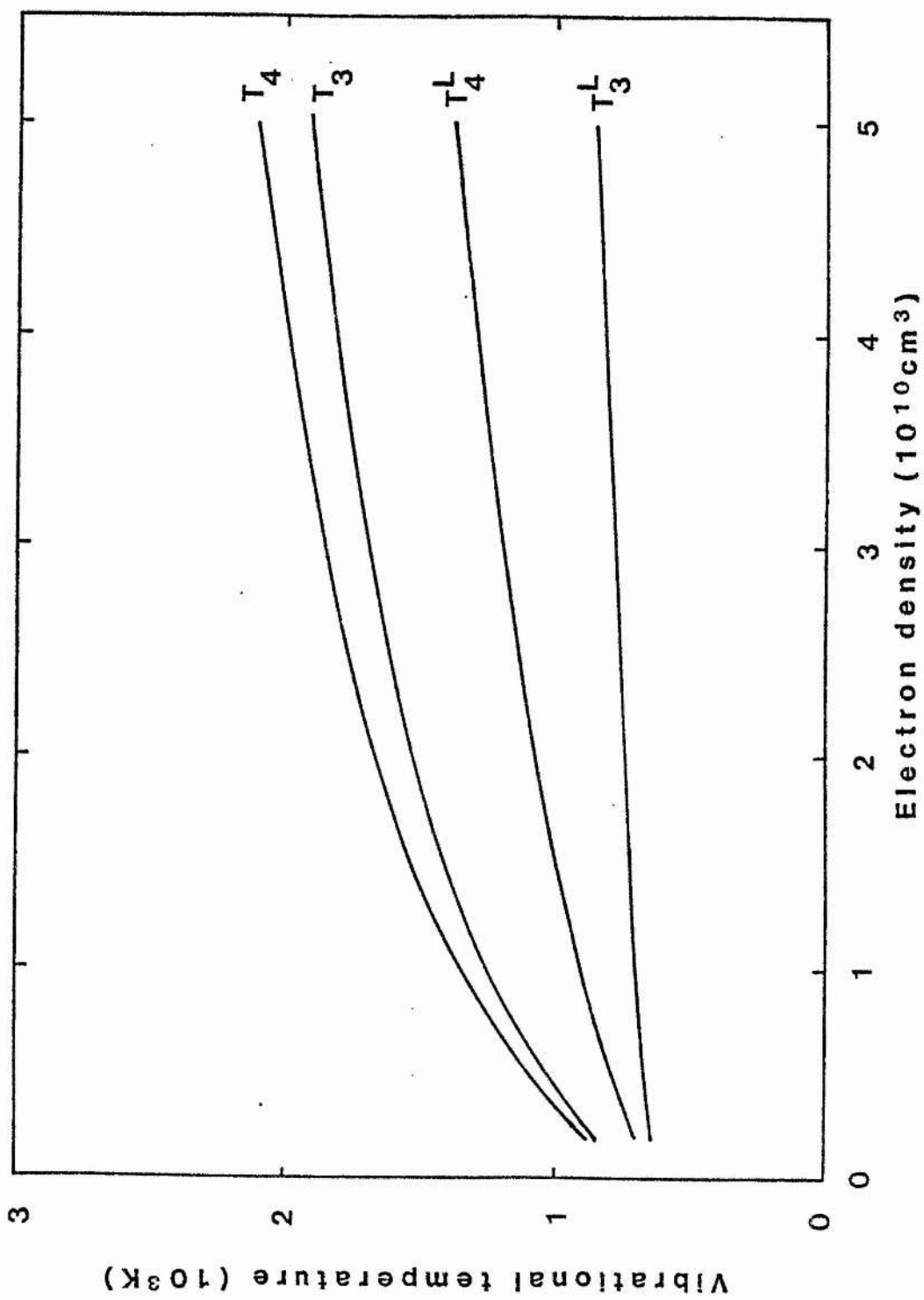


Fig. 6.19. Effect of saturating laser field ( $560 \text{ W cm}^{-2}$ ) on calculated  $T_3$ ,  $T_4$   
 (9%  $\text{CO}_2$  : 11%  $\text{N}_2$  : 80% He, 20 torr)

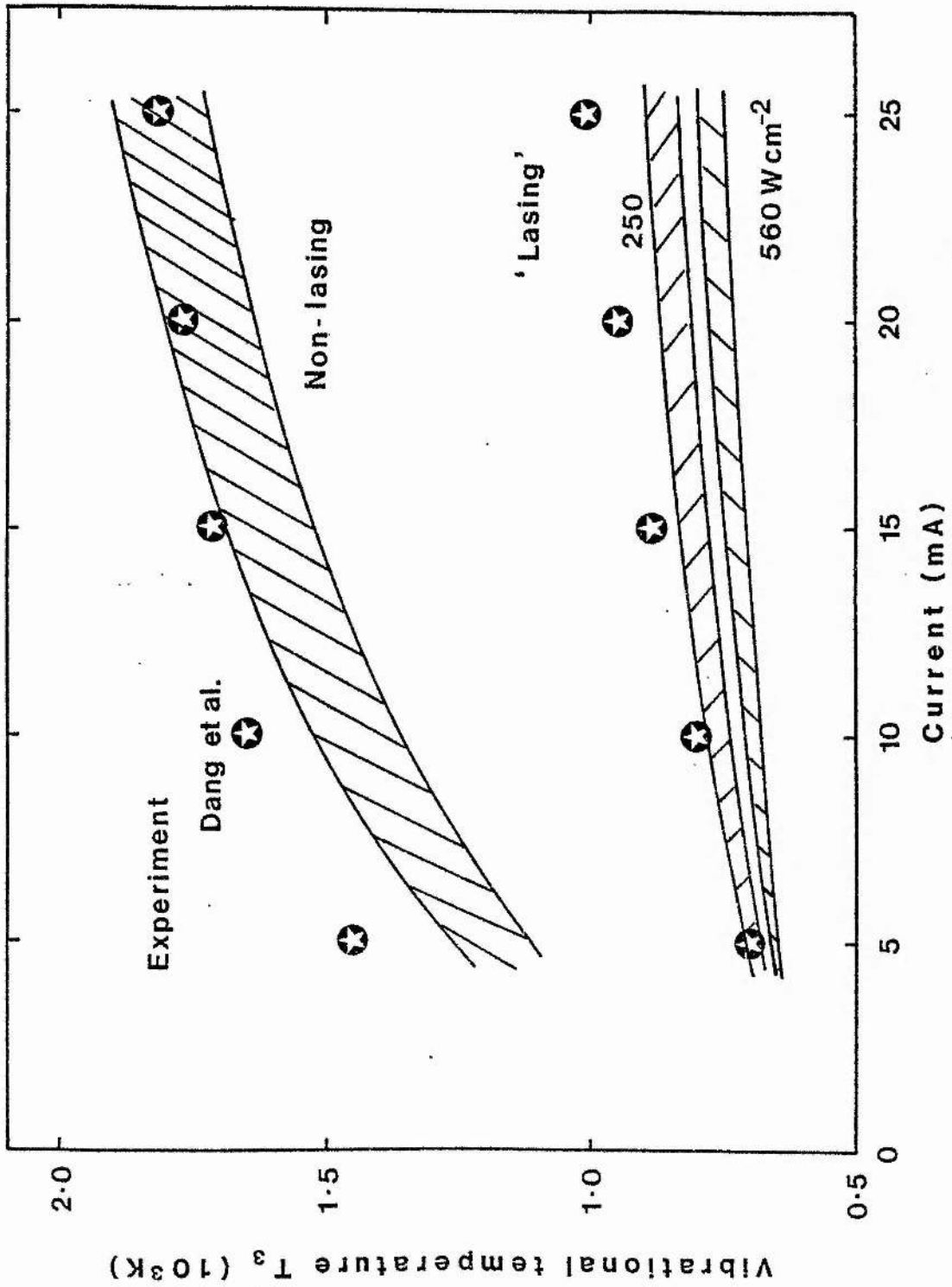


Fig. 6.20. Comparison of calculated and measured  $T_3$  in 20 torr of 9 CO<sub>2</sub> : 11 N<sub>2</sub> : 80 He in presence and absence of saturating laser field.

560Wcm<sup>-2</sup> laser field is assumed, the model underestimates the CO<sub>2</sub>(v<sub>3</sub>) temperature by several hundred degrees. This fault can be traced to the approximation of pure pressure broadening, which is good at atmospheric pressure but inaccurate at 20 torr, where the contribution of Doppler broadening should be included to produce a lineshape which is a convolution of Lorentzian and Gaussian functions. This modification would reduce the population inversion available for interaction with the laser field at line-centre, and increase the calculated "lasing" T<sub>3</sub> (T<sub>3</sub><sup>L</sup>), improving the agreement with experiment. Nevertheless, the inclusion of stimulated emission in the kinetics model yields results in reasonable agreement with experiment in the low-pressure regime.

#### 6.4.4 Consideration of third-order superelastic effects

The effects of superelastic electron collisions with excited molecules have been considered in both the BOLTZ calculations of electron energy distribution functions (E.D.F.'s) and transport coefficients, and in the VIBEX vibrational temperature calculations. However the Boltzmann code assumed molecular vibrational mode temperatures of 300K whereas the steady-state temperatures predicted by VIBEX are in the region of 1500-2500K. For self-consistency, the predicted vibrational temperatures should be "fed back" as initial values for the Boltzmann code, and the E.D.F. and excitation rates re-calculated. This would test the formal possibility that the vibrational temperature effects previously described (saturation, non-equality of N<sub>2</sub>, CO and CO<sub>2</sub>(v<sub>3</sub>) steady-states, etc.) are simply aberrations of a model which is internally inconsistent in its treatment of the electron-molecule energy balance. Therefore a series of BOLTZ runs, including

TABLE 6.4 Effect of initial vibrational temperatures on  
BOLTZOLD calculation of excitation rates and  
average electron energy  
(superelastic collisions included).

<u>Input</u>		<u>Output</u>		
$T_3, T_4$ (K)	$X_4$ ( $\text{cm}^3 \text{s}^{-1}$ )	$X_3$ ( $\text{cm}^3 \text{s}^{-1}$ )	$X_T$ ( $\text{cm}^3 \text{s}^{-1}$ )	$\bar{u}$ (eV)
300	2.55(-8)	5.5(-9)	4.20(-8)	1.60
1000	2.55(-8)	5.5(-9)	4.21(-8)	1.60
2000	2.56(-8)	5.5(-9)	4.26(-8)	1.62
4000	2.61(-8)	5.5(-9)	4.40(-8)	1.67

Note: Calculations assume a 13 CO<sub>2</sub> : 9 N<sub>2</sub> : 78 He mixture,  
with E/N = 30 Td.

the effect of superelastic collisions, was performed to examine the effect of the initially assumed vibrational temperatures on the calculated excitation rate constants and average electron energy. The calculations used a coarse mesh (BOLTZOLD) and are summarised in Table 6.4. Clearly the influence of the initial temperatures is very small and can be neglected. This confirms the self-consistency of the previous calculations and demonstrates the insensitivity of E.D.F.'s to superelastic collisions.

### 6.5 Discussion and conclusions

A broad comparison of the computed and observed behaviour of  $T_3$  in  $\text{CO}_2$  laser discharges allows several important deductions. Both in theory and experiment, the vibrational temperature saturates <sup>with</sup> increasing discharge current, and this effect limits  $T_3$  to values far lower than those which would maximise the population of the  $00^0_1$  upper laser level ( $\sim 4000\text{K}$ ) or the  $00^0_2$  upper sequence band level ( $\sim 8000\text{K}$ ). Computer model experiments have shown that the saturation is caused by electron superelastic collisions with excited molecules at a rate determined by the vibrational excitation rate and the principle of detailed balance. It is interesting to compare the theoretically determined rate to recent experimental measurements by Dang et al.<sup>19</sup> who used their tunable diode laser to monitor the recovery of discharge-excited  $\text{CO}_2(\nu_3)$  population after depletion by an intense  $10\ \mu\text{m}$  laser pulse. Measurements on a 9.2% $\text{CO}_2$ : 11% $\text{N}_2$ : 79.8% $\text{He}$  mixture at 19.4 torr revealed a  $\text{N}_2 + \text{CO}_2(\nu_3)$  mode excitation rate of  $92 \pm 8\ \text{s}^{-1}\ \text{mA}^{-1}$  and an electron de-excitation rate of  $340 \pm 35\ \text{s}^{-1}\ \text{mA}^{-1}$ . For a 13% $\text{CO}_2$ : 9% $\text{N}_2$ : 78% $\text{He}$  mixture, and assuming an axial discharge electron density of  $2 \times 10^9\ \text{electrons cm}^{-3}\ \text{mA}^{-1}$  then BOLTZ data predicts a combined  $\text{N}_2$  and



and  $\text{CO}_2(\nu_3)$  mode excitation rate of  $60\text{s}^{-1}\text{mA}^{-1}$  and a superelastic rate of  $270\text{s}^{-1}\text{mA}^{-1}$ . Thus the measured ratio of electron de-excitation/ electron excitation is  $\sim 3.7$  compared to the theoretical value of  $\sim 4.5$ , reasonable agreement which tends to support the principle of detailed balance and the superelastic averaging procedure of section 6.3.2. However the measured excitation rate is noticeably larger than the Boltzmann-code prediction. The discrepancy cannot be reduced by an upward revision of the estimated discharge electron density, since the figure of  $2 \times 10^9 \text{cm}^{-3} \text{mA}^{-1}$  already assumes that the on-axis density is twice the typical radial average value measured in Chapter 4. This suggests that the BOLTZ cross-sections for  $\text{N}_2$  and  $\text{CO}_2(\nu_3)$  vibrational excitation may be too small. Since the predictions of the vibrational kinetics model depend largely on the ratio of electron excitation/ de-excitation, considerable errors in the excitation cross-sections might produce only minor changes in the calculated vibrational temperatures, which are in good agreement with experiment.

Tunable laser diode measurements of CO vibrational temperatures <sup>15</sup> also support the computer model predictions of high  $\text{N}_2$  and CO temperatures, and the sequence band gain measurements of 6.3.3 confirm the predicted trend towards high  $\text{CO}_2(\nu_3)$  temperatures in mixtures with low  $\text{CO}_2$  content at low pressure. Some improvement in the model's treatment of stimulated emission is required, since calculations of  $T_3$  in the presence of an intense laser field are under-estimates, due to the assumption of pure pressure broadening. However the calculations illustrate clearly that "lasing" tends to remove the saturation of vibrational temperature with current. Hence superelastic collisions are of reduced importance in cw  $\text{CO}_2$  laser oscillators, where strong

stimulated emission is the dominant control on vibrational temperature. Vibrational temperature saturation imposes a limitation of small-signal gain, as discussed in Appendix D, but has little effect on the output power and efficiency of cw laser oscillators. These conclusions will not apply to pulsed TEA lasers, whose case is considered separately in the next Chapter.

References for Chapter 6

1. B.F. Gordiets, N.N. Sobolev and L.A. Shelepin, Sov. Phys. JETP, 26, 5, 1039 (1968).
2. K.R. Manes and H.J. Seguin, J. Appl. Phys. 43, 12, 5073, (1972).
3. J. Tulip, IEEE J. Quant. Electron. QE-6, 4, 206 (1970).
4. J.C. Comly, W.T. Leland, C.J. Elliott, A.M. Hunter and M.J. Kircher, IEEE J. Quant. Electron. QE-17, 9, 1786, (1981).
5. D.C. Tyte, in "Progress in Quantum Electronics", Vol. 1, (Academic Press 1970).
6. M.Z. Novgorodov, V.N. Ochkin and N.N. Sobolev, Sov. Phys. Tech. 15, 6, 977 (1970).
7. V.M. Doroshenko, N.N. Kudryavtsev and S.S. Novikov, Sov. J. Quant. Electron, 11, 7, 891 (1981).
8. D.L. Lyon, IEEE J. Quant. Electron, QE-9, 1, 139 (1973).
9. A.R. Davies, K. Smith and R.M. Thomson, J. Appl. Phys. 47, 5, 2037 (1976).
10. J. Reid and K. Siemsen, Appl. Phys. Lett., 29, 250 (1976).
11. K. Siemsen, J. Reid and C. Dang, IEEE J. Quant. Electron, QE-16, 668, (1980).
12. The factor of 2 arises as the ratio of the optical transition strengths (or square of the ratio of the transition matrix elements) which has been measured as 1.89 for the 9  $\mu\text{m}$  bands and close to 2.0 for the 10  $\mu\text{m}$  bands. See reference 11 and also J. Reid, J. Shewchun and B.K. Garside, Appl. Phys. 17, 349 (1978).
13. C. Dang, J. Reid and B.K. Garside, Appl. Phys. B. 27, 145 (1982).
14. C.E. Treanor, J.W. Rich and R.G. Rehm, J. Chem. Phys. 48, 1798 (1968).

15. J. Reid, private communication.
16. J. Mellis and A.L.S. Smith, Opt. Comm. 41, 2, 121 (1982).
17. K. Smith and R.M. Thomson in "Computer modelling of gas lasers", p.50 (Plenum Press, New York, 1978).
18. American Institute of Physics Handbook, 3rd Edition (McGraw-Hill, New York, 1972) p.2-252.
19. C. Dang, J. Reid and B.K. Garside, to be published in IEEE J. Quant. Electron. QE-19, 4, 755 (1983).
20. A.A. Mikaberidze and V.N. Ochkin, Sov. J. Quant. Electron. 1, 3, 276 (1971).

CHAPTER 7: MODELLING PULSED TE CO<sub>2</sub> LASERS.7.1 Introduction.

It has been seen that in cw laser oscillators, vibrational de-excitation by molecular collisions, superelastic electron collisions and stimulated emission are all important and will occur simultaneously. In a high pressure, pulsed, transversely-excited (TE) oscillator the situation is different: usually laser action is inhibited during the discharge current pulse by the large population excited to the CO<sub>2</sub> ( $\nu_1, \nu_2$ ) modes which contain the lower laser levels. This population relaxes after the end of the excitation pulse on a time-scale which is pressure dependent, but on the order of 1  $\mu$ s. Only then does laser oscillation occur. Under these circumstances, superelastic de-excitation during the current pulse should limit the vibrational energy available for subsequent stimulated emission, and thereby crucially affect the operating characteristics of the TE oscillator. This scenario is investigated below.

7.2 Background.

The high excitation efficiency of the CO<sub>2</sub> laser is mainly due to the large N<sub>2</sub> and CO<sub>2</sub> ( $\nu_3$ ) cross-sections for vibrational excitation by electron impact, and was first enumerated by Nighan<sup>1</sup>, Nighan and Bennett<sup>2</sup> and Lowke et al.,<sup>3</sup> who used Boltzmann codes to calculate electron distribution functions and to estimate the fractional power lost by discharge electrons to various inelastic processes in the CO<sub>2</sub> - N<sub>2</sub> - He system. Their calculations predict that, at typical E/N, 50% - 80% of the electrical input power is used usefully in N<sub>2</sub> and CO<sub>2</sub>( $\nu_3$ ) vibrational excitation (i.e. the excitation efficiency  $\eta_{ex} = 50 - 80\%$ ). Allowing for the quantum efficiency of the CO<sub>2</sub> 10  $\mu$ m transition ( $\eta_q = 41\%$ ) and assuming that optical cavity and other losses

are small, predicted laser radiation yield efficiencies ( $\eta_y = \eta_{ex} \eta_q$ ) are in the range of 20% - 33%. Such laser efficiencies have been approached in practice, but many observers have reported a deterioration in laser performance with increasing discharge excitation. Ballik et al.<sup>4</sup> considered the reduction in pumping efficiency experienced in a low-pressure TE resistor-pin amplifier, and concluded that the mechanism responsible was not connected to the well-known effects of gas heating or discharge instability. Explanations<sup>5</sup> involving the "overpumping" of  $N_2$  and  $CO_2$  ( $v_3$ ) vibrational temperatures to above the optimum 4000 K have been precluded by the vibrational temperature saturation described previously. Indeed sequence band gain experiments by Dang et al.<sup>6</sup> on a 92 torr TE amplifier revealed a strong saturation of  $T_3$  as measured at the time of peak gain. The only measurements of vibrational temperatures in atmospheric pressure (TEA) discharges have been those of Lavigne et al.<sup>7</sup> which are restricted to low input energies and show little evidence of  $T_3$  saturation. Nevertheless it is clear that vibrational temperature saturation with increasing input energy could degrade the operating efficiency of high pressure TE lasers. To test this idea a series of time-resolved vibrational temperature calculations were made using the computer model.

### 7.3 Computer Modelling.

#### 7.3.1 Method

The methods employed to calculate the time evolution of vibrational temperatures for high-pressure pulsed excitation were very similar to those described previously in the low-pressure cw modelling. However, to ensure smooth and accurate computation the time-step size was reduced (to  $1 \times 10^{-8}$  sec. for the first few steps) and the assumed initially excited populations were adjusted to correspond to initial  $N_2$

and  $\text{CO}_2$  ( $\nu_3$ ) temperatures of 300 K. The calculations assumed a current pulse of square profile, with constant electron density ( $n_e$ ) and effective electric field ( $E/N$ ). As before, electron density could be scaled to a more measurable experimental parameter, namely the specific discharge energy input,  $E_{in}$  ( $\text{J l}^{-1} \text{atm}^{-1}$ ). In principle the conversion can be achieved using knowledge of the electrical excitation pulse length and current density by the current transport equation

$$j = en_e v_d \quad (7.1)$$

where the electron drift velocity  $v_d$  is around  $5 \times 10^6 \text{ cm s}^{-1}$  for  $\text{CO}_2$  laser mixtures at normal  $E/N$ . The current density  $j$  is determined by the storage capacitance and charging voltage of the excitation circuit, and the cross-sectional area through which the main discharge current flows. Unfortunately this cross-section is difficult to measure or estimate. For example Dang et al. used the resistor-pin configuration described by Ballik et al.<sup>4</sup> as having a total discharge length variable between 23 and 92 cm, formed by resistors 3.8 mm apart. This arrangement renders any estimate of discharge cross-section very uncertain. Another conversion method was therefore preferred, in which the electron density was related to the input discharge energy by:

$$\eta_{ex} E_{in} = \Delta t n_e (h\nu_4 X_4 N_4 + h\nu_3 X_3 N_3) \quad (7.2)$$

where  $X_3$  and  $X_4$  are the  $\text{CO}_2$  ( $\nu_3$ ) and  $\text{N}_2$  vibrational excitation rates, the  $h\nu$ 's are vibrational mode quanta and the  $N$ 's are total number densities of  $\text{CO}_2$  and  $\text{N}_2$  molecules normalised to 1 atmosphere total pressure.  $\Delta t$  is the current pulse duration in seconds and  $\eta_{ex}$ , the fraction of total input energy which goes to  $\text{N}_2$  and  $\text{CO}_2$  ( $\nu_3$ ) excitation, is taken as 60% from the work in reference 3. For a given  $E/N$ , pulse length and gas mixture, equation 7.2 implies a linear relationship between the electron density ( $n_e$ ) and the input energy density ( $E_{in}$ ).

Given a 13% CO<sub>2</sub> : 9% N<sub>2</sub> : 78% He mixture, E/N = 30 Td and Δt = 200 ns, we obtain

$$E_{in} = 1.33 \times 10^{-12} n_e$$

for  $n_e$  in (cm<sup>-3</sup>) and  $E_{in}$  (J l<sup>-1</sup> atm<sup>-1</sup>).

### 7.3.2 Results

Short pulse (Δt ~ 100 ns), atmospheric pressure conditions are typical of modern photopreionised TE lasers. Computed vibrational temperature time evolutions for such conditions are shown in figure 7.1. The assumed electron density during the excitation pulse was  $n_e = 1.5 \times 10^{14}$  cm<sup>-3</sup>, corresponding to a specific energy input of 100 J l<sup>-1</sup> atm<sup>-1</sup>. Due to the larger N<sub>2</sub> excitation rate, T<sub>4</sub> > T<sub>3</sub> throughout the current pulse. In the period following current switch-off, N<sub>2</sub> - CO<sub>2</sub> (ν<sub>3</sub>) V - V exchange tends to equilibriate T<sub>4</sub> and T<sub>3</sub> in about 1.5 μs. The CO<sub>2</sub> (ν<sub>1</sub>, ν<sub>2</sub>) temperature relaxes on about the same time-scale, resulting in the clearance of population from the lower laser level. Thus 1.5 μs is the time of maximum population inversion and peak laser gain. Figure 7.2 shows comparable results for 92 torr, 200 ns and 760 torr, 3 μs pulses, chosen to simulate the conditions of Dang et al. and Lavigne et al. respectively. The lower pressure results in a longer time for T<sub>3</sub> - T<sub>4</sub> equilibration, and the predicted peak gain time is now 10 - 15 μs, comparing well with the experimentally observed time of 15 μs. By contrast, at atmospheric pressure the predicted peak gain time is 4 - 5 μs despite the relatively long (3 μs) current pulse. This prediction also agrees well with the observed value of 4 μs (see figure 4 of reference 8). It is noticeable that the longer current pulse produces less heating of the CO<sub>2</sub> (ν<sub>1</sub>, ν<sub>2</sub>) mode, since bending mode → ground state deactivating collisions are very effective on the microsecond time-scale.



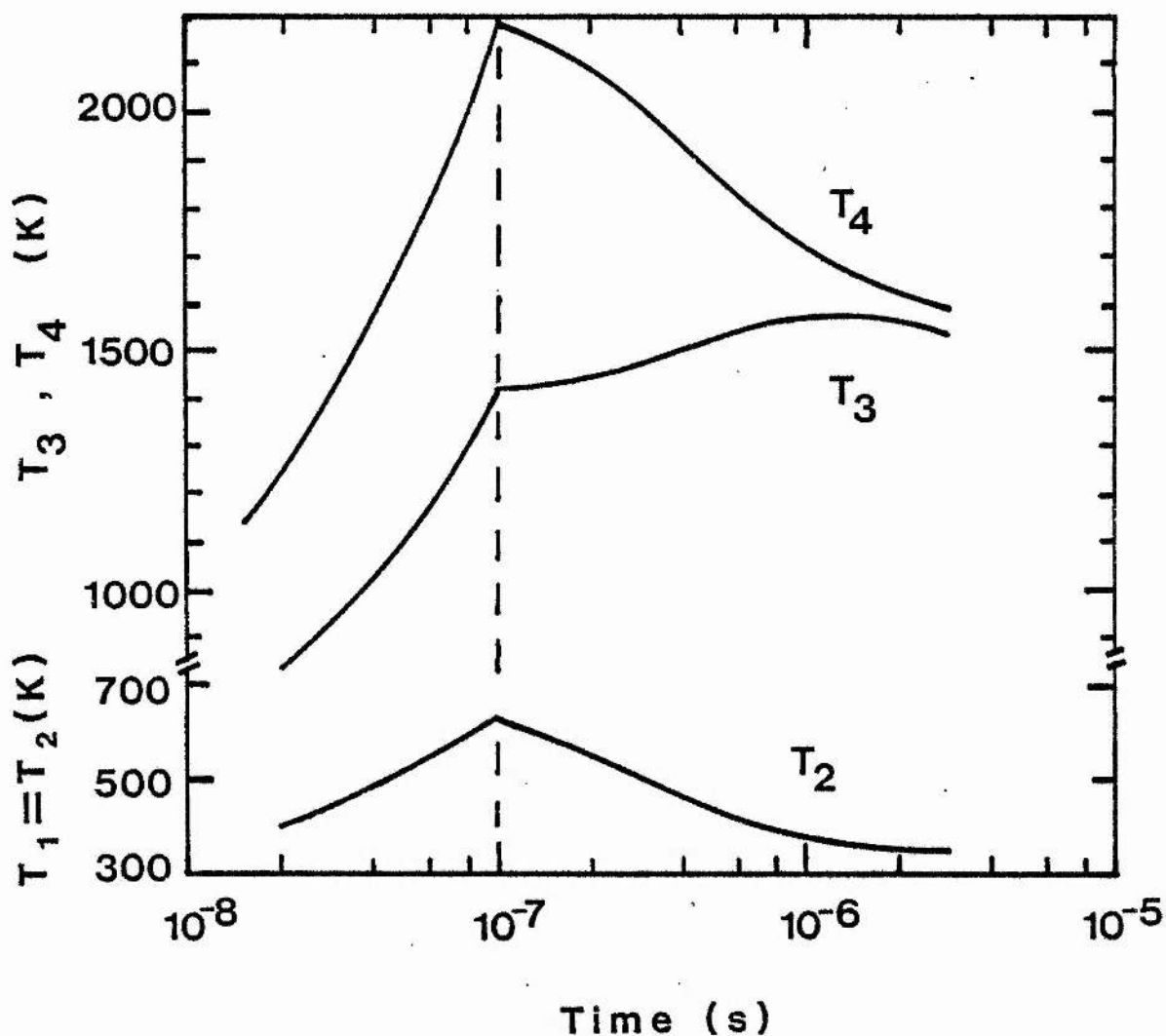


Fig. 7.1. VIBEX calculation of vibrational temperature time evolutions in  $^{13}\text{CO}_2 : 9\text{N}_2 : 78\text{He}$  mixture at atmospheric pressure. The dashed line indicates the end of the electrical excitation pulse, which was assumed to be "square" with a constant electron density of  $1.5 \times 10^{14} \text{ cm}^{-3}$  and  $E/N = 30 \text{ Td}$ , giving an input energy  $E_{\text{in}} = 100 \text{ J l}^{-1} \text{ atm}^{-1}$ .

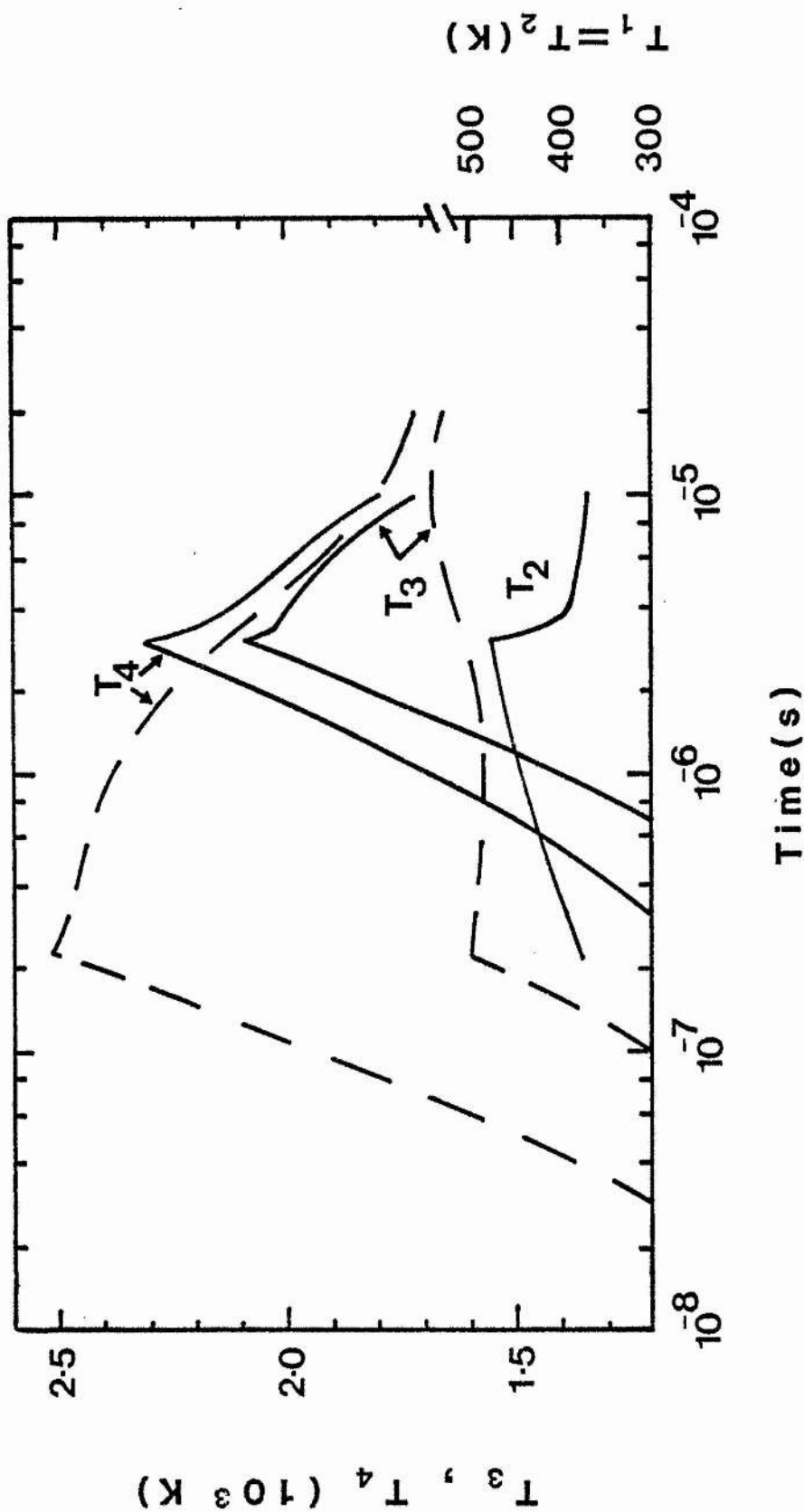


Fig. 7.2. Calculated vibrational temperatures in  $^{13}\text{CO}_2 : 9\text{N}_2 : 78\text{He}$  gas mixture assuming 200ns, pulse at 92 torr pressure ( $E_{\text{in}} = 133 \text{ J } \ell^{-1} \text{ atm}^{-1}$ , dashed curves) and 3  $\mu\text{s}$  pulse at 760 torr ( $200 \text{ J } \ell^{-1} \text{ atm}$ , solid curves).

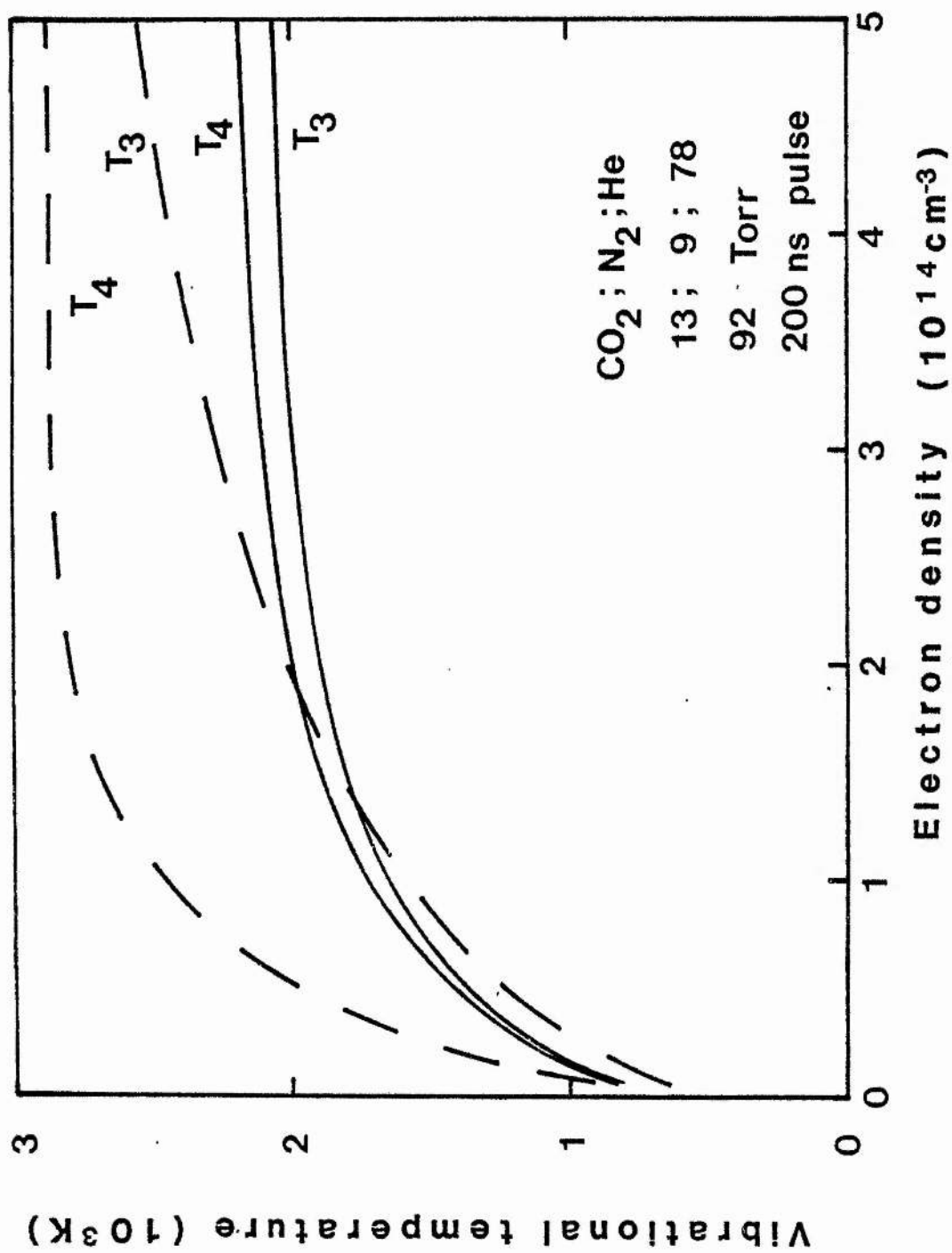


Fig. 7.3. Calculated vibrational temperatures at end of excitation pulse (dashed) and at time of peak gain (15  $\mu$ s, solid curves).

Several series of time-evolution calculations were performed and it was found that varying the electron density (input energy) caused little variation in the time of peak gain. Figure 7.3 shows  $N_2$  and  $CO_2$  ( $\nu_3$ ) temperatures for the 92 torr conditions, both at the end of the current pulse and at peak-gain time. In each case strong saturation is predicted for  $E_{in} > 200 J \ell^{-1} atm^{-1}$ . As before, the  $N_2$  is most affected due to the large  $N_2$  vibrational cross-section. Conversely at  $t = 200 ns$ ,  $T_3$  is least affected. However, at  $t = 15 \mu s$ , considerable  $N_2 - CO_2$  ( $\nu_3$ ) energy exchange has occurred and the  $T_3$  saturation is more severe. These calculations are compared to the experiment of Dang et al. in figure 7.4. Also plotted (curve a) is a comparison of theory and experiment for the conditions of Lavigne et al. whose measurements were limited to low energy. In both cases, agreement between calculations and measurements is excellent. Curve (c) is a calculation for the 1 atm, 100 ns conditions for which no measurements are available. The similarity between the three curves suggests that  $E_{in}$  ( $J \ell^{-1} atm^{-1}$ ) is a reasonable scaling parameter over the range of pressure and pulse length.

The temperatures  $T_3$  and  $T_4$  are easily converted to estimate the total energy stored in the  $N_2$  and  $CO_2$  ( $\nu_3$ ) modes

$$\begin{aligned}
 E_s &= h\nu_3 N_3 \frac{x_3}{1-x_3} + h\nu_4 N_4 \frac{x_4}{1-x_4} \\
 &= E_3 + E_4
 \end{aligned}
 \tag{7.3}$$

where the symbols have their previous meanings.  $E_3$ ,  $E_4$  and  $E_s$  are plotted for the 92 torr conditions in figure 7.5, which displays both the effects of superelastic collisions (saturation of  $E_s$  with increasing  $E_{in}$ ) and V-T molecular collisions (decreasing  $E_s$  with

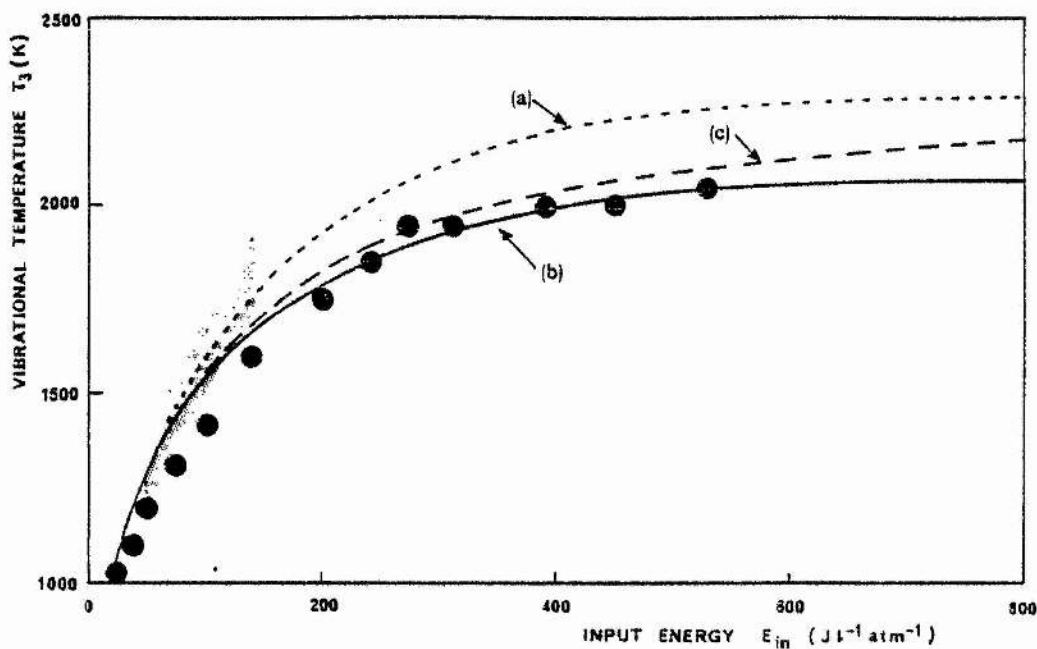


Fig. 7.4. Calculated  $CO_2$  asymmetric mode temperatures ( $T_3$ ) at time of peak gain for 13  $CO_2$  : 9  $N_2$  : 78 He mixture: (a) 760 torr, 3  $\mu s$  excitation pulse, and corresponding experimental results of Lavigne et al. (20 : 10 : 70 mix, shaded area); (b) 92 torr, 200ns pulse and corresponding results of Dang et al. (13 : 10 : 77, solid symbols); (c) 760 torr, 100ns pulse typical of U.V. pre-ionised lasers.

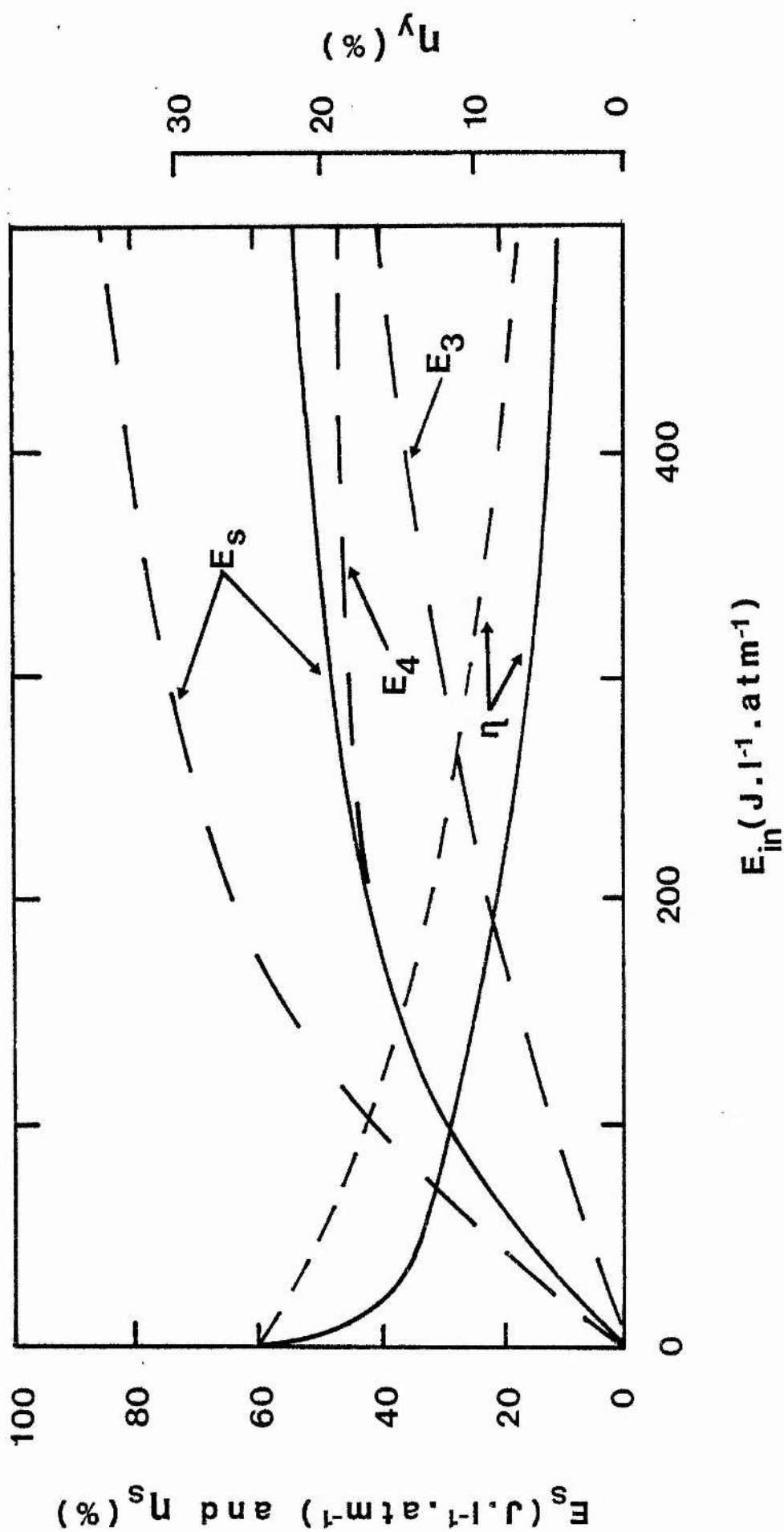


Fig. 7.5. Energy storage and storage efficiencies in 13:9:78 mixture for 92 torr pressure both at the end of the excitation pulse ( $t = 200ns$ , dashed curves) and  $t = 20 \mu s$  (solid curves).

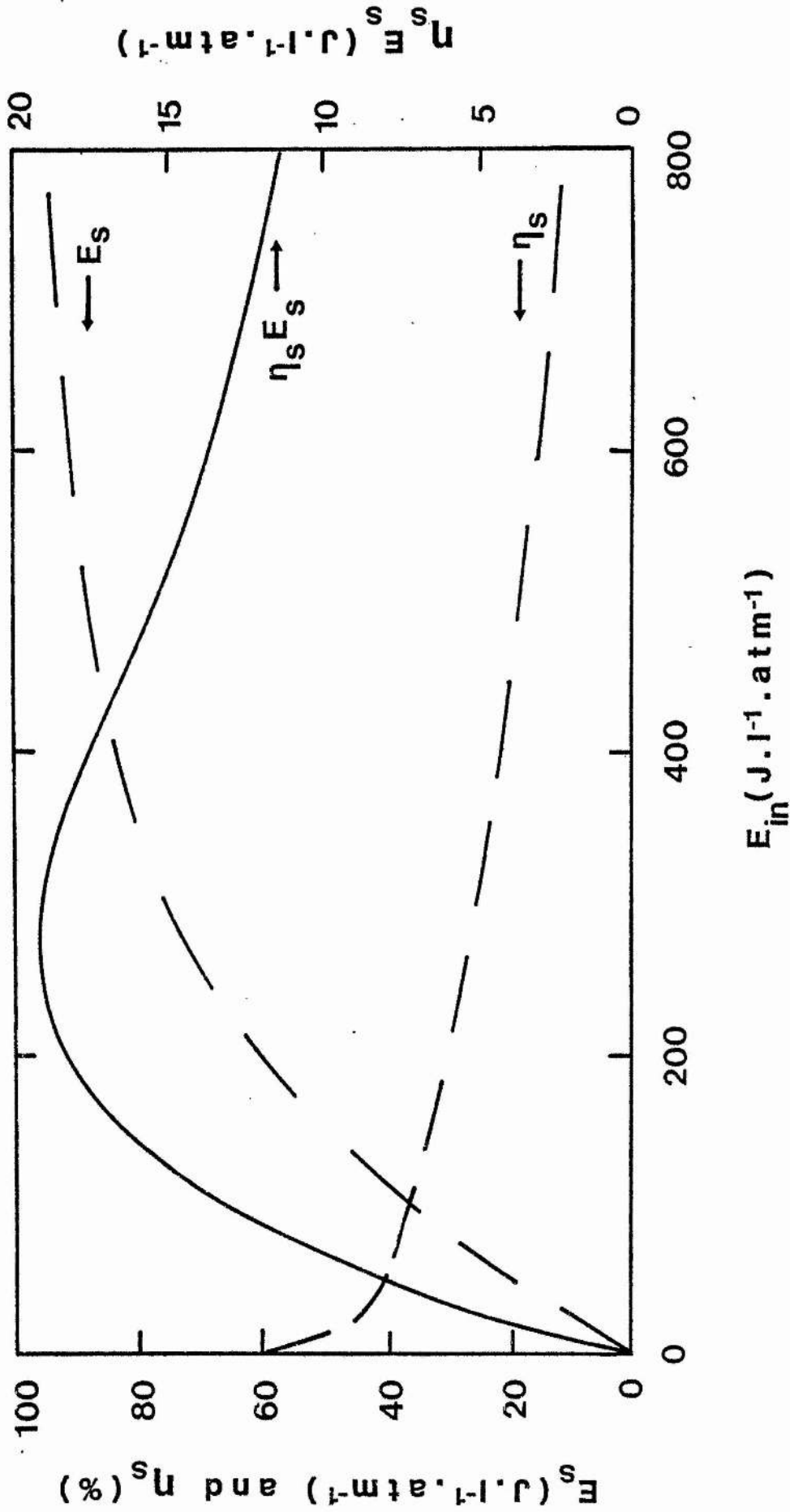


Fig. 7.6. Energy storage and storage efficiency in atmospheric pressure 13:9:78 mix at end of excitation pulse ( $t = 3 \mu s$ ). Also shown is the efficient storage figure of merit  $\eta_s E_s$ .

time after the excitation pulse). The slope of the  $E_s$  curves at low input energy approaches 60%, the assumed excitation efficiency. This suggests the use of an energy storage efficiency,  $\eta_s = E_s/E_{in}$ , which is also shown in the diagram, and which falls rapidly to ~20% at  $E_{in} = 200 \text{ J } \ell^{-1} \text{ atm}^{-1}$ . The storage efficiency is related to the laser radiation energy yield by the quantum efficiency:

$$\eta_y = \eta_q \eta_s = 0.41\eta_s \quad (7.5)$$

Thus, for  $E_{in} = 200 \text{ J } \ell^{-1} \text{ atm}^{-1}$  figure 7.5 predicts  $\eta_y \sim 8\%$ . This is far below the 20 - 33% efficiency predicted by a simple excitation analysis, but corresponds well to values realised in typical modern lasers.

In a working laser both high efficiency and high output energy are usually desirable. Therefore the product  $\eta_s E_s$  is a useful figure of merit to describe the efficiently stored system energy. This is plotted in figure 7.6 for the Lavigne et al. conditions and is a maximum for  $E_{in} = 260 \text{ J } \ell^{-1} \text{ atm}^{-1}$ , which is therefore an optimum excitation level. In practice, the optimum electrical input energy will also depend on charging circuit and optical cavity losses. These will impose an energy input threshold below which laser oscillation does not occur.

#### 7.4 Conclusions.

The model calculations are a valuable guide to optimum excitation levels and realisable TE laser operating efficiencies. Clearly the degradation of laser efficiency by superelastic collisions is severe, even in the normal working regime of input energy; this effect should be included in any accurate model of the  $\text{CO}_2$  kinetic system, and in the modelling of other pulsed gas laser systems where discharge



excitation and stimulated emission are not simultaneous. Predictions of laser efficiency based on the work of Nighan and Lowke et al. are over-simple and can be misleading.

The present work suggests that a fruitful approach to high-efficiency TE laser operation might be the use of long excitation pulses (which allow the relaxation of lower laser level population) and produce concurrent excitation and stimulated emission. Such high-efficiency long-pulse operation has been reported<sup>9</sup>, but it is not yet clear that the high efficiency is attributable to an overlap of the excitation and laser output pulses.

Some additional calculations and a summary of the TE modelling work are presented in reference 10, included here as Appendix E.

References for chapter 7.

1. W.L. Nighan, Appl. Phys. Lett. 15, 355 (1969).
2. W.L. Nighan and J.H. Bennett, Appl. Phys. Lett. 14, 240, (1969).
3. J.J. Lowke, A.V. Phelps and B.W. Irwin, J. Appl. Phys. 44, 4664 (1973).
4. E.A. Ballik, B.K. Garside, J. Reid and T. Tricker, J. Appl. Phys. 46, 1322 (1975).
5. A.R. Davies, K. Smith and R.M. Thomson, J. Appl. Phys. 47, 2037, (1976).
6. C. Dang, J. Reid and B.K. Garside, I.E.E.E. J. Quant. Electron, QE - 16, 1097 (1980).
7. P. Lavigne, J.L. Lachambre and G. Otis, J. Appl. Phys. 49, 3714 (1978).
8. J.L. Lachambre, J. Gilbert, F. Rheault, R. Fortin and M. Blanchard, I.E.E.E. J. Quant. Electron. QE - 9, 459 (1973).
9. M.J. Pechersky and R.J. Spreadbury, paper K - 1, 35th Gaseous Electronics Conference, Dallas, October, 1982.
10. A.L.S. Smith and J. Mellis, Appl. Phys. Lett. 41, 1037, (1982).

CHAPTER 8 : OPERATING CHARACTERISTICS OF CO<sub>2</sub> SEQUENCE  
BAND LASERS

8.1 Introduction

Thirty -six new lines in the 9-11  $\mu\text{m}$  wavelength region were observed in continuous emission from a CO<sub>2</sub> laser by Reid and Siemsen<sup>1</sup> in 1976. The lines were identified as rotational-vibrational transitions in the  $00^{\circ}2 - (10^{\circ}1, 02^{\circ}1)_{\text{I}}$  and  $00^{\circ}2 - (10^{\circ}1, 02^{\circ}1)_{\text{II}}$  bands, that is, the  $00^{\circ}2$  "sequence" bands. These behave similarly to the fundamental  $00^{\circ}1$  CO<sub>2</sub> bands, consisting of P and R branches with alternate J values missing, and a room temperature maximum gain in the region  $J = 19$ . However, the anharmonicity of the anti-symmetric stretch vibration in the CO<sub>2</sub> molecule causes the sequence lines to appear between the fundamental lines in frequency space (see figure 8.1) and the usual selection rules, when applied to the  $00^{\circ}2$  bands, allow only transitions with odd J values in the lower level.

The initial measurement of  $00^{\circ}2$  sequence band lasing produced sub-watt power levels from a conventional flowing gas CO<sub>2</sub> laser operated with a gas mixture of 15%CO<sub>2</sub>: 20%N<sub>2</sub>: 65%He at around 10 torr. However the only lines observed in the unmodified cavity were P(37) - P(43) of the 10  $\mu\text{m}$  branch, despite the fact that lines below P(37) were calculated to be above threshold. This was attributed to the lack of sufficient laser cavity wavelength discrimination to separate the weak sequence lines from their stronger fundamental band neighbours. The problem was partially overcome by the insertion of a 2mm-thick uncoated ZnSe etalon in the cavity, allowing the suppression of unwanted fundamental lines and resulting in the oscillation of additional sequence lines.

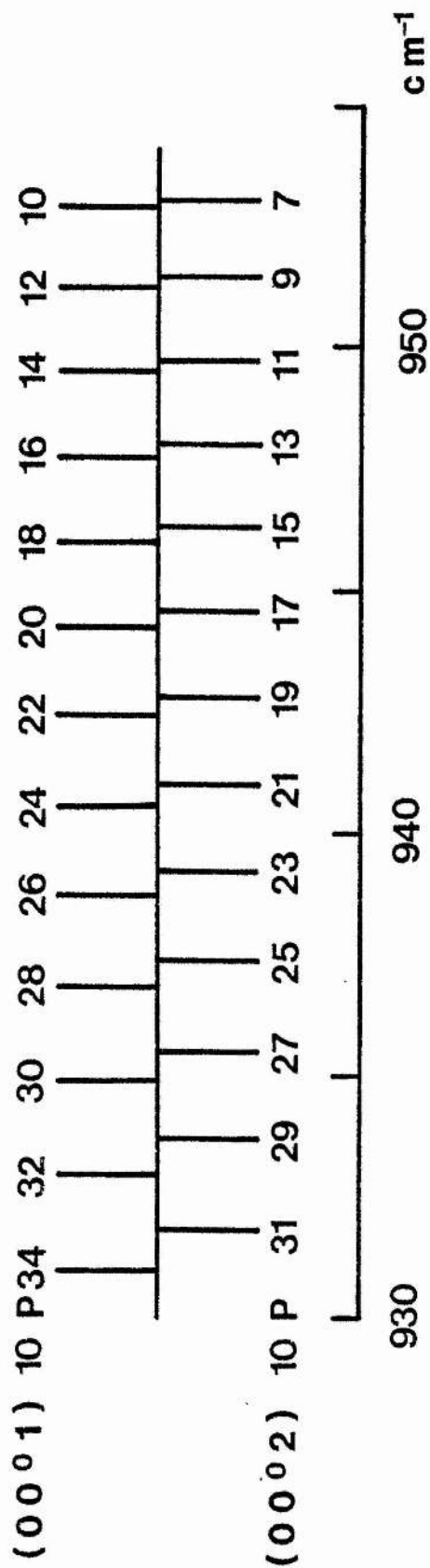


Fig. 8.1. Wavelengths of principal 10 μm P-branch laser transitions on the 00<sup>0</sup>1 and 00<sup>0</sup>2 bands (data from reference 1).

A much more efficient suppression technique<sup>2,3</sup> involves the use of an intra-cavity  $\text{CO}_2$  hot-cell. By heating the  $\text{CO}_2$  to a temperature of 300-500 °C, a large population is thermally excited to the  $10^0_0$  and  $02^0_0$  levels ( $\sim 1300 \text{ cm}^{-1}$  above ground state), and this introduces large absorption losses on the fundamental band laser transitions. Such temperatures have little effect on the population of the  $10^0_1$  and  $02^0_1$  levels ( $\sim 3700 \text{ cm}^{-1}$  above ground state) and therefore produce negligible absorption on the sequence band transitions. The hot-cell technique can induce a conventional  $\text{CO}_2$  laser to oscillate exclusively on the  $00^0_2$  sequence bands. A combination of hot-cell and diffraction grating has also allowed laser oscillation on the  $00^0_3 - (10^0_2, 02^0_2)_1$  sequence band.<sup>3</sup> The principle of intra-cavity absorption is not restricted to the use of hot  $\text{CO}_2$ ; room temperature  $\text{NH}_3$  has also been used as a  $00^0_1$  band suppressant<sup>4</sup> by taking advantage of fortuitous  $\text{CO}_2$ - $\text{NH}_3$  line coincidences.

Absorption in  $\text{CO}_2$  provides an important method of identifying the sequence lines, since the small frequency difference between  $00^0_1$  and  $00^0_2$  transitions make identification by frequency dispersion rather difficult. However if fundamental band radiation is passed through a cell containing low pressure  $\text{CO}_2$ , strong fluorescence at  $4.3 \mu\text{m}$  is emitted by molecules which are excited to the  $00^0_1$  level before decaying radiatively to ground state. Sequence band lines are not absorbed, produce no fluorescence in  $\text{CO}_2$  and can be thus distinguished from fundamental lines.

## 8.2 Recent Background

Recently much improved sequence band power and energy outputs have been reported in the literature. Reid and Siemsen<sup>3</sup> have

obtained 10 watts on the P branch of the  $10.4 \mu\text{m } 00^0_2$  band from a cw laser (140 cm active length) operating at 16mA in 5 torr of a  $14\% \text{CO}_2$ :  $20\% \text{N}_2$ :  $66\% \text{He}$  mixture. Using a low loss resonator, including a 98% reflecting output coupler, they observed a total of 86 lines in oscillation in the  $00^0_2$  sequence bands. By comparison, the strongest fundamental band line gave 16 watts under the same conditions. Optimising the discharge for the fundamental bands gave a maximum power of 20W on the 10P(20) line. Sequence band laser efficiency was therefore 60% of that obtainable on the  $00^0_1$  bands; in a longer, more powerful laser this relative efficiency might be improved, dependent on gain saturation as a function of laser intensity for the sequence band. This subject has so far received no attention, but will be discussed later.

Sequence band oscillation in pulsed TE lasers was obtained nearly simultaneously by Feldman et al.<sup>5</sup> and Lavigne et al.<sup>6</sup> In the first case a hot  $\text{CO}_2$  cell was used in a cavity containing a pulsed low pressure discharge as well as the main gain cell which was an ultra-violet preionised 3-atmosphere discharge (154 cm long, 3.5 cm aperture). With the low pressure discharge providing temporal smoothing, 100mJ single-line sequence band pulses were observed on all lines from 10P(13) to 10P(25). Pulse length was approximately 80ns FWHM. Electrical input energy and laser efficiency were not reported. By contrast, Lavigne's group used two different methods to discriminate against fundamental band lasing in a 100 cm long, atmospheric TEA module. The conventional hot cell technique was employed to produce sequence pulses of 185 mJ total energy at an excitation level of  $125 \text{ J l}^{-1}$  in a  $20\text{CO}_2$ :  $10\text{N}_2$ :  $70\text{He}$  mixture. For this excitation energy it was estimated that about  $7\text{J}(19 \text{ J l}^{-1})$  of optical energy was

stored in the active volume, and therefore the laser yield efficiency on the sequence bands (optical energy out/electrical energy in) was around 0.5%. Such poor performance was attributed to the high insertion losses of the hot CO<sub>2</sub> filter cell, due to sequence band absorption at cell pressures above 150 torr caused by the pressure broadened wings of 00<sup>0</sup>1 fundamental and 01<sup>1</sup>0 hot band lines. A second method of band discrimination was therefore introduced, involving the removal of the hot cell and the use of Michelson interferometer as the output coupler. In this case the active discharge length was limited to 33 cm to prevent damage to the optical components in the interferometer; nevertheless for an energy input of 200 Jℓ<sup>-1</sup>, a laser output energy of 140mJ(1.7 Jℓ<sup>-1</sup>) was reported, corresponding to a laser efficiency nearly twice that obtained using hot-cell quenching. It was concluded that hot cell losses are so large as to necessitate the use of oscillator-amplifier combinations to generate high energy sequence band pulses. However, Brimacombe et al <sup>7</sup> have obtained multi-Joule sequence pulses from a 100 cm discharge TEA laser using an in-cavity hot cell. This important performance improvement was obtained using relatively long (~1 μs) current pulses to excite a 12%CO<sub>2</sub>: 20%N<sub>2</sub>: 68%He gas mixture at an energy loading of 135 Jℓ<sup>-1</sup>atm<sup>-1</sup>, and by limiting the hot cell CO<sub>2</sub> pressure to 450 torr to minimise absorption at sequence band frequencies. Maximum sequence output energy was 6 J per pulse (4.5 Jℓ<sup>-1</sup>atm<sup>-1</sup>) with 10P(15) and 10P(17) lasing simultaneously in the non-selective cavity. This represents a laser yield efficiency of ~3.5%, and demonstrates that conventional TEA CO<sub>2</sub> lasers can be converted to efficient operation on the sequence transitions by the inclusion of an

in-cavity hot cell, contrary to the conclusions of Ref. 6. Careful design of the laser is crucial, however. In particular, the maximum optical energy extractable on the sequence bands depends on the difference between the vibrational temperature of the  $\text{CO}_2(\nu_3)$  mode at the beginning and end of the optical pulse, when the sequence band gain has dropped below the threshold for oscillation.<sup>8</sup> High cavity losses therefore have the result that a substantial portion of the energy initially stored in the upper laser levels in the vibrationally excited  $\text{N}_2$  cannot be extracted. This residual energy can be minimised (i) by ensuring that the initial value of  $T_3$  is as high as possible, and (ii) by reducing unwanted optical cavity losses.

High vibrational temperatures and low optical losses are also requirements for the efficient operation of cw sequence band lasers, as will be shown.

### 8.3 Operating characteristics of a cw $\text{CO}_2$ laser on the $00^0_2$ sequence band

#### 8.3.1 Experimental arrangement and initial results

The characteristics of  $\text{CO}_2$   $00^0_2$  band cw oscillation were studied using the laser shown schematically in Figure 6.1. The active length was 80 cm, formed by a twin-arm discharge in a silica tube of 1 cm internal diameter, enclosed by a water cooling jacket and a gas ballast volume. The tube was sealed by a ZnSe Brewster-angle window and a gold-coated total reflector of 5 m radius of curvature. An intra-cavity hot cell was used; this was of simple construction, using a 2 cm diameter quartz tube as a mandrel for externally wound Nichrome heating coils. The number of turns per centimetre increased from the centre outwards to achieve a more uniform axial temperature profile. Ring-shaped water jackets pro-



tected against any heating of the KCl Brewster-angled sealing windows. The total heated cell length was 17 cm and thermocouple measurements indicated an internal temperature of 450 °C at "full power", i.e. with 260 volts applied across the heater windings. Optical output coupling was by a flat partial reflector (normally  $R = 94\%$ ) mounted on a ceramic piezo-electric translator (PZT). The overall length of the Invar-stabilised laser cavity structure was 157 cm. Further laser constructional details can be found in Reference 9.

Figure 8.2 illustrates the dependence of the laser output on the hot-cell pressure. The laser mixture was  $1\text{CO}_2 : 2\text{Xe} : 3\text{N}_2 : 10\text{He}$  at variable total pressure. For an oscillator pressure of 32 torr, increasing the hot cell pressure caused a continuous fall in laser output power and eventually oscillation was quenched at a hot-cell pressure of 13 torr. However, lowering the oscillator pressure to 24.8 torr produced a sequence band power of around 1W above the hot-cell transition pressure of 15 torr. This transition pressure was strongly affected by the hot-cell temperature (Figure 8.3). Also, considerable hysteresis was observed; the  $00^{\circ}1 \rightarrow 00^{\circ}2$  transition-point always occurred at higher hot-cell pressures (pressure increasing) than the corresponding  $00^{\circ}2 \rightarrow 00^{\circ}1$  transition-point (pressure decreasing) due to line competition favouring the line already in oscillation. For hot-cell temperatures less than about 260 °C it was found that fundamental band lasing could not be quenched, since the required pressure exceeded the pressure at which  $\text{CO}_2$  absorption lines are fully pressure-broadened. Thus further increases in  $\text{CO}_2$  pressure produced no further absorption at line centre.

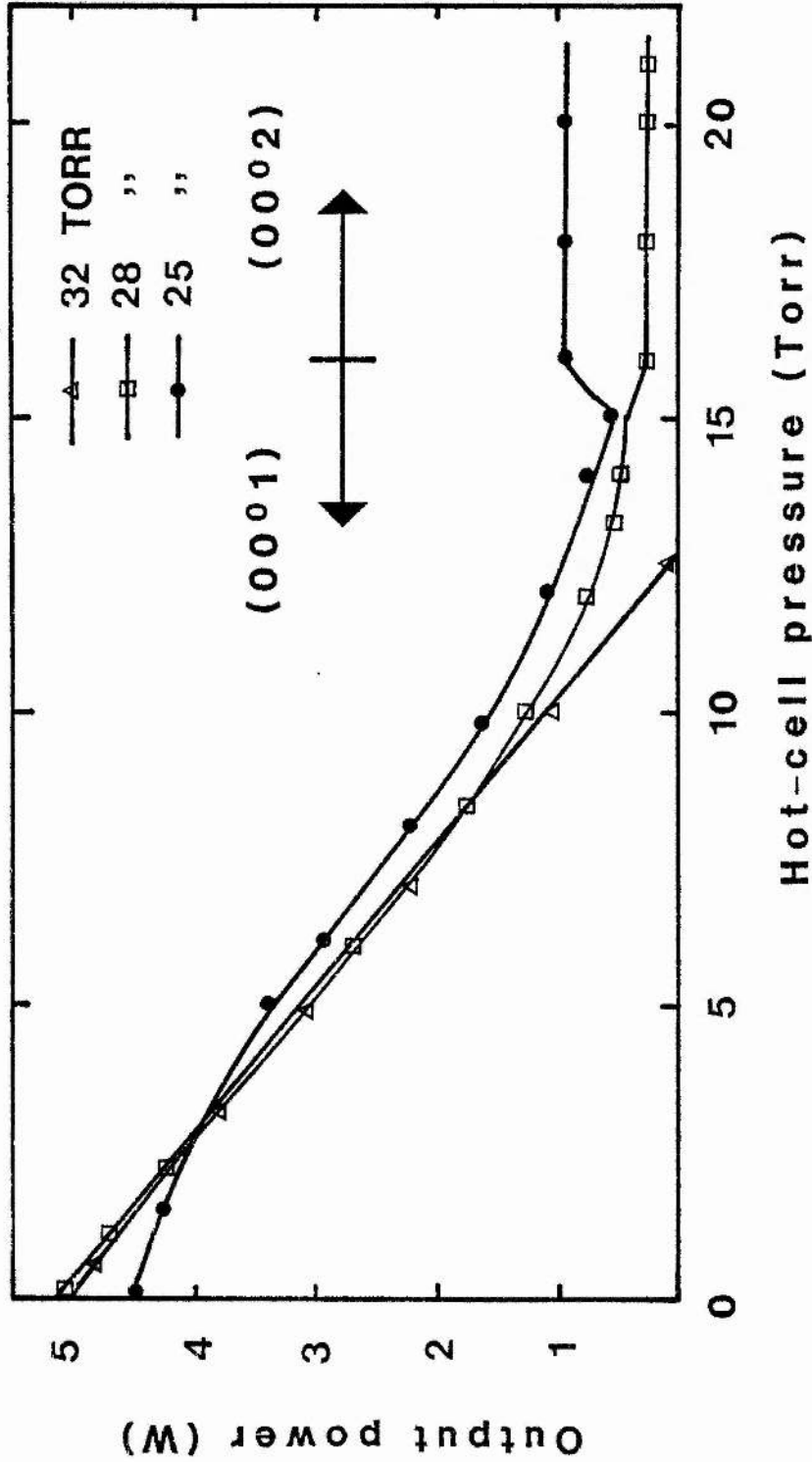


Fig. 8.2. Dependence of laser output power on hot-cell pressure for a hot-cell temperature of  $400^{\circ}\text{C}$ . 1  $\text{CO}_2$  : 2  $\text{Xe}$  : 3  $\text{N}_2$  : 10  $\text{He}$  gas mixture, discharge current = 10 mA. Output coupler reflectivity  $R_0 = 94\%$ .

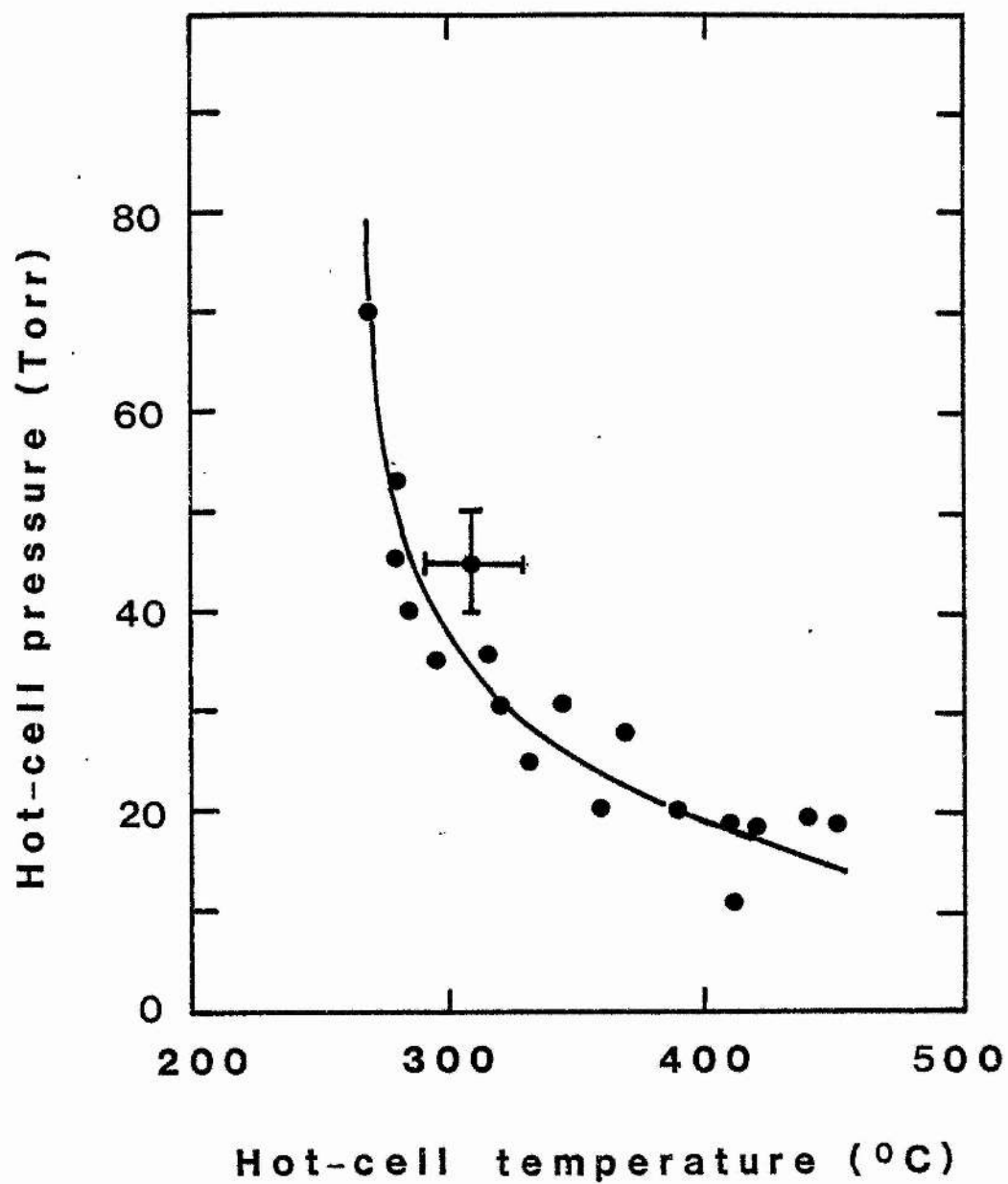


Fig. 8.3. Dependence of  $00^{\circ}1 \rightarrow 00^{\circ}2$  band transition pressure on hot-cell temperature. (Gas mixture 1  $\text{CO}_2$  : 2 Xe : 3  $\text{N}_2$  : 10 He, 20 torr pressure, 10 mA discharge current).

Sequence band lasing could only be obtained for relatively narrow ranges of oscillator pressure, current and gas mixture. Figure 8.4 shows the effect of pressure on sequence band output power for a near-optimum gas mixture. Clearly the sequence band output is maximised at around 20 torr. No sequence band laser action is obtained above 36, torr, despite the fact that the  $00^0_1$  power is a maximum at about 40 torr. This is consistent with the gain and vibrational temperature measurements of Chapter 6 in which the inverse pressure dependence of  $T_3$  reduced the  $00^0_2$  band gain above 24 torr, and agrees qualitatively with Reid and Siemsen who observed<sup>3</sup> an inverse dependence of sequence power on  $\text{CO}_2$  partial pressure above 0.7 torr. Thus the optimum pressure for cw sequence band lasing is defined by a trade-off between the conflicting requirements of (i) a high vibrational temperature,  $T_3$ , and (ii) a high  $\text{CO}_2$  partial pressure.

Sequence band laser discharge current was found to be optimised around 10mA, compared to an optimum  $00^0_1$  laser current of 15mA, dependent on pressure (Figure 8.5). This is an initially surprising result, since the small-signal gain measurement of Chapter 6 showed that peak  $00^0_2$  gain always occurs at higher currents than does peak  $00^0_1$  gain. However, in a laser oscillator the optimum excitation current is influenced by the degree of output coupling, as shown in Figure 8.6 for  $00^0_1$  lasing. As output coupling is increased, and the cavity round-trip gain approaches the minimum oscillation threshold, so the optimum discharge current falls to approach the current for maximum small-signal gain ( $\sim 10\text{mA}$ ). Conversely, when output coupling is low and the intra-cavity laser field intensity is high, stimulated

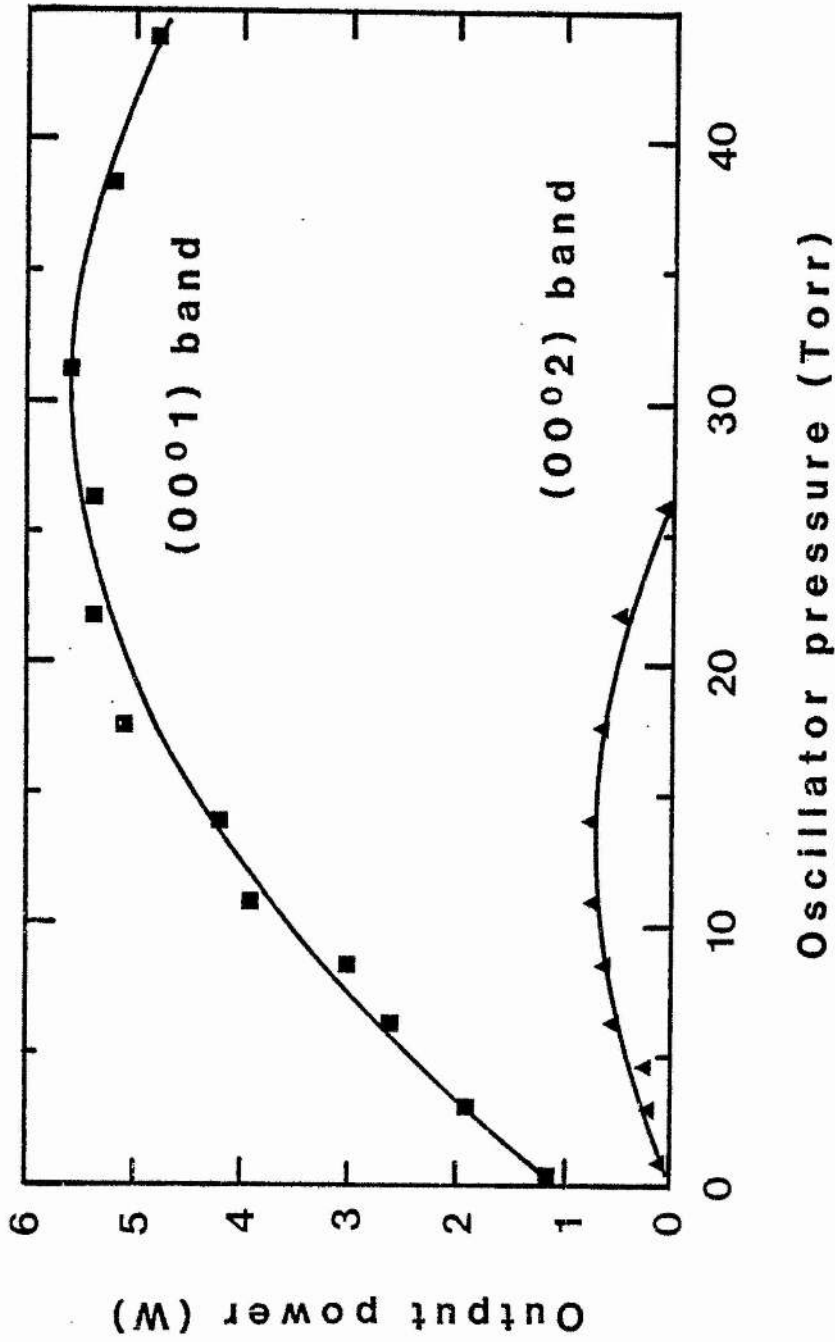


Fig. 8.4. Pressure dependence of laser output power for 00<sup>0</sup>1 and 00<sup>0</sup>2 bands.

(Gas mixture 1 CO<sub>2</sub> : 1 Xe : 3 N<sub>2</sub> : 13 He, discharge current = 10 mA,

$R_0 = 94\%$ ).

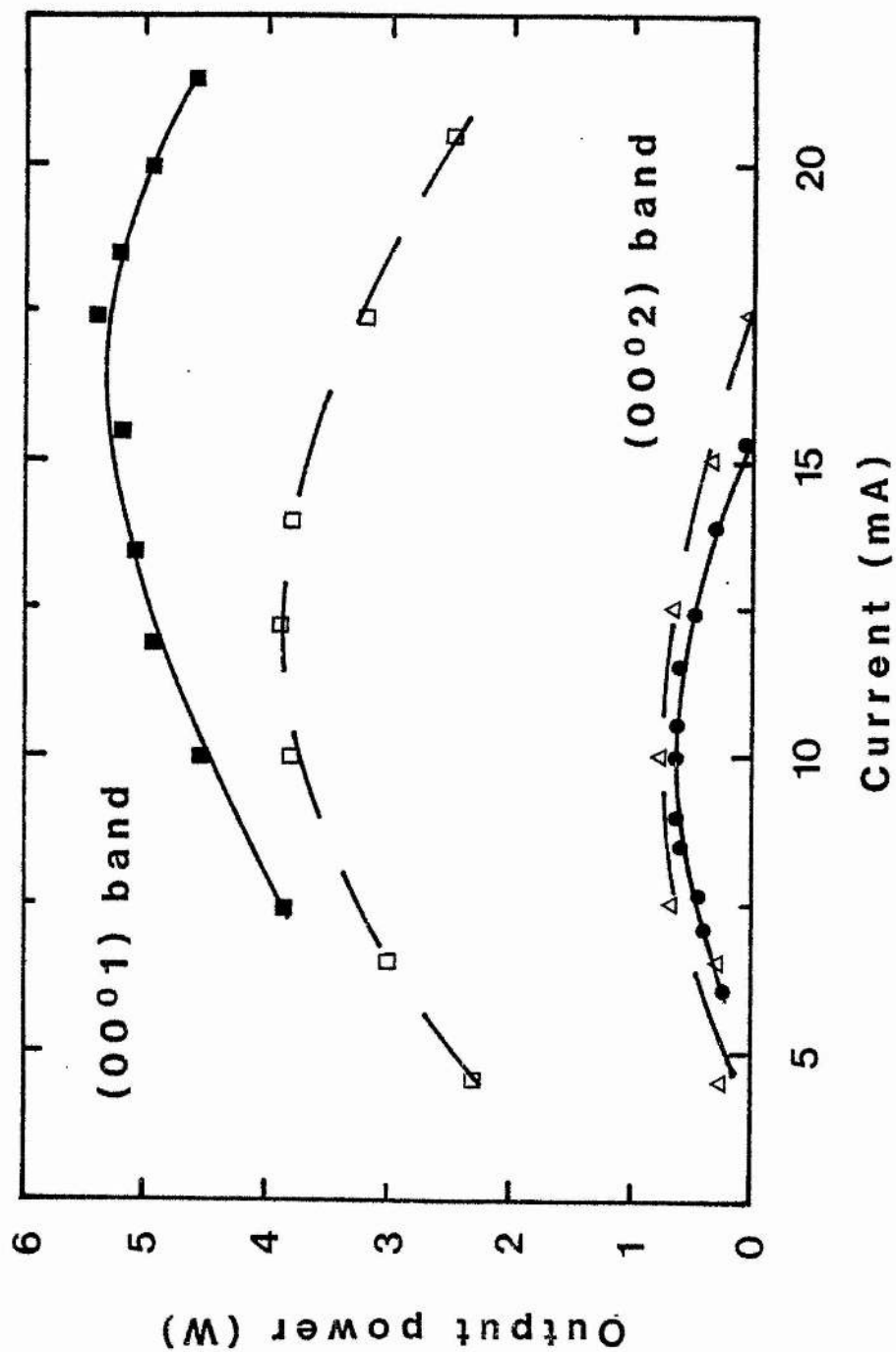


Fig. 8.5. Discharge current dependence of  $00^01$  and  $00^02$  laser output power. Gas mixture 1  $\text{CO}_2$  : 1 Xe : 3  $\text{N}_2$  : 13 He; total pressures 21 torr (dashed curves) and 28 torr (solid curves).

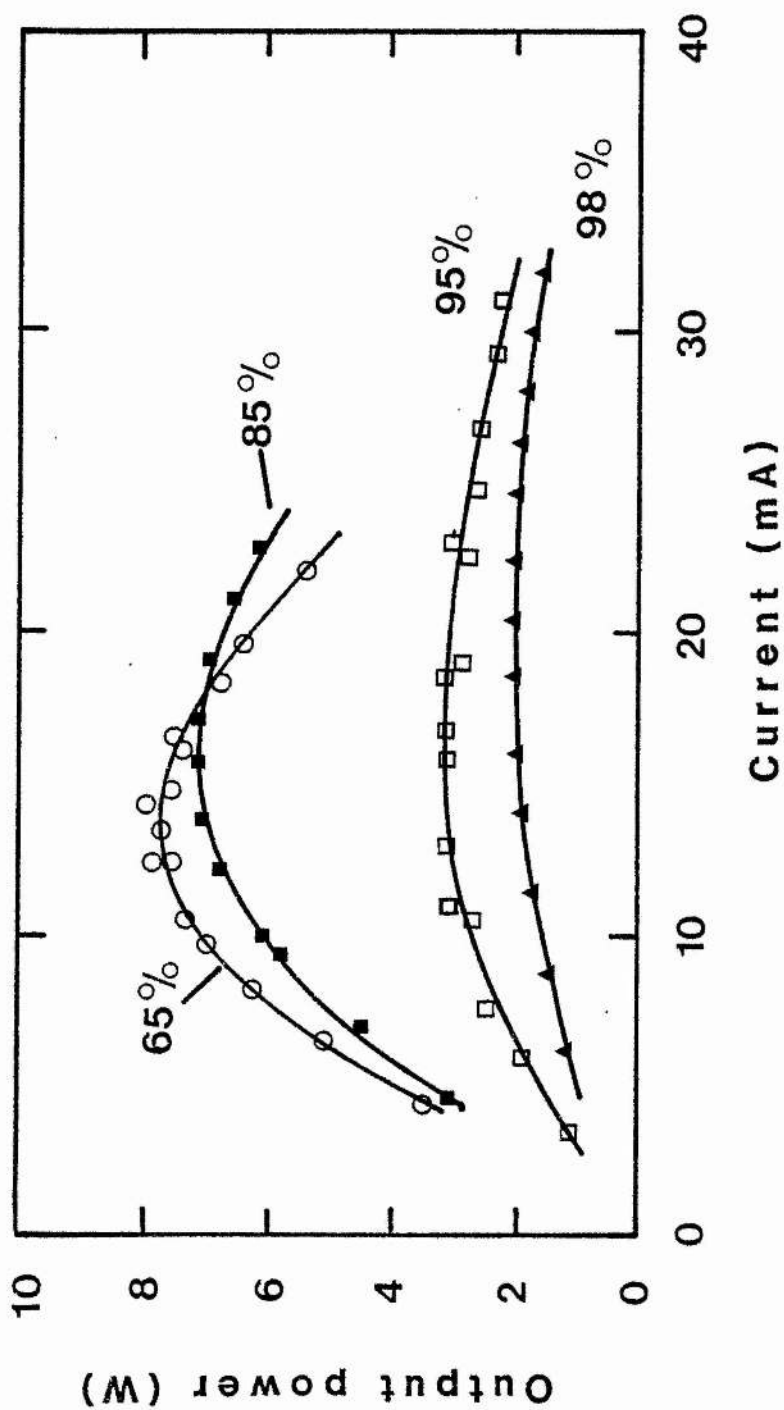


Fig. 8.6. Current dependence of  $00^{\circ}1 P(20)$  output power for various output coupler reflectances. Gas mixture 1  $\text{CO}_2$  : 2  $\text{Xe}$  : 3  $\text{N}_2$  : 12  $\text{He}$ , total pressure 18 torr.

emission is the major loss from the upper laser level, and competes favourably with collisional de-excitation. The effective gain is controlled by the balance of electron excitation and stimulated emission, and small-signal gain is not relevant. Therefore with decreasing output coupling, the optimum discharge current moves to higher values. The observed difference in  $00^{\circ}1$  and  $00^{\circ}2$  band optimum currents is thus explained by the 'near-threshold' nature of the sequence band oscillation, contrasting with the saturated gain conditions which apply to fundamental band lasing.

### 8.3.2 Effects of gas additives: Xe, CO and H<sub>2</sub>

It was found that the addition of small amounts of Xenon to a basic CO<sub>2</sub>-N<sub>2</sub>-He mixture produced a significant increase in  $00^{\circ}2$  band output power, and shifted the maximum of output power to higher discharge currents (see Figure 8.7). Traditionally the beneficial effect of Xe in CO<sub>2</sub> lasers has been ascribed to an increase in the constant-current plasma electron density<sup>10</sup> which provides higher excitation rates without incurring extra v-i gas heating. More recently it has been suggested<sup>11</sup> that the addition of Xe to flowing gas lasers causes a reduction in the rate of CO<sub>2</sub> dissociation. In order to test these ideas, the gain measurement system of Chapter 6 was used to monitor changes in small-signal gain produced by the Xe addition, while the sealed discharge CO<sub>2</sub> dissociation level was measured by the MS10S mass spectrometer. The effects of CO and H<sub>2</sub> addition were also tested, and the results (Figs. 8.8-8.10) are summarised in Table 8.1. The basic gas mixture (1 torrCO<sub>2</sub>: 3N<sub>2</sub>: 12He) displayed a CO<sub>2</sub> dissociation level of  $50 \pm 5\%$  at 10mA (measured by running the discharge for around 1 hour before admitting the discharged gas into a previously evacuated sampling volume). Adding 2 torr of



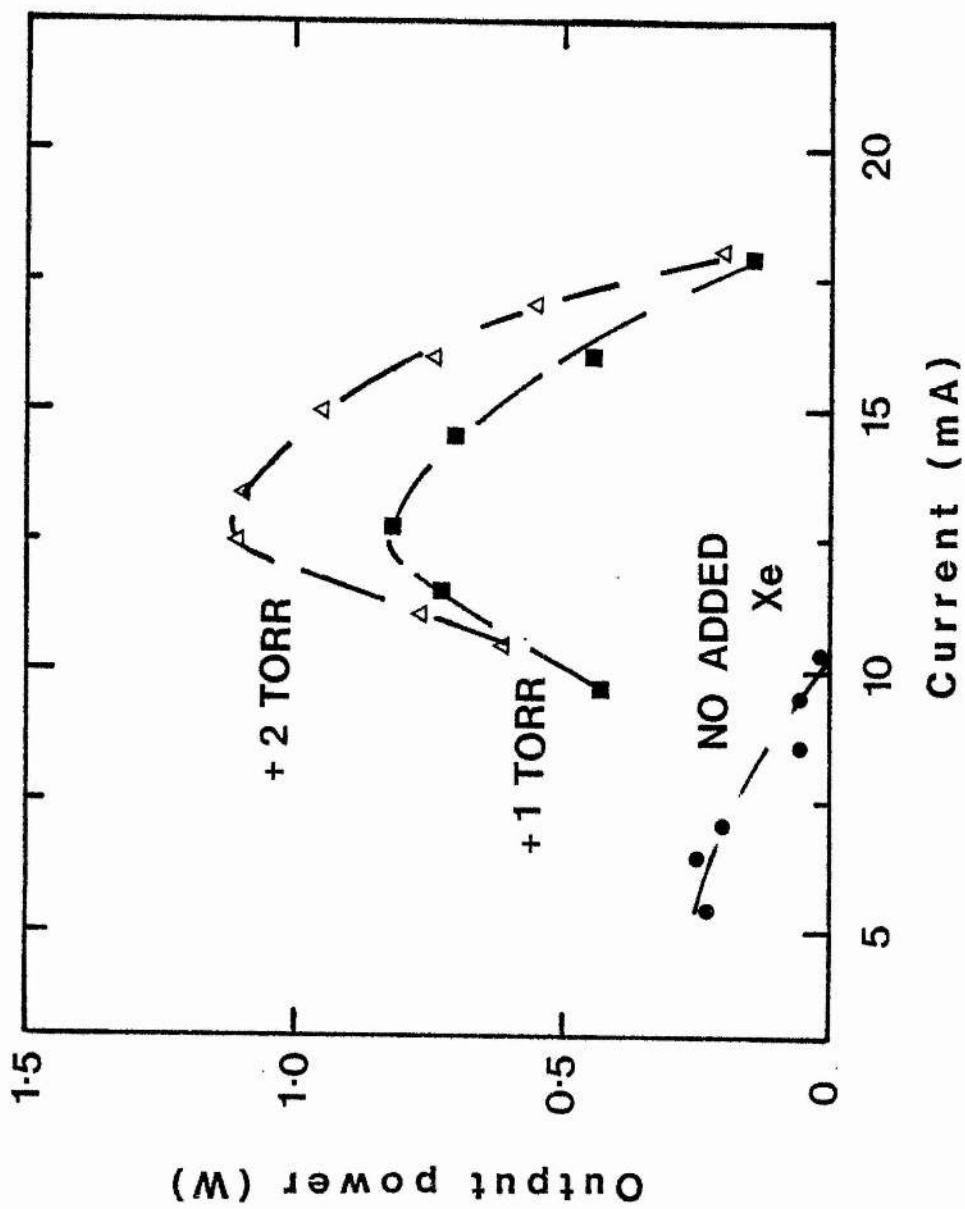


Fig. 8.7. Effect of Xe addition on 00<sup>o</sup>2 band output power for a basic mixture of 1 CO<sub>2</sub> : 2 N<sub>2</sub> : 11 He at 21 torr pressure.

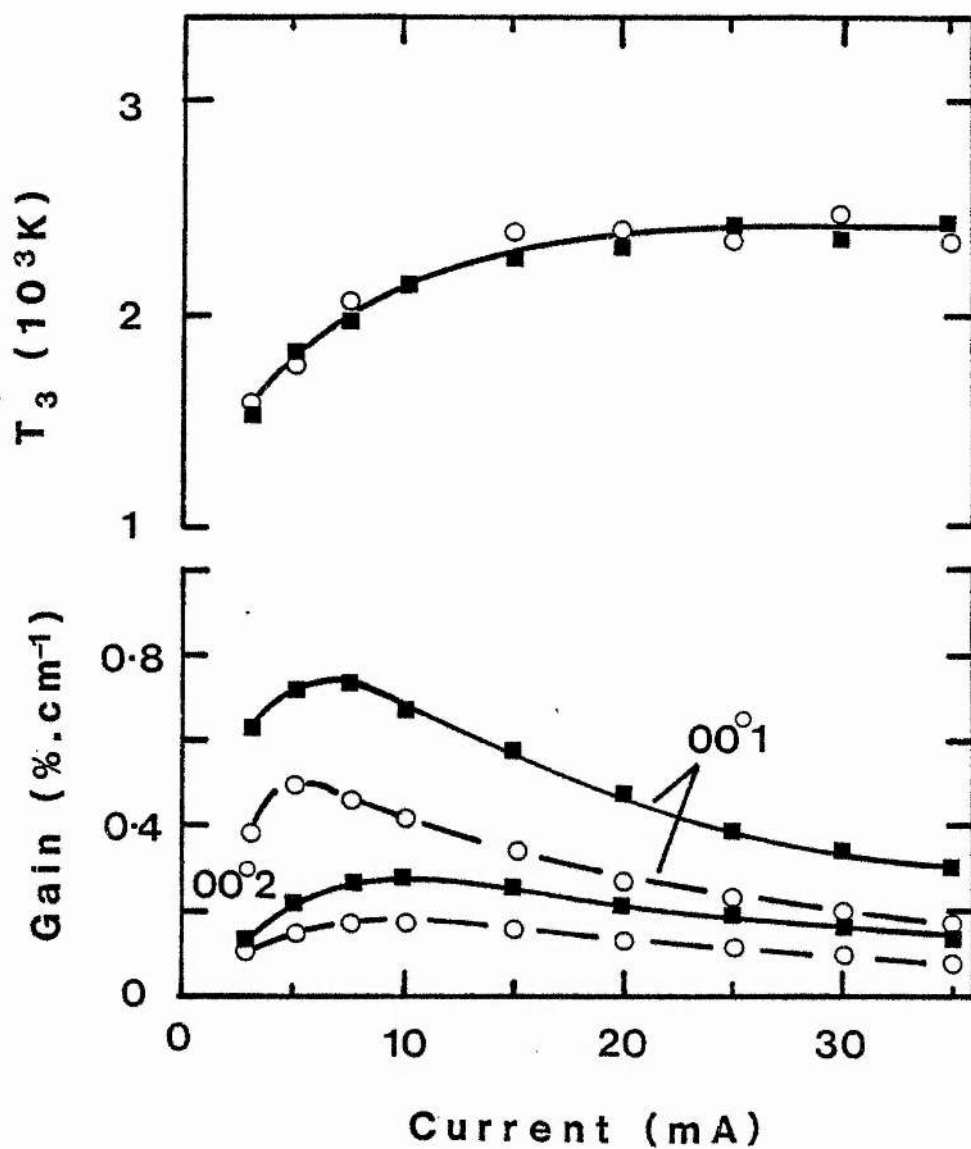


Fig. 8.8. Measured small-signal gain and derived asymmetric mode temperature ( $T_3$ ) in 1 torr  $\text{CO}_2 : 3 \text{N}_2 : 12 \text{He}$  (dashed curves) and with 2 torr added Xe (solid curves).

TABLE 8.1    Effect of gas additives on small-signal  
gain and vibrational temperature.

<u>Gas mixture</u> (Torr)	<u>Measured CO<sub>2</sub></u> <u>dissociation</u> D (%)	<u>00<sup>0</sup>1</u> <u>gain</u> $\alpha_2$ (% cm <sup>-1</sup> )	<u>00<sup>0</sup>2</u> <u>gain</u> $\alpha_2$ (% cm <sup>-1</sup> )	<u>Vibrational</u> <u>temperature</u> T <sub>3</sub> (K)
1 CO <sub>2</sub> : 3 N <sub>2</sub> : 12 He	50	0.43	0.18	2150
1 CO <sub>2</sub> : 3 N <sub>2</sub> : 12 He + 1 CO	0	0.50	0.17	1900
1 CO <sub>2</sub> : 3 N <sub>2</sub> : 12 He + 2 Xe	20	0.68	0.28	2150
1 CO <sub>2</sub> : 3 N <sub>2</sub> : 12 He + 0.8 H <sub>2</sub>	17	0.57	0.15	1667

Note:    All measurements at 10 mA discharge current in sealed tube.

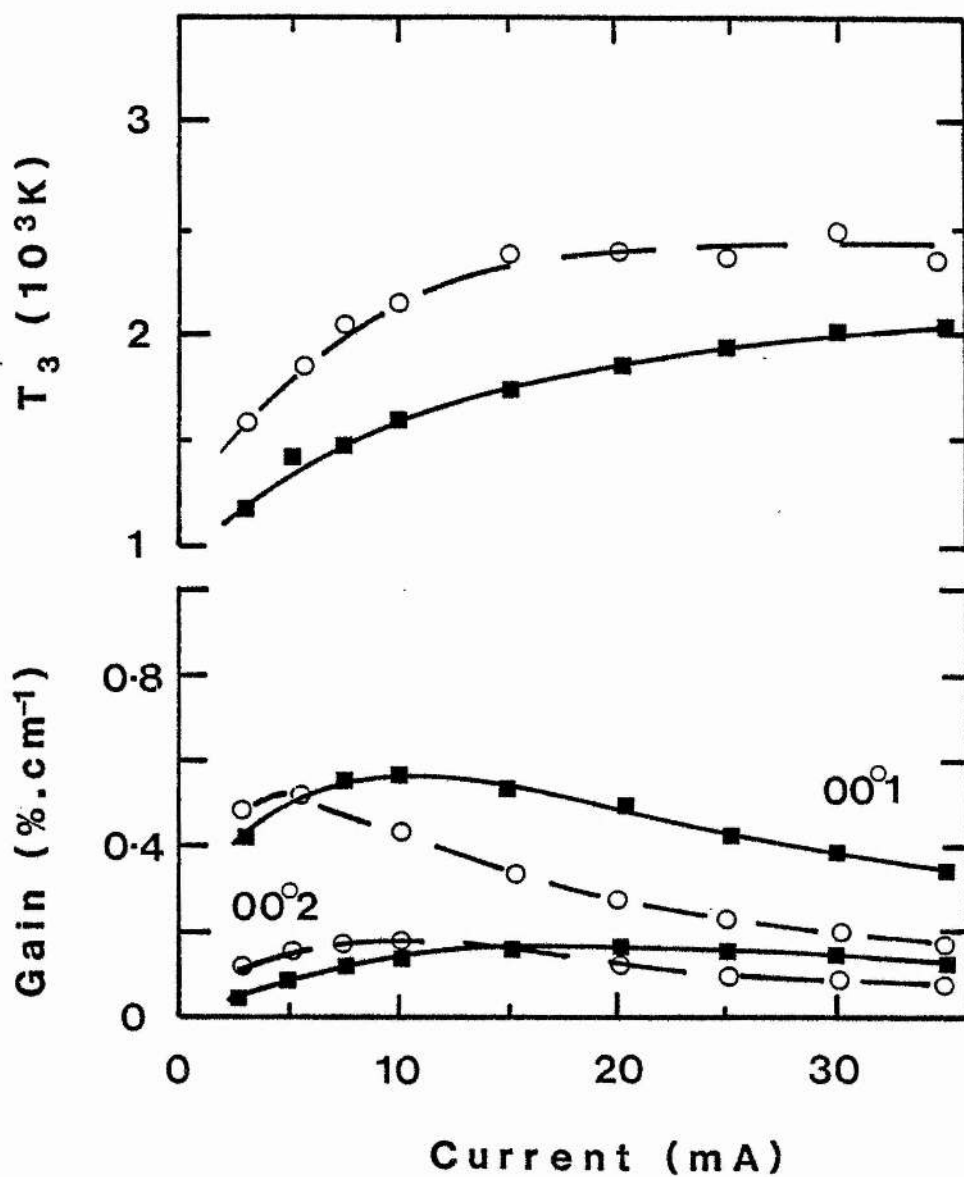


Fig. 8.9. Measured small-signal gain and derived  $T_3$  in 1 torr  $\text{CO}_2 : 2 \text{N}_2 : 12 \text{He}$  (dashed curves) and with 0.8 torr added  $\text{H}_2$  (solid curves).

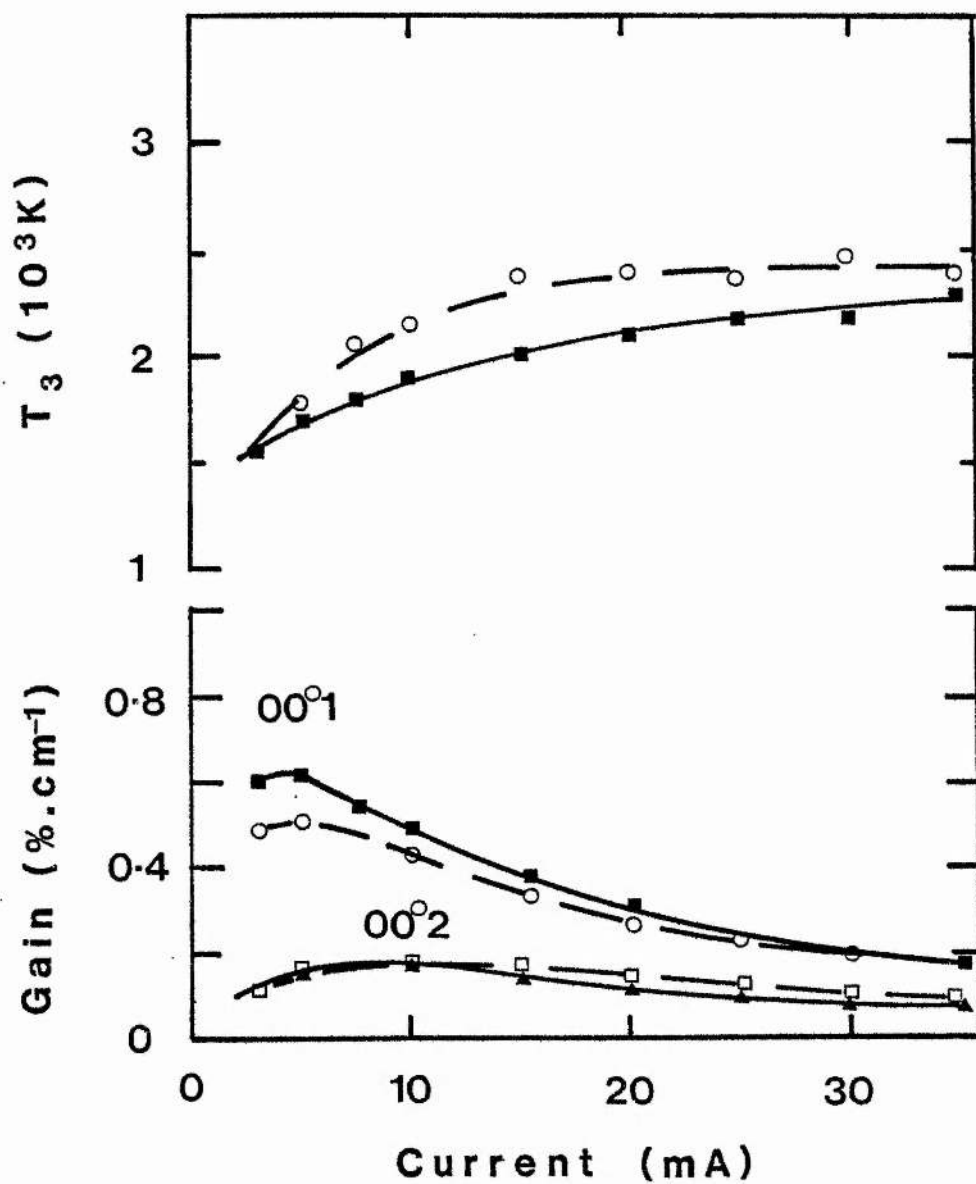


Fig. 8.10. Measured gains and derived  $T_3$  in 1 torr  $\text{CO}_2$  :  
 $3\text{N}_2 : 12\text{He}$  (dashed curves) and with 1 torr  
 added  $\text{CO}$  (solid curves).

Xe increased the measured  $00^{\circ}1$  and  $00^{\circ}2$  gains by approximately equal proportions ( $\sim 50\%$ ). Thus the derived  $\text{CO}_2$  asymmetric mode temperature,  $T_3$ , was unaltered by Xe addition.  $\text{CO}_2$  dissociation in the Xe admixture was measured as  $20 \pm 5\%$ . Therefore the beneficial effect of Xe on small-signal gain is explained by a reduction in  $\text{CO}_2$  dissociation (which increases the  $\text{CO}_2$  content by  $\sim 50\%$ ) producing a corresponding gain increase. Under most circumstances an increase in  $\text{CO}_2$  content would be accompanied by a decrease in vibrational temperature  $T_3$  due to faster  $\text{CO}_2$  V-V-T relaxation (Chapter 6). No such decrease is observed here, presumably due to the higher specific electron densities which occur in Xe admixtures (see Figure 4.9); these tend to produce higher vibrational temperatures, counter-acting the effect of V-V-T collisions. In Figure 8.8 these conflicting tendencies have resulted in a  $T_3$  which is unchanged within experimental uncertainty.

The addition of 5%  $\text{H}_2$  to the basic mixture reduced  $\text{CO}_2$  dissociation (to 17%) and  $T_3$  (to 1667K) at 10mA. However,  $00^{\circ}1$  band small-signal gain was increased, especially at high current (Figure 8.9). The measured decrease in  $\text{CO}_2$  dissociation is too small to account for the increase in gain in the presence of such a marked fall in  $T_3$ : some other beneficial effect of  $\text{H}_2$  addition must be invoked. The rate constant for  $\text{CO}_2(\nu_2) \rightarrow$  ground state de-activation by collision with  $\text{H}_2$  is  $7 \times 10^4 \text{ torr}^{-1} \text{ s}^{-1}$  compared to  $4 \times 10^3 \text{ torr}^{-1} \text{ s}^{-1}$  for  $\text{CO}_2(\nu_3) \rightarrow (\nu_2)$  de-activation (reference 5.1). Since the  $\text{H}_2$  addition causes a large reduction in  $T_3$  it is reasonable to suppose that a similarly large reduction in the  $\text{CO}_2(\nu_1, \nu_2)$  mode temperature ( $T_2$ ) is very probable. Therefore we may postulate that the main effects of  $\text{H}_2$  addition are (i) a reduction in  $\text{CO}_2$  dissociation level

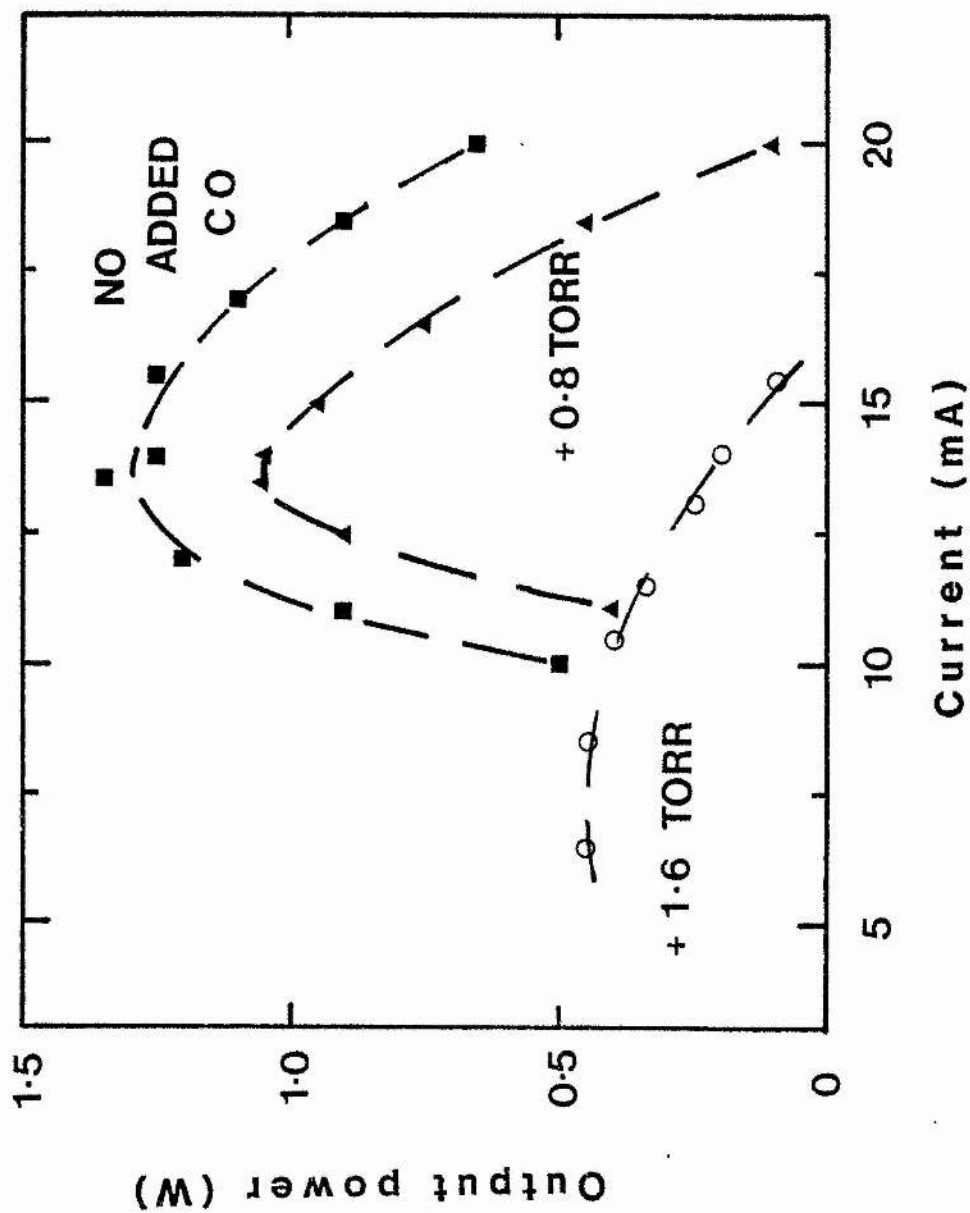


Fig. 8.11. Effect of CO addition on 00<sup>0</sup>2 band laser output power (basic mixture 2 CO<sub>2</sub> : 2 Xe : 4 N<sub>2</sub> : 12 He, 20 torr pressure).

due to hydroxyl-enhanced  $\text{CO}_2$  re-formation (equation 3.5), (ii) a reduction in  $T_3$  due to increased  $\nu_3$  mode V-V-T relaxation, (iii) a reduction in  $T_2$  due to much increased  $\nu_1, \nu_2$  mode V-T relaxation. Further work is required to establish the quantitative relationship of these effects.

Figure 8.10 shows the effect of CO addition on gains and vibrational temperature. A slight increase in  $00^0_1$  band gain is accompanied by a slight fall in  $00^0_2$  gain, corresponding to a decrease in  $T_3$ ; this decrease is explained by mass spectrometry measurements which showed that  $\text{CO}_2$  dissociation in the CO admixture was negligible compared to experimental error ( $\pm 5\%$ ). For the  $00^0_1$  band, the increased  $\text{CO}_2$  content is sufficient to produce an increase in gain, despite the reduced vibrational temperature. The fall in  $T_3$  is more serious for the  $00^0_2$  band (see Figure 2.4) and results in reduced sequence band gain. It is not necessary to postulate any effect of CO addition on  $T_2$ . The detrimental influence of CO on sequence band performance was confirmed by measurements of sequence band laser output power with small amounts of added CO (Figure 8.11).

In conclusion, of the additives tested only Xe is useful in producing an improvement in sequence band gain and output power.

### 8.3.3 Output power and gain measurements

It is interesting to compare the behaviour of a sequence band laser oscillator to the small-signal gain of its active medium. This was achieved using the gain measurement system by running the oscillator and amplifier discharges under identical conditions of pressure, gas mixture and coolant temperature. Small-signal gain measurements for a 1 torr  $\text{CO}_2$ : 2Xe: 3N<sub>2</sub>: 12He mixture are plotted in



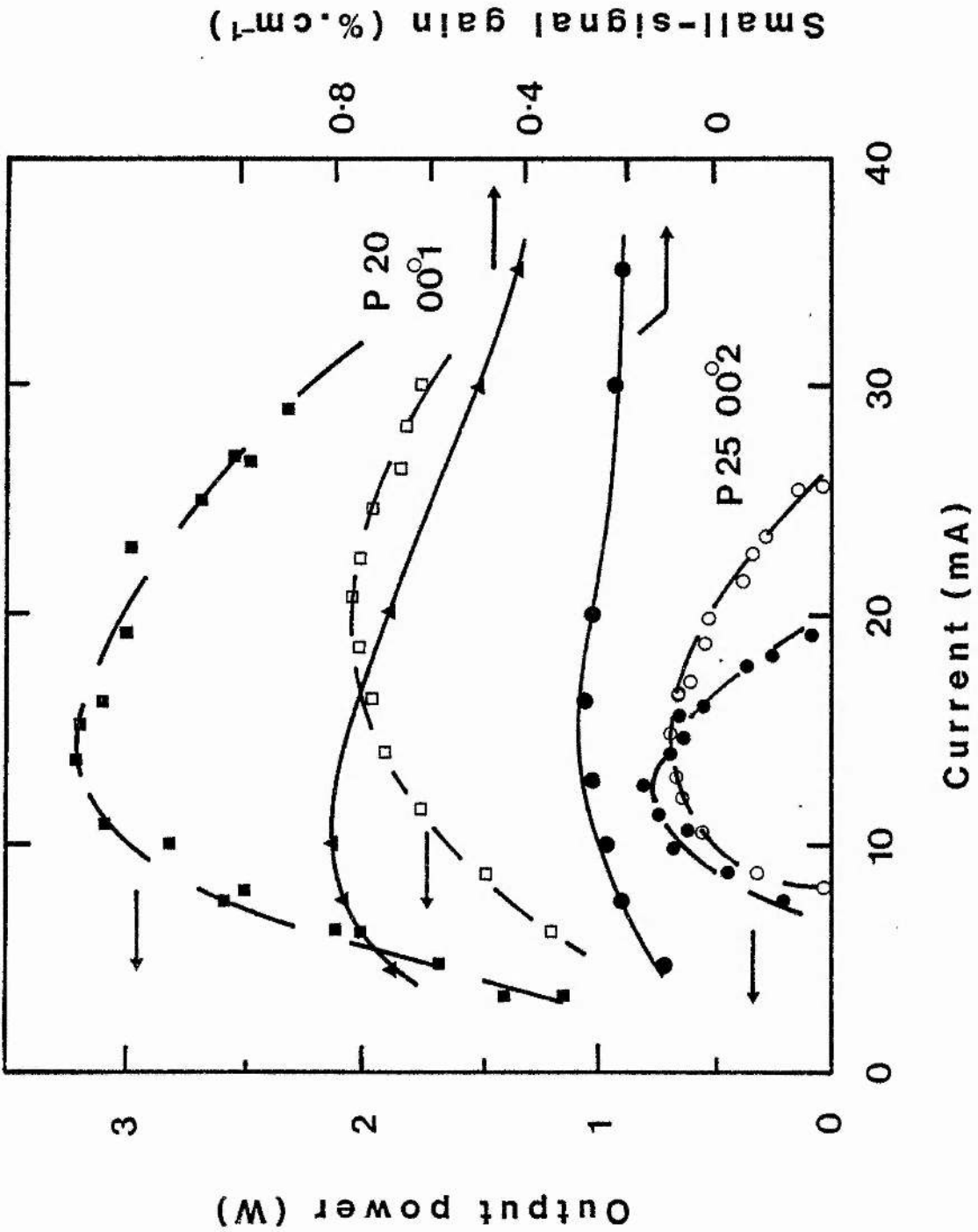


Fig. 8.12. Measured small-signal gains and powers for 1 CO<sub>2</sub> : 2 Xe : 3 N<sub>2</sub> : 12 He at 18 torr. Output coupling 94.0% (closed symbols) and 97.5% (open symbols).

Fig. 8.12 (solid curves). The coolant temperature was 0 °C. Also shown (dashed) are laser output powers on the 00<sup>0</sup>1 and 00<sup>0</sup>2 bands for identical conditions using two different output couplers of nominal reflectances 95% (closed symbols) and 98% (open symbols). The nominal reflectivities were checked at 10.6 μm using an infra-red spectrophotometer and were found to be 94.0 ± 0.5% and 97.5 ± 0.5% respectively. Figure 8.12 shows that, as before, moving to high output coupler reflectivity reduces the output power and shifts the peak power to higher current.

#### 8.3.4 Analysis and discussion

The data of Figure 8.12 can be combined with optical cavity parameters to infer the effective cavity round-trip gain. This is related to the small-signal gain via the saturation intensity, which is crucial in determining the length/power scaling of the laser. No measurements of sequence band saturation intensity have been yet reported in the literature, so even indirect measurements are of interest.

For any cw laser oscillator

$$G^2(1-L)^2(1-T) = 1 \quad (8.1)$$

where

$$G = \exp(\alpha \ell) \quad (8.2)$$

is the cavity single-pass gain, with  $\alpha$  the effective gain per unit length and  $\ell$  the active length of the laser medium.  $T$  represents the useful output mirror transmission ( $= 1-R_o$ ) and  $L$  is the non-distributed single-pass cavity loss (e.g. absorption and scattering from mirrors and windows). Combining (8.1) and (8.2) yields

$$\alpha = \frac{1}{2\ell} \ln \left[ \frac{1}{(1-L)^2(1-T)} \right] \quad (8.3)$$

The laser output intensity is simply related to the output power

$$I_o = P_o/A \quad (8.4)$$

where A is the cross-sectional area of the output beam, and the intracavity intensity (summing the average forward and backward travelling wave intensities) is

$$I = 2I_o/T \quad (8.5)$$

If we make the assumption of pure homogeneous broadening then the ratio of large to small-signal gain coefficients is

$$\frac{\alpha}{\alpha_o} = \frac{1}{1 + I/I_s} \quad (8.6)$$

where  $I_s$  is the saturation intensity. Equations 8.4 to 8.6 imply that

$$I_s = \frac{2P_o\alpha}{AT(\alpha_o - \alpha)} \quad (8.7)$$

where  $\alpha(\ell, L, T)$  is given by (8.3). Equation 8.7 relates the saturation intensity of the active medium to the power output of the cw laser, given knowledge of the relevant optical cavity losses and the small-signal gain.

It should now be noticed that  $\alpha$ , the effective gain coefficient defined in equation 8.3, is independent of the laser discharge current and depends only on the optical cavity losses and output coupling. Furthermore, when the laser is just at the threshold of oscillation, then the small-signal gain coefficient of the active medium must be equal to the effective gain given by (8.3), that is

$$\alpha_o(i) = \alpha(\ell, L, T) \quad (8.8)$$

where  $i$  represents the laser discharge current. We can therefore apply the output power and small-signal gain data of figure 8.12 to

estimate  $\alpha$  (for a given output coupling T) without explicit consideration of the unwanted optical cavity losses. For example, with  $T = 0.025$  (97.5% reflecting output coupler) we see that  $00^0_2$  band oscillation is just brought to threshold by a discharge current of  $26 \pm 1 \text{ mA}$ , corresponding to an effective gain  $\alpha = 0.22 \pm 0.02\% \text{ cm}^{-1}$  (determined from the  $00^0_2$  band small-signal gain curve). Crucially, this value of the effective gain will apply whether or not the laser is running close to threshold. Thus for the discharge current of  $16 \text{ mA}$ , which produces  $0.68 \pm 0.02 \text{ W}$  of sequence band power (figure 8.12), we can use equation 8.7 to estimate the  $00^0_2$  band saturation intensity with

$$P_o = 0.68 \pm 0.02 \text{ W}$$

$$\alpha = 0.22 \pm 0.02\% \text{ cm}^{-1}$$

$$\alpha_o = 0.29 \pm 0.02\% \text{ cm}^{-1}$$

$$T = 0.025$$

and

$$A = 0.283 \text{ cm}^2$$

corresponding to a 6 mm output beam diameter. The uncertainty in  $(\alpha_o - \alpha)$  dominates the other uncertainties which may be neglected; equation 8.7 then indicates a sequence band saturation intensity  $I_{s2} \sim 600 \text{ W cm}^{-2}$ , with upper and lower bounds of 1500 and  $350 \text{ W cm}^{-2}$ , respectively. For the  $00^0_1$  band at  $16 \text{ mA}$  we have

$$P_o = 1.98 \pm 0.02 \text{ W}$$

$$\alpha = 0.22 \pm 0.02\% \text{ cm}^{-1}$$

$$\alpha_o = 0.76 \pm 0.02\% \text{ cm}^{-1}$$

so the  $00^0_1$  band saturation intensity is  $I_{s1} \sim 230 \pm 40 \text{ W cm}^{-2}$ .

This is larger than the values ( $\sim 100 \text{ W cm}^{-2}$ ) which are typical of low-pressure cw  $00^0_1$  band lasers<sup>13</sup>, but the saturation intensities derived here must not be regarded as absolute because of the

assumption of pure pressure broadening (a poor one at 18 torr) and because of the approximate nature of the analysis (8.1) to (8.7). Nevertheless, the analysis clearly suggests that  $I_{s2} > I_{s1}$  by a factor of  $\sim 2.5$  (although this could be as small as 1.3 or as large as 8). Repeating the procedure for the 94% reflecting coupler and the corresponding oscillation threshold at around 20 mA, then the effective gain is  $\alpha = 0.26 \pm 0.02\% \text{ cm}^{-1}$  (see figure 8.12). Once more applying this to the situation at 16 mA, where for the sequence band  $P_o = 0.55\text{W}$  and for the fundamental band  $P_o = 2.0\text{W}$ , it can be again shown that evaluation of equation 8.7 implies that  $I_{s2}/I_{s1} > 1$ .

The suggestion of a relatively large  $00^0_2$  band saturation intensity, although tentative, is surprising: a prima facie guess might be that  $I_{s2}$  should be smaller than  $I_{s1}$ , because the sequence band cross-section for stimulated emission is roughly twice the fundamental band value, resulting in a stronger coupling between the laser radiation field and the  $00^0_2$  band population inversion. The apparent anomaly of large  $I_{s2}$  values is resolved in the next section, which considers the theory of gain saturation on the  $00^0_1$  and  $00^0_2$  bands.

Finally, it is worth noting the implications of the data of figure 8.12 for the single pass non-distributed cavity loss  $L$ . Putting  $\alpha = 0.22\% \text{ cm}^{-1}$ ,  $T = 0.025$  and  $l = 80 \text{ cm}$  in equation 8.3 and solving for  $L$  gives  $L \sim 0.15$ . This seems slightly high, even for a cavity with 3 internal Brewster windows; however the cavity has a total length of 1.5 m and 2 cm diameter optics. We can therefore expect that diffraction losses will be important<sup>12</sup>, and these probably make a major contribution.

#### 8.4 Modelling gain saturation on the $00^0_1$ and $00^0_2$ bands

The processes of fundamental and sequence band gain saturation (i.e. the reduction of  $00^0_1$  and  $00^0_2$  band population inversion and effective gain with increasing stimulated emission) can be modelled by the vibrational exchange rate equations of Chapter 5 assuming:

(i) rapid intra-mode V-V transfer, so that vibrational temperatures remain good numbers even in the presence of saturating laser fields (shown to be an excellent approximation by the measurements of reference 6.13).

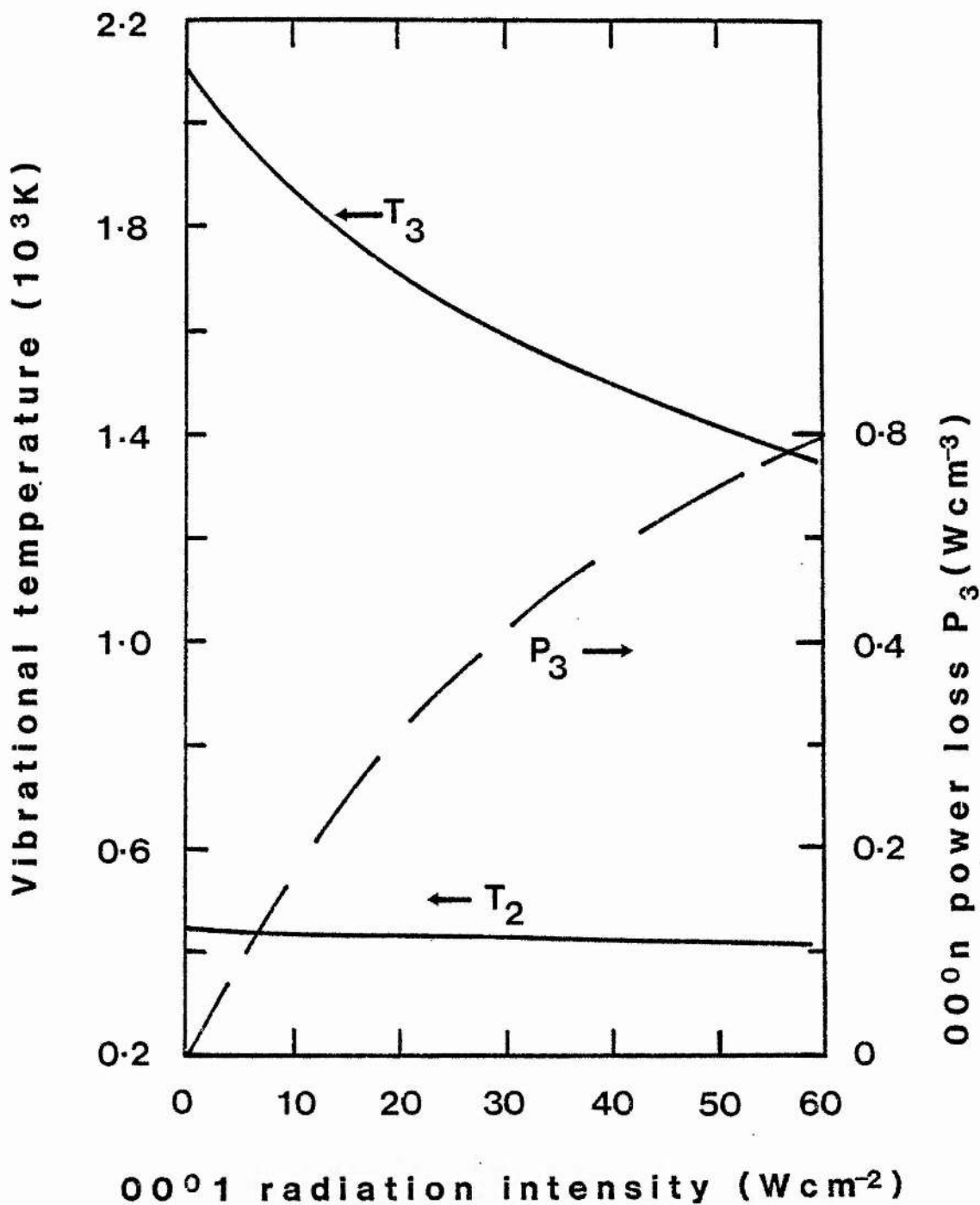


Fig. 8.13. Calculated effect of  $00^0 1$  laser field on vibrational temperatures in  $6 \text{CO}_2 : 12 \text{N}_2 : 82 \text{He}$  mixture at 20 torr assuming electron density =  $3 \times 10^{10} \text{cm}^{-3}$  and  $E/N = 3.0 \times 10^{-16} \text{Vcm}^2$ . Also shown (dashed) is power lost to stimulated emission from  $\text{CO}_2$  asymmetric stretch mode.

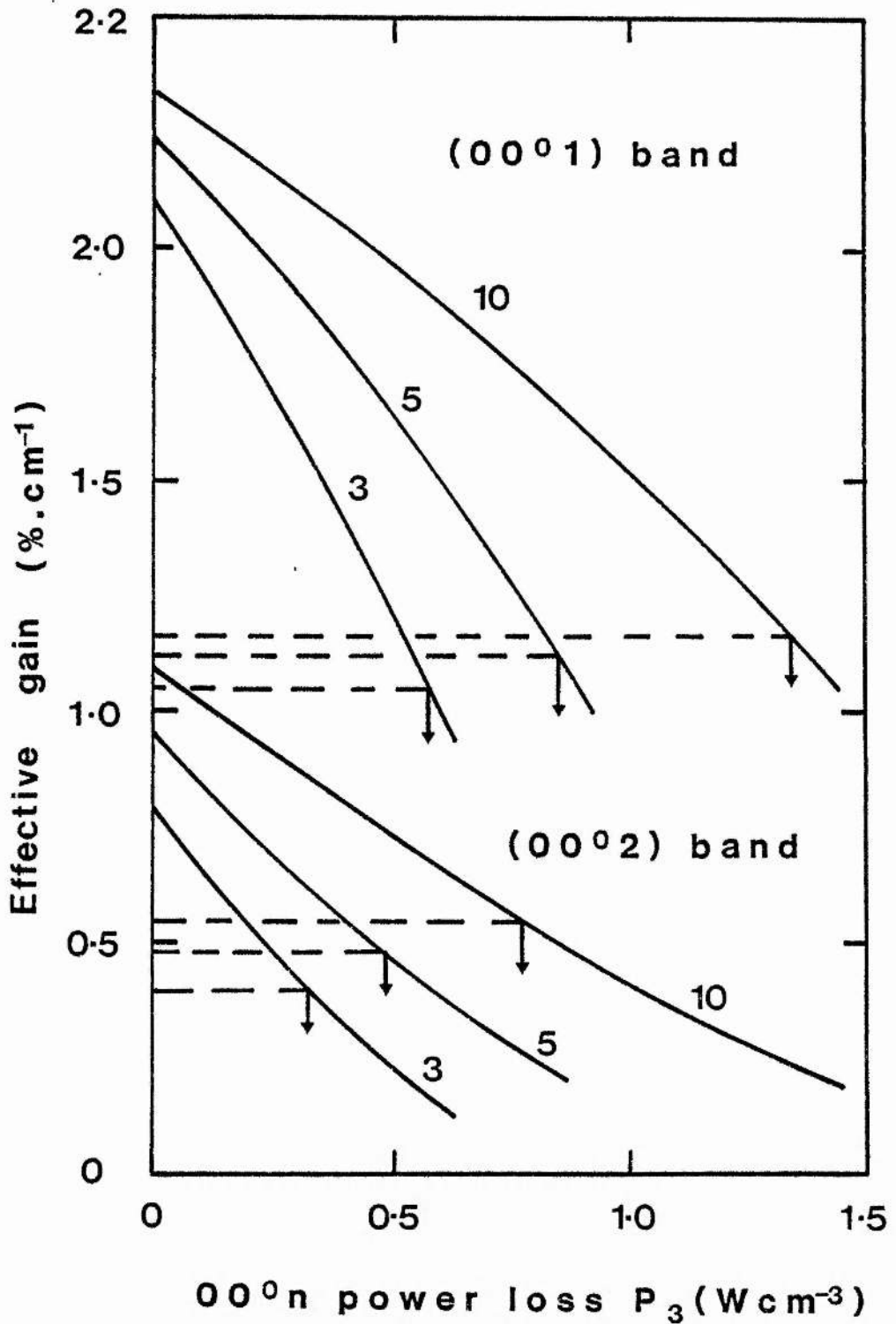


Fig. 8.14. Calculated effect of stimulated emission power loss on gain of 00<sup>0</sup>1 10 P(18) and 00<sup>0</sup>2 10 P(19) laser transitions for 20 torr 6 CO<sub>2</sub> : 12 N<sub>2</sub> : 82 He mixture at various electron densities (10<sup>10</sup> cm<sup>-3</sup>, indicated).



(ii) the main saturation mechanism is the reduction of the  $\text{CO}_2$   $00^{\circ}n$  mode temperature ( $T_3$ ) by stimulated emission, and this depends only on the excitation conditions and the rate of vibrational energy loss to the radiation field, irrespective of whether lasing is on the  $00^{\circ}1$  or  $00^{\circ}2$  band.

The application of a laser field of intensity  $I$  ( $\text{Wcm}^{-2}$ ) to a  $\text{CO}_2$  laser medium of effective gain  $\propto(\text{cm}^{-1})$  will decrease  $T_3$  by an amount determined by the gas mixture, discharge conditions and the power lost from the  $\nu_3$  mode ( $\text{W cm}^{-3}$ ):

$$P_3 = \alpha I \quad (8.13).$$

This is equivalent to a stimulated emission rate

$$\rho = \frac{\alpha I}{h\nu} \quad (8.14)$$

where  $h\nu$  is the energy of a  $10 \mu\text{m}$  photon. The dependence of the steady-state  $\text{CO}_2$  vibrational temperatures ( $T_2$ ,  $T_3$ ) and laser power loss ( $P_3$ ) on applied  $00^{\circ}1$  band laser field intensity was calculated using VIBEX. Results for a  $6\text{CO}_2: 12\text{N}_2: 82\text{He}$  gas mixture at 20 torr are shown in Figure 8.13 where a discharge electron density of  $3 \times 10^{10} \text{ cm}^{-3}$  has been assumed. As expected,  $T_3$  falls quickly with increasing laser intensity and the power in stimulated emission rises steadily. The symmetric-stretch and bending mode temperature  $T_2$  is little affected by the laser action. Knowledge of  $T_2$  and  $T_3$  allows the calculation of population inversions and effective gains (using equations 2.21 to 2.26) and the results are plotted in the form of effective gain versus  $00^{\circ}n$  mode power loss (Figure 8.14). For a given electron density it is clear that the  $00^{\circ}2$  band gain is reduced to half its small-signal value by smaller power losses than those required to half the  $00^{\circ}1$  gain (e.g. for  $n_e = 3 \times 10^{10} \text{ cm}^{-3}$ , the  $00^{\circ}2$  gain is halved at

$P_3'' = 0.32 \text{ Wcm}^{-3}$  while the  $00^0_1$  "half-gain" power loss is  $P_3' = 0.58 \text{ Wcm}^{-3}$ ). This is due to the higher sensitivity at the  $00^0_2$  population to changes in  $T_3$ .

The half-gain power losses can be converted to laser field intensities using equation 8.13, so that the fundamental band saturation intensity for  $n_e = 3.0 \times 10^{10} \text{ cm}^{-3}$  is

$$I_{s1} = \frac{2P_3'}{\alpha_{01}}$$

where  $\alpha_{01}$  is the small-signal  $00^0_1$  gain ( $= 2.10\% \text{ cm}^{-1}$  from Fig. 8.14).

Therefore

$$\begin{aligned} I_{s1} &= \frac{2 \times 0.58 \text{ W cm}^{-3}}{2.10 \times 10^{-2} \text{ cm}^{-1}} \\ &= 55.2 \text{ W cm}^{-2}. \end{aligned}$$

Similarly  $I_{s2} = 2P_3''/\alpha_{02}$  and putting  $\alpha_{02} = 0.79\% \text{ cm}^{-1}$  gives  $I_{s2} = 81.0 \text{ W cm}^{-2}$ . Thus the sequence band saturation intensity is larger than the corresponding fundamental band value because the relatively small  $00^0_2$  band gain requires the application of stronger laser fields to extract similar power from the  $\text{CO}_2(\nu_3)$  mode.

Fundamental and sequence band saturation intensities were calculated for a series of electron densities and are shown in Figure 8.15 for the 6:12:82 mixture and a 9.6 $\text{CO}_2$ : 10.9 $\text{N}_2$ : 79.5He mixture. In each case the saturation intensities generally increase with increasing electron density (as expected) and  $I_{s2} > I_{s1}$  by a factor between 1.2 and 8.0, which decreases with increasing electron density in agreement with the measurements of the previous section. The upturn in  $I_{s2}$  at low electron density is caused by a vanishingly-small  $00^0_2$  gain at low vibrational temperatures, which in turn requires increasingly large  $00^0_2$  laser fields to saturate the gain. For the 9.6: 10.9:

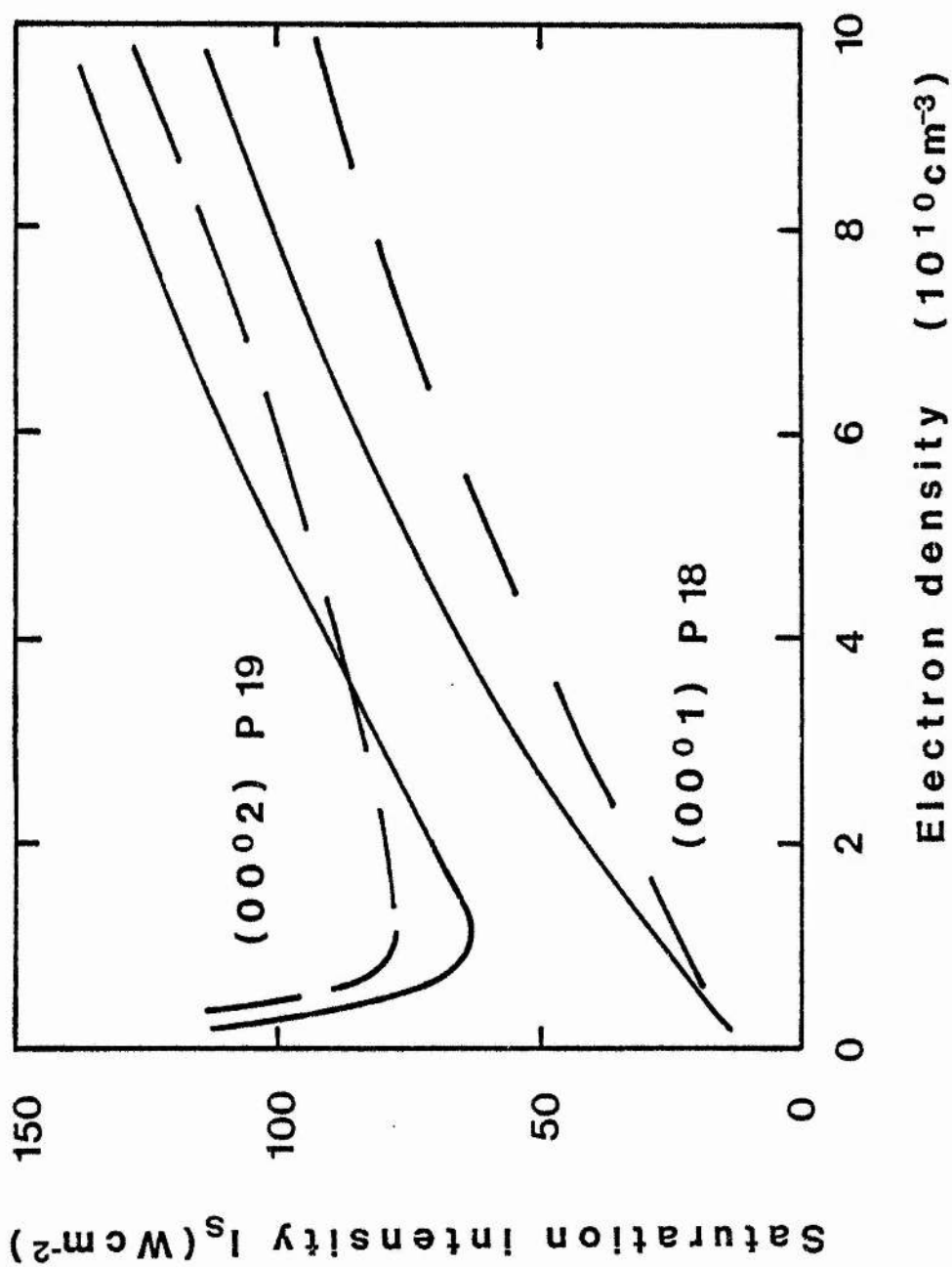


Fig. 8.15. Predicted fundamental and sequence band saturation intensities at 20 torr in 6 CO<sub>2</sub> : 12 N<sub>2</sub> : 82 He mix (solid curves) and 10 CO<sub>2</sub> : 10 N<sub>2</sub> : 80 He mix (dashed curves).

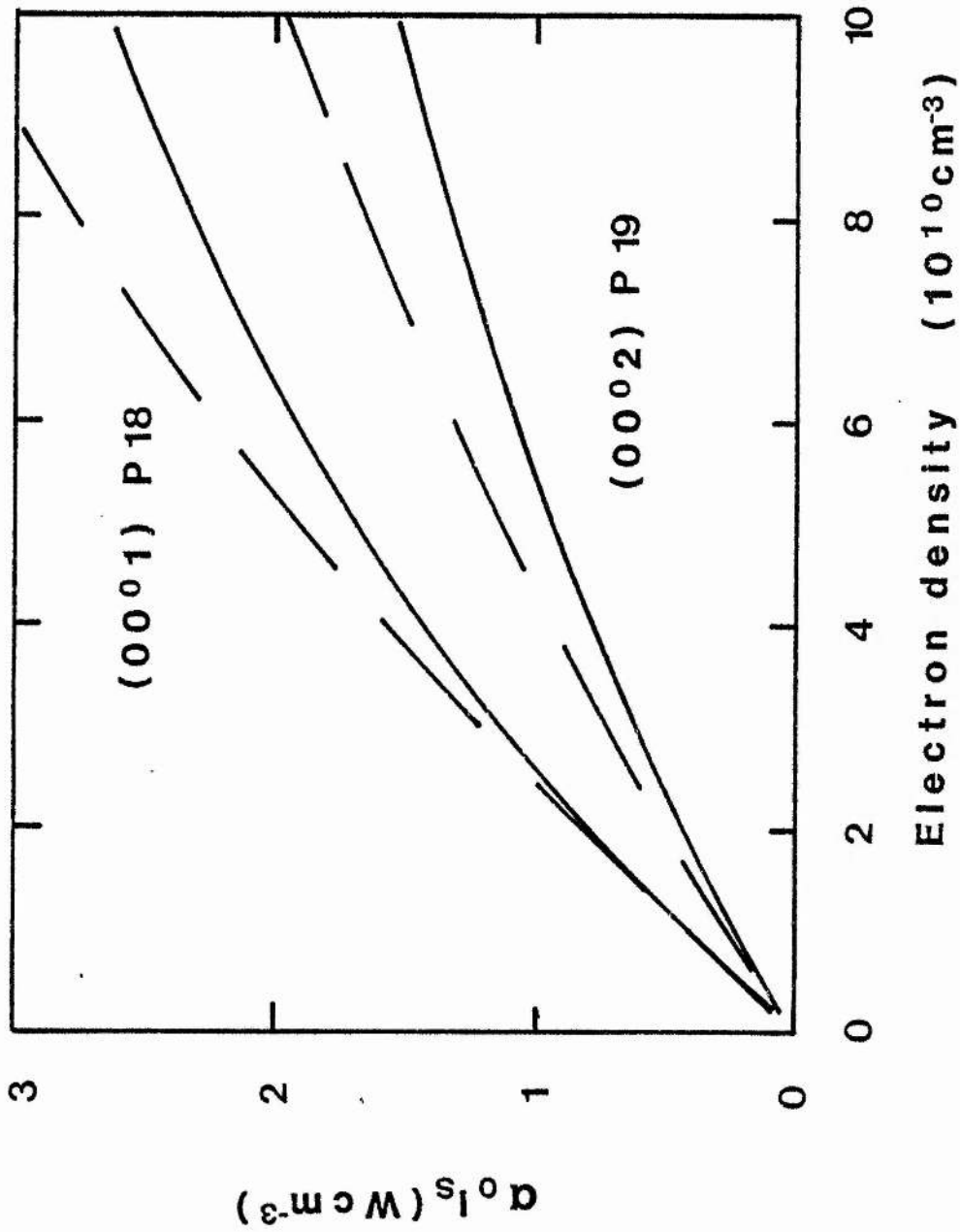


Fig. 8.16. Predicted extractable power densities on fundamental and sequence bands at 20 torr in 6:12:82 mix (solid curves) and 10:10:80 mix (dashed curves).

79.5 mixture the increased  $\text{CO}_2$  content has reduced  $T_3$  at constant electron density. This increases the ratio  $I_{s2}/I_{s1}$  compared to the other gas mixture.

The saturation intensity is important in determining the maximum power extractable from the laser system. Combining (8.6) and (8.13) shows that the power extracted from a medium of gain  $\alpha_0$  by a laser field intensity  $I$  is

$$P_x = \frac{\alpha_0 I_s}{1 + I/I_s}$$

in the pressure broadened approximation. In the limit  $I \gg I_s$  then  $P_x \rightarrow \alpha_0 I_s$  which is the maximum extractable power. The calculated saturation intensities of Fig. 8.15 were multiplied by the appropriate small-signal gains (e.g. from Figure 8.14) to predict the laser power available on the  $00^0_1$  and  $00^0_2$  bands in idealised zero-loss conditions. The results (Fig. 8.16) show that for both gas mixtures and for the whole range of electron density the extractable  $00^0_2$  power is 50-60% of that available on the  $00^0_1$  band.

### 8.5 Summary and conclusions

The characteristics of cw  $00^0_2$  sequence band lasing have been examined experimentally and theoretically. Laboratory measurements show that the behaviour of the sequence band output is determined by the requirement of a high vibrational temperature for the  $\text{CO}_2$  asymmetric stretch mode and (in the case of the present 80 cm active length device) the near-threshold nature of the  $00^0_2$  band oscillation. A comparison of laser power output and small-signal gain shows that optical cavity losses are approximately 30% per round-trip, and that the saturation intensity of the  $00^0_2$  transition ( $I_{s2}$ ) is larger than the  $00^0_1$  band value ( $I_{s1}$ ).

Computer model calculations also predict that  $I_{s2} > I_{s1}$  by an amount which decreases with increasing discharge current. However despite the superior  $00^0_2$  saturation intensities, the extractable  $00^0_2$  band power ( $\propto I_s$ ) is typically 50 to 60% of the available  $00^0_1$  power. This conclusion applies to the ideal case of a zero-loss, infinitely long oscillator cavity or to high-power amplifiers subjected to saturating laser fields. In most practical situations the output power of a sequence band oscillator also depends on optical cavity losses (such as hot-cell absorption and scattering, and diffraction loss in long cavities) and efficient sequence band lasing requires careful optimisation of gas mixture, pressure and discharge current.

References for Chapter 8

1. J. Reid and K. Siemsen, *Appl. Phys. Lett.* 29, 4, 250 (1976).
2. W. Berger, K. Siemsen and J. Reid, *Rev. Sci. Instrum.* 48, 8, 1031 (1977).
3. J. Reid and K. Siemsen, *J. Appl. Phys.* 48, 7, 2712 (1977).
4. K.J. Siemsen and J. Reid, *Appl. Opt.* 17, 22, 3523 (1978).
5. B.J. Feldman, R.A. Fisher, C.R. Pollok, S.W. Simons and R.G. Tercovich, *Opt. Lett.* 2, 1, 16 (1978).
6. P. Lavigne, J.L. Lachambre and G. Otis, *Opt. Lett.* 2, 5, 127 (1978).
7. R.K. Brimacombe, J. Reid and T.A. Znotins, *Appl. Phys. Lett.* 39, 302, (1981).
8. T.A. Znotins, J. Reid and R.K. Brimacombe, *J. Appl. Phys.*, 53, 4, 2843, (1982).
9. S. Moffatt, Ph.D. thesis, University of St. Andrews, (1983).
10. P.O. Clark and J.Y. Wada, *IEEE J. Quant. Electron.* QE-4, 5, 263 (1968).
11. K.J. Siemsen, *Appl. Optics.* 19, 5, 818, (1980).
12. T.S. Fahlen, *Appl. Optics.* 12, 10, 2381, (1973).
13. J. Tulip, *IEEE J. Quant. Electron.* QE-6, 206, (1970).

## CHAPTER 9 : CONCLUSIONS AND RECOMMENDATIONS

### 9.1 Summary

Two important general conclusions may be drawn from the experimental measurements of vibrational temperature,  $00^{\circ}1$  and  $00^{\circ}2$  band gain, and their comparison to theory via the computer model. First, the observed behaviour of fundamental and sequence band small-signal gain is well described by the vibrational temperature approximation, which successfully accounts for the relative magnitudes of  $00^{\circ}1$  and  $00^{\circ}2$  gains as well as their dependences on discharge current, gas mixture and gas pressure. Supportive evidence for the validity of vibrational temperature in the  $\text{CO}_2$  laser system is provided by the tunable diode laser spectroscopy of Reid et al. Second, the absolute magnitudes of measured vibrational temperatures, and their dependence on discharge current and gas pressure, are predicted with tolerable accuracy by the model rate equations using V-V and V-V-T rates available in the open literature, and electron excitation and de-excitation rates related by the principle of detailed balance. In particular, the current-dependent saturation of vibrational temperature is adequately explained by electron superelastic de-excitation, which plays a dominant role in the discharge laser kinetics.

The validity of vibrational temperatures, and their limitation by superelastic collisions, have important repercussions for  $\text{CO}_2$  laser performance. The optimal  $\text{CO}_2$  asymmetric stretch mode temperatures for population of the  $00^{\circ}1$  or  $00^{\circ}2$  levels (around 4500K and 9000K respectively) are not attained in conventional electric-discharge laser media. As shown in Appendix D this imposes small-signal gain restrictions, although in practice the gain of laser amplifiers is also greatly



determined by the prevailing level of  $\text{CO}_2$  dissociation. When the amplifier operates in the presence of intense laser radiation fields (as in the cavity of a cw laser oscillator) then the restrictive influence of electron de-excitation is reduced: the energy dynamics of the system become dominated by the balance of electron excitation and stimulated emission, and the saturation of vibrational temperature with increasing discharge excitation is much less pronounced. In this sense the operating characteristics of cw  $\text{CO}_2$  lasers are little affected by superelastic de-excitation. This is not true of pulsed TE lasers, in which laser oscillation is usually inhibited during the electrical current pulse. The vibrational energy available for laser output is therefore subject to limitation by electron superelastic collisions, and the predicted saturation of vibrational temperature and stored energy with increasing input energy is in excellent agreement with experiment. The saturation implies a deterioration of laser energy yield efficiency with increasing input energy; it is calculated that TE laser operating efficiencies are degraded at even moderate input energy. Predicted  $00^0_1$  band laser efficiencies are in the range 2% - 24%, in agreement with laboratory observations, but contrasting with the 20% - 33% expected on the basis of a simple analysis of excitation efficiency.

The distinctive features of laser operation on the  $00^0_2$  band are also explained by the proposed model. The relatively large  $00^0_2$  band saturation intensities result from the fact that a Boltzmann distribution is maintained among the vibrational levels of the  $\text{CO}_2(v_3)$  mode even in the presence of strong stimulated emission: the ratio of  $00^0_2/00^0_1$  population is thus always much less than unity, producing

concomitantly small  $00^{\circ}2$  band gains. The extraction of  $\nu_3$  mode energy by stimulated emission on the  $00^{\circ}2$  band therefore requires the application of relatively large  $00^{\circ}2$  laser radiation fields, and the modelling studies predict that  $00^{\circ}2$  band saturation intensities are larger than the corresponding  $00^{\circ}1$  values by a ratio which decreases with increasing discharge excitation but which is typically 1.5. This result has interesting implications for the design of high-power sequence band lasers: although sequence band small-signal gain is usually around 40% of that obtainable on the  $00^{\circ}1$  band, the power extractable ( $\propto I_s$ ) from an idealised (infinite length, zero-loss)  $00^{\circ}2$  band laser oscillator is  $\sim 60\%$  of that extractable on the  $00^{\circ}1$  band.

## 9.2 Discussion

The above conclusions illustrate the importance of electron de-excitation of excited species in  $\text{CO}_2$  laser media, an effect not previously accepted as significant. It is interesting to note that in many other gas laser systems the role of electron de-excitation is widely acknowledged. For example, the production of  $2^1\text{S}$  and  $2^3\text{S}$  He metastable pump species in He-Ne and He-Cd positive column discharge lasers shows strong saturation with discharge current, and in the very high electron density discharge of the  $\text{Ar}^+$  laser, even the radiating levels of neutral Argon have saturated populations.<sup>1,2</sup> Even in the  $\text{CO}_2$  system some earlier work has indicated that electron de-excitation is important. Gibbs and Kellock<sup>3</sup> reported that the decay rate of the  $00^{\circ}1$  level in pulsed  $\text{CO}_2\text{-N}_2$  discharges was found to increase with current, giving rates more than twice that expected; they suggested as a possible explanation the discharge formation of long-lived species which subsequently depopulate the upper laser level by collisions, but

it is more likely that they directly observed the effect of electron superelastic collisions. Christophe and Offenberger<sup>4</sup> applied Q-switched 10.6  $\mu\text{m}$  pulses to  $\text{CO}_2$  discharge cell and measured the decay rate of  $00^0_1$  level population as a function of pressure and current. The results showed that the deactivation rate by electron collisions was similar to that by molecular collisions and in pure  $\text{CO}_2$  the electron de-excitation rate was estimated as roughly  $30\text{-}100 \text{ s}^{-1} \text{ mA}^{-1}$ .

Further experimental determinations of electron de-excitation rates are required to allow detailed comparison to theoretically predicted rates. The recent work of Dang et al. (reference 6.19) currently provides the only measurements of excitation and de-excitation rates in  $\text{CO}_2$ :  $\text{N}_2$ : He discharges: the indicated de-excitation/excitation ratio of 3.7 (1:1:8 mix) compares well to the value of 4.5 which was calculated in VIBEX by assuming the principle of detailed balance and averaging over the first 8 levels of the  $\text{N}_2$  and  $\text{CO}_2(\nu_3)$  modes. A comparison of the absolute magnitudes of the measured and predicted rates is more difficult due to the factor of 2 uncertainty in the relationship of average discharge current to electron density as determined by microwave resonance and Boltzmann code calculation. If we assume that the Dang et al. rate measurements refer to the centre-axis of their discharge tube (where the current density is around twice the radial average) then the maximum possible specific electron density for a  $13\text{CO}_2$ :  $9\text{N}_2$ :  $78\text{He}$  mixture is given by Table 4.3 as around  $2 \times 10^9 \text{ cm}^{-3} \text{ mA}^{-1}$ ; combining this value with the BOLTZ excitation rate constants (Table 3.1) gives a predicted  $\text{N}_2 + \text{CO}_2(\nu_3)$  mode excitation rate of  $60 \text{ s}^{-1} \text{ mA}^{-1}$  and an electron de-excitation rate of  $270 \text{ s}^{-1} \text{ mA}^{-1}$ . These figures are still lower than the respective

measured values of  $92\text{s}^{-1}\text{mA}^{-1}$  and  $340\text{s}^{-1}\text{mA}^{-1}$ . The saturation of vibrational temperature with increasing electron density means that the VIBEX calculations are fairly insensitive to the absolute magnitude of the electron excitation rate over a wide range. Therefore the agreement between measured and calculated vibrational temperatures does not necessarily imply the accuracy of the model's excitation rates, and we must accept the possibility that the BOLTZ excitation rate constants are under-estimates. A comparison of the BOLTZ calculations with the predictions of the other Boltzmann codes (those of Nighan<sup>5</sup> and Judd<sup>6</sup>) reveals excellent agreement for the effective  $\text{N}_2$ ,  $\text{CO}$  and  $\text{CO}_2(\nu_3)$  excitation rate constants; therefore any bias in the BOLTZ results is shared by other Boltzmann codes, possibly because all the codes depend on basically the same set of excitation cross-sections. However, too much emphasis should not be placed on a comparison of calculated and measured excitation rates until many more measurements are made under a variety of experimental conditions.

### 9.3 Recommendations

It is clear that more and better experimental measurements of electron excitation and de-excitation rates are required to subject Boltzmann codes to stringent test, and that tunable diode laser spectroscopy (as used by Dang et al.) provides a powerful laboratory tool for such investigations. It is also possible to identify areas where theoretical modelling procedures and approximations can be improved. The calculation of effective superelastic collision rates from the corresponding BOLTZ excitation rates was based on (2.18), the relationship between the rate constants:

$$X_{-l} = X_l \exp\left(\frac{u_l}{kT_e}\right)$$

where  $u_{\ell}$  is the energy of vibrational level  $\ell$ . However this equation applies rigorously only when the electron energy distribution function is Maxwellian, and this is rarely true in molecular gas discharges. For the non-Maxwellian case the more general relationship between excitation and de-excitation cross sections should be used;

$$Q_{-\ell}(u) = \frac{U_{\ell} + u}{u} Q_{\ell}(u_{\ell} + u)$$

and the superelastic rate constants obtained as integrals over the distribution function:

$$\begin{aligned} X_{-\ell} &= \langle Q_{-\ell}(u) \cdot v \rangle \\ &= \langle \frac{u_{\ell} + u}{u} Q_{\ell}(u) \cdot v \rangle \end{aligned}$$

Such a calculation must be internal to a Boltzmann code since a numerical integration is necessary. A suitably modified code would predict effective electron de-excitation rate constants as well as the normal excitation rate constants, eliminating the need for the approximation of equation 2.18 and the subsequent averaging over high-lying energy levels in each vibrational mode.

The need for an improved treatment of line broadening in VIBEX is also apparent. Pure pressure broadening is not a good approximation at total pressures of less than 50 torr. Accurate calculation of laser gain and stimulated emission rates in this pressure regime requires the evaluation of Voigt-profiled lineshapes which include the effects of both pressure and Doppler broadening. Again a numerical method is required since the Voigt convolution integral is not analytically soluble. A convenient FORTRAN program for the calculation of Voigt lineshapes has been developed by Armstrong.<sup>7</sup>

The rate-equation modelling has been restricted to the calcul-

ation of vibrational temperatures and small-signal gain (both steady-state and time-dependent). It is relatively simple to add to the system an equation which describes the photon cavity lifetime, relating the instantaneous laser field intensity and stimulated emission rate to the optical parameters of a laser cavity. Solution of the extended rate equation system would allow prediction of laser output powers and pulse shapes. Such a predictive model, well-tested at the fundamental level of vibrational temperature, may prove useful in further studies of CO<sub>2</sub> laser dynamics.

References for Chapter 9

1. C.E. Webb, "High-Power Gas Lasers" (Inst. Phys. Conf. Ser. No. 29, 1, 1976), pp 11-14.
2. A. Corney, "Atomic and Laser Spectroscopy," (Clarendon Press, Oxford, 1977) pp 335-337.
3. W.E.K. Gibbs and H.A. Kellock, Phys. Lett. 29A, 4, 190 (1969).
4. B.M. Christophe and A.A. Offenberger, Can. J. Phys. 50, 368 (1972).
5. W.L. Nighan, Phys. Rev. A, 2, 1989 (1970).
6. O. Judd, J. Appl. Phys. 45, 4572 (1974).
7. B.H. Armstrong, J. Quant. Spectrosc. Radiat. Transfer 7, 61-88, (1967).

Appendix A. Voltage - current characteristics of typical  
CO<sub>2</sub> laser discharges.

As described in section 3.2.3, knowledge of discharge voltage - current characteristics is essential for the estimation of operating E/N values, electron densities and vibrational excitation rates. Figures A.1 - A.4 show measured V - i characteristics for CO<sub>2</sub> : N<sub>2</sub> : He mixtures in the pressure range 10 - 30 torr. Discharge voltage was measured across electrodes of spacing 3.35 cm (inserted in the positive column) to an estimated precision of  $\pm 1\%$ . The measured voltages were used to calculate corresponding E/N values assuming the gas heating power law (equation 3.10) as displayed in figs. A5 - A7. In general an increase in gas pressure at constant current (or at constant P/L) produced a decrease in E/N.



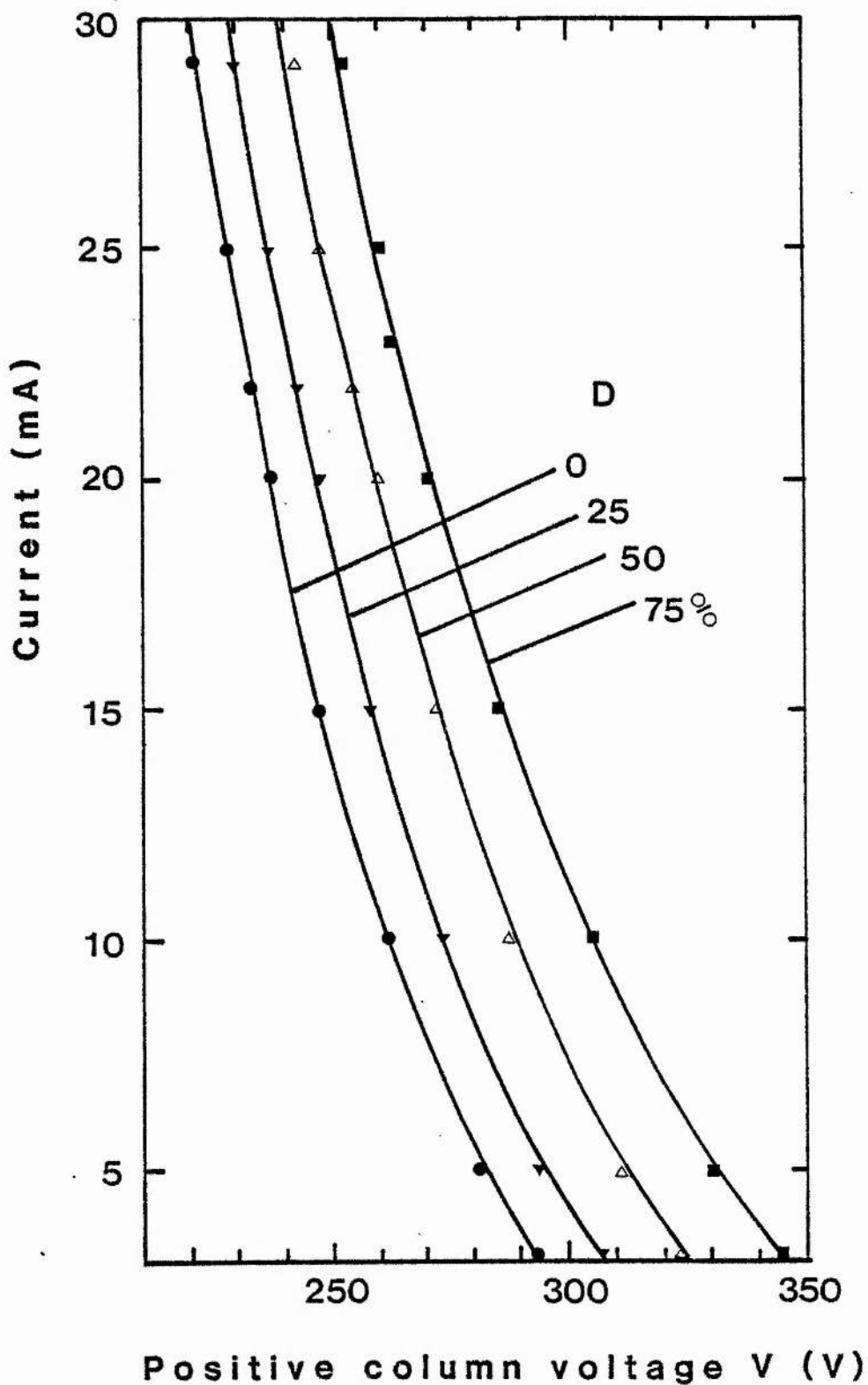


Fig. A.1. Voltage-current characteristics for 13%  $\text{CO}_2$ : 9%  $\text{N}_2$ : 78% He mixture at 10 torr and various levels of  $\text{CO}_2$  dissociation.

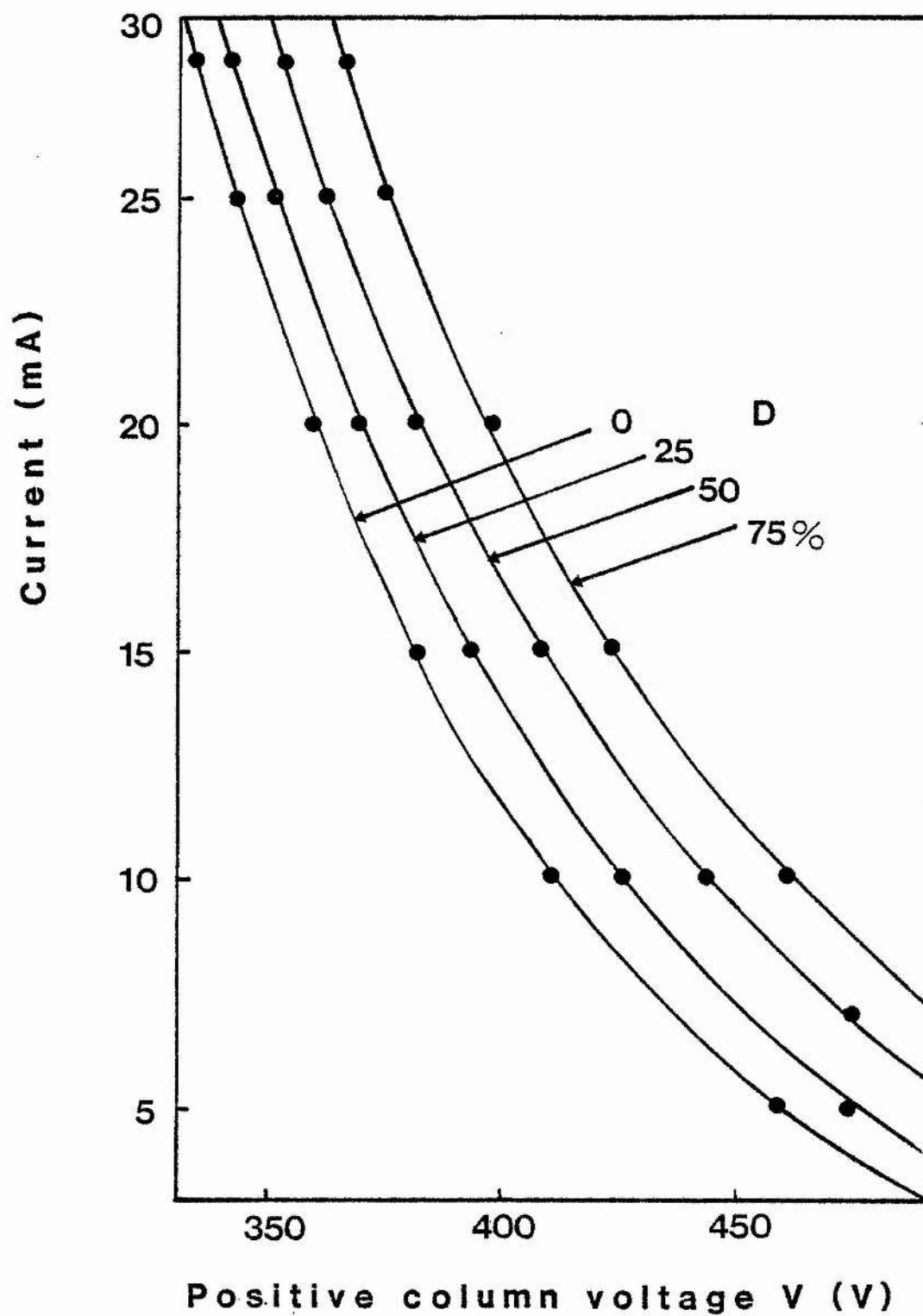


Fig. A.2.  $V-i$  characteristics for 13%  $\text{CO}_2$ : 9%  $\text{N}_2$ : 78% He,  
20 torr.

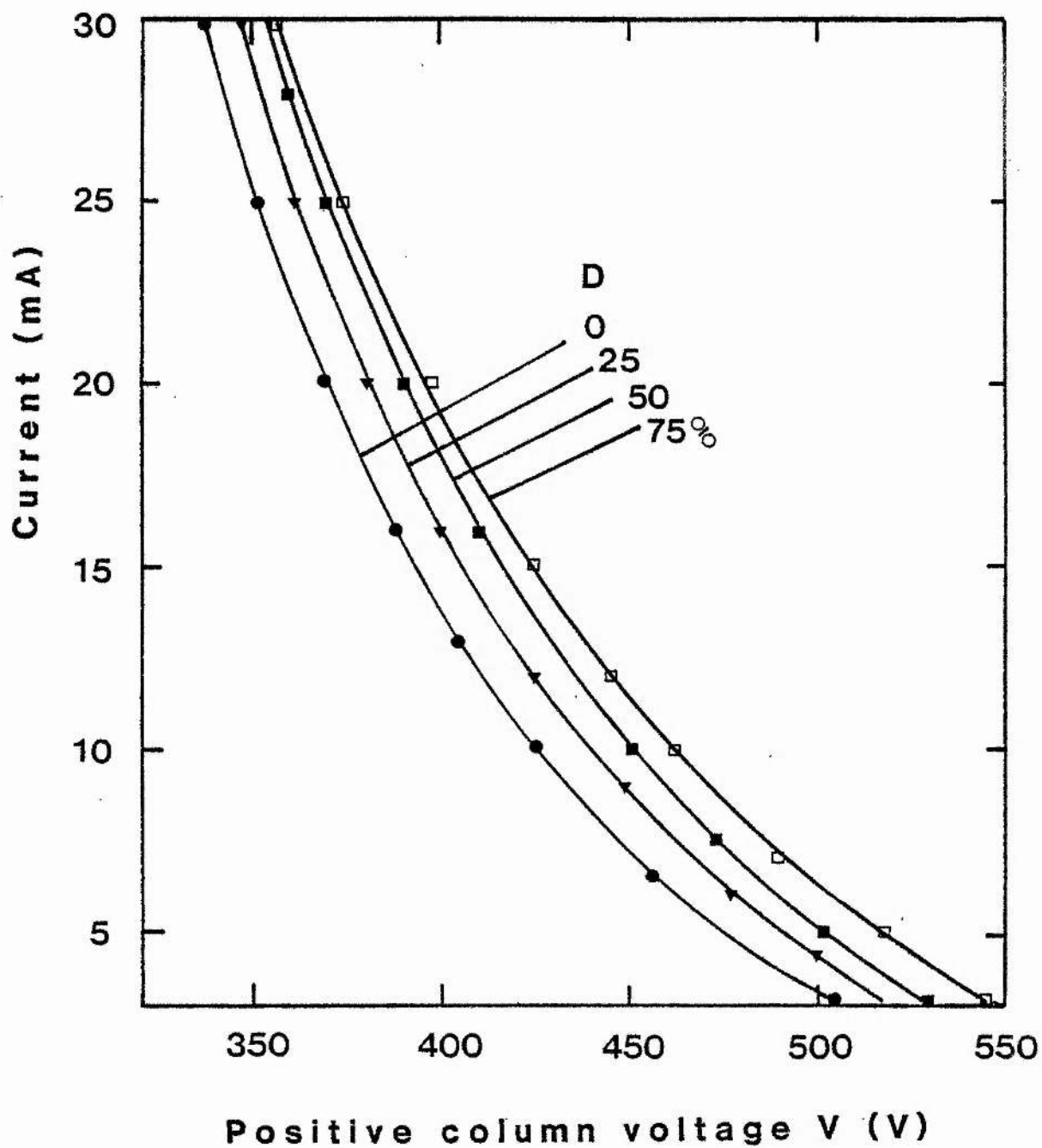


Fig. A.3. V-i characteristics for 6% CO<sub>2</sub>: 12% N<sub>2</sub>: 82% He,  
20 torr.

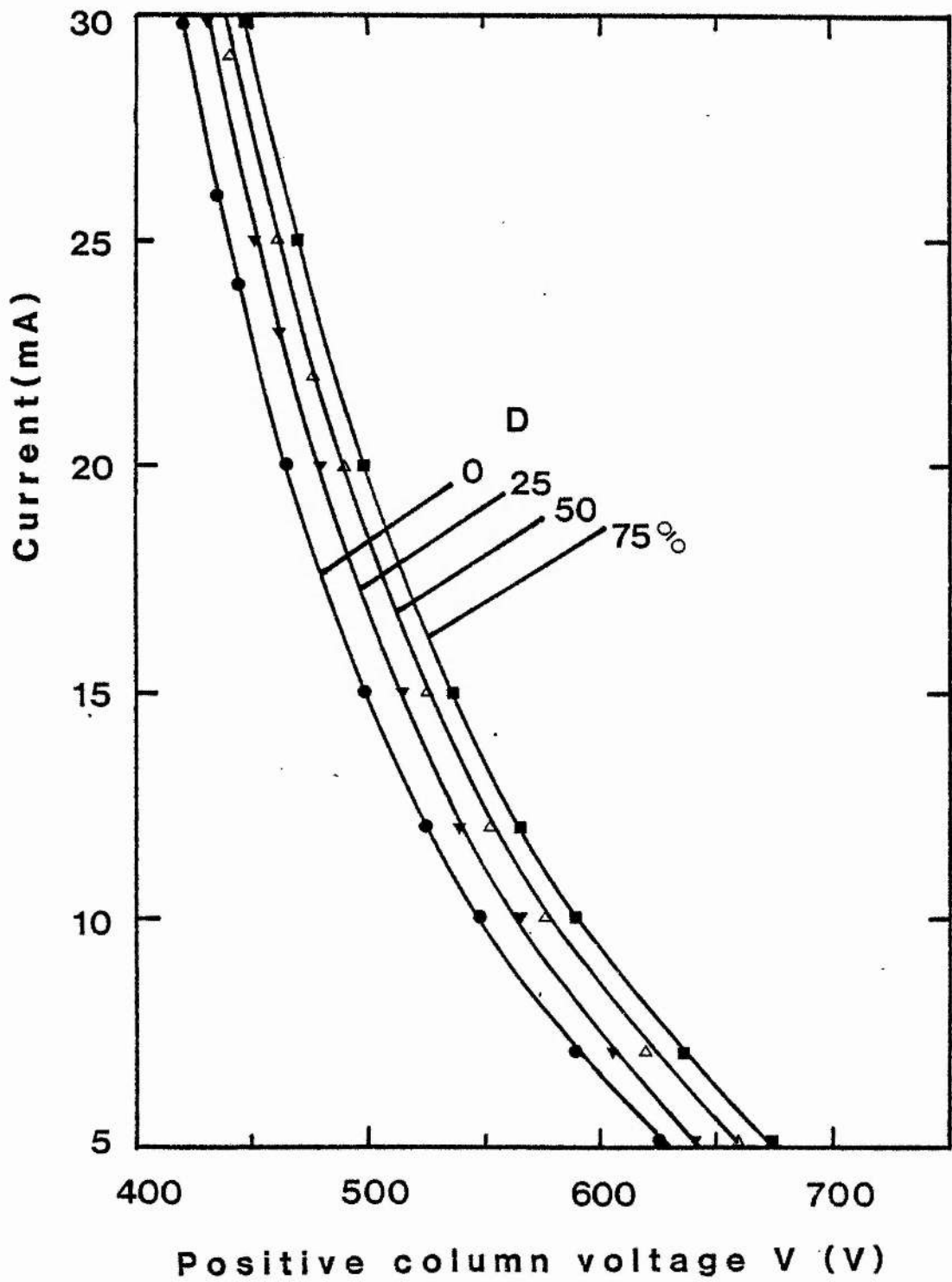


Fig. A.4. V - i characteristics for 6% CO<sub>2</sub>: 12% N<sub>2</sub>: 82% He,  
30 torr.

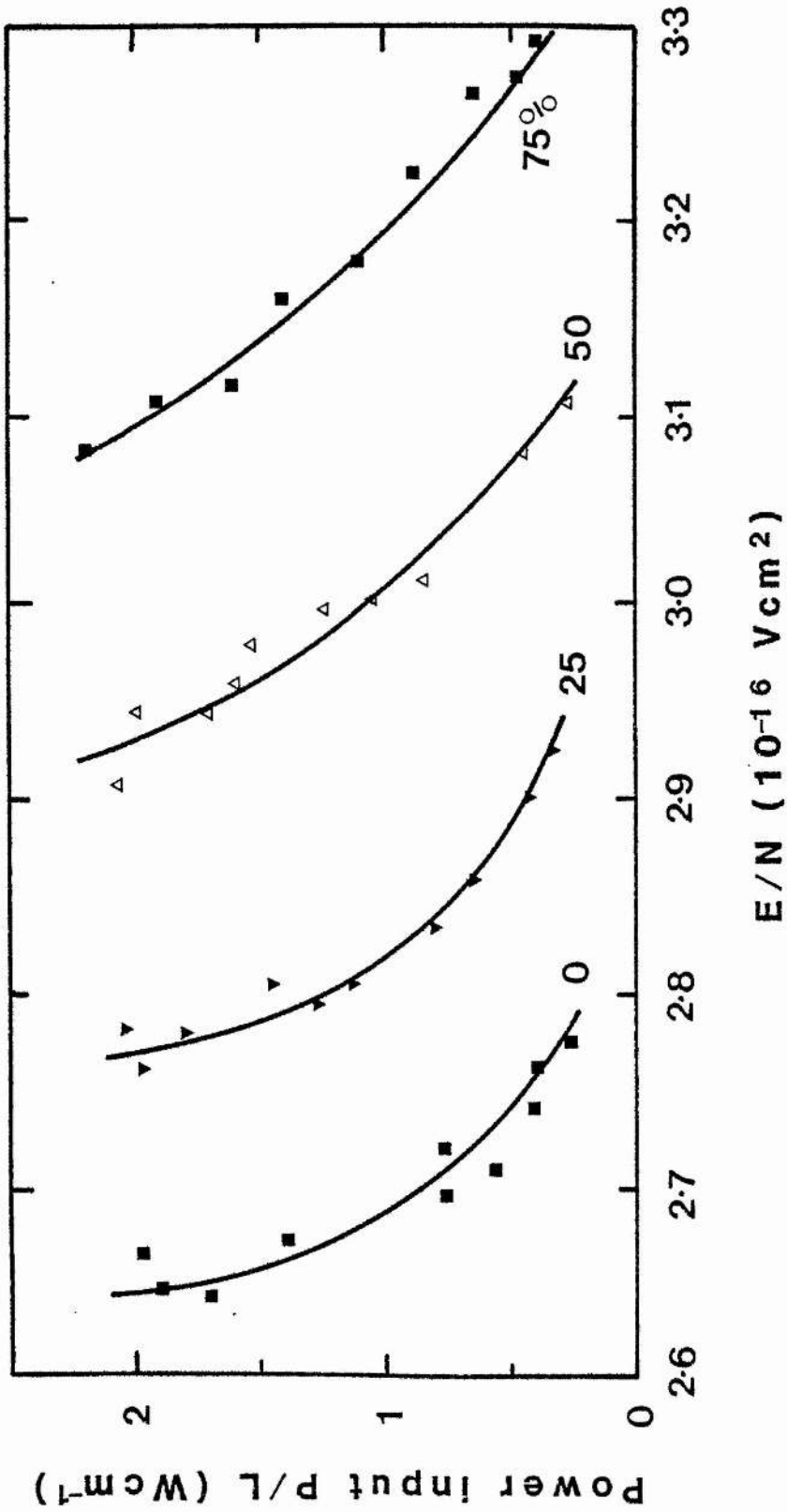


Fig. A.5. Power input versus effective electric field ( $E/N$ ) for 13:9:78 mixture at 10 torr (from data of figure A.1).

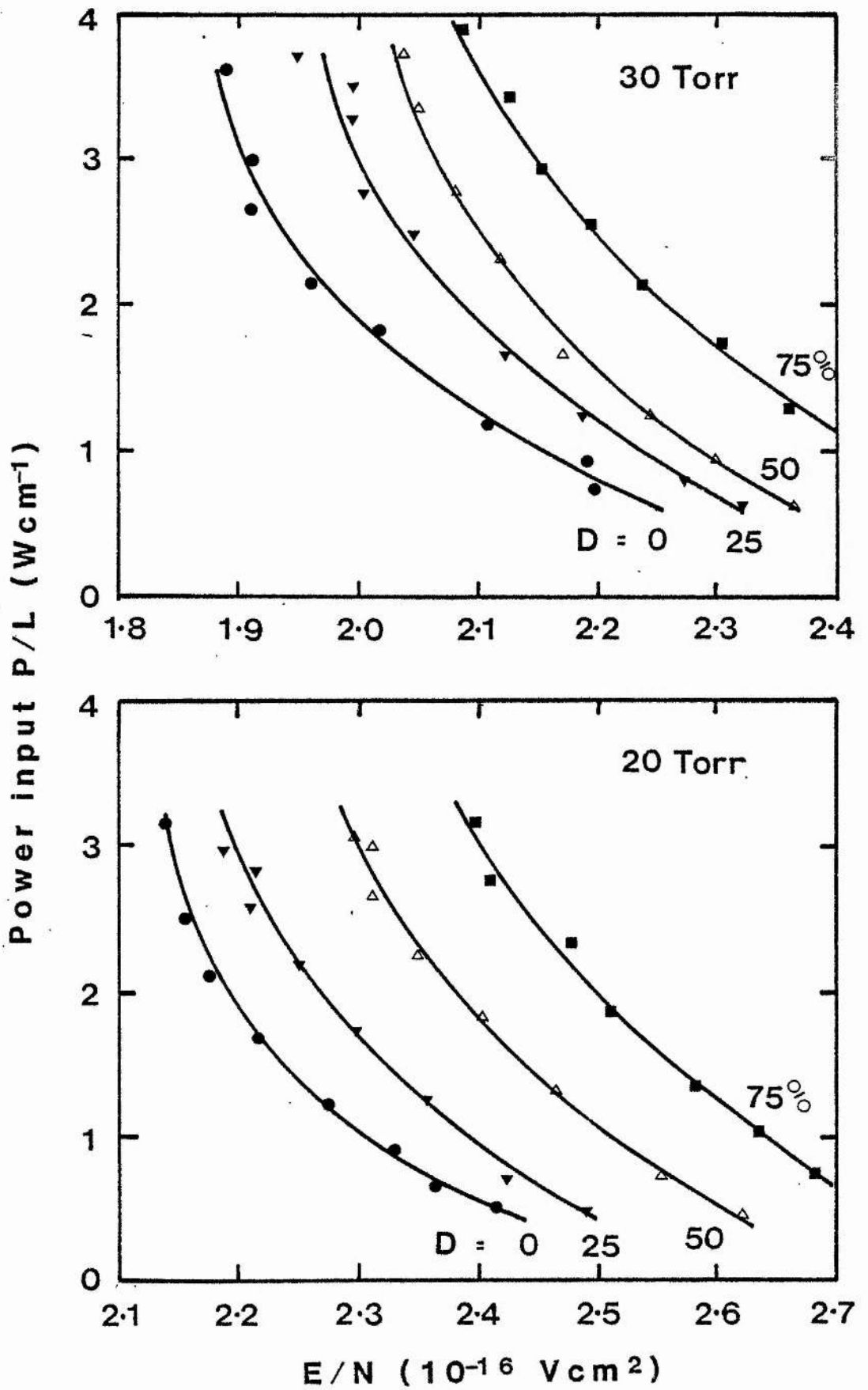


Fig. A.6. P/L versus E/N for 13 : 9 : 78 mixture.

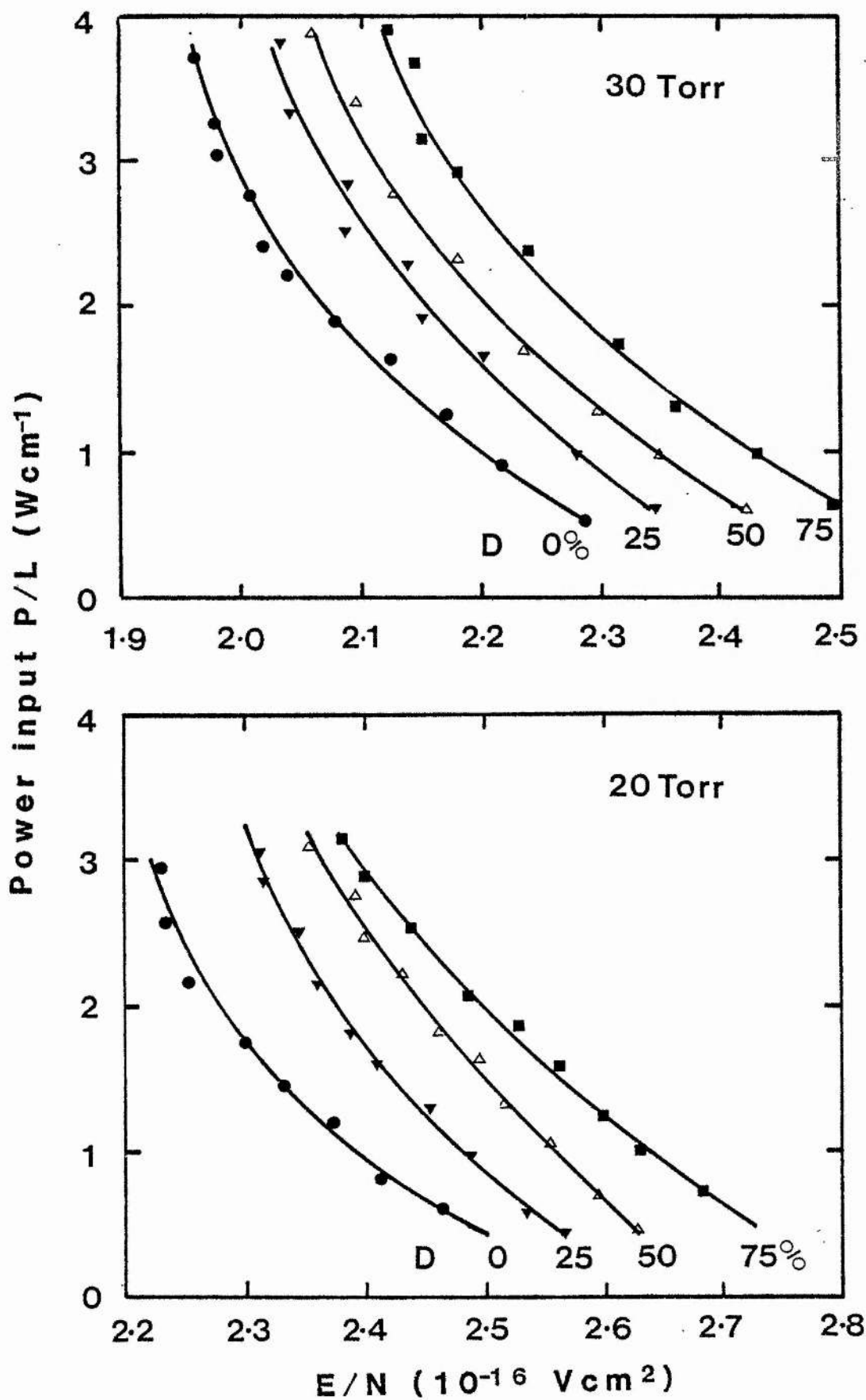


Fig. A.7.  $P/L$  versus  $E/N$  for 6:12:82 mixture (from figures A.3 and A.4).

Appendix B. The observation of an anomalous dependence of electron density on pressure.

In the microwave cavity resonance measurements (chapter 4) it was noted that the electron density at constant current exhibited a slight inverse dependence on pressure. Typical results are plotted in figure B.1 which shows that, for 7 mA discharge current, a pressure increase from 10 to 40 torr produces a 30% decrease in average electron density. The relative decrease is greater for higher currents. A similar negative pressure dependence of electron density has been reported by Novgorodov et al. (ref. 4.8), but was not considered significant. However, such a dependence is clearly anomalous, since an increase in pressure at constant current produces a decrease in the discharge  $E/P$ , and therefore a decrease in the electron drift velocity. By the current transport equation (4.1), this should result in an increased averaged electron density, as is the case for Helium (see figure 4.2).

To investigate the anomaly measurements were made on various other pure, flowing gases. The results showed that for  $\text{CO}_2$ ,  $\text{CO}$  and  $\text{N}_2$  the electron density decreases with increasing pressure above 10 torr, despite a decreasing discharge  $E/P$  (figure B.2). The possibility of systematic error was considered. Molecular gases at moderate pressures exhibit relatively large electron collision frequencies ( $\nu_m$ ) and resultant  $\gamma$ -factors ( $\gamma = \nu_m/\omega$ ) can be as large as 0.8 - 1.0. It has been shown by Persson (ref.4.3) that the derivation of equation 4.10, which relates the average electron density to  $\Delta f$  and  $\gamma$ , depends on the assumption  $\gamma^2 \ll 1$ . If this assumption is discarded then a more complicated relationship is obtained:



$$\frac{2 \Delta f}{f_0} + \frac{\alpha \eta}{1 + \gamma^2} \left[ 1 + \frac{\alpha \gamma^2 \eta K}{1 + \gamma^2} \right] = 0 \quad (\text{B.1})$$

where as before  $\eta$  is the ratio of electron density to the critical electron density.  $K$  is an overlapping mode factor defined

$$K = \sum_i \left( 1 + \frac{f_0}{f_i} \right)^{-2} \left( \frac{f_i}{f_0} - 1 \right)^{-1} \quad (\text{B.2})$$

where the summation is over the  $i$  modes of the microwave cavity with resonance frequencies  $f_i$ .  $K$  represents the perturbative influence of neighbouring modes on the resonant frequency of the observed mode. The perturbation will be greater as resonance broadening increases.

An experimental search for additional cavity resonances in the range 8.2 - 12.5 GHz revealed a single extra resonance at 9.071 GHz (attributed to the TE 011 mode). Using this value for  $f_1$  in equation (B.2), and putting  $f_0 = 9.245$  GHz for the TM 020 mode, we obtain  $K = -13$ . Re-arranging (B.1) to reveal quadratic nature of the equation gives

$$\eta^2 \left[ \frac{\alpha^2 \gamma^2 K}{1 + \gamma^2} \right] + \eta \left[ \frac{\alpha}{1 + \gamma} \right] + \frac{2 \Delta f}{f_0} = 0 \quad (\text{B.3})$$

which can be straight-forwardly solved for  $\eta$ . Putting  $K = -13$ ,  $\alpha = 0.16$ , it is easy to show that for  $\gamma = 1.0$  and  $\Delta f$  in the range  $\sim 5$  MHz, then the change in  $\eta$  by using (B.3) rather than equation 4.10 is only about 3%. This is far smaller than the observed electron density decrease, and it can be concluded that large  $\gamma$  - values and overlapping mode effects are not responsible for the anomalous pressure dependence.

A more likely systematic effect concerns the radial averaging of electron density, as expressed by equations (4.5) - (4.9). For the TM020 mode the measured electron density will be a weighted radial average defined by

$$\bar{n}_e = \frac{\int_0^{R_p} r n_e(r) \left| J_0 \left( x_{02} \frac{r}{R} \right) \right|^2 dr}{\int_0^R r \left| J_0 \left( x_{02} \frac{r}{R} \right) \right|^2 dr} \quad (\text{B.5})$$

where the exact form of the radial electron density profile is unknown. Vlachos and Hsuan<sup>2</sup> have measured radial electron density profiles in mercury discharge positive columns by comparing the resonances of two microwave cavities, using the TE011 and TM020 modes. Similar measurements were made by Burkley and Sexton<sup>3</sup>. In each case some general form of the radial profile was assumed. Nevertheless the results showed that:

- (i) At the lowest pressures the radial distribution is peaked on the axis with a shape somewhere between the Bessel and trapezoidal forms and remaining reasonably constant over the current range.
- (ii) As the pressure is raised an increasingly flatter distribution emerges, and the trend is accentuated with increasing current.
- (iii) The difference in measured electron density values which is produced by evaluating the radial average instead of the axial density is 20 - 30%.

These effects could explain the observations in the molecular gas discharges. Since the TM 020 mode is sensitive to the on-axis electron density with increasing pressure may be evidenced by a decrease in the weighted radial average value (B.5). Since the tendency towards a flatter radial profile is exaggerated at higher current, then the observed non-linearity of electron density with current at high pressure is also explained. The tendency towards flatter radial profiles at high pressures and currents has also been predicted by the theoretical analysis of Ecker and Zöller<sup>4</sup> for thermally inhomogeneous helium positive columns. At still higher pressures and currents the phenomenon of discharge constriction occurs, greatly increasing the axial current density. However, no constriction was visible during the laboratory electron density measurements.

A conclusive demonstration of the importance the radial profile pressure dependence would require the evaluation of (B.5) for real electron density profiles at various pressures in CO<sub>2</sub> laser mixtures. No such density profile measurements are presently available. However, Rogoff has recently developed a model<sup>5</sup> of electron production and loss in diffusion-controlled gas discharge columns and used it to calculate the effect of diffusion on CO<sub>2</sub> laser discharges<sup>6</sup>. The analysis predicts radial profiles which are close to zero-order Bessel functions at low pressure but whose axial electron densities decrease with increasing pressure in a number of cases<sup>7</sup>. Thermal inhomogeneities are not included in the model, and this may limit its applicability. Nevertheless the insertion of the predicted electron density profiles in equation B.5 remains the most promising way to estimate the effect of pressure on the cavity-field-averaged electron density, and this possibility is currently being investigated.

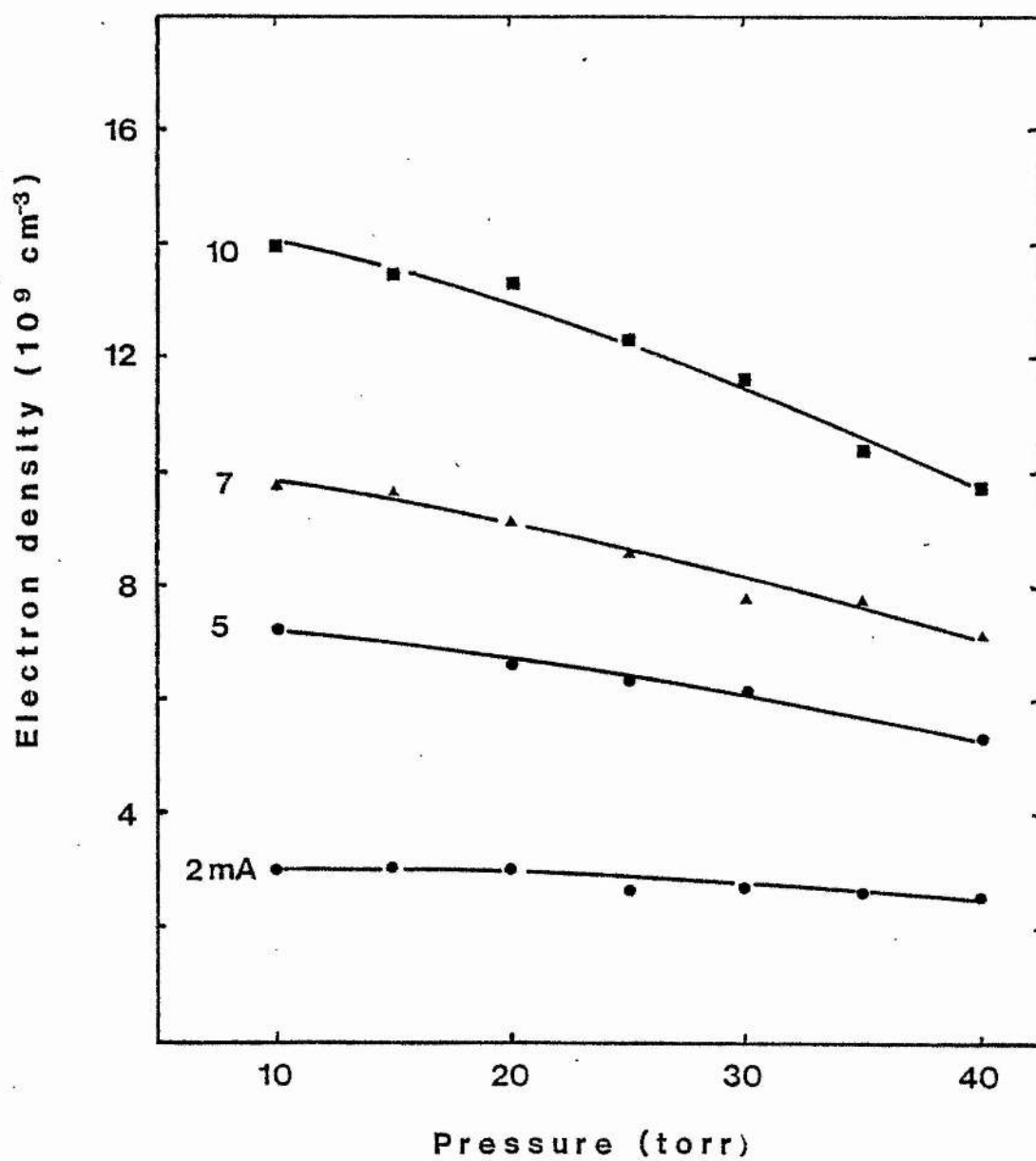


Fig. B.1. Pressure dependence of electron density at constant current in 13%  $\text{CO}_2$  : 9%  $\text{N}_2$  : 78% He mixture (flow rate 50 sccm).

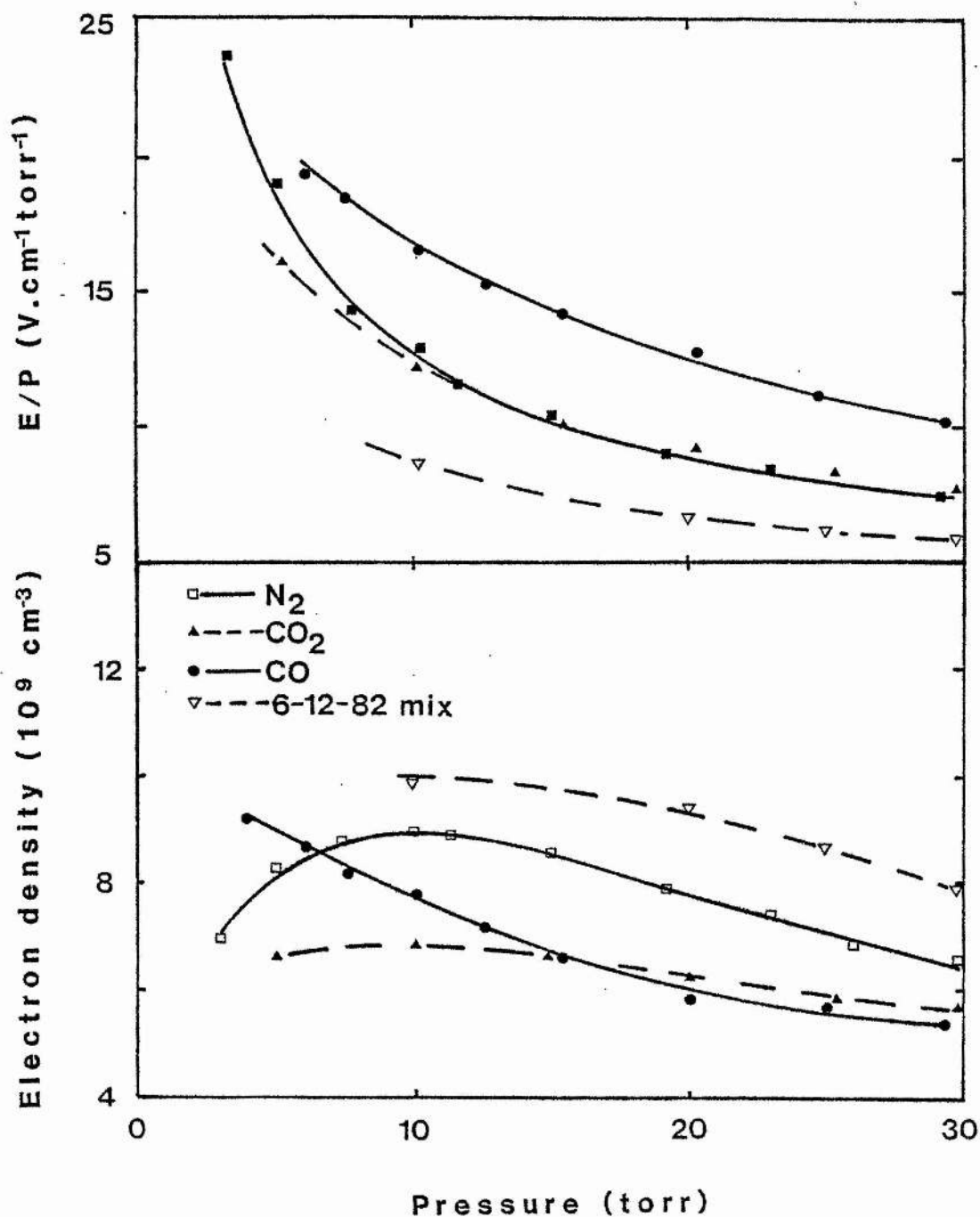


Fig. B.2. Constant-current (7 mA) pressure dependence of measured E/P and electron density in pure, flowing N<sub>2</sub>, CO<sub>2</sub>, CO and in 6% CO<sub>2</sub> : 12% N<sub>2</sub> : 82% He laser mixture.

References for Appendix B.

1. B.E. Cherrington, "Gaseous Electronics and Gas Lasers" (Pergamon Press, Oxford, 1980), chapter 5.
2. M.A.W. Vlachos and H.C.S. Hsuan, J. Appl. Phys. 39, 11, 5009 (1968).
3. C.J. Burkley and M.C. Sexton, J. Appl. Phys. 39, 11 5013 (1968).
4. G. Ecker and O. Zöllner, Phys. Fluids 7, 12, 1996, (1964).
5. G.L. Rogoff, J. Appl. Phys. 50, 11, 6601 (1981).
6. G.L. Rogoff, paper BB - 8, 35th Gaseous Electronics Conf. Dallas, Texas, 19 - 22nd Oct. 1982.
7. G.L. Rogoff, private communication.

Appendix C: The calculation of  $T_1 = T_2$  in VIBEX.

In the vibrational temperature approximation the total population density of the combined  $\text{CO}_2$  symmetric stretch and bending modes is

$$n_1 = \sum_{\ell=1}^{\infty} n_{\ell 00} + \sum_{m=1}^{\infty} n_{0m0}$$

$$= \sum_{\ell=1}^{\infty} \frac{n}{Q_V} (x_1)^\ell + \sum_{m=1}^{\infty} \frac{n}{Q_V} (m+1)(x_2)^m$$

where as usual  $n$  is the total number density of  $\text{CO}_2$  molecules,  $Q_V$  is the vibrational partition function:

$$Q_V = [(1-x_1)(1-x_2)^2(1-x_3)]^{-1} = \frac{n}{n_0} \quad (\text{C.1})$$

$$x_i = \exp\left(-\frac{h\nu_i}{kT_i}\right), \quad i = 1, 2, 3.$$

and  $n_0$  is the ground state population. Applying the infinite series summations of (5.10) and (5.11) we obtain:

$$n_1 = \frac{n}{Q_V} \left( \frac{1}{1-x_1} + \frac{1}{1-x_2} + \frac{x_2}{(1-x_2)^2} - 2 \right) \quad (\text{C.2})$$

From (C.1),

$$\frac{1}{1-x_1} = \frac{n}{n_0} (1-x_2)^2 (1-x_3) \quad (\text{C.3})$$

Substituting (C.3) in (C.2) gives

$$\frac{n_1}{n_0} = \frac{n}{n_0} (1-x_2)^2 (1-x_3) + \frac{1}{1-x_2} + \frac{x_2}{(1-x_2)^2} - 2 \quad (\text{C.4})$$

which can be solved for  $x_2$  if  $x_3$  is known.

Introducing the new variables

$$X = 1 - x_2$$

$$A = 1 - x_2$$

then

$$\frac{n_1}{n_0} = \left( \frac{An}{n_0} \right) X^2 + \frac{1}{X} + \frac{1-X}{X^2} - 2$$

which, when multiplied by  $X^2$  is equivalent to

$$\left( \frac{An}{n_0} \right) X^4 - \left( \frac{n_1}{n_0} + 2 \right) X^2 + 1 = 0 \quad (C.5)$$

This is the quartic equation which relates the combined mode population  $n_1$  to the combined mode temperature  $T_1 = T_2$ .



GAIN LIMITATIONS IN CO<sub>2</sub> LASERS

J. MELLIS and A.L.S. SMITH

*Department of Natural Philosophy, University of Strathclyde, Glasgow G4 0NG, Scotland, U.K.*

Received 22 December 1981

We have measured the carbon dioxide  $\nu_3(00^0n)$  mode vibrational temperature ( $T_3$ ) in sealed and flowing CO<sub>2</sub> laser discharges. Results confirm  $T_3$  saturation at high current. The observed behaviour is compared to theory using a comprehensive numerical model of the CO<sub>2</sub> kinetic system, and explained in terms of microscopic processes. The analysis is extended to the calculation of laser gain, and the relative importance of thermal and dissociative effects is elucidated.

## 1. Introduction

With increasing discharge excitation saturation (and subsequent reduction) of the gain and oscillation output power in cw and TEA CO<sub>2</sub> lasers has frequently been observed in the past, and Ballik et al. [1] have shown that this cannot be completely accounted for by discharge deterioration and gas heating effects. Davies et al. [2] have sought to show that such output reduction with increased input energy is explained by "overpumping" of the CO<sub>2</sub> to very high values of the  $\nu_3(00^0n)$  mode vibrational temperature ( $T_3$ ) beyond the optimum for  $00^01$  level population ( $\sim 5000$  K, see fig. 2 below). They used a computer model which assumed that the CO<sub>2</sub> populations in the symmetric stretch, bending and anti-symmetric stretch modes are described by temperatures  $T_1$ ,  $T_2$  and  $T_3$ , and found that they needed  $T_3$  values of 3000–7000 K to match experimental gain peaking results.

The advent of the CO<sub>2</sub> sequence band laser [3] has made possible for the first time direct experimental measurements of  $T_3$  in laser discharges. The Reid and Siemsen measurement technique [4] compares the amplification of a beam from a fundamental  $00^01 \rightarrow [10^00, 02^00]_{I,II}$  oscillator with the amplification of a beam from a sequence  $00^02 \rightarrow [10^01, 02^01]_{I,II}$  oscillator in a gain cell, and the anti-symmetric stretch mode temperature of CO<sub>2</sub> is obtained immediately as

$$T_3 = h\nu_3/k \ln(2\alpha_1/\alpha_2)$$

where  $\alpha_1$  is the fundamental band gain and  $\alpha_2$  that of a comparable first sequence band line. Siemsen et al. [4] have measured vibrational temperatures in low pressure (5 to 15 Torr) flowing gas laser mixtures of 1200–2500 K and Dang et al. [5] have obtained temperatures of 1000–2000 K in TE discharges at 92 torr. In all instances the temperatures saturated at high discharge currents (dc discharges) or input energies (pulsed discharges). Thus the results indicate that a chief limitation on CO<sub>2</sub> laser gain in both cw and TEA systems is the saturation of the  $\nu_3$  mode vibrational temperature with high excitation rates and that this effect depends on some unidentified, but non-thermal mechanism.

## 2. Gain and vibrational temperature measurements

We have used an oscillator-amplifier system similar to that of ref. [4] to measure CO<sub>2</sub>( $\nu_3$ ) mode vibrational temperatures in flowing and sealed-off discharges. Our probe laser (sealed active length 80 cm, hot cell length 17 cm) is tunable over a number of lines on the  $00^01$  and  $00^02$  bands using a PZT mounted output coupler, and the gain cell is a simulated laser tube of active length 52 cm and 1 cm internal diameter. The tubes and vacuum system are of clean quartz and stainless steel construction with gain cell pressures and flow rates regulated by a MKS Baratron Type 254 multi-channel flow controller monitoring thermal conductance flow meters, and capacitance manometers on the

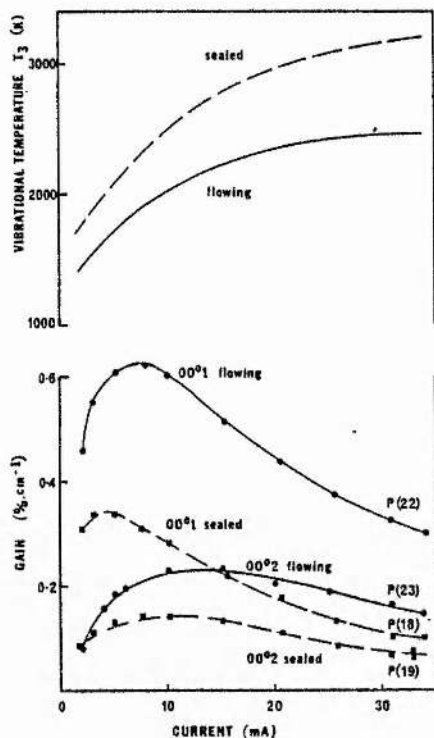


Fig. 1. Variation with current of measured gain on  $00^0 1$  fundamental and  $00^0 2$  sequence transitions and derived  $\nu_3$  temperature  $T_3$  for sealed and flowing (50 sccm) 6-12-82,  $\text{CO}_2\text{-N}_2\text{-He}$  gas mixture with 10 torr total pressure.

tube inlet and outlet. Research grade was flowed through the gain cell or the tube was sealed.  $\text{CO}_2$  dissociation levels at the amplifier tube outlet were measured with a Kratos-AEI MS 105 magnetic sector mass spectrometer. Measurements were taken alternatively on  $00^0 1$  fundamental and equivalent  $00^0 2$  sequence lines [4] using a chopped two beam ratiometric system to minimise noise and system intensity fluctuations.

Results obtained with this system are shown in fig. 1 for a 6-12-82  $\text{CO}_2\text{-N}_2\text{-He}$  laser mix under sealed and flowing conditions. Sequence band gain is lower than the fundamental band gain in each case ( $\approx 1:2$ ), and it is noticeable that fundamental gain peaks at lower discharge current. Sealed gains are much reduced, and peak at lower current than the corresponding flowing gain. Additionally, fig. 1 plots the vibrational temperatures ( $T_3$ ) derived using eq. (1) from the smooth curves through the experimental gain points. The tendency for  $T_3$  saturation at high current is confirmed;

Table 1  
Current dependent variables used in gain model of 6-12-82,  $\text{CO}_2\text{-N}_2\text{-He}$  mixture at 10 torr total pressure

Discharge current (mA)	Measured $\text{CO}_2$ dissociation (%)	Gas temperature $T$ [13] (K)	Temperature $T_1 = T_2$ [4] (K)
2	32	291	317
5	46	306	340
10	57	328	379
20	69	359	456
30	80	384	533

however, the sealed-off saturated temperature (3200 K) is significantly higher than that of the flowing gas discharge (2500 K). Gain cell outlet  $\text{CO}_2$  dissociation levels were measured for the flowing gas mixture and the results are tabulated in table 1.

Fig. 2 shows the fractions of the  $\text{CO}_2$  population which should be in the  $00^0 1$  and  $00^0 2$  levels for different  $T_3$  vibrational temperatures, using the standard expression for the population of a level ( $l, m, n$ ) in  $\text{CO}_2$  (see for instance Mellis and Smith [6]). Two points are immediately apparent, first the values of  $T_3$  actually measured (fig. 1) are considerably less than those which would maximise the  $00^0 1$  and  $00^0 2$  populations (and hence laser gains). Second, the ratio of the sizes of the  $00^0 1$  and  $00^0 2$  gains for a set of conditions (fig. 1) can be immediately matched by taking the ratio of the  $00^0 1$  and  $00^0 2$  fractional populations for the determined value of  $T_3$  (together with the known ratio of the transition matrix element,  $\sim 1.9$  [4]) without allowing for any

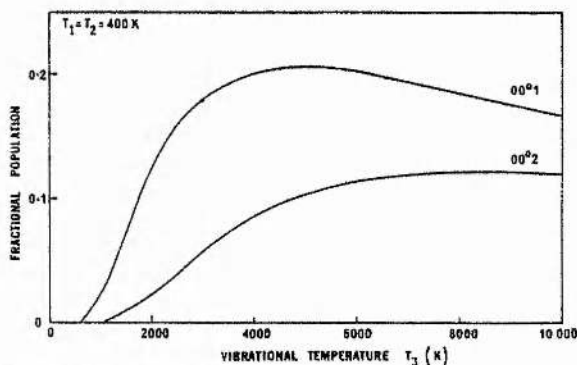


Fig. 2. Calculated vibrational temperature dependence of  $\text{CO}_2$   $\nu_3$   $00^0 1$  and  $00^0 2$  level populations.

lower laser state populations. This suggests the relative unimportance of lower laser level populations in controlling the small-signal gains.

### 3. Vibrational mode model

In order to understand more fully the current-dependent behaviour of the gain and asymmetric mode vibrational temperature, we have constructed a detailed kinetics model of the  $\text{CO}_2\text{-N}_2\text{-CO-O}_2\text{-He}$  system. The basis of the model, of which details will be given in a subsequent paper, is the conventional vibrational mode scheme whose use is justified by the very fast resonant exchange rates which occur within molecular vibrational modes. The comparatively slow exchange processes between modes are included using the temperature dependent rate constants available in the literature [7]. Relaxation processes from the excited states include (i) (V-V-T) and (V-T) molecular collisions and (ii) superelastic electron collisions (collision of the second kind). The rate constants for the superelastic processes are calculated using the principle of detailed balance from the corresponding excitation rate constants. These in turn are calculated by a numerical solution of the electron Boltzmann equation, BOLTZ [8] which has been extended to include the inelastic collision processes of the CO and  $\text{O}_2$  as well as the usual  $\text{CO}_2$  and  $\text{N}_2$ . The system of vibrational rate equations is solved on a computer, using a predictor-corrector iterative scheme, for the excited mode populations and vibrational temperatures  $T_2$ ,  $T_{\text{N}_2}$  and  $T_{\text{CO}}$ .

Fig. 3 shows results for the  $\text{CO}_2\text{-N}_2\text{-He}$  mixture assuming constant 50%  $\text{CO}_2$  dissociation. Apart from superelastic processes the major deactivation of the excited CO,  $\text{N}_2$  and  $\text{CO}_2(\nu_3)$  is by V-V-T collisions ( $\text{CO}_2(\nu_3) \rightarrow \text{CO}_2(\nu_1, \nu_2)$ ); V-T deactivation of  $\text{CO}_2$ , CO or  $\text{N}_2$ , wall collisions and spontaneous decay are all much slower. The "drain" of energy from the  $\text{CO}_2(\nu_3)$  mode is transmitted to the excited  $\text{N}_2$  mode, and to a lesser extent to the excited CO mode, by the V-V coupling between them. Thus it is the relative inefficiency of the  $\text{CO-CO}_2(\nu_3)$  coupling which allows the CO to maintain a high vibrational temperature despite the energy loss channel through the  $\text{CO}_2$ . This explanation is supported by the dashed curves in fig. 3, which were calculated assuming inter-mode V-V rate constants ap-

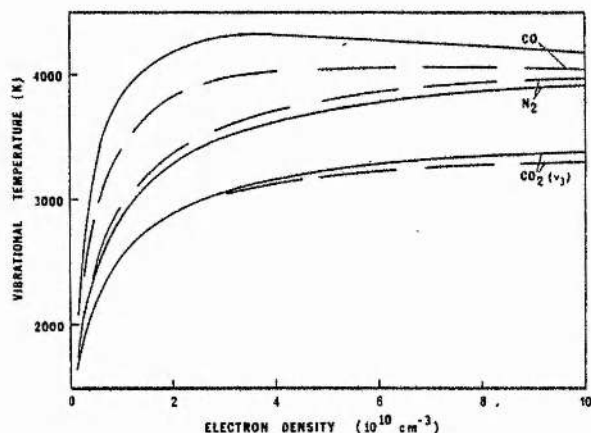


Fig. 3. Computer model prediction of variation of  $\text{CO}_2(\nu_3)$ ,  $\text{N}_2$  and CO vibrational temperatures with discharge electron density in a 6-12-82,  $\text{CO}_2\text{-N}_2\text{-He}$  gas mixture (50%  $\text{CO}_2$  dissociation,  $E/N$   $3.0 \times 10^{-26} \text{ V cm}^2$ ). Solid lines with 400 K as the gas temperature for the V-V inter-mode rate constants, dashed lines for 600 K.

propriate to a higher value of the ambient gas temperature. This increases the  $\text{CO-CO}_2(\nu_3)$  coupling, decreasing  $T_{\text{CO}}$ , but reduces the coupling between  $\text{N}_2$  and  $\text{CO}_2(\nu_3)$  which increases  $T_{\text{N}_2}$ .

As was shown in fig. 1, the  $\text{CO}_2(\nu_3)$  saturation temperature increased from  $\sim 2500$  K in the flowing discharge to  $\sim 3200$  K in the sealed discharge where higher  $\text{CO}_2$  dissociation levels prevail. The general form of this behaviour can be understood by considering the two competing processes: (i)  $\text{CO}_2(\nu_3) \rightarrow \text{CO}_2(\nu_1, \nu_2)$  deactivation and (ii) CO and  $\text{N}_2$  V-V exchange pumping to the  $\text{CO}_2(\nu_3)$ . In a considerably dissociated mixture the excitation of the remaining  $\text{CO}_2$  molecules is favoured both by the increased CO content and by the decrease in  $\text{CO}_2\text{-CO}_2$  deactivation. The dominant effect is the deactivation decrease and this leads to relatively high  $T_3$  values in mixtures with low  $\text{CO}_2$  partial pressures.

### 4. Model explanations of gain and temperature effects

A detailed comparison of the calculated and measured  $\text{CO}_2(\nu_3)$  temperatures  $T_3$  and the calculated and measured fundamental band gains for the sealed  $\text{CO}_2\text{-N}_2\text{-He}$  mixture is shown in fig. 4. It should be noted that the computer model predicts vibrational tempera-

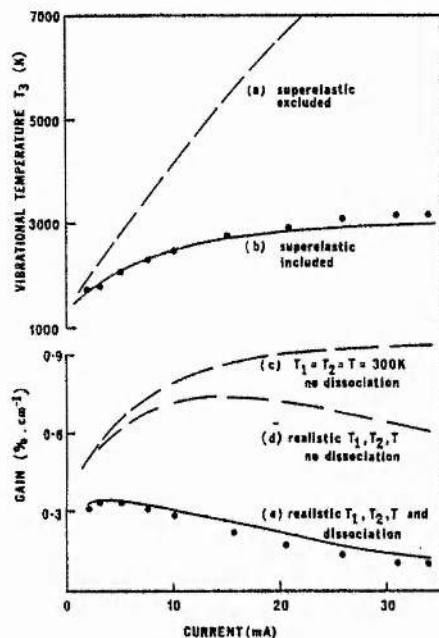


Fig. 4. Comparison of experimental (plotted points) and model (smooth curves) vibrational temperature  $T_3$  and gains for discharges in a sealed 6-12-82,  $\text{CO}_2\text{-N}_2\text{-He}$  gas mixture.

ture variation with electron density rather than with discharge current, so the electron density values have been converted to current values using experimental microwave resonant cavity electron density measurements [9]. Curve (b) shows the predicted vibrational temperature and its saturation with increased current, and exhibits excellent agreement with the experimentally determined points (from fig. 1). The effect of neglecting superelastic collisions in the kinetic model is to remove the saturation effect, producing predicted vibrational temperatures far exceeding the observed values (curve (a)). Clearly superelastic processes are both necessary and sufficient to explain the  $T_3$  saturation and must be included in any detailed model of the  $\text{CO}_2$  laser system.

The analysis is extended in the lower half of fig. 4 to illustrate the relationship of  $T_3$  to  $(00^01)$  small-signal gain (P(18) line). Here we have used the standard expression for the gain at line centre [10]:

$$\alpha_0 = \frac{\lambda^2 A_{21}}{8\pi^2 (\Delta\nu)} g_2 \left( \frac{N_2}{g_2} - \frac{N_1}{g_1} \right), \quad (3)$$

where  $\lambda$  is the transition wavelength,  $A_{21}$  is the spontaneous transition probability, and  $N_2$  and  $N_1$  are the population densities of the upper and lower laser levels with statistical weights  $g_2$  and  $g_1$ . We have taken  $A_{21} = 0.21 \text{ s}^{-1}$  from the measurements of Gerry and Leonard [11], and used Abrams' [12] expression for the pressure broadened linewidth of  $\text{CO}_2\text{-N}_2\text{-He}$  mixtures. The total population of a particular vibrational level ( $N_V$ ) is obtained from the vibrational temperatures (see section 2 above and fig. 2) and the number density ( $N_i$ ) of a rotational sub-level ( $J_i$ ) is given by the usual expression [10]:

$$N_i = N_V (2hcB_i/kT) \exp[-B_i J_i(J_i + 1)hc/kT],$$

$$i = 1, 2, \quad (4)$$

where  $B_1 = 0.3897 \text{ cm}^{-1}$  and  $B_2 = 0.3866 \text{ cm}^{-1}$ .

Curve (c) in fig. 4 is the gain calculated from the measured  $T_3$  (using eqs. (3) and (4)), but assuming  $T_1 = T_2 = T = 300 \text{ K}$  with zero  $\text{CO}_2$  dissociation. The flat shape of this curve reflects the  $T_3$  current dependence. Next we have introduced realistic variations in the ambient gas temperature  $T$  and lower laser level temperatures  $T_1$  and  $T_2$  as listed in table 1. The values of  $T$  are calculated using an empirical fit to the gas heating versus electrical power input data of Shields and Smith [13].  $T_1$  and  $T_2$  were calculated using the straight-line current dependence measured by Siemsen in fig. 9 of [4]. Although the effect of introducing these realistic temperature variations is considerable (fig. 4(d)), the predicted gain curve still differs both in shape and magnitude to that observed. If, however, current-dependent dissociation is introduced on the basis of the measurements in table 1, the predicted gain (fig. 4(e)) agrees very well with the experimental values and the peak occurs at the observed lower discharge current.

Therefore, we draw several conclusions on the modelling of  $\text{CO}_2$  vibrational temperatures and small signal gains. The dominant control on vibrational temperature saturation, and hence on the maximum attainable  $T_3$ , is imposed by electron superelastic processes which limit  $T_3$  to values far below those predicted by previous work, and must be included in any accurate description of the  $\text{CO}_2$  kinetic system. Such a description can successfully predict observed vibrational temperatures (although the precision of agreement of fig. 4 does not occur under all conditions). Both in theory and experiment, the highest values of  $T_3$  are obtained in gas mix-

tures which are low in  $\text{CO}_2$  content. Finally, agreement between the observed and calculated small-signal gains is obtained only when due account is taken of the current dependent  $\text{CO}_2$  dissociation which has the main influence on the gain-current characteristic of sealed and slow-flow discharges, rather than the gas heating effects which are usually invoked.

#### Acknowledgements

We would like to thank Dr. R.M. Thomson for providing us with output from the BOLTZ code including CO and  $\text{O}_2$  gas components, the UK Science Research Council and British Aerospace for financial assistance and to acknowledge the technical assistance of F. Akerboom, N. Campbell and D. Cringean.

#### References

- [1] E.A. Ballik, B.K. Garside, J. Reid and T. Tricker, *J. Appl. Phys.* 46 (1975) 1322.
- [2] A.R. Davies, K. Smith and R.M. Thomson, *J. Appl. Phys.* 47 (1976) 2037.
- [3] J. Reid and K. Siemsen, *Appl. Phys. Lett.* 29 (1976) 250.
- [4] K. Siemsen, J. Reid and C. Dang, *IEEE J. Quant. Electron.* QE-16 (1980) 668.
- [5] C. Dang, J. Reid and B.K. Garside, *IEEE J. Quant. Electron.* QE-16 (1980) 1097.
- [6] J. Mellis and A.L.S. Smith, 5th British National Quantum Electronics Conf. (Hull 1981), in press.
- [7] R.L. Taylor and S. Bitterman, *Rev. Mod. Phys.* 41 (1969) 26.
- [8] R.M. Thomson, K. Smith and A.R. Davies, *Comp. Phys. Comm.* 11 (1976) 369.
- [9] J. Mellis and A.L.S. Smith, to be published.
- [10] A.M. Robinson, *Can. J. Phys.* 50 (1972) 2471.
- [11] E.T. Gerry and D.A. Leonard, *Appl. Phys. Lett.* 8 (1966) 227.
- [12] R.L. Abrams, *Appl. Phys. Lett.* 25 (1974) 609.
- [13] H. Shields and A.L.S. Smith, *J. Appl. Phys.* 48 (1977) 4807.

## Operating efficiencies in pulsed carbon dioxide lasers

A. L. S. Smith and J. Mellis

Department of Natural Philosophy, University of Strathclyde, Glasgow G4 ONG, Scotland, United Kingdom

(Received 19 July 1982; accepted for publication 17 September 1982)

Computer models of the  $\text{CO}_2\text{-N}_2\text{-He}$  laser system usually predict that 20%–33% of the discharge energy should be available as radiation output. Using a comprehensive kinetics model to study vibrational temperatures and stored energies, we find a deterioration in laser efficiency with increasing input energy, due to electron superelastic losses during the excitation pulse.

Experimental observations support the calculated vibrational temperatures and likewise our predicted 8%–12% yield efficiency at optimum excitation is in good agreement with the values realized in working lasers.

PACS numbers: 42.55.Dk

The high excitation efficiency for the  $\text{CO}_2$  laser, due mainly to the large  $\text{N}_2$  and  $\text{CO}_2(\nu_3)$  cross sections for vibrational excitation by electron impact, was first enumerated in the work of Nighan,<sup>1</sup> Nighan and Bennett,<sup>2</sup> and Lowke *et al.*,<sup>3</sup> who calculated the fractional power lost from the discharge electrons by inelastic processes in the  $\text{CO}_2\text{-N}_2\text{-He}$  system. At typical values of the operating  $E/N$ , their calculations predict that 50%–80% of the electrical input power is used usefully in  $\text{N}_2$  and  $\text{CO}_2(\nu_3)$  vibration excitation ( $\eta_{\text{ex}} = 50\%\text{--}80\%$ ). After allowing for the quantum efficiency of the  $\text{CO}_2$  transition ( $n_q \sim 41\%$ ) and assuming optical cavity and other losses are small, predicted radiation yield efficiencies ( $\eta_y = \eta_{\text{ex}} \eta_q$ ) are in the range 20%–33%. Although such values have been approached in practice, many observers have reported a deterioration in laser performance with increasing discharge excitation in both cw and TE devices. Ballik *et al.*<sup>4</sup> considered the reduction in pumping efficiency experienced in a low pressure TE resistor-pin amplifier, and conclude that the mechanism responsible was not connected with the well-known effects of gas heating or discharge instability. Another explanation<sup>5</sup> suggested the "overpumping" of the  $\text{N}_2$  and  $\text{CO}_2(\nu_3)$  modes to vibrational temperatures above 4000 K, the optimum for (00<sup>1</sup>) level population density. This has been precluded, however, by experimental observations of  $\text{CO}_2(\nu_3)$  mode temperature ( $T_3$ ) saturation at low values ( $\sim 2500$  K) under various conditions. Such experiments<sup>6,7</sup> use a probe oscillator-gain cell technique to measure fundamental (00<sup>1</sup>) band and sequence (00<sup>2</sup>) band small-signal gains in  $\text{CO}_2$  discharges; the (00<sup>0</sup> $n$ ) mode temperature  $T_3$  is then derived from the (00<sup>2</sup>)/(00<sup>1</sup>) gain ratio.

Recently, we have used a computer model of the  $\text{CO}_2$  kinetic system to study the behavior of vibrational temperatures in low pressure cw discharges.<sup>7,8</sup> The calculations agree well with the available experimental data, and the process responsible for vibrational temperature saturation has been identified as the deactivation of vibrationally excited  $\text{N}_2$  and  $\text{CO}_2$  molecules by electron superelastic collisions. In the cw laser oscillator electron superelastic, stimulated, and molecular collisional de-excitation are all important and occur simultaneously, whereas in a TE oscillator the situation is different: it is usual for laser action to be inhibited during the current pulse by the large population excited to the  $\text{CO}_2(\nu_1, \nu_2)$  mode which contains the lower laser level. This

population relaxes on a time scale approximately 1  $\mu\text{s}$  after the end of the excitation pulse, and only then does oscillation occur. Under these circumstances, superelastic losses during the current pulse should limit the vibrational energy available for subsequent conversion to laser radiation. To our knowledge, the only measurements of vibrational temperatures in atmospheric pressure TE discharges are those of Lavigne *et al.*,<sup>9</sup> which are restricted to low input energies and show little evidence of  $T_3$  saturation. However, experiments by Dang *et al.*<sup>10</sup> on a 92 Torr TE amplifier revealed a strong saturation of  $T_3$  (and hence stored vibrational energy) as measured at the time of peak gain.

We have adapted our vibrational kinetics model to produce the time evolution of vibrational temperatures, during and after the excitation pulse, in conditions appropriate to moderate and high pressure TE laser discharges. The calculations assume a current pulse of square profile, with constant electron density ( $n_e$ ) and effective electric field ( $E/N$ ). Electron excitation rates are taken from a numerical solution of the Boltzmann equation.<sup>11</sup> These are relatively weak functions of gas mixture in the optimum  $E/N$  range, but our results assume a 13  $\text{CO}_2$ , 9  $\text{N}_2$ , and 78 He mixture with  $E/N = 3.0 \times 10^{-16}$  V  $\text{cm}^2$ . Superelastic de-excitation rate constants are calculated from the appropriate excitation rate constants by applying the principle of detailed balance.<sup>12</sup> The excitation rates (quanta  $\text{cm}^3 \text{s}^{-1}$ ) are scaled to discharge energy inputs,  $E_{\text{in}}$  ( $\text{J l}^{-1} \text{atm}^{-1}$ ), with knowledge of the operating pressure and excitation pulse length, and assuming the  $\text{N}_2 + \text{CO}_2(\nu_3)$  pumping efficiency  $\eta_{\text{ex}}$  is 60%, in keeping with the results of Refs. 1–3 for our assumed optimum  $E/N$  ( $3.0 \times 10^{-16}$  V  $\text{cm}^2$ ).

Computed results for an atmospheric pressure, 100 ns excitation pulse,  $\text{CO}_2\text{-N}_2\text{-He}$  laser are shown in Fig. 1. Due to the large  $\text{N}_2$  electron excitation rate the nitrogen vibrational temperature  $T_4$  is greater than  $T_3$  throughout the excitation period, although superelastic collisions moderate the rate of increase of  $T_4$  as the excited population rises. In the time period following current switch off,  $\text{N}_2 \leftrightarrow \text{CO}_2(\nu_3)$  V-V exchange tends to equilibrate  $T_3$  and  $T_4$ . The initial fall in  $T_3$  is caused by the draining of population from the  $(\nu_1, \nu_2)$  mode to the ground state, reducing the effective temperature of the  $\nu_3$  mode. The clearing of the population of the mode containing the lower laser level is completed approximately 1  $\mu\text{s}$

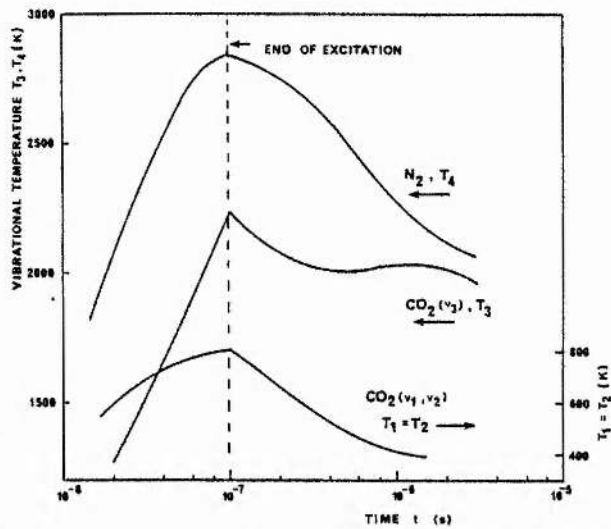


FIG. 1. Calculated time evolution of vibrational temperatures in 13 CO<sub>2</sub>: 9 N<sub>2</sub>: 78 He, 760 Torr, 100-ns excitation pulse. Energy input is  $E_{in} = 400 \text{ J l}^{-1} \text{ atm}^{-1}$ .

after the excitation ends, and this is the time of maximum population inversion and peak gain. Both  $T_3$  and  $T_4$  continue to decrease slowly under the influence of  $V-V-T$  and  $V-T$  molecular collisional relaxation, to which the CO<sub>2</sub> is much more susceptible. Thus,  $T_3$  remains depressed relative to  $T_4$  during this relaxation period.

Figure 2 shows comparable results for the same gas mixture at 92 Torr total pressure with a 200-ns excitation pulse, chosen to stimulate the conditions of Dang *et al.*<sup>10</sup> Here, the reduced pressure increases the characteristic time for  $V-V$  energy exchange and the peak gain is delayed until 10–15  $\mu\text{s}$  after the current pulse, in good agreement with the experimental observations. A series of such calculations was performed for different input energies (see Fig. 2 for 25 and 250  $\text{J l}^{-1} \text{ atm}^{-1}$ ) and there was little variation in the peak

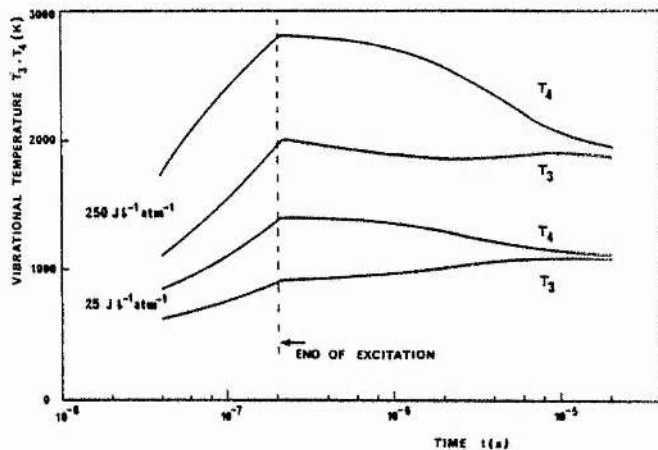


FIG. 2. Calculated vibrational temperature time evolutions for 200-ns excitation pulse in 92 Torr 13 CO<sub>2</sub>: 9 N<sub>2</sub>: 78 He. Upper curves  $E_{in} = 250 \text{ J l}^{-1} \text{ atm}^{-1}$ , lower curves  $E_{in} = 25 \text{ J l}^{-1} \text{ atm}^{-1}$ .

gain time. Figure 3 shows the peak gain vibration temperatures for the conditions of Figs. 1 and 2, and also for the conditions of the laser of Lavigne *et al.*, which used a La-flamme-type double discharge geometry with long excitation pulses<sup>13,14</sup> of duration 2–5  $\mu\text{s}$ . We have found that the best agreement between our calculations and the results of Lavigne *et al.* is obtained for a 3- $\mu\text{s}$  pulse length, resulting in a peak gain time of  $t = 5 \mu\text{s}$  [curve (a), Fig. 3]. Strong saturation of vibrational temperature  $T_3$  is predicted for  $E_{in} \gtrsim 200 \text{ J l}^{-1} \text{ atm}^{-1}$ . Also plotted in Fig. 3 are results calculated for the conditions of Dang *et al.* [curve (b)]. In this case agreement with experiment is excellent throughout the range of input energy. Finally, curve (c) shows the predicted  $T_3$  saturation for the short-pulse atmospheric pressure conditions typical of modern photopreionized TEA lasers. It is interesting to note the similarity between (a), (b), and (c), suggesting that  $E_{in} (\text{J l}^{-1} \text{ atm}^{-1})$  remains a reasonable scaling parameter despite the differences in operating pressure and excitation pulse length.

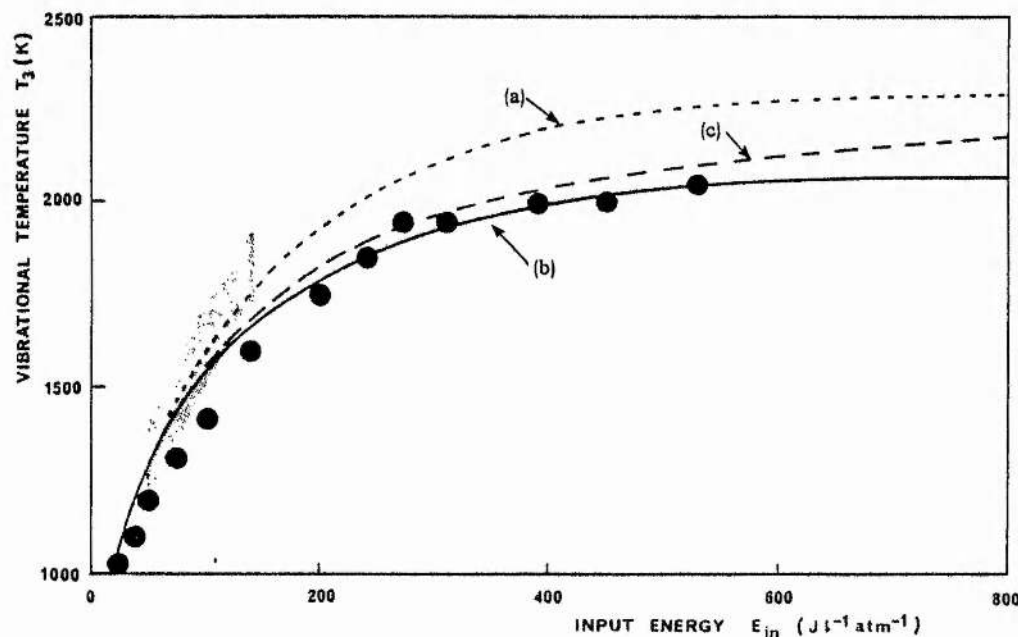


FIG. 3. Calculated CO<sub>2</sub>( $v_3$ ) vibrational temperatures ( $T_3$ ) at time of peak gain vs input energy for CO<sub>2</sub>: N<sub>2</sub>: He mixture 13:9:78; (a) 760 Torr, 3- $\mu\text{s}$  excitation pulse, and corresponding experimental results of Lavigne *et al.* (20:10:70 mix, shaded area); (b) 92 Torr, 200-ns pulse and corresponding results of Dang *et al.* (13:10:77, ●); (c) 760 Torr, 100-ns pulse.

```

100 VIBEX SIMULATES THE VIBRATIONAL ENERGY EXCHANGE PROCESSES IN THE CO2
200 LASER SYSTEM. THE NON-LINEAR DIFFERENTIAL EQUATIONS DESCRIBING THE
300 RATES OF POPULATION CHANGES BETWEEN THE VIBRATIONAL MODES ARE SOLVED
400 USING THE IMPROVED EULER METHOD FOLLOWED BY PREDICTOR-CORRECTOR
500 ITERATIONS. IT IS ASSUMED THAT A BOLZEMANN DISTRIBUTION DESCRIBES THE
600 DISTRIBUTION OF POPULATION WITHIN ANY VIBRATIONAL MODE. THUS THE
700 VIBRATIONAL TEMPERATURE OF A MODE IS A FUNCTION OF THE GROUND
800 STATE AND TOTAL EXCITED STATE POPULATIONS, AND IN TURN THE POPULATION
900 OF ANY INDIVIDUAL VIBRATIONAL LEVEL MAY BE CALCULATED
1000
1100
1200
130 FUNCTION QUART(X, CF4, CF2)
140 QUART=CF4*X**4-CF2*X**2+1.0
150 RETURN
160 END
170 SUBROUTINE LASE(DT3, DT2, DTEMP, ESTIM, DELEN)
180 COMMON PTOT, FCO2, FCO, FN2, F02, FHE, TEMP, RAD1
190C CALCULATES STIMULATED EMISSION RATE
200 ZL=10.57E-4
210C LASER WAVE LENGTH IN CM
220 A=0.21
230 ZJ2=17.0
240 ZJ1=16.0
250 PI=3.1416
260 ZK=1.32E-23
270 CVRT=1.386E-23
280C CONVERTS FROM CM-1 TO J
290 THETA=6.626E-34*2.997E8/ZK
300C THETA IS HC OVER K
310 HW=7.58+PTOT*(300/TEMP)**0.5*1.0E3/2.0*(FCO2+0.73*(FN2+FCO)+0.64*FHE)
320C HW IS HALFWIDTH OF PRESSURE BROADENED LINE ACCORDING TO ABRAMS(SEC-1)
330C WITH CO TREATED AS EQUIVALENT TO N2
340 CO=1.0/(PI*HW)
350C LINE SHAPE FUNCTION
360 W=ZL**2/(8.0*PI)*A*(2.0*ZJ2+1.0)*CO
370C NOW CALCULATE POP. INVERSION
380 CN=FCO2*PTOT*3.5258E16
390C TOTAL CO2 NO. DENSITY
400
410
420
430 X1=EXP(-1337*CVRT/(ZK*DT3))
440 X2=EXP(-667*CVRT/(ZK*DT2))
450 X3=EXP(-2349*CVRT/(ZK*DT3))
460 ZQ=((1-X1)*(1-X2)**2*(1-X3))**(-1)
470C VIB. PARTITION FUNCTION
480 DNU=CN*X3/ZQ
490 DNL=CN*X1/ZQ
500C 001, 100 LEVEL POPS.
510 B1=0.3897E2
520 B2=0.3866E2
530C ROTATIONAL CONSTANTS
540 DN2=DNU*2*B2*(THETA/TEMP)*EXP(-B2*ZJ2*(ZJ2+1)*(THETA/TEMP))
550 DN1=DNL*2*B1*(THETA/TEMP)*EXP(-B1*ZJ1*(ZJ1+1)*(THETA/TEMP))
560C UPPER, LOWER ROTL. SUB POPS WITH DEGENERACIES CANCELLED
570 DELEN=DN2-DN1
580 ESTIM=DELEN*W*RAD1/1.372E-20
590C ESTIM IN /SEC/CM; 1.372E-20 IS ENERGY OF 10.6 MICRON PHOTON
600 RETURN
610 END

```



```

20 SUBROUTINE STEPS(DUM1, DC3, DC2, X1, X2)
30 H=0.02
40 X=0.75
50 Y1=DUM1(X, DC3, DC2)
60 1 X=X+H
70 Y2=DUM1(X, DC3, DC2)
80 IF(Y2*Y1)3, 2, 2
90 2 Y1=Y2
00 GO TO 1
10 3 X1=X-H
20 X2=X
30 RETURN
40 END
50 SUBROUTINE ZERO2(DUM2, DC3, DC2, A, B, VA, VB, X)
60 X=(A*VB-B*VA)/(VB-VA)
70 9 X1=X
80 V=DUM2(X, DC3, DC2)
90 IF(V)11, 15, 10
00 10 B=X
10 VB=V
20 GO TO 12
30 11 A=X
40 VA=V
50 12 X=(A+B)/2.0
60 V=DUM2(X, DC3, DC2)
70 IF(V)14, 15, 13
80 13 B=X
90 VB=B
00 GO TO 15
10 14 A=X
20 VA=V
30 15 X=(A*VB-B*VA)/(VB-VA)
40 D1=0.001
50 IF(ABS(X1-X)/X-D1)16, 15, 9
60 16 RETURN
70 END
80C
90 SUBROUTINE CTEMP(PN1, PN2, DT3, DT2)
000 EXTERNAL QUART
010C CALCULATES CO2 VIB TEMPS GIVEN (LMO) AND (OON) GROUP POPULATIONS
020 COMMON/AREA2/TCO2
030 COL=1-(1+PN2/(TCO2-PN2-PN1))**(-1)
040
050
060 HOL=ALOG(COL)
070 CONT=1.502E-19/1.390E-23
080C CONVERTS EV TO J AND DIVIDES BY BOLTZMANN'S CONSTANT
090 DT3=-0.2913*CONT/HOL
100
110
120 12 CONTINUE
130 COF4=(1-COL)*TCO2/(TCO2-PN2-PN1)
140 COF2=PN1/(TCO2-PN2-PN1)+2.0
150 CALL STEPS(QUART, COF4, COF2, BU, BU)
160 V1=QUART(BU, COF4, COF2)
170 V2=QUART(BU, COF4, COF2)
180 CALL ZERO2(QUART, COF4, COF2, BU, BU, V1, V2, ROOT)
190
200 ROL=1.0-ROOT
210C ROL IS EXP(-HV/KT2)
220
230
240 DT2=-0.0827*CONT/ALOG(ROL)

```

```

250 GO TO 30
260
270
280 30 CONTINUE
290 RETURN
300 END
310 SUBROUTINE SUPER(DELE,DELTEMP,DSUM)
320 DSUM=0.0
330 DO 10 I=1,8
340 TERM=EXP(I*DELE*1.24E-4/DELTEMP)
350 10 DSUM=DSUM+TERM
360C 1.24E-4 CONVERTS CM-1 TO EV
370 RETURN
380 END
390C.....
400C.....
410C.....MAIN.....
420C.....
430 R1(X2,X1,STIM)=TK21*X2-TK10*X1+TK01*(TCO2-X1-X2)+OMGA*(TCO2-X1-X2)
440* +STIM
450 R2(X1,X2,X3,X4,STIM)=ALPH*(TCO2-X1-X2)-ZETA*X2-VK32*(TCO2-X1-X2)*
460* X3+(-STIM)+
470* VK42*(TCO2-X1-X2)*X4-VK23*X2*(TN2-X3)-VK24*X2*(TCO-X4)-TK21*X2
480 R3(X3,X1,X2,X4)=GAMM*(TN2-X3)-EPSI*X3-VK32*X3*(TCO2-X1-X2)+VK43*X4*
490* (TN2-X3)-VK34*(TCO-X4)*X3+VK23*X2*(TN2-X3)
500 R4(X4,X3,X1,X2)=BETA*(TCO-X4)-DELT*X4-VK43*(TN2-X3)*X4+VK34*X3*(TCO-X4)
510* -VK42*(TCO2-X1-X2)*X4+VK24*X2*(TCO-X4)
520 EXTERNAL QUART
530 COMMON PTOT,FCO2,FCO,FM2,FO2,FHE,TEMP,RADI
540 COMMON/AREA2/TCO2
550
560 WRITE(S,111)
570 MAX=99
580 CHANGE=1.0E-4
590 TOLER=1.0E-4
600 CLOS=8.6E15
610 VK23=9.0E9/CLOS
620 VK42=3.5E9/CLOS
630 VK34=7.0E2/CLOS
640 READ(S,115)ELN
650 WRITE(S,112)
660 READ(S,117)RADI
670
680 TEMP=350.0
690 ALPH=ELN*5.57E-9
700 BETA=ELN*3.27E-8
710 GAMM=ELN*2.60E-8
720 OMGA=ELN*4.57E-8
730C E/N=3.0E-16,DISB=0.0,13-9-78 MIX
740 DIMENSION E(7),E(7),Z(7),A(7),B(7)
750 100 PTOT=30.0
760 FCO2=9.6
770 FCO=0.001
780 FM2=10.9
790 FHE=79.5
800 FO2=0.00
810
820
830 111 FORMAT("ENTER ELECTRON DENSITY (PER CC)")
840 112 FORMAT("ENTER RADIATION INTENSITY (W cm-2)")
850 115 FORMAT(E10.4)
860 117 FORMAT(F6.2)
870 A(1)=400.00/CLOS

```

```

70 A(1)=400.00/CLOS
80
90 A(2)=150.0/CLOS
00 A(3)=300.0/CLOS
10 A(4)=170.0/CLOS
20 A(5)=100.0/CLOS
30 B(1)=6.0E-15
40 B(2)=2.0E-15
50 B(3)=6.9E-13
60 B(4)=2.0E-15
70 B(5)=0.15E-12
80 Z(1)=0
90 Z(2)=0
00 Z(3)=0
10 Z(4)=0
20 Z(5)=0
30 D(1)=0
40 D(2)=0
50 D(3)=3.7E-19
60 D(4)=1.0E-16
70 D(5)=3.7E-17
80 E(1)=0
90 E(2)=1.0E-18
00 E(3)=0
10 E(4)=1.0E-18
20 E(5)=5.3E-18
30 WRITE(6,151)FCO2,FN2,FCO,FO2,FHE
40 151 FORMAT(2X,"GAS MIX IS ",5(F4.1,1X),"CO2/N2/CO/O2/HE")
50
60
70 WRITE(6,155)PTOT,TEMP
80 155 FORMAT(2X,"TOTAL PRESSURE= ",F5.2," TORR   GAS TEMP= ",F5.2," K")
90   CLOS=0.35353E 17
000 WRITE(6,166)CLOS
010 166 FORMAT(2X,"CLOS= ",E10.4)
020C CLOS IS LOSCHMIDTS NUMBER( MOLECULES-PER CCP&PER TORR )
030 RATIO=CLOS*PTOT/100.
040 WRITE(6,183)RATIO
050 183 FORMAT(1X,"RATIO=",E10.4)
060 TCO2=RATIO*FCO2
070 TCO=RATIO*FCO
080 TN2=RATIO*FN2
090 TO2=RATIO*FO2
000 THE=RATIO*FHE
010 WRITE(6,233)TCO2,TN2,TCO,TO2,THE
020 233 FORMAT(5(2X,E10.4),1X,"TOT DENS")
030 WRITE(6,250)ELN
040 250 FORMAT(2X,"ELECTRON DENSITY= ",E10.4," CM-3")
050 WRITE(6,251)RADI
060 251 FORMAT(2X,"RADIATION INTENSITY= ",F7.2," W cm-2")
070 WAVE=1.986E-23/1.38E-23
080C WAVE IS A CONVERTER FROM CM**-1 TO JOULES, UPON BOLTZMANNS CONST
090 VK32=VK23*EXP(-19.0*WAVE/TEMP)
000 VK24=VK42*EXP(206.0*WAVE/TEMP)
010 VK43=VK34*EXP(-198.0*WAVE/TEMP)
020
030
040
050
060
070

```

```

480 340 CONTINUE
490
500
510
520
530 ELTEMP=1.80
540 ZETA=Z(1)*TCO2+Z(2)*TN2-Z(3)*TCO+Z(4)*TC2+Z(5)*THE
550
560 DELT=D(1)*TCO2+D(2)*TN2-D(3)*TCO+D(4)*TC2+D(5)*THE
570 EPSI=E(1)*TCO2+E(2)*TN2+E(3)*TCO+E(4)*TC2-E(5)*THE
580 CALL SUPER(2349.0, ELTEMP, SUMZ)
590 ZETA=ZETA+(ALPH/8.0)*SUMZ
600 CALL SUPER(2330.0, ELTEMP, SUME)
610 EPSI=EPSI+(GAMM/8.0)*SUME
620 CALL SUPER(2150.0, ELTEMP, SUMD)
630 DELT=DELT+(BETA/8.0)*SUMD
640C 2349, 2330, 2150 ARE ENERGIES IN CM-1 OF CO2(001), N2(V=1), CO(V=1) RESPY.
650 TK21=A(1)*TCO2+A(2)*TN2+A(3)*TCO+A(4)*TC2+A(5)*THE
660 TK10=B(1)*TCO2+B(2)*TN2+B(3)*TCO+B(4)*TC2+B(5)*THE
670 TX1=EXP(-1337.0*WAVE/TEMP)
680 TX2=EXP(-667.0*WAVE/TEMP)
690 RLM0=1.0/(1.0-TX1)-1.0+TX2/((1.0-TX2)**2.0)+1.0/(1.0-TX2)-1.0
700C RLM0 IS RATIO OF LMO TO GROUND STATE POPULATION AT EQUILIBRIUM TEMP
710 TK01=TK10*RLM0
720C THIS COMPUTES TK01 BY DETAILED BALANCING
730 TK10=TK10+EXP(667.0*1.24E-4/ELTEMP)*OMGA
740C THIS ADDS SUPERELASTIC CONTRIBUTION TO TK10
750C INITIAL CONDITIONS NOW STATED
760 X10=0.1*TCO2
770 X20=0.001*TCO2
780 X30=0.01*TN2
790 X40=0.1*TCO
800 CALL CTEMP(X10, X20, T30, T20)
810
820
830 CALL LAGE(T30, T20, TEMP, STIM0, ZINV)
840 T0=0
850 H=0.5E-5
860C THIS SPECIFIES THE TIME STEP IN THE PREDICTOR EQUATIONS
870 WRITE(6, 558)H
880 558 FORMAT(2X, "TIME STEP= ", E10.4, " SECONDS")
890 R10=R1(X20, X10, STIM0)
900 R20=R2(X10, X20, X30, X40, STIM0)
910 R30=R3(X30, X10, X20, X40)
920 R40=R4(X40, X30, X10, X20)
930 WRITE(6, 592)
940 592 FORMAT(2X, "INITIAL EXCITED POPULATIONS AS FOLLOWS")
950 WRITE(6, 594)
960 594 FORMAT(5X, "LM0", 10X, "OON", 10X, "N2", 10X, "CO", 10X, "T")
970 WRITE(6, 596)X10, X20, X30, X40, T0
980 596 FORMAT(4(2X, E10.4), 5X, E10.4)
990 R10H=R1(X20+H*R20, X10+H*R10, STIM0)
000 R20H=R2(X10+H*R10, X20+H*R20, X30+H*R30, X40+H*R40, STIM0)
010 R30H=R3(X30+H*R30, X10+H*R10, X20+H*R20, X40+H*R40)
020 R40H=R4(X40+H*R40, X30+H*R30, X10+H*R10, X20+H*R20)
030
040
050C NOW THE IMPROVED EULER METHOD IS USED TO PREDICT X11, X21, X31, X41
060 CONTINUE
070 T1=T0+H
080 WRITE(6, 103)T1
090 103 FORMAT(2X, "TIME T =", E10.4)
100

```

```

10 X11=X10+H/2*(R10+R10H)
20 X21=X20+H/2*(R20+R20H)
30 X31=X30+H/2*(R30+R30H)
40 X41=X40+H/2*(R40+R40H)
50
60 CALL CTEMP(X11, X21, T31, T21)
70 CALL LASE(T21, T21, TEMP, STIM1, ZINV)
80
90
100
110 710 CONTINUE
120 T1=T1+H
130 R11=R1(X21, X11, STIM1)
140 R21=R2(X11, X21, X31, X41, STIM1)
150 R31=R3(X31, X11, X21, X41)
160 R41=R4(X41, X31, X11, X21)
170
180
190 X12=X10+2.0*H*R11
200 X22=X20+2.0*H*R21
210 X32=X30+2.0*H*R31
220 X42=X40+2.0*H*R41
230 STIM2=STIM1
240
250C THESE PREDICTIONS FOR X1(2), X2(2) ETC, ARE NOW CORRECTED
260 X12OLD=X12
270 X22OLD=X22
280 X32OLD=X32
290 X42OLD=X42
300 ITN=1
310 870 CONTINUE
320 R12=R1(X22, X12, STIM2)
330 R22=R2(X12, X22, X32, X42, STIM2)
340 R32=R3(X32, X12, X22, X42)
350 R42=R4(X42, X32, X12, X22)
360 X12NEW=X11+H/2*(R11+R12)
370 X22NEW=X21+H/2*(R21+R22)
380 X32NEW=X31+H/2*(R31+R32)
390 X42NEW=X41+H/2*(R41+R42)
400
410
420C TEST FOR CONVERGENCE FOLLOWS
430 IF (ABS((X22NEW-X22)/X22NEW)-TOLER)980, 1010, 1010
440 980 IF(ABS((X12NEW-X12)/X12NEW)-TOLER)990, 1010, 1010
450 990 IF(ABS((X32NEW-X32)/X32NEW)-TOLER)1000, 1010, 1010
460
470
480 1000 IF(ABS((X42NEW-X42)/X42NEW)-TOLER)1005, 1010, 1010
490 1005 IF(ABS((X22NEW-X22)/X22NEW)-TOLER)1100, 1010, 1010
500 1010 ITN=ITN+1
510
520
530 IF(ITN-MAX)1050, 1030, 1030
540 1030 WRITE(5, 1040)MAX
550 1040 FORMAT(3X, "FAILS TO CONVERGE IN", I3, "ITERATIONS")
560 GO TO 1380
570 1050 X12=X12NEW
580 X22=X22NEW
590 X32=X32NEW
600 X42=X42NEW
610 CALL CTEMP(X12, X22, T32, T22)
620 CALL LASE(T32, T22, TEMP, STIM2, ZINV)

```

```

40 1090 GO TO 870
50 1100 ERRX1=0.2*(X12OLD-X12NEW)
60   ERRX2=0.2*(X22OLD-X22NEW)
70   ERRX3=0.2*(X32OLD-X32NEW)

80   ERRX4=0.2*(X42OLD-X42NEW)
90
900
910 X12=X12NEW+ERRX1
920 X22=X22NEW+ERRX2
930 X32=X32NEW+ERRX3
940 X42=X42NEW+ERRX4
950C THESE ARE THE CORRECTED VALUES OF X1,X2,X3,X4 AT T=T2
960
970
980 CALL CTEMP(X12, X22, T32, T22)
990 CALL LASE(T32, T22, TEMP, STIM2, ZINV)
990
910 IF(((X12-X11)/X11)*100, -CHANGE)1220, 1250, 1250
920 1220 IF(((X22-X21)/X21)*100, -CHANGE)1230, 1250, 1250
930 1230 IF(((X32-X31)/X31)*100, -CHANGE)1240, 1250, 1250
940 1240 IF(((X42-X41)/X41)*100, -CHANGE)1340, 1250, 1250
950 1250 X10=X11
960 X20=X21
970 X30=X31
980 X40=X41
990 X11=X12
990 X21=X22
990 X31=X32
990 X41=X42
990 CALL CTEMP(X11, X21, T31, T21)
990 CALL LASE(T31, T21, TEMP, STIM1, ZINV)
990
990 IDBUG=0
990 IF(IDBUG.EQ.0)GOTO 1300
990 WRITE(6, 1305)T31, T21, T1, ITN
990 1305 FORMAT(3(2X, E10.4), I4)
990 1300 CONTINUE
990 IF(T1.LE.1.0E-4)GO TO 710
990 H=0.5E-5
990 IF(T1.LE.1.0E-3)GO TO 710
990 H=0.5E-5
990 IF(T1.LE.1.0E-2)GO TO 710
990 H=1.0E-5
990 IF(T1.LT.1.0E-1)GO TO 710
990 H=2.0E-5
990 GO TO 710
990 1340 WRITE(6, 85)CHANGE
990 85 FORMAT(3X, "POPN. BALANCE ESTABLISHED WITHIN", F8.5, " % PER TIMESTEP")
990 COL=1-(1+X22/(TCO2-X22-X12))**(-1)
990 HCL =ALOG(COL)

```

```

180
190 CONT=1.502E-19/1.890E-23
200 T3=-0.1918*CONT/HOL
210 POL=1-(TN2-X32)/TN2
220 TEMPN=-0.2889*CONT/ALOG(POL)
230 GOL=1-(T50-X42)/T50
240 TEMPC=-0.2866*CONT/ALOG(GOL)
250 COF4=(1-GOL)*TCO2/(TCO2-X12-X32)
260 COF2=X12/(TCO2-X22-X12)+2.0
270 CALL STEPS(QUART,COF4,COF2,BL,BU)
280 V1=QUART(BL,COF4,COF2)
290 V2=QUART(BU,COF4,COF2)
300 CALL ZEPD2(QUART,COF4,COF2,BL,BU,V1,V2,ROOT)
310 ROL=1.0-ROOT
320 ROL IS EXP(-HVE/KT2)
330 T2=-0.0827*CONT/ALOG(ROL)
340 WRITE(6,1363)
350 1363 FORMAT(1X,"EQUILIBRIUM VIBRATIONAL TEMPERATURES (KELVIN) ARE")

360 WRITE(6,1365)
370 1365 FORMAT(5X,"CO2(OON)",10X,"N2",10X,"CO",10X,"CO2(LM0)")
380 WRITE(6,1367)T3,TEMPN,TEMPC,T2
390 1367 FORMAT(4(4X,E10.4))
400 WRITE(6,1369)T1
410 1369 FORMAT(1X,"TIME AT STEADY STATE= ",E10.4," SECONDS")
420 WRITE(6,1375)X22
430 1375 FORMAT(1X,"OON MODE POPULATION = ",E10.4," PER CC")
440 WRITE(6,1377)X12
450 1377 FORMAT(1X,"LM0 MODE POPULATION = ",E10.4," PER CC")
460 WRITE(6,1378)STIM2
470 1378 FORMAT(1X,"STIMULATED EMISSION RATE= ",E10.4," cm-3.sec-1")
472 WRITE(6,1379)ZINV
474 1379 FORMAT(1X,"ROTATIONAL POPULATION INVERSION= ",E10.4," PER CC")
480 1380 STOP
490 END

```